



HAL
open science

Clinical dosimetry in Molecular Radiotherapy

Gunjan Kayal

► **To cite this version:**

Gunjan Kayal. Clinical dosimetry in Molecular Radiotherapy. Medical Imaging. Université Paul Sabatier - Toulouse III, 2022. English. NNT : 2022TOU30018 . tel-03715049

HAL Id: tel-03715049

<https://theses.hal.science/tel-03715049>

Submitted on 6 Jul 2022

HAL is a multi-disciplinary open access archive for the deposit and dissemination of scientific research documents, whether they are published or not. The documents may come from teaching and research institutions in France or abroad, or from public or private research centers.

L'archive ouverte pluridisciplinaire **HAL**, est destinée au dépôt et à la diffusion de documents scientifiques de niveau recherche, publiés ou non, émanant des établissements d'enseignement et de recherche français ou étrangers, des laboratoires publics ou privés.



THÈSE

En vue de l'obtention du
DOCTORAT DE L'UNIVERSITÉ DE TOULOUSE
Délivré par l'Université Toulouse 3 - Paul Sabatier

Présentée et soutenue par
Gunjan KAYAL

Le 31 mars 2022

Dosimétrie clinique en radiothérapie moléculaire

Ecole doctorale : **GEETS - Génie Electrique Electronique, Télécommunications et Santé : du système au nanosystème**

Spécialité : **Radiophysique et Imagerie Médicales**

Unité de recherche :
CRCT - Centre de Recherche en Cancérologie de Toulouse

Thèse dirigée par
Manuel BARDIES et Maxime CHAUVIN

Jury

M. Gerhard GLATTING, Rapporteur
Mme Marta CREMONESI, Rapporteur
M. Luc SIMON, Examineur
M. Ludovic FERRER, Examineur
M. Florent CACHIN, Examineur
M. Pierre PAYOUX, Examineur
M. Manuel BARDIES, Directeur de thèse
M. Maxime CHAUVIN, Co-directeur de thèse



THÈSE

En vue de l'obtention du
DOCTORAT DE L'UNIVERSITÉ DE TOULOUSE
Délivré par l'Université Toulouse 3 - Paul Sabatier

Présentée et soutenue par
Gunjan KAYAL

Le 31 mars 2022

Dosimétrie clinique en radiothérapie moléculaire

Ecole doctorale : **GEETS - Génie Electrique Electronique, Télécommunications et Santé : du système au nanosystème**

Spécialité : **Radiophysique et Imagerie Médicales**

Unité de recherche :
CRCT - Centre de Recherche en Cancérologie de Toulouse

Thèse dirigée par
Manuel BARDIES et Maxime CHAUVIN

Jury

M. Gerhard GLATTING, Rapporteur
Mme Marta CREMONESI, Rapporteur
M. Luc SIMON, Examineur
M. Ludovic FERRER, Examineur
M. Florent CACHIN, Examineur
M. Pierre PAYOUX, Examineur
M. Manuel BARDIES, Directeur de thèse
M. Maxime CHAUVIN, Co-directeur de thèse

sck cen
Exploring a better tomorrow



Inserm

La science pour la santé
From science to health

Acknowledgements

My dissertation is capable of awarding just one doctoral degree, despite the fact that it is the culmination of the efforts of several individuals who mentored and supported me during this PhD. There is no better place to express my gratitude than at the outset of my dissertation. This thesis is more than my efforts at the keyboard; it represents a milestone in almost four years of collaboration, particularly between the two teams: CRCT, INSERM, and SCK CEN. Since the beginning of my PhD, I have felt home. Throughout this timespan, I've been entrusted with one-of-a-kind opportunities, which I have embraced. This among all others, include learning from experts in nuclear medicine or multidisciplinary fields; visiting any lab; participating in any conference (with or without accepted work) or webinar/seminars, or participating in European and international level research projects. Many individuals from all around the world have enhanced my life in ways I never imagined. I would like to express my heartfelt gratitude to everyone, but words would likely fall short.

I am indebted to my supervisor Dr *Manuel Bardiès* from CRCT, INSERM Toulouse, France (and currently at IRCM, ICM Montpellier), without whom this research would not have been achievable. From inception to the completion of this thesis, Manu (as he is affectionately known) has not only aided in the research but also emotionally bolstered my confidence. His vast knowledge, motivation, and patience have infused me with the zeal and spirit to excel in research work. Recently, when he was presenting my work at one of the seminars in my absence, he said something like 'you would have done the presentation better, I simply tried' in order to encourage me and boost my morale. How could I forget his unwavering support and freedom he offered me to dive in a range of research initiatives? He has played a major role in polishing my research writing skills. His endless guidance is hard to forget throughout my life. Thank you Manu for everything.

I would like to express my sincere gratitude to my second supervisor *Dr Lara Struelens* from SCK CEN, Belgium for her tremendous supervision, support, and tutelage during my PhD work. She supported me academically and emotionally through the rough road to finish this thesis. From offering intellectual advice for articles to presentations to the thesis and the complete workflow of the thesis work, she made it a point to assist me in the best ways possible. Throughout my academic

career and everyday life, her vast knowledge and wealth of experience have been a source of inspiration for me. I thank you Lara for everything.

Besides my supervisors, I would like to thank all the members of the jury: the reviewers *Prof. Dr. rer. nat Gerhard Glattig* and *Prof. Dr. Marta Cremonesi*; the examiners *Dr Luc Simon*, *Dr Ludovic Ferrer* and *Prof Dr Florent Cachin*; the president of the jury *Prof Dr Pierre Payoux*; and the invited members *Dr Lara Struelens* and *Dr Peter Knoll* for making my dissertation a memorable experience and also for providing their insightful comments and positive constructive criticism which incited me to widen my research from various perspectives.

I owe *Maxime Chauvin* and *Erick Mora-Ramirez* more than words can express. Since the day I started my PhD, you have been a rock, whether in good times, such as when my work was accepted for presentation at conferences or publications, or in bad times, when nothing seemed to work. I would not have gotten this far without you. Max assisted me in keeping up with simulation physics, while Erick kept me current on clinical expertise. Today, thanks to Max, I can think of writing any Python code I want.

Thanks to all the members of CRCT group 15 “Multi-scale dosimetry for radiotherapy optimization” including *Marie-Claude Bordage*, *Luc Simon*, *Laure Vielleveigne*, *Jeremy Leste*, *Jonathan Tranel*, *Belinda Stiles*, *Alex-Vergara Gil*, *Gustavo Costa*, *Tony Younes*, *Ana Rita Barbeiro* and *Angela Patricia Morales Salcedo* for your support and stimulating discussions. I would like to express my gratitude to all the administrative personnel at the CRCT, particularly *Sébastien Guibert*, *Laurence Granier* and at INSERM office, especially *Muriel Serthelon* for your assistance throughout my stay. Thank you *Pierre Cosson* and *Nicolas Jurado* for all the technical support.

I cannot continue without expressing my gratitude to *Marie-Hélène Lalaux* for assisting me with all mission requests. She also stepped up at the last minute to finalise the necessary travel arrangements regardless of whether I stayed in France or Belgium. Thank you for all your assistance; without you, I would not have been able to travel so smoothly.

I would also like to express my gratitude to *Filip Vanhavere* and the members of the Research on Dosimetric Applications (RDA) group at SCK CEN for welcoming me to their team. Thank you *Dayana Castillo*, *Giulia Tamborino*, *Clarita Saldarriaga Vargas*, *Sunay Rodríguez Pérez*, *Melissa Crabbé*, *Marijke De Saint-Hubert*, *Jérémie Dabin* and *Werner Schoonjans* for your insightful suggestions and comments, as well as for always providing yet another viewpoint. *Anna Bianchi*, thank you for sparking discussions and for the little time we spent together, it was refreshing. Thank you *Luana de Freitas Nascimento*, *Mahmoud Abdelrahman*, *Pasquale Lombardo*, *Racell Nabha* and *Olivier Van Hoey* for the enjoyable time

and short talks during the coffee break. I cannot express my gratitude to the team without acknowledging *Babs Van Hees* for orchestrating everything to ensure the smooth sailing of the team. I would also extend my gratitude to the SCK Academy particularly *Michèle Coeck* and the administration personnel - *An-Sofie Craninx* and *Sylvia Claeys* for your support and cooperation.

A special thank you goes out to *Jean-Pierre Pouget* and his team members at the Institute for Research in Cancer Research (IRCM) along with the team of *Lore Santoro* at the L'Institut du Cancer de Montpellier (ICM) for their welcoming and helpful conversations whenever I visited Montpellier. *Ali Parach* and *José-Alejandro Fragoso-Negrin* were always a pleasure to talk to. It was such a pleasure spending time with you, Ali, because of your great sense of humour isn't it José? Thank you Manu and Jean-Pierre for organising team dinners in Montpellier, I got the chance to talk and discuss with *Julie Constanzo*, *Stanislas Dumanoir*, *Bérengère Piron* and *Sébastien Vauchin*. Thank you all, you have been very supportive.

I would like to express my gratitude to all the collaborators of the European collaborative research project - MRT Dosimetry for giving me the opportunity to expand my knowledge of GATE simulations especially *Johannes Tran-Gia* and *Michael Lassmann* (Germany) for providing the image dataset, *Nicholas Calvert* and *Jill Tipping* (UK) for assisting with additional image acquisitions and phantom images, *Michael Ljungberg* and *Katarina Sjogreen Gleisner* (Sweden) for deciphering DICOM header and CT image simulation, respectively, *Jérémie Dabin* (Belgium) for guidance with DICOM headers, and *Andrew Robinson* (UK) for coordinating collaboration efforts. The published article in the framework of this project is devoted to *Maria Kotzassarlidou*, an MRT Dosimetry project member who passed away during the first COVID wave. She will be remembered not only for her critical contribution to the project, but also for her upbeat and compassionate nature, as well as her incredible hospitality during one of the project's meetings in her adopted hometown of Thessaloniki, Greece.

I had the opportunity to participate in the coordinated research project initiated by the IAEA titled "Dosimetry in Molecular Radiotherapy for Personalized Patient Treatments". My sincere thanks goes to all the members of this project for their support and encouragement.

To *Nathaly Barbosa Parada* (Colombia), for being an excellent organiser and a go-to person in times of need. I cherish our relatively short but memorable stay in Vienna.

To *Carlos Calderón Marín* (Cuba) and *Nur Rahmah Hidayati* (Indonesia), *Darko Grosev* (Croatia), *Santosh Kumar Gupta* (India) and *Parul Thakral* (India) for your encouraging and kind words.

To *Tumelo CG Moalosi* (South Africa), for not only providing us with an image

dataset but also helping me with additional information when needed.

To *Sébastien Vaucelin* (France), for your assistance with Planet[®] Dose at the very first - from minor to major concerns, you have been there. Our interactions have always been a mixture of work and social life either during this project or during our meets in Montpellier and I treasure them. Thank you for always praising me and appreciating my efforts. It means a lot.

To *Robert Hobbs* (USA), for consistently offering excellent insights on the work. I treasure the wonderful memories I have of our brief stay in Vienna.

To *Peter Knoll* (Vienna), for spearheading all the collaborative efforts and hosting the in-person meeting in Vienna. Your appreciation and kind words have kept me on my toes over the years. Despite your hectic schedule, you have responded promptly to my concerns. Thank you so much for everything.

Lastly, to *Ludovic Ferrer* (France), not only for helping me during this project but for being an excellent professor. You were the one who introduced me to the realm of simulations, particularly GATE. I recall our first acquaintance during my Masters, and the rest, as they say, is history. From the first year of GATE courses (in English) to those in French in the second year, you were really patient with me and led me along. You aided me tremendously during my PhD research, advancing my clinical perspective in the area of Nuclear Medicine. You hosted me in Nantes during the darkest hours and assisted me resolve the strange image reconstruction conundrum. Thank you so much Ludo.

I am grateful to the members of the OpenGATE community for their support and technical aid. Thank you *David Sarrut* and *Lydia Maigne* for organising biannual GATE workshops and facilitating scientific and technical interaction among users. I want to thank you David also for helping me enhance my GATE skills throughout my master internship which allowed me to perform simulations during my PhD.

All the simulations performed during my PhD work were only possible due to the access to the regional high performance computing centre CALMIP (CALcul en MIDI-Pyrénées). A big thanks to all the CALMIP personnel especially *Christophe Marteau* and *Nicolas Renon* for approving our project (P19001), offering us computational hours (even the extra additional hours in times of need) and providing the technical assistance.

The next round of acknowledgements is for a bunch of colleagues and friends for a memorable time spent together in the lab and in social environments. Thank you, *Joey Labour* and *Juan Camillo Ocampo Ramos*, for making me laugh even during the most stressful moments of the day, for providing me with your creative ideas for problem solving and for coordinating frequent get-togethers to unwind. Thank you, Joey and Erick, for accompanying me to the office late at night to meet deadlines. *Viviana Meoño Alvarado*, thank you for supporting and uplifting

me. I had a wonderful time with you in Toulouse. *Naomi Clayton*, I would like to express my gratitude for your company and guidance in both my professional and personal life; they were very helpful. I treasure my time with James, Elliot, and you. Many thanks for constantly reviewing my papers and thesis and providing grammatical and scientific improvements.

Thank you *Ketan Kadukar* and *Rameshwari Powar* for providing support and friendship that I needed and being my go-to-Indian-family in Toulouse. Thank you *Snehal Kagde*, *Amit Ravindra Patil*, *Debabrata Ghosh*, *Dileesha Jayahansani Kottehewa* and *Kiran Gautam* for your presence throughout the last years of my PhD and for helping me sail during my final days in Belgium. Apart from the excellent culinary sessions, our get-togethers provided much-needed respite. Thank you, *Sumit Srivastava*, for your friendship and company in Mol. Despite being in a totally different domain, you were able to hear all my perspectives on medical physics and stood beside me. I will never forget our late-night walks after supper and conversing about unrelated topics; it was rejuvenating. Thank you (soon to be Dr.) *Nor Kamariah LP'ers* for being there and supporting me. Thank you, *Shavika Rastogi*, for listening out to me, for being there for me and supporting me from the day I began my PhD; our conversations have always been energising. Thank you, *Prashant Dwivedi*, for being a great buddy and sticking with me in tough times. Thank you, *Vivek Maradia*, for being such a steadfast ally during this roller coaster ride. Whether deliberately or inadvertently, you have pushed me beyond my perceived limits in ways that have bolstered my self-confidence while also inspiring me to dream big. Thank you, *Raman Goswami*, for being my support system; and patiently dealing with my work frustrations and comforting me. The trio - *Vinay Singhal*, *Shanshank Vaishnav* and *Parveen Singhal*, you have always motivated me in ways words can't explain. I remember you saying - keep going whatever be it , after all the Universe is a big genie, it always says your wish is my command. Thank you brothers.

Nobody has been more important in my quest for this work than my family members. I owe a debt of gratitude to my *parents* for all they have done for me over the years, including everything they have given of themselves in the form of unconditional love, care and prayers. This work is a token of their sacrifices in educating me and preparing me for the future. Additionally, I am grateful to my *brother and sisters* and my *brother-in-law* for uplifting me in the rough ride and for standing by me. It wouldn't have been possible to conduct this research without their precious support.

Finally I bow down to *God, the lord Almighty* for the countless blessings, knowledge, and opportunities that have been bestowed upon me.

Abstract

Molecular radiotherapy (MRT) is a systemic radiotherapy where the radiopharmaceutical binds specifically to tumours to selectively kill cancer targets while sparing healthy organs. Lutathera[®] (¹⁷⁷Lu-DOTATATE) is a recently FDA/EMA approved radiopharmaceutical for the treatment of the GastroEnteroPancreatic NeuroEndocrine Tumours (GEP-NETs).

In clinical practice, patients are administered with a fixed activity of Lutathera[®], assuming that radiopharmaceutical distribution is the same for all patients. Patient-specific dosimetry allows for a major paradigm shift in the administration of MRT from “one-size-fits-all” approach, to “real personalised medicine” where administered activity is assessed specifically on the base of the irradiation delivered to each patient. This usually requires determining the spatial distribution of the radiopharmaceutical in various organs via imaging at different times (quantitative imaging), estimating the total number of radioactive decays by integrating activity over time (pharmacokinetic assessment) and calculating the absorbed dose using the physical characteristics of the radionuclide and implementing radiation transport in patient’s tissues.

Currently, there are no standardised procedures to perform clinical dosimetry. In addition, the assessment of the uncertainties associated with the dosimetry procedure is not trivial. The DosiTest project (<http://www.dositest.org/>) was initiated to evaluate uncertainties associated with each of the steps of the clinical dosimetry workflow, via a multicentric inter-comparison based on Monte Carlo (MC) modelling.

The first phase of the thesis compared dosimetry analysis performed by various centres using the same software and protocol on the same patient dataset as a part of IAEA-CRP E23005 project in order to appraise the precision of clinical dosimetry. To our knowledge, this is the first time that a multi-centric dosimetry comparison of a single clinical patient dataset has been undertaken using the same protocol and software by many centres worldwide. It highlighted the critical need to establish checkpoints and conduct sanity checks to eliminate significant disparities among results, and distinguish erroneous practice with acceptable inter-operator variability. A significant outcome of this work was the lack of quality assurance in clinical nuclear medicine dosimetry and the need for the development of quality

control procedures. While dosimetry is gaining popularity in nuclear medicine, best practices should be adopted to ensure that results are reliable, traceable, and reproducible. It also brings forward the need to deliver sufficient training after the acquisition of the relatively new software packages beyond a couple of days. This is clearly insufficient in a context of an emerging field where the professional experience is quite often lacking.

Next, the study of clinical dosimetry accuracy requires generating test datasets, to define the ground truth against which clinical dosimetry procedures can be benchmarked. The second section of the thesis addressed the simulation of three-dimensional scintigraphic SPECT imaging by implementing auto-contouring detector motion in the GATE Monte Carlo toolkit. Following the validation of SPECT/CT projections on anthropomorphic models, a series of realistic clinical patient images were generated.

The last part of the thesis established the proof of concept of the DosiTest project, using a virtual (simulated) SPECT/CT dataset at various time points, with various gamma cameras, enabling comparison of various dosimetric techniques and to assess the clinical feasibility of the project in selected nuclear medicine departments.

Résumé

La radiothérapie moléculaire (RTM) est une radiothérapie systémique, où le produit radiopharmaceutique se lie spécifiquement sur les tumeurs pour tuer sélectivement les cibles cancéreuses tout en préservant les organes sains. Lutathera[®] (¹⁷⁷Lu-DOTATATE) est un radiopharmaceutique récemment approuvé par la FDA/EMA pour le traitement des tumeurs neuro-endocrines gastro-entéro-pancréatiques (GEP-NETs).

Dans la pratique clinique, les patients reçoivent une activité fixe de Lutathera[®], 4 cycles de 7,4 GBq, en supposant que la pharmacocinétique du radiopharmaceutique est même entre les patients. La dosimétrie spécifique au patient permet un changement de paradigme majeur dans l'administration de la RTM, passant d'une approche "taille unique" à une véritable médecine personnalisée où l'activité administrée est évaluée spécifiquement sur la base de l'irradiation délivrée à chaque patient. Pour ce faire, il faut généralement déterminer la distribution spatiale du radiopharmaceutique dans les organes par imagerie à différents moments (imagerie quantitative), estimer le nombre total de désintégrations radioactives en intégrant l'activité dans le temps (évaluation pharmacocinétique) et calculer la dose absorbée à partir des caractéristiques physiques du radionucléide et du transport de l'énergie dans les tissus du patient.

Actuellement, il n'existe pas de procédures normalisées pour effectuer la dosimétrie clinique. En outre, l'évaluation des incertitudes associées à la procédure de dosimétrie n'est pas triviale. Le projet DosiTest a été lancé pour évaluer les incertitudes associées à chacune des étapes du flux de travail de la dosimétrie clinique, via une inter-comparaison multicentrique basée sur la modélisation de Monte Carlo (MC).

La première phase de la thèse a consisté à comparer les analyses dosimétriques effectuées par différents centres utilisant le même logiciel et le même protocole sur le même ensemble de données de patients dans le cadre du projet IAEA-CRP E23005 afin d'évaluer la précision de la dosimétrie clinique. À notre connaissance, c'est la première fois qu'une comparaison dosimétrique multicentrique d'un seul ensemble de données cliniques sur un patient a été entreprise en utilisant le même protocole et le même logiciel par de nombreux centres dans le monde entier. Elle a mis en évidence le besoin crucial d'établir des points de contrôle et d'effectuer des vérifications de bon sens pour éliminer les disparités significatives entre les résultats et distinguer les pratiques erronées de la variabilité inter-opérateurs acceptable. Un résultat important de ce travail a été le manque d'assurance qualité en dosimétrie de médecine nucléaire clinique et la nécessité de développer des procédures de contrôle qualité. Alors que la dosimétrie gagne en popularité en médecine nucléaire, les meilleures pratiques doivent être adoptées pour garantir la fiabilité, la traçabilité

et la reproductibilité des résultats. Cela met également en avant la nécessité de dispenser une formation suffisante après l'acquisition des logiciels relativement nouveaux, au-delà de quelques jours. Ceci est clairement insuffisant dans le contexte d'un domaine émergent où l'expérience professionnelle fait souvent défaut.

Ensuite, l'étude de l'exactitude de la dosimétrie clinique nécessite de générer des ensembles de données de test, afin de définir la vérité de base par rapport à laquelle les procédures de dosimétrie clinique peuvent être comparées. La deuxième section de la thèse traite de la simulation de l'imagerie TEMP scintigraphique tridimensionnelle en implémentant le mouvement du détecteur d'auto-contournement dans la boîte à outils Monte Carlo GATE. Après la validation des projections TEMP/TDM sur des modèles anthropomorphes, une série d'images réalistes de patients cliniques a été générée.

La dernière partie de la thèse a établi la preuve de concept du projet DosiTest, en utilisant un ensemble de données TEMP/TDM virtuelles (simulées) à différents moments, avec différentes gamma-caméras, permettant de comparer différentes techniques dosimétriques et d'évaluer la faisabilité clinique du projet dans certains départements de médecine nucléaire.

सारांश

नाभिकीय चिकित्सा (अंग्रेजी:न्यूक्लियर मेडिसिन) एक प्रकार की चिकित्सकीय जाँच तकनीक होती है। इसकी एक विशेषता है जो रोगियों का निदान और इलाज दोनों के लिए रेडियोधर्मी तत्व (रेडियोट्रेसर्स) द्वारा उत्सर्जित आयनीकरण विकिरण का उपयोग करती है। रेडियोधर्मी तत्व को फार्मास्युटिकल से जोड़ा जाता है (रेडियोफार्मास्युटिकल्स) और इंजेक्शन के द्वारा छोटे मात्रा में प्रविष्ट करा दिया जाता है। इसका उद्देश्य शरीर में कुछ ऊतकों या शारीरिक कार्यों को लक्षित करना है। ये रेडियोफार्मास्युटिकल रोगी के शरीर में घूमते हैं और विकिरण (गामा किरणें) उत्सर्जित करते हैं। ये विकिरण विशेष कैमरों से टकराते हैं जो शरीर की छवियां बनाते हैं। आणविक रेडियोथेरेपी (एमआरटी) एक प्रणालीगत रेडियोथेरेपी है, जहाँ रेडियोफार्मास्युटिकल स्वस्थ अंगों को बचाते हुए, ट्यूमर नष्ट करने के लिए विशेष रूप से उससे जुड़ता है।

लुटेथेरा® नामक एक रेडियोफार्मास्युटिकल जीईपी-नेट्स (गैस्ट्रोएंटेरोपेक्रिएटिक न्यूरोएंडोक्राइन ट्यूमर) के उपचार के लिए हाल ही में एफडीए द्वारा अनुमोदित दवा है। यह आमतौर पर पेट, छोटी आंत, अपेन्डिक्स, कोलन और मलाशय सहित अग्न्याशय या जठरांत्र संबंधी मार्ग जैसे हार्मोन स्रावित अंगों में बनता है।

नैदानिक अभ्यास में, रोगियों को लुटेथेरा® की एक निश्चित गतिविधि के साथ प्रशासित किया जाता है, यह मानते हुए कि ट्यूमर और स्वस्थ ऊतकों में विकिरण का उत्थान रोगियों के बीच समान है, या कम से कम रोग का कुशलतापूर्वक इलाज करने के लिए पर्याप्त है। ट्यूमर के ग्रहण और निकासी में रोगी-से-रोगी भिन्नता के कारण हमेशा ऐसा नहीं होता है।

इसके लिए वास्तविक व्यक्तिगत दवा दी जानी चाहिए जहां दी खुराक का मूल्यांकन विशेष रूप से प्रत्येक रोगी के लिए किया जाता है। यह सभी रोगियों के लिए "एक उपचार" से "रोगी-विशिष्ट उपचार" की ओर बढ़ने में मदद करेगा। इसके लिए, प्रत्येक रोगी के शरीर की चिकित्सा छवि ली जाती है यह जानने के लिए कि इंजेक्शन के बाद (जैसे 1 घंटा, 4 घंटे, 24 घंटे और इसी तरह) किन अंगों में विकिरण अवशोषित हुआ है। फिर समय के साथ खुराक को एकीकृत करके रेडियोधर्मी क्षय की कुल संख्या का अनुमान लगाया जाता है। इसके बाद अवशोषित खुराक की गणना रेडियोधर्मी तत्व की भौतिक विशेषताओं का उपयोग करके की जाती है।

वैश्विक नैदानिक डोसिमेट्री सटीकता शामिल प्रत्येक चरण की सटीकता पर निर्भर करती है, और वर्तमान में, कोई मानक संचालन प्रक्रिया नहीं है। इसके लिए, मॉटे कार्लो मॉडलिंग (एमसी) पर आधारित एक बहुकेंद्रीय अंतर-तुलना के माध्यम से, क्लिनिकल डॉसिमेट्री वर्कफ्लो के प्रत्येक चरण से जुड़ी अनिश्चितताओं का मूल्यांकन करने के लिए डोसिटेस्ट प्रोजेक्ट (www.dositest.org) शुरू किया गया था।

थीसिस के पहले चरण में नैदानिक डोसिमेट्री की 'सटीकता' का पता लगाने के लिए एक ही रोगी स्कैन (एसपीईसीटी/सीटी) पर एक ही सॉफ्टवेयर और प्रक्रिया का उपयोग करके विभिन्न केंद्रों द्वारा किए गए डॉसिमेट्री विश्लेषण की तुलना की गई। इन परिणामों के बीच महत्वपूर्ण असमानताओं को खत्म करने के लिए चेकपॉइंट को स्थापित करने और विवेक जांच करने की महत्वपूर्ण आवश्यकता पर प्रकाश डाला। डॉसिमेट्री परिणामों की 'सटीकता' का आकलन करने और डॉसिमेट्री दृष्टिकोण को मानकीकृत करने के लिए कंप्यूटर द्वारा उत्पन्न नकली रोगी स्कैन का उपयोग करना भी महत्वपूर्ण है। थीसिस के दूसरे खंड में GATE MC टूलकिट का उपयोग करके यथार्थवादी त्रि-आयामी SPECT इमेजिंग के अनुकरण को संबोधित किया गया था। फैंटम (ऑर्गन इंसर्ट के साथ पानी से भरे सिलेंडर) पर SPECT/CT स्कैन के सत्यापन के बाद, यथार्थवादी रोगी SPECT/CT छवियों का मॉडल तैयार किया गया। थीसिस का अंतिम चरण परियोजना की व्यवहारता का आकलन करने के लिए एक मॉडल रोगी स्कैन का उपयोग करके डॉसिटेस्ट परियोजना के लिए अवधारणा का प्रमाण स्थापित करता है।

Preface

All of the research work presented henceforth has been conducted in part at the Cancer Research Centre of Toulouse (CRCT), INSERM, Toulouse, and in part at SCK CEN, the Belgian Nuclear Research Centre, Belgium.

Some of the works presented here contributed to the MRT Dosimetry project, a joint research project within EMPIR and the IAEA CRP E23005 “Dosimetry in Molecular Radiotherapy for Personalized Patient Treatment”.

The research presented in Chapter 3 is being prepared for publication in a scientific journal. G Kayal^{*}, N Barbosa Parada^{*}, C Calderón Marín, L Ferrer, J-A Fragoso-Negrín, D Grosev, SK Gupta, NR Hidayati, T CG Moalosi, GL Poli, P Thakral, V Tsapaki, S Vauclin, A Vergara-Gil, P Knoll, R Hobbs[†], M Bardiès[†]. *Roadblocks in clinical dosimetry analysis performed on a patient dataset using Planet[®] Dose - An IAEA study*. I (with N Barbosa Parada) collected all the dosimetry results provided by each coauthor, automatised all the work to prevent errors, analysed the results, summarised the work and wrote the manuscript with the senior supervisors - R Hobbs and M Bardiès.

The research presented in Chapter 4 is being prepared for publication in a scientific journal. G Kayal^{*}, N Barbosa Parada^{*}, C Calderón Marín, L Ferrer, J-A Fragoso-Negrín, D Grosev, SK Gupta, NR Hidayati, T CG Moalosi, GL Poli, P Thakral, V Tsapaki, S Vauclin, A Vergara-Gil, P Knoll, R Hobbs[§], M Bardiès[®]. *Creation of a benchmarking dataset via a round-table dosimetry analysis using Planet[®] Dose - An IAEA study*. I (with N Barbosa Parada) collected all the dosimetry results provided by each coauthor, used the automatised python codes for the analysis of the dosimetric results and wrote the manuscript with the senior supervisors - R Hobbs and M Bardiès.

The research presented in Chapter 5, Chapter 6 and Chapter 7 has been published.

All the simulations were performed at the regional high-performance computing (HPC) centre CALMIP under the project number P19001. Renewal/extension of computational hours were demanded every year and has always been granted with the clear implication that more hours may be requested as necessary.

Contents

List of Figures	xxiii
List of Tables	xxvii
List of Abbreviations	xxix
Introduction générale	1
1 Introduction	11
1.1 Targeted Radionuclide Therapy	12
1.1.1 Selective Internal Radiotherapy (SIRT)	13
1.1.2 Molecular Radiotherapy (MRT)	14
1.2 Treatment planning in molecular radiotherapy	15
1.2.1 One-size-fits-all approach	16
1.2.2 Patient-specific treatment method	16
1.3 Outline of the dissertation	17
2 Background - Clinical dosimetry workflow	21
2.1 Introduction	22
2.2 Gamma camera: detector composition and image formation	25
2.2.1 Components of gamma camera	26
2.2.1.1 Collimator	27
2.2.1.2 Scintillation crystal	28
2.2.1.3 PMTs	29
2.2.2 Signal processing	30
2.2.3 Image formation	31
2.3 Image Acquisition	32
2.3.1 Acquisition modes	32
2.3.2 Data acquisition settings	33
2.4 Image reconstruction	34
2.4.1 Filtered back projection (FBP)	35
2.4.2 Iterative reconstruction algorithm	35
2.5 Image degrading factors and their corrections	38

2.5.1	Attenuation	38
2.5.2	Scatter	39
2.5.3	Spatial resolution	41
2.5.4	Partial volume effect	42
2.5.5	Other image degrading factors and corrections	43
2.6	Absolute Quantification	44
2.7	Pharmacokinetics determination	45
2.7.1	Image Registration	45
2.7.2	Image Segmentation	47
2.7.2.1	Manual segmentation	48
2.7.2.2	Threshold based segmentation	48
2.7.2.3	Segmentation based on Machine Learning methods	49
2.7.3	Time-activity curves integration	50
2.8	Absorbed Dose calculations	52
2.8.1	Absorbed Dose Algorithms	53
2.8.1.1	Local energy deposition (LED)	53
2.8.1.2	Dose point kernel convolution method	53
2.8.1.3	Monte Carlo simulation approach	54
2.8.1.4	Selection of the relevant approach for absorbed dose calculations	55
2.8.2	Absorbed Dose Approaches	55
2.8.2.1	Reference dosimetry	55
2.8.2.2	Patient-specific dosimetry	56
2.9	Assessment of variations in clinical dosimetry	57
2.9.1	Current status	57
2.9.2	Uncertainty assessment	58
2.9.3	The DosiTest project	59
2.10	Summary and presentation of the PhD work	61
3	Pitfalls in dosimetry analysis on a patient SPECT/CT dataset using Planet[®] Dose - An IAEA study	65
3.1	Introduction	65
3.2	Materials & Methods	66
3.2.1	Participants	66
3.2.2	Clinical patient SPECT/CT dataset	67
3.2.2.1	Patient images acquisition	67
3.2.2.2	Calibration acquisition	67
3.2.2.3	Reconstruction and derivation of a calibration factor	67
3.2.3	Definition of clinical workflow	68

3.2.3.1	Registration	68
3.2.3.2	Segmentation	68
3.2.3.3	Absorbed dose rate (ADR)	69
3.2.3.4	Absorbed dose computation (AD)	69
3.2.3.5	Data exportation	70
3.2.4	Statistical analysis	70
3.2.5	Iterations	72
3.3	Results	74
3.3.1	Activity quantification	74
3.3.1.1	Volume segmentation	74
3.3.1.2	Derivation of counts and activity	75
3.3.2	Absorbed Dose Rate (ADR)	78
3.3.3	Absorbed dose computation (AD)	81
3.4	Discussion	83
3.5	Conclusion	88
4	Creation of a benchmarking dataset on clinical patient images using Planet[®] Dose	91
4.1	Introduction	91
4.2	Materials & Methods	92
4.2.1	Participants	92
4.2.2	Clinical patient SPECT/CT dataset	93
4.2.2.1	Patient & calibration image(s) acquisition	93
4.2.2.2	Reconstruction and derivation of calibration factor	93
4.2.3	Definition of clinical workflow	94
4.2.4	Statistical analysis	95
4.3	Results	95
4.3.1	Activity quantification	95
4.3.1.1	Volume segmentation	95
4.3.1.2	Determination of counts and activity	96
4.3.1.3	Determination of activity concentration	99
4.3.2	Absorbed dose rate (ADR)	99
4.3.3	Absorbed Dose calculations (AD)	101
4.4	Discussion	102
4.5	Conclusion	105

5	Modelling SPECT auto-contouring acquisitions using new developments in GATE	107
5.1	Introduction	107
5.2	Materials & Methods	109
5.2.1	Experimental acquisitions and development of NCO modelling	110
5.2.1.1	Experimental setup	110
5.2.1.2	Simulation setup in GATE	113
5.2.2	CO vs NCO comparison: ^{177}Lu and ^{131}I SPECT modelling	121
5.2.3	Image comparison metrics	122
5.3	Results	124
5.3.1	Validation of gamma camera models	124
5.3.1.1	Siemens Symbia T2 for ^{177}Lu with 2-organ MRTD phantom	124
5.3.1.2	GE Discovery 670 for ^{131}I with the lung and spine ANT phantom	128
5.3.2	Simulation time	130
5.3.3	Auto-contouring motion vs. circular camera motion using ^{177}Lu and ^{131}I	130
5.4	Discussion	132
5.5	Conclusion	135
6	Generation of patient SPECT/CT dataset for DosiTest	137
6.1	Introduction	137
6.2	Materials & Methods	138
6.2.1	Gamma camera model	139
6.2.2	Generation of the calibration factor (simulations)	140
6.2.3	Patient model	141
6.2.3.1	CRP patient	141
6.2.3.2	From CRP patient to digital patient model	142
6.2.4	Source modelling	145
6.2.4.1	Definition of the activity map	145
6.2.4.2	Source definition, physics list used for the simulations and output	145
6.2.5	Comparison metrics	147
6.2.6	Reconstruction	148
6.3	Results	148
6.3.1	Calibration images	148
6.3.2	Clinical images	149
6.3.2.1	Simulated patient SPECT projections	149

6.3.2.2	Comparison of simulated and experimental patient images	150
6.3.3	Computation Time	153
6.3.4	Reconstruction	153
6.3.4.1	Reconstruction with Hermes TM	153
6.3.4.2	Reconstruction with Xeleris TM	154
6.4	Discussion	155
6.5	Conclusion	157
7	Proof-of-concept of DosiTest, a virtual multicentric clinical trial for assessing uncertainties in Molecular Radiotherapy dosimetry	159
7.1	Introduction	159
7.2	Materials & Methods	161
7.2.1	Clinical dataset	161
7.2.1.1	Patient model	162
7.2.1.2	Description of patient geometry	162
7.2.1.3	Description of activity distribution	162
7.2.2	Reference dosimetry generation	163
7.2.3	Monte Carlo based image generation	164
7.2.3.1	Calibration image modelling	165
7.2.3.2	Patient image modelling	167
7.2.4	Validation procedure	168
7.2.4.1	Activity-indexed images	168
7.2.4.2	Absorbed Dose Rate (ADR)	169
7.2.4.3	Integration of absorbed dose rates in time	169
7.2.4.4	Absorbed Dose (AD)	170
7.3	Results	170
7.3.1	Reference dosimetry generation	170
7.3.2	Monte Carlo based image generation	170
7.3.2.1	Generation and validation of calibration images	170
7.3.2.2	Generation and validation of patient images	172
7.3.3	Comparison of activities, absorbed dose rates and absorbed doses	173
7.3.3.1	Activity-indexed images	173
7.3.3.2	Absorbed Dose Rate (ADR)	175
7.3.3.3	Absorbed Doses (AD)	176
7.4	Discussion	176
7.5	Conclusion	179

8 Conclusion and perspectives	181
8.1 Summary of the work	181
8.2 Contribution to the field	184
8.3 Future suggestions and perspectives	185
8.3.1 Clinical Aspect	185
8.3.2 Modelling Aspect	186
8.3.3 DosiTest project	187
Conclusions et perspectives futures	189
Appendices	
A Sample Google spreadsheet used for the data collection	199
B Benchmark Dataset	213
B.1 Reconstructed patient SPECT/CT data at five time points	213
B.2 Associated calibration factor	213
B.3 Standard Protocol (SOP) in Planet® Dose	214
B.4 Step-by-step Dosimetry Results	253
Bibliography	259
Scientific production	277

List of Figures

2.1	“Conventional” clinical radionuclide dosimetry workflow	24
2.2	Alternative workflows for computing clinical dosimetry depending on the sequence of time integration and dosimetry step	25
2.3	Schematic of a gamma camera	27
2.4	Schematic of a photomultiplier tube	30
2.5	Signal processing in gamma camera	31
2.6	The process from the emission of gamma photons to the image formation	32
2.7	2-D projection profiles of a radioactive point source displayed as sinograms	36
2.8	Schematic of iterative reconstruction	37
2.9	Energy spectrum of ^{177}Lu representing the triple energy windows (TEW)	41
2.10	Image registration mechanism	46
2.11	Computation of time-integrated activity using trapezoidal method	51
2.12	Schematic overview of the DosiTest project	60
3.1	Workflow used for analysing the data and computing the final results and recommendations	73
3.2	Anatomical and functional segmentation	74
3.3	Volumes of each VOI in first treatment cycle	75
3.4	Total counts in each VOI for the third treatment cycle	76
3.5	Activity for each VOI in the third treatment cycle	77
3.6	Derivation of activity and counts ratio for each volume of interest in the third treatment cycle	78
3.7	Absorbed Dose Rate (ADR) for each volume of interest in the third treatment cycle.	79
3.8	Activity concentration (AC) for each volume of interest in the third treatment cycle	80
3.9	ADR/AC ratio for each volume of interest in the third treatment cycle	81
3.10	Absorbed Doses for each volume of interest in the first treatment cycle	82

3.11 Absorbed Doses for each volume of interest in the third treatment cycle	83
3.12 Absorbed Doses (in Gy) for each volume of interest (organs and lesions) for each treatment cycle	83
3.13 Typical error illustrating the selection of a small bounding box for anterior lesion while performing threshold-based segmentation	86
4.1 Benchmark: Volumes of each VOIs in in the second treatment cycle	96
4.2 Benchmark: Activity in each VOI	98
4.3 Benchmark: Activity/count ratio for each VOI	98
4.4 Benchmark: Activity concentration in each VOI	99
4.5 Benchmark: Absorbed dose rate in each VOI	100
4.6 Benchmark: ADR/AC ratio in each VOI	100
4.7 Benchmark: Absorbed dose for each VOI	102
4.8 Benchmark: Variation in absorbed dose for each VOI among participants	103
4.9 Consistent volume of anterior lesion among participants	104
5.1 The MRTdosimetry 2-organ (spleen and right kidney) phantom	111
5.2 Anthropomorphic torso phantom (ECT/TOR/P) with lungs, liver and cylindrical spine inserts	111
5.3 Schematic of modelling the gamma camera components and its response	113
5.4 Implementation of circular detector motion in GATE	114
5.5 Implementation of auto-contouring detector motion in GATE	114
5.6 Extraction of auto-contour mode information from Siemens Symbia T2 DICOM header	115
5.7 Radial position information from GE Discovery 670 DICOM header	116
5.8 Extraction of auto-contour mode information from GE Discovery 670 DICOM header	116
5.9 Illustration of the geometry modelling issue in GATE	117
5.10 Creation of individual tessellated volumes of the 2-organ phantom model	118
5.11 Elliptical 4-organ phantom	121
5.12 Auto-contouring motion of the gamma camera around the 2-organ phantom model	125
5.13 Simulated SPECT projections for the 2-organ phantom at different projection angles	125
5.14 Simulated energy spectrum of ^{177}Lu and simulated non-circular orbit of detector head	126

5.15	Comparison of experimental and simulated SPECT projections of the 2-organ phantom	127
5.16	Profiles of experimental and simulated projections at different projection angles	127
5.17	Experimental and simulated ^{131}I SPECT projection	129
5.18	Profiles of experimental (blue) and simulated (orange) ^{131}I SPECT projections of the ANT phantom at different projection angles	129
5.19	Simulated projections for the 4-organ phantom with ^{177}Lu	131
5.20	Profiles for comparison of circular vs. non-circular SPECT gamma camera motion for ^{177}Lu and the 4-organ MRTD phantom	131
5.21	Profiles for comparison of circular vs. non-circular SPECT gamma camera motion for ^{131}I and the ANT phantom	132
5.22	Circular (CO) vs non-circular orbits (NCO) acquisitions	134
6.1	Schematic of the modelled gamma camera along with its components	139
6.2	A sample of python script for extracting information from experimental DICOM headers for modelling auto-contour detector motion	140
6.3	Segmentation of different volumes of interest in OpenDose3D Slicer module	142
6.4	Generation of labelled maps from the patient CT images in OpenDose3D Slicer toolkit	142
6.5	Collision of volumes in virtual GATE environment	143
6.6	Generation of object files of the patient geometry with python script	144
6.7	Simplification of meshes in Blender along with implemented checks and STL exportation for GATE	144
6.8	Activities at each time point for the segmented VOI	145
6.9	Total activities at each time point in the whole field of view	146
6.10	^{177}Lu energy spectrum used in simulations	146
6.11	Visualisation of different tessellated volumes of interest from the voxelised patient CT	149
6.12	Visualisation of the patient mesh model with different volumes of interest	150
6.13	Simulated SPECT projections at various detector angles	150
6.14	Simulated energy spectrum of ^{177}Lu	151
6.15	Simulated SPECT projections for three energy windows	151
6.16	Simulated vs clinical patient SPECT projections	151
6.17	Flattened profiles on x-axis for comparison of clinical and simulated images at different projection angles	152
6.18	Simulated patient SPECT projections at different time points post injection	152

6.19 Profile comparison of clinical vs simulated SPECT projections at different time points	153
6.20 Reconstructed simulated SPECT images on Hermes	154
6.21 Reconstructed simulated SPECT images on Xeleris	155
7.1 Descriptive schematic of DosiTest project	160
7.2 Total activity corresponding to each time point post injection	163
7.3 Workflow of Monte Carlo-based image generation	165
7.4 Schematic describing the workflow for assessing the feasibility of DosiTest	168
7.5 Constant incorporation of absorbed dose rate (ADR) with time	170
7.6 The geometry & activity input along with 3D absorbed dose rate map for the first time point	171
7.7 Absorbed dose rate for each time point post activity administration	171
7.8 Simulated SPECT projections of the IEC calibration phantom	171
7.9 Profile comparison of experimental and simulated calibration SPECT projections	172
7.10 Simulated SPECT projections at different time points post a.a.	172
7.11 Profile comparison of clinical vs simulated patient SPECT projections at different time points post a.a.	173
7.12 Simulated activity maps for time points 1 hour to 96 hours post a.a.	174
7.13 Comparison of the activity input and simulated activity-indexed maps (this comparison is referred to as ‘Activity comparison’ in Figure 7.4)	174
7.14 Absorbed dose rate maps for time points from 1 hour to 96 hours post a.a.	175
7.15 Profile comparison of the reference and image-based absorbed dose rate maps	176

List of Tables

2.1	Characteristics of various collimators from the different manufacturers	28
2.2	Summary of dosimetric approaches in radionuclide therapy	57
3.1	Volumes of each volume of interest (VOIs) for each cycle	76
3.2	Minimum and maximum variation of volume and activity in volume of interest for each cycle among participants	77
3.3	Fitting chosen by the different centres to obtain ADR for each VOI	81
3.4	Absorbed doses in each volume of interest for each treatment cycle	84
4.1	Benchmark: The mean and CoV (along with min, max and std dev) of volumes for each VOI	97
4.2	Fitting chosen by the different centres to obtain ADR for each VOI	101
4.3	Benchmark: Mean absorbed doses in each VOI	102
5.1	Acquisition parameters for experiments at UKW <i>SC: scatter window; PP: photopeak or main window</i>	112
5.2	Acquisition parameters for experiments at The Christie <i>SC: scatter window; PP: photopeak or main window</i>	112
5.3	Activities in the 2-organ MRTD and Lung & Spine ANT phantom .	113
5.4	Energy of the gamma photons for ^{177}Lu and ^{131}I with their respec- tive yields used in simulations	119
5.5	Conversion of activity to primaries	120
5.6	^{177}Lu activity in 4-organ phantom model	122
5.7	Computation of primaries for the 4-organ phantom with ^{177}Lu . . .	122
6.1	Volumes and densities of each segmented region of interest in the patient	143
6.2	Energy of the gamma photons with their respective yields used in simulations	147
6.3	Activities and number of primaries used in the simulations	147
7.1	SPECT/CT gamma camera characteristics and acquisition parameters	162
7.2	Comparison of the activity input and activity indexed maps using relative difference and gamma index metrics	175

7.3	Gamma metric comparison of the reference and image-based absorbed dose rate maps for each time point	176
7.4	Comparison of the absorbed dose obtained from reference and image-based ADRs	177
7.5	Use of phantom vs patient models as reference	180

List of Abbreviations

A.A.	Activity administration
AC	Activity Concentration
AD	Absorbed Dose
ADR	Absorbed Dose Rate
ADR/AC	. . .	Absorbed Dose Rate to Activity Concentration ratio
CDR	Collimator-detector response
CDW	Conventional clinical dosimetry workflow
CF	Calibration factor
CO	Circular orbit
COR	Centre of rotation
CoV	Coefficient of variation
CRP	Coordinated Research Project
CT	Computed Tomography
DD	Dose difference
DICOM	Digital Imaging and Communications in Medicine
DTA	Distance-to-agreement
EMA	European Medical Agency
FDA	Food & Drug Administration
FoV	Field of view
FWHM	Full Width at Half Maximum
GATE	Geant4 Applications for Tomographic Emission
GEHC	General Electric Healthcare
GEP-NET	. .	GastroEnteroPancreatic NeuroEndocrine Tumour
GIPR	Gamma index passing rate
HE	High energy

HU	Hounsfield unit
IAEA	International Atomic Energy Agency
ICRP	International Commission on Radiological Protection
IQR	Interquartile range
LED/LDM	..	Local energy deposition method
MC	Monte Carlo simulations
ME	Medium energy
MLEM	Maximum Likelihood Expectation Maximisation
MRI	Magnetic Resonance Imaging
MRT	Molecular Radiotherapy
MSE/D	Mean square error/deviation
NCO	Non Circular orbit
NEMA	National Electrical Manufacturers Association
NET	NeuroEndocrine Tumour
NM	Nuclear medicine
OSEM	Ordered Subset Expectation Maximisation
PDOSE	Planet Dose
PET	Positron Emission Tomography
PMT	Photo-multiplier tube
PRRT	Peptide Receptor Radiotherapy
PSF	Point-spread function
PVE/C	Partial Volume Effect / Correction
RC	Recovery Coefficient
RNT	RadioNuclide Therapy
RR	Resolution recovery
SPECT	Single Photon Emission Computed Tomography
TAC	Time-Activity Curve
TEW	Triple energy window
TIA	Time-integrated activity
TIAC	Time-integrated activity coefficient
TRT	Targeted Radionuclide Therapy
VOI	Volume of interest

Introduction générale

La médecine nucléaire (MN) est une spécialité de la médecine qui utilise les rayonnements ionisants émis par des substances radioactives à des fins diagnostiques et thérapeutiques. Ces radiotraceurs sont souvent fixés à des produits pharmaceutiques ou à des implants médicaux dans le but de cibler certains tissus ou fonctions physiologiques de l'organisme.

Approche diagnostique: La médecine nucléaire diagnostique fournit des informations sur la biodistribution du médicament radiopharmaceutique dans le corps qui, à son tour, contient des détails révélateurs du fonctionnement biochimique ou physiologique d'un certain tissu, organe, ou permet d'identifier une tumeur présente dans le corps du patient. Cette distribution spatiale du radiotraceur peut être imagée à l'aide de plusieurs techniques: la scintigraphie planaire 2D, c'est-à-dire la création d'images 2D, la tomographie par émission monophotonique 3D (TEMP) ou la tomographie à émission de positrons 3D (TEP). Chacune de ces techniques utilise un détecteur externe (placé à l'extérieur du patient) pour déterminer le site d'interaction du rayonnement dans le patient en détectant les rayons gamma (dans le cas de la planaire/TEMP) ou les photons d'annihilation (dans le cas de la TEP) émis par le produit radiopharmaceutique injecté. Comme ces images fonctionnelles ont une faible résolution spatiale, elles sont souvent fusionnées avec une image anatomique (TDM ou IRM) ayant une résolution spatiale plus élevée, pour une visualisation précise des structures du corps.

Ces images fonctionnelles pures et/ou en combinaison avec des images anatomiques (TEMP/TEP avec CT/IRM) permettent la réalisation de scintigraphies osseuses (pour déterminer les zones de métastases et le stade de développement du cancer des os) (Love et al. 2003; Francis et al. 2015; Van den Wyngaert et al. 2016; Bartel et al. 2018; Ichikawa et al. 2020), la scintigraphies rénales (pour objectiver des dysfonctionnements des reins) (Lycklama à Nijeholt et al. 1986; Taylor 2014; Taylor et al. 2018; H et al. 2021), pour la localisation de tumeurs et de métastases (Keidar et al. 2003; Virgolini et al. 2005; Levi et al. 2007; Lee, Park, et al. 2017) et comme données d'entrée pour la planification du traitement en thérapie par radionucléides (Munley et al. 1999; Bombardieri et al. 2001; Teunissen et al. 2011).

Les applications de la médecine nucléaire se trouvent également en neurologie, en cardiologie et en pneumologie.

Approche thérapeutique: L'aspect thérapeutique de la MN est principalement consacré à l'oncologie (en dehors de quelques applications en rhumatologie) et consiste à administrer un matériau radioactif au patient afin de détruire les cellules tumorales par irradiation. Dans sa définition plus générique, le radionucléide attaché à une molécule joue le rôle d'une charge toxique aux effets locaux (Zimmermann [2019](#)). Le composant de la molécule est généralement chargé de se fixer spécifiquement sur un tissu ou un organe particulier. C'est ce qu'on appelle la thérapie ciblée par radionucléides, qui est examinée en détail dans la section suivante.

Approche théranostique: L'imagerie diagnostique permet de visualiser la distribution du radiotracer à l'intérieur d'un patient. Une molécule marquée avec un radio-isotope de diagnostic peut être utilisée pour l'imagerie (quantitative) (TEMP/TEP) de la tumeur. Cela permet au clinicien d'anticiper si un patient bénéficiera d'une certaine thérapie avec cette molécule particulière. Ensuite, la même molécule ciblée ou du moins une molécule ciblée similaire, mais avec un radionucléide thérapeutique, se concentrant sur l'absorption du rayonnement dans le but de détruire des tissus spécifiques, peut être administrée (Henrich et al. [2019](#)). Cette combinaison d'une thérapie ciblée et d'un diagnostic ciblé est appelée approche théranostique. Cette approche "voir et traiter" peut être utile pour l'estimation de la réponse potentielle et de la toxicité éventuelle (Yordanova et al. [2017](#)).

Thérapie ciblée par radionucléides

La thérapie ciblée par radionucléides (targeted radionuclide therapy ou TRT en anglais) utilise un radionucléide thérapeutique, le plus souvent un émetteur bêta ou plus récemment un émetteur alpha, ayant une courte portée dans les tissus pour concentrer l'irradiation au niveau de la tumeur ciblée tout en épargnant les tissus sains environnants. La TRT s'est imposée comme une méthode privilégiée de traitement du cancer (Yeong et al. [2014](#)). Contrairement à la radiothérapie externe où le rayonnement est délivré à partir d'une source externe, la TRT délivre le rayonnement de manière systémique ou loco-régionale, par analogie avec la chimiothérapie ou d'autres thérapies ciblées (Sgouros, Bodei, et al. [2020](#)).

De plus, grâce à la combinaison de la molécule de ciblage et de la courte portée du rayonnement impliqué, le rayonnement cytotoxique est directement délivré aux cellules cancéreuses ou à leur microenvironnement, évitant ainsi l'irradiation du reste du corps. Pour reprendre les termes de Paul Ehrlich, le fondateur de

la chimiothérapie, la TRT peut être considérée comme une “*balle magique*” qui découvre et délivre une irradiation à une cible spécifique afin d’inhiber sa fonction et de la détruire. Depuis le milieu du XXème siècle, plusieurs radionucléides ont été proposés pour des applications thérapeutiques. L’un des radionucléides thérapeutiques les plus fréquemment utilisés et les plus connus est l’iode-131, sous forme d’iodure de sodium ($^{131}\text{I-NaI}$). Il est administré par le biais de capsules ou sous forme liquide pour le traitement de maladies liées à la thyroïde, telles que la maladie de Basedow ou le carcinome thyroïdien métastatique (Goldsmith 2020). Depuis, il a été largement employé dans une variété d’applications thérapeutiques.

La thérapie ciblée par radionucléides (TRT) peut être classée en deux catégories, en fonction du mode d’administration du matériau radioactif au patient: la radiothérapie interne sélective (RIS) et la radiothérapie interne vectorisée (RIV). Le terme radiothérapie moléculaire (RTM) est aussi utilisé par traduction du terme anglais Molecular Radiotherapy (MRT) à la place de RIV.

Radiothérapie interne sélective (RIS)

La radiothérapie interne sélective (RIS) consiste à injecter de minuscules microsphères radioactives dans les artères qui alimentent la tumeur. Ces microsphères sont administrées par un cathéter et transportées par le flux sanguin jusqu’à ce qu’elles se logent dans les petits vaisseaux tumoraux. Un exemple type d’application concerne les tumeurs du foie, celles-ci dépendant de l’artère hépatique pour leur approvisionnement en sang, les microsphères sont injectées dans l’artère hépatique, ce qui permet de cibler uniquement les tumeurs et d’épargner le foie sain. Par conséquent, une forte irradiation est délivrée localement dans les tumeurs (Nijssen et al. 2002; Salem et al. 2006; Gates et al. 2007).

La RIS est donc considérée comme une thérapie loco-régionale. Étant donné que cette procédure combine l’irradiation et l’embolisation, elle est souvent appelée radioembolisation ou radioembolisation transartérielle (TARE en anglais pour Trans Arterial Radio Embolisation) par analogie à la chimioembolisation transartérielle (Trans Arterial Chemo Embolisation ou TACE). La RIS devient une option thérapeutique de plus en plus populaire pour les tumeurs hépatiques primaires ou inopérables dans le monde entier (Saini et al. 2019).

Les microsphères adaptées à la RIS sont des dispositifs médicaux (et pas des médicaments radiopharmaceutiques, ce qui implique une législation différente) et elles sont disponibles dans le commerce sous trois types différents (d’Abadie et al. 2021), dont deux utilisent un émetteur bêta de forte énergie, l’yttrium-90 (^{90}Y) sous forme de microbilles de verre (TheraSphere[®], Boston Scientific, Boston, MA,

USA) ou inclus dans des microbilles de résine (SIR-Spheres[®], Sirtex Medical, Sirtex Medical Ltd, Sydney, Australie) (Westcott et al. 2016). Le troisième type de microsphères (QuiremSpheres[®], Quirem Medical B.V., Deventer, Pays-Bas) est basé sur l'holmium-166 (¹⁶⁶Ho) enrobé dans du PLLA (poly-acide l-lactique).

Outre son utilisation principale dans le traitement du carcinome hépatocellulaire (CHC), la RIS a également été utilisée pour traiter les métastases hépatiques de nombreux autres types de tumeurs, notamment les tumeurs neuroendocrines (TNE), le cancer du sein et le mélanome uvéal, ainsi que la tumeur hépatique primaire, le cholangiocarcinome intrahépatique (CIC) (Kennedy et al. 2017).

Radiothérapie interne vectorisée (RIV)

La radiothérapie interne vectorisée (RIV) est une technique établie dans laquelle un médicament radiopharmaceutique consistant en un radionucléide attaché à une molécule biologiquement active (appelée vecteur) est administré au patient afin de délivrer une irradiation thérapeutique localisée au site de la maladie.

L'administration systémique de produits radiopharmaceutiques ayant une cytotoxicité radio-induite établie permet de cibler les populations de cellules cancéreuses. Le choix du vecteur de ciblage est essentiel pour développer un produit radiopharmaceutique efficace, car l'efficacité de ces thérapies ciblées dépend de la capacité de liaison du vecteur, tel qu'un antigène ou un récepteur, aux cellules tumorales (Vértes et al. 2010).

Comme le vecteur est marqué avec un radionucléide, il est généralement possible de suivre le parcours et la distribution du médicament radiopharmaceutique dans l'organisme du patient grâce à l'imagerie à différents moments après l'injection. La pharmacocinétique fait référence au comportement temporel du médicament dans l'organisme - de l'administration du médicament à son absorption, sa distribution, son métabolisme et jusqu'à son excrétion de l'organisme. Cela inclut divers processus physiques, chimiques et biologiques, complexes par nature.

Comme mentionné précédemment, les radiopharmaceutiques thérapeutiques sont souvent marqués avec des émetteurs bêta qui ont un effet cytocide potentiel et une pénétration tissulaire de quelques millimètres seulement (Ahmadzadehfar 2016). Par conséquent, ils peuvent détruire les cellules tumorales sans irradier les tissus sains environnants.

L'iode-131 et le phosphore-32 figurent parmi les premiers radio-isotopes utilisés respectivement pour les maladies de la thyroïde (Hertz et al. 1946) et la leucémie (Lawrence et al. 1949). Dans les années suivantes, d'autres radionucléides destinés à pallier les douleurs osseuses ont été proposés, notamment le strontium-89 (Firusian

et al. [1976]) et le samarium-153 (Fischer et Kampen, 2012). En outre, des agents de radio-immunothérapie à base d'yttrium-90 et d'iode-131 ont été approuvés par la FDA pour le traitement du lymphome non hodgkinien (LNH). Parmi les produits radiopharmaceutiques commercialement disponibles/approuvés figurent le ^{131}I (par Jubilant Draximage/Malkincrodt) pour le cancer de la thyroïde et le ^{131}I -mIBG (par Progenics) pour le neuroblastome (Schmidt et al. [2016]; Sgouros, Bodei, et al. [2020]), le chlorure de ^{89}Sr et le ^{153}Sm -lexidronate (par Lantheus) pour les douleurs osseuses liées au cancer et le ^{131}I -tositumomab et le ^{90}Y -ibritumomab tiuxetan pour le traitement des LNH (Davies [2007]).

La RIV gagne également en popularité en tant qu'approche thérapeutique pour les tumeurs neuroendocrines (TNE). En effet, les TNE sont souvent diagnostiquées tardivement avec des maladies disséminées qui ne peuvent pas être traitées chirurgicalement et sont généralement résistantes à la chimiothérapie (Caplin et al. [1998]). Dans ce contexte, les peptides sont souvent choisis comme vecteurs thérapeutiques car ils présentent une pharmacocinétique rapide (c'est-à-dire l'absorption, la distribution, le métabolisme et l'excrétion du médicament) et de bonnes caractéristiques de ciblage des tumeurs avec la capacité de pénétrer efficacement dans les sites tumoraux (Dash et al. [2015]). C'est pourquoi cette thérapie est également appelée radiothérapie des récepteurs peptidiques (peptide receptor radionuclide therapy - PRRT).

Différents analogues de la somatostatine ont été proposés, ^{111}In -DTPA-octreotide, ^{90}Y -DOTA⁰-Tyr³-octreotide (^{90}Y -DOTATOC), ^{90}Y -DOTA⁰-Tyr³-octreotate (^{90}Y -DOTATATE) et ^{177}Lu -DOTA⁰-Tyr³-octreotate (^{177}Lu -DOTATATE) sont parmi les produits radiopharmaceutiques les plus utilisés pour le traitement des TNE (Dash et al. [2015]). Le ^{177}Lu -DOTATATE ou Lutathera® (by AAA, Novartis) a été approuvé par l'Agence Médicale Européenne (EMA) en 2017 et par la Food and Drug Administration (FDA) en 2018 pour le traitement des TNE gastro-entéro-pancréatiques (Henrich et al. [2019]). En plus d'être un émetteur bêta, le ^{177}Lu émet également des rayons gamma appropriés qui peuvent être utilisés pour l'imagerie, ce qui permet de suivre le devenir du traceur dans l'organisme. Ceci contraste avec l'yttrium 90 qui n'émet pas de rayons gamma adéquats avec une énergie suffisante pour être correctement imagé, bien que des images de faible qualité puissent encore être acquises en utilisant le rayonnement de freinage généré par l'interaction des particules bêta avec les tissus (Ferrer et al. [2006]; Cwikla et al. [2010]).

Ces dernières années, le ^{223}Ra -Cl₂ Xofigo (par Bayer) (Costa, Cardile, et al. [2018]; Sgouros, Bodei, et al. [2020]) et le ^{177}Lu -PSMA-617 (par Novartis) (Kind et al.

[2021] gagnent en popularité pour le traitement du cancer de la prostate résistant à la castration (mCRPC), et devraient avoir un impact sur la médecine nucléaire thérapeutique en augmentant énormément le nombre de patients qui bénéficieront finalement du traitement. Ce ^{177}Lu -PSMA-617 a été approuvé très récemment (Mars 2022) par la FDA sous le nom de Pluvicto™. De même, le ^{131}I -PSMA (par Molecular Insight Pharmaceuticals, Inc.) pour la thérapeutique ainsi que le ^{124}I -PSMA pour le diagnostic (Zechmann et al. [2014]) ont été proposés comme une approche alternative pour le traitement du mCRPC.

Planification du traitement en radiothérapie moléculaire

Dans toute radiothérapie, l'objectif principal est de délivrer une dose absorbée élevée aux cellules tumorales tout en épargnant les tissus sains environnants. La radiothérapie externe (RTE) utilise des schémas de traitement complexes impliquant une planification adaptée à chaque patient afin d'atteindre cet objectif.

L'approche "One-size-fits-all"

Dans la plupart des cas de radiothérapie ciblée, l'activité thérapeutique à administrer est déterminée en fonction de la littérature ou de l'expérience antérieure sur l'activité maximale qui peut être injectée en toute sécurité dans un individu. Pour le ^{131}I NaI, on administre généralement une activité fixe comprise entre 1,11 et 7,4 GBq (Stokke et al. [2017]). Pour les traitements Lutathera, la stratégie de traitement la plus fréquemment utilisée consiste à administrer 7,4 GBq quatre fois avec un intervalle de huit semaines entre chaque injection. Cet intervalle de perfusion peut être prolongé jusqu'à 16 semaines en cas de toxicité possible ou observée (Henrich et al. [2019]).

Cette approche peut être considérée comme une "chimiothérapie radioactive" (Bardiès [2019]) où l'escalade de l'activité est effectuée par rapport à l'activité maximale tolérée pour des groupes de radiopharmaceutiques et/ou de patients spécifiques (Glatting, Bardiès, et al. [2013]). Bien que ce régime d'activité fixe empirique puisse être considéré comme une stratégie "simple" (Stabin, Madsen, et al. [2019]), les patients traités avec cette thérapie "universelle" ne reçoivent pas un traitement optimal. Même si cette approche est simple d'un point de vue logistique, elle ne tient pas compte de nombreuses autres variables (biocinétique, nombre et taille des tumeurs, sensibilité aux dommages causés par les rayonnements induits

par les traitements précédents, etc.) qui ont un impact direct sur les doses absorbées délivrées à la tumeur et aux tissus sains et sur leur impact potentiel (efficacité et toxicité). Bien que les activités administrées puissent être ajustées en fonction du poids corporel ou de la surface corporelle dans le cadre de ce régime d'activités fixes, cela conduit généralement à un traitement sous-optimal (sous-dosage), puisque le régime n'est pas adapté à l'individu, mais plutôt conçu pour limiter l'induction de toxicité en se basant sur les patients les plus faibles (Flux et al. 2006).

Une méthode de traitement plus individualisée est proposée, où l'activité à administrer est basée sur la pharmacocinétique spécifique, et donc sur l'irradiation réellement délivrée à chaque patient.

Méthode de traitement spécifique au patient

Le traitement spécifique au patient ou personnalisé ou individualisé est un traitement dans lequel la dose absorbée est utilisée comme indice objectif de l'irradiation délivrée par le traitement à chaque patient. Une approche de traitement spécifique au patient permet un changement de paradigme majeur, passant d'une approche unique avec administration d'une activité fixe à une approche de traitement personnalisée où l'activité optimale est évaluée spécifiquement pour chaque patient. De nombreux auteurs (Flux et al. 2006; McGowan et al. 2015; Ljungberg and Sjögren Gleisner 2016; Stokke et al. 2017; Bardiès and Gear 2021) ont démontré le rôle central de la planification de traitement en RIV, en termes d'amélioration des résultats du traitement et de réduction de la toxicité dans les tissus sains. Les patients peuvent aussi bénéficier de cycles de traitement supplémentaires si la stratégie des "quatre cycles pour tous" est abandonnée au profit d'une stratégie de prescription optimisée (Chiesa et al. 2017).

La planification du traitement spécifique nécessite la quantification de la biocinétique du radiopharmaceutique par imagerie quantitative, afin d'estimer la dose absorbée délivrée au patient par le radionucléide. Dans le cas d'administrations séquentielles, la dose absorbée par les organes à risque ou par la tumeur peuvent ensuite être utilisées pour déterminer l'activité qui doit être administrée à chaque patient lors des cycles de traitement suivants (Glatting, Bardiès, et al. 2013).

La chaîne dosimétrique clinique comprend plusieurs étapes, de l'acquisition de l'image au calcul de la dose absorbée aux tissus. La précision de la chaîne dosimétrique dépend de la précision de chaque étape impliquée dans l'obtention des doses absorbées. Actuellement, la dosimétrie n'est pas largement mise en œuvre dans les établissements cliniques, car elle est considérée comme un processus long et complexe, en raison du manque de ressources et d'expertise appropriées

(Haug 2020; Sgouros, Bodei, et al. 2020). En outre, les procédures développées diffèrent entre les centres où la dosimétrie est envisagée, en termes d'approche et de sophistication (Sjögreen Gleisner et al. 2017), ce qui entraîne une grande hétérogénéité des approches dosimétriques mises en œuvre.

Outre ces approches dosimétriques non standardisées, un obstacle majeur au développement de la dosimétrie en routine clinique est lié à l'évaluation de la précision de l'ensemble de la chaîne dosimétrique, sachant que la dose absorbée dans les tissus du patient ne peut être mesurée expérimentalement *in situ*.

L'objectif de ce travail était d'évaluer la précision et l'exactitude de la chaîne dosimétrique globale en évaluant l'impact des différentes étapes de l'exécution d'une étude dosimétrique. Pour ce faire, nous avons mis en place un essai de dosimétrie multicentrique virtuel basé sur la modélisation de Monte Carlo dans le cadre du projet DosiTest. (Home - Dositest 2021).

Schéma de la dissertation

La thèse est divisée en plusieurs sections:

- a. Étude dosimétrique multicentrique basée sur des images TEMP/TDM de patient

La première phase de la thèse compare les analyses dosimétriques effectuées par plusieurs centres cliniques utilisant le même logiciel dosimétrique sur le même ensemble de données de patient, en utilisant une méthodologie identique, afin de déterminer la précision de la dosimétrie dans un contexte simplifié et contraint. Cette étude mesure l'importance critique de l'utilisation d'ensembles de données simulées, pour étudier davantage l'exactitude des procédures de dosimétrie, dans le but de standardiser les approches.

- b. Modélisation de l'imagerie quantitative et génération de données simulées

La détermination précise de la radioactivité dans les différents volumes d'intérêt d'un patient est une condition préalable à la dosimétrie personnalisée. La modélisation de jeux de données d'imagerie simulées (basée sur la simulation Monte-Carlo) pour la quantification de l'activité est donc essentielle.

La deuxième partie de ce travail de thèse se concentre sur la simulation d'une imagerie TEMP scintigraphique tridimensionnelle réaliste à l'aide des outils de simulation Monte-Carlo GATE. La validation de la modélisation de l'image TEMP/TDM a été effectuée sur des fantômes anthropomorphes, après quoi des images TEMP/TDM de patients cliniques ont été générées. Ce faisant, la modélisation d'un mode d'acquisition réaliste répliquant le mode auto-contour des acquisitions TEMP/TDM a été réalisée et validée.

c. Mise en place d'un essai de dosimétrie multicentrique virtuel

La dernière phase de la thèse vise à évaluer l'incertitude associée à chaque phase du flux de dosimétrie clinique en utilisant un ensemble de données virtuelles (simulées) afin de pouvoir proposer des approches standardisées de dosimétrie clinique en radiothérapie interne vectorisée.

The thesis contains eight chapters.

- Ce chapitre (1) introduit le contexte général et présente les travaux réalisés au cours du projet de doctorat.
- Le chapitre 2 décrit les différentes étapes de la chaîne dosimétrique, depuis les systèmes d'imagerie, l'acquisition d'images, la reconstruction d'images et les corrections associées jusqu'à l'estimation de la distribution du radiopharmaceutique chez les patients, l'évaluation de la pharmacocinétique et la détermination de l'activité intégrée dans le temps et des algorithmes et approches de calcul de la dose absorbée.
- Le chapitre 3 traite de l'intercomparaison de la dosimétrie réalisée par différents participants à partir du même ensemble de données sur les patients, en suivant le même protocole standard et en utilisant un logiciel identique. Ce travail faisait partie d'un projet de recherche coordonné (CRP) initié par l'Agence Internationale de l'Énergie Atomique (AIEA) à Vienne, en Autriche, et a associé 8 centres internationaux basés en Afrique du Sud, Colombie, Croatie, Cuba, Inde, Indonésie, assistés par des centres cliniques français (ICO, Nantes et américains (Johns Hopkins, Baltimore), et la participation d'un industriel (DOSIsoft, Cachan, France).
- Le chapitre 4 résume la conception et le développement d'un ensemble de données de référence (composé de séries chronologiques d'images TEMP/TDM du patient, d'un protocole standard et du résultat souhaité à différentes étapes de la chaîne dosimétrique), nécessaire pour former les personnes au logiciel de dosimétrie (Planet[®] Dose) et évaluer leur propre maîtrise du logiciel.

- Le chapitre 5 traite de la modélisation et de la validation de l'imagerie TEMP sur fantôme réaliste avec l'iode 131 et le lutétium 177. Ce travail faisait partie du projet MRTDosimetry (*MRTDosimetry* 2016) dans le cadre du programme européen de métrologie pour l'innovation et la recherche (EMPIR).
- Le chapitre 6 présente la simulation d'images TEMP de patients dérivées d'un ensemble de données de patients cliniques du CRP de l'AIEA, à différents moments après l'administration de l'activité, ainsi que la possibilité d'intégrer l'ensemble des données simulées dans un logiciel de dosimétrie commercial (GE et HERMES).
- Le chapitre 7 explique le principe du projet DosiTest en démontrant la mise en place d'un essai de dosimétrie multicentrique virtuelle, la génération de la dosimétrie de référence et la validation du projet DosiTest à l'aide de l'exemple d'un centre.
- Le chapitre 8 présente une conclusion de l'ensemble de l'étude en mettant l'accent sur les résultats clés, souligne la contribution au domaine de la radiothérapie moléculaire et discute des perspectives futures sur l'amélioration de la dosimétrie personnalisée.

1

Introduction

Nuclear medicine (NM) is a specialty of medicine that utilises the ionising radiation released by radioactive substances for both diagnostic and therapeutic purposes. These radionuclides are often attached to pharmaceuticals or medical implants with the intent to target certain tissues or physiological functions in the body.

Diagnostic Application: The diagnostic component of NM provides information of the biodistribution of the labelled drug in the body which in turn contains insightful details of the biochemical or physiological functioning of a certain human body system, organ, or tumour. This spatial distribution of the radiotracer can be imaged using several techniques: 2D planar scintigraphy i.e. creation of two dimensional images, 3D single emission computed tomography (SPECT) or 3D positron emission tomography (PET) images. Each of these techniques employs an external detector (positioned outside the patient) to determine the radiation interaction site in the patient by detecting the gamma rays (in case of planar/SPECT) or annihilation photons (in case of PET) emitted by the injected radiopharmaceutical. Since these functional images have low spatial resolution, they are often registered to an anatomical image (CT or MRI) having higher spatial resolution for accurate visualisation of the structures in the body.

These pure functional images and/or in combination with anatomical images have been useful (SPECT/PET with CT/MRI) for bone scintigraphy (to determine metastasis areas and development stage of bone cancer) (Love et al. 2003; Francis et al. 2015; Van den Wyngaert et al. 2016; Bartel et al. 2018; Ichikawa et al. 2020), kidney scintigraphy (to check for renal dysfunction) (Lycklama à Nijeholt et al. 1986; Taylor 2014; Taylor et al. 2018; H et al. 2021), for tumours and metastases

localisation requiring a tissue specific molecule (Keidar et al. 2003; Virgolini et al. 2005; Levi et al. 2007; Lee, Park, et al. 2017) and as input data for for treatment planning in radionuclide therapy (RNT) (Munley et al. 1999; Bombardieri et al. 2001; Teunissen et al. 2011).

Therapeutic Application: The therapeutic aspect of NM is mainly devoted to oncology (apart from some applications in rheumatology) and involves the administration of a radioactive material into the patient in order to destroy tumour cells through radiation. In its more generic definition, the radionuclide attached to a molecule plays the role of a toxic load with local effects (Zimmermann 2019). The molecule component is usually responsible for specifically attaching to a particular tissue or organ. This is referred to as targeted radionuclide therapy and discussed in detail in the next section.

Theragnostic Application: Imaging in diagnostics permits the visualisation of the radiotracer distribution inside a patient. A molecule tagged with a diagnostic radioisotope may be used for (quantitative) imaging (SPECT/PET) of the organs and tumour(s). This enables the clinician to anticipate whether a patient will benefit from a certain therapy with this particular molecule. Then, the same or at least similar targeted molecule but with a therapeutic radionuclide, concentrating on radiation absorption for the purpose of destroying specific tissues, can be administered (Henrich et al. 2019). This combination of targeted therapeutic with a targeted diagnostic is referred to as theragnostic approach. This ‘see-and-treat’ approach can be useful for the estimation of potential response and eventual toxicity (Yordanova et al. 2017).

1.1 Targeted Radionuclide Therapy

Targeted radionuclide therapy (TRT) uses a therapeutic radionuclide, most often a beta- or more recently an alpha-emitter, having a short range in tissue to concentrate the absorbed dose within the targeted tumour while sparing the surrounding healthy tissues. TRT has risen to prominence as a preferred method of cancer treatment (Yeong et al. 2014). Unlike external beam radiotherapy where the radiation is delivered from an external source, TRT delivers radiation in a systemic or locoregional fashion, analogous to chemotherapy or biologically targeted therapy (Sgouros, Bodei, et al. 2020). Also, due to the combination of the targeting molecule and the short range of radiation involved, the cytotoxic radiation is directly delivered to the cancer cells or their microenvironment thereby preventing irradiation of the rest of the body. In the words of Paul Ehrlich, the founder of

chemotherapy, TRT can be regarded as a “*magic bullet*” that uncovers and delivers irradiation to a specific target in order to inhibit its function and destroy it.

Since the early 1900s, several radionuclides have been proposed for therapeutic applications. One of the most frequently used and well known therapeutic radionuclides is iodine-131 in the form of sodium iodide ($^{131}\text{I-NaI}$). It is administered through capsules or in liquid form for the treatment of thyroid-related diseases, such as Graves’ disease or metastatic thyroid carcinoma (Goldsmith 2020). Since then, it has been widely employed in a variety of therapeutic applications.

Targeted radionuclide therapy (TRT) can be categorised into Selective Internal Radiotherapy (SIRT) and Molecular radiotherapy (MRT) depending on how the radioactive material is delivered to the patient (medical devices in SIRT, and radiopharmaceuticals in MRT).

1.1.1 Selective Internal Radiotherapy (SIRT)

Selective internal radiotherapy (SIRT) involves the injection of tiny radioactive microspheres in the arteries supplying the tumour. These microspheres are administered via a catheter and carried by the blood flow until they lodge in small tumoural vessels. Since liver tumours depend on hepatic artery for blood supply, microspheres are injected in the hepatic artery thereby targeting the tumours only and sparing healthy liver. As a consequence, a large amount of irradiation is locally deposited in tumours (Nijsen et al. 2002; Salem et al. 2006; Gates et al. 2007).

SIRT is therefore regarded as locoregional therapy. Due to the fact that this procedure combines radiation with embolisation, it is often referred to as radioembolisation or transarterial radioembolisation (TARE). In some situations, embolisation is combined with chemotherapy and is referred to as trans-arterial chemoembolisation (TACE). SIRT is becoming an increasingly popular treatment option for primary or inoperable liver tumours worldwide (Saini et al. 2019).

SIRT microspheres are commercially available in three different types, two of which make use of a beta emitter yttrium-90 (^{90}Y) with glass (TheraSphere[®], Boston Scientific, Boston, MA, USA) or resin (SIR-Spheres[®], Sirtex Medical, Sirtex Medical Ltd., Sydney, Australia) (Westcott et al. 2016) and the third is based on holmium-166 (^{166}Ho) with poly(l-lactic acid) PPLA (QuiremSpheres[®], Quirem Medical B.V., Deventer, The Netherlands) (d’Abadie et al. 2021).

Aside from its primary use in the treatment of hepatocellular carcinoma (HCC), SIRT has also been used to treat liver metastasis of many other tumour types including neuroendocrine tumours (NETs), breast cancer and uveal melanoma, as well as the primary hepatic tumour intrahepatic cholangiocarcinoma (ICC) (Kennedy et al. 2017).

1.1.2 Molecular Radiotherapy (MRT)

Molecular radiotherapy (MRT) is an established technique in which a radiopharmaceutical consisting of a radionuclide attached to a biologically active molecule (referred to as a vector) is administered to the patient in order to deliver a therapeutic level of ionising radiation to the disease site.

By systemically administering radiopharmaceuticals with a known radiation-induced cytotoxicity, the cancerous cell populations can be targeted. The targeting vector chosen is critical in developing an efficient radiopharmaceutical, as the efficacy of these targeted therapies is dependent on the binding capacity of the vector such as an antigen or receptor to the tumoural cells (Vértes et al. 2010).

As the vector is labelled with a radionuclide in molecular radiotherapies, it is usually possible to follow the path and distribution of the radiopharmaceutical drug in the patient's body by means of imaging at various times post injection. Pharmacokinetics refers to the temporal behaviour of the drug in the body - from the drug administration to its absorption, distribution, metabolism and until its excretion from the body. This includes various physical, chemical and biological processes that are complex in nature.

As previously mentioned, therapeutic radiopharmaceuticals are often labelled with beta emitters that have a potential cytocidal effect and tissue penetration of only a few millimetres (Ahmadzadehfard 2016). Therefore, they can destroy the tumoural cells without penetrating healthy tissues.

Iodine-131 and phosphorus-32 are amongst the earliest used radioisotopes for thyroid diseases (Hertz et al. 1946) and leukaemia (Lawrence et al. 1949) respectively. In the following years, other bone pain palliation radionuclides were proposed including strontium-89 (Firusian et al. 1976) and samarium-153 (Fischer et al. 2012). Further, yttrium-90 and iodine-131 based radioimmunotherapy agents were approved by FDA for the treatment of non-Hodgkin's lymphoma (NHL). Some commercially available/approved radiopharmaceuticals include ^{131}I (by Jubilant Draximage/Malkincrodt) for thyroid cancer and ^{131}I -mIBG (by Progenics) for neuroblastoma (Schmidt et al. 2016, Sgouros, Bodei, et al. 2020), ^{89}Sr -chloride and ^{153}Sm -lexidronate (by Lantheus) for cancer bone pain and ^{131}I -tositumomab and ^{90}Y -ibritumomab tiuxetan for NHL therapy (Davies 2007).

Molecular radiotherapy is gaining popularity as a theragnostic approach for neuroendocrine tumours (NETs). This is because NETs are often diagnosed late with disseminated diseases that cannot be treated surgically and are generally resistant to chemotherapy (Caplin et al. 1998). In this context, peptides are often chosen as therapeutic vectors as they exhibit rapid pharmacokinetics (i.e.

absorption, distribution, metabolism, and excretion of the drug) and good tumour-targeting characteristics with the ability to penetrate efficiently into the tumour sites (Dash et al. 2015). Therefore, this therapy is also referred to as Peptide Receptor RadioTherapy (PRRT).

^{111}In -DTPA-octreotide, ^{90}Y -DOTA⁰-Tyr³-octreotide (^{90}Y -DOTATOC), ^{90}Y -DOTA⁰-Tyr³-octreotate (^{90}Y -DOTATATE) and ^{177}Lu -DOTA⁰-Tyr³-octreotate (^{177}Lu -DOTATATE) are among the most commonly used radiopharmaceuticals in PRRT for NET treatment (Dash et al. 2015). ^{177}Lu -DOTATATE or Lutathera[®] (by AAA, Novartis) has been approved by the European Medical Agency (EMA) in 2017 and by the Food and Drug Administration (FDA) in 2018 for the treatment of gastroenteropancreatic NETs (Hennrich et al. 2019). Along with being a beta emitter, ^{177}Lu also emits suitable gamma-rays that can be useful for imaging thereby making it a theragnostic drug. On the other hand, ^{90}Y does not emit adequate gamma rays with sufficient energy to be imaged, although low-quality images may still be acquired using bremsstrahlung radiation generated by beta particle interaction with tissues. (Forrer et al. 2006; Cwikla et al. 2010).

In recent years, ^{223}Ra -Cl₂ Xofigo (by Bayer) (Costa, Cardile, et al. 2018; Sgouros, Bodei, et al. 2020) and ^{177}Lu -PSMA-617 (by Novartis) (Kind et al. 2021) is gaining popularity for the treatment of castration-resistant prostate cancer (mCRPC), and is expected to impact therapeutic nuclear medicine by increasing tremendously the number of patients that will eventually benefit from the treatment. This ^{177}Lu -PSMA-617 has been approved very recently (March 2022) by the FDA under the name Pluvicto[™]. Also, ^{131}I -PSMA (by Molecular Insight Pharmaceuticals, Inc.) for therapeutics along with ^{124}I -PSMA for diagnostics (Zechmann et al. 2014) has been proposed as an alternative approach for mCRPC treatment.

1.2 Treatment planning in molecular radiotherapy

In any radiation therapy, the main objective is to deliver a high absorbed dose to the tumour cells while sparing the surrounding healthy tissues. External beam radiation therapy (EBRT) uses comprehensive treatment regimens tailored to each patient in order to accomplish this goal.

1.2.1 One-size-fits-all approach

In most cases of targeted radiotherapy, the therapeutic activity to be administered is determined based on literature or previous experience on the maximum activity that may be safely injected into an individual. For ^{131}I NaI, typically a fixed activity between 1.11 - 7.4 GBq is administered (Stokke et al. 2017). For Lutathera treatments, the most frequently used treatment strategy is to deliver 7.4 GBq four times with an eight week interval between each injection. This infusion interval can be prolonged to 16 weeks when toxicity (concerning the applied radioactivity) occurs (Hennrich et al. 2019).

This approach can be regarded as ‘radioactive chemotherapy’ (Bardiès 2019) where activity escalation is performed in relation to maximum tolerated activity for specific radiopharmaceutical and/or patient groups (Glatting, Bardiès, et al. 2013). While this empirical fixed activity regimen can be claimed to be a ‘straightforward’ strategy (Stabin, Madsen, et al. 2019), patients treated with this ‘one-size-fits-all’ therapy do not receive an optimal treatment. Even though this approach is logistically simple, it disregards many other variables (severity of disease/ biokinetics/ size of tumour, radiation damage susceptibility induced by previous treatments, etc.) that directly impact the absorbed doses delivered to the tumour and healthy tissues and their potential impact (efficacy/toxicity). While the administered activities can be adjusted for the body weight or body surface area within this fixed-activity regimen, it generally leads to a suboptimal treatment (underdosing), since the regimen is not tailored for the individual, but rather to avoid induction of toxicity based on the weakest patients (Flux et al. 2006).

This calls for a more individualised treatment method where absorbed doses and/or biological parameters can be assessed on an individual patient basis.

1.2.2 Patient-specific treatment method

Patient-specific / personalised / individualised treatment is a treatment in which the absorbed dose is used as an objective index of the irradiation administered to each patient. A patient-specific treatment approach allows a major paradigm shift from a one-size-fits-all approach with fixed activity administration to a personalised treatment approach where the optimal activity is specifically assessed for each patient. Numerous authors (Flux et al. 2006; McGowan et al. 2015; Ljungberg and Sjögren Gleisner 2016; Stokke et al. 2017; Bardiès and Gear 2021) have demonstrated the pivotal role of patient-specific treatment in molecular radiotherapy in terms of improved treatment outcomes and reduced toxicity in healthy tissues.

Patients may benefit from extra treatment cycles if the “four cycles fits all” strategy is abandoned in favour of an optimum prescription strategy (Chiesa et al. 2017).

Patient-specific treatment planning requires the quantification of patients’ biokinetics through imaging in order to estimate the absorbed dose using the radionuclide’s physical characteristics. The absorbed dose to critical organs (organs at risk) and the tumour location can then be used to determine the amount of irradiation that should be delivered to each patient in subsequent treatment cycles (Glattig, Bardiès, et al. 2013). Recent advancements in imaging techniques (such as quantitative SPECT/PET imaging) allow the accurate determination of absorbed doses to tumours and critical organs for pre-therapeutic treatment planning.

The clinical dosimetry chain consists of several steps, starting with image acquisition to the absorbed dose calculation. The accuracy of the dosimetric chain relies on the accuracy of each step involved in obtaining the absorbed doses. Currently, dosimetry is not widely implemented in clinical facilities as it is argued to be a time-consuming and complex process, due to the lack of availability of suitable resources and expertise (Haug 2020; Sgouros, Bodei, et al. 2020). Moreover, between the centres where dosimetry is considered, the procedures developed differ in approach and sophistication (Sjögreen Gleisner et al. 2017), thereby resulting in a large heterogeneity of implemented dosimetric approaches.

Aside from these non-standardised dosimetric approaches, a major roadblock is related to the assessment of the accuracy of the whole dosimetry chain knowing that the absorbed dose within the patient’s tissues cannot be experimentally evaluated *in situ*.

The aim of this work was to assess the precision and accuracy of the global dosimetric chain by evaluating the impact of the various steps involved in the execution of a dosimetric study. This was accomplished through the establishment of a virtual multicentric dosimetry trial based on Monte Carlo modelling as part of the DosiTest project (Home - Dositest 2021).

1.3 Outline of the dissertation

The thesis is divided into the following sections:

- a. Multi-centric dosimetric study on *clinical* patient SPECT/CT images

The first phase of the thesis compares dosimetry analyses performed by several clinical centres using the same workstation on the same patient dataset and using a similar methodology in order to determine the *precision* of dosimetry in NM practice. It emphasises the critical nature of utilising simulated datasets to further study the *accuracy* of dosimetry procedures in order to standardise dosimetry approaches.

b. Modelling quantitative imaging

Accurate radioactivity determination in various volumes of interest within a patient is a prerequisite for individualised dosimetry, and hence the modelling of simulated imaging datasets (based on Monte Carlo simulation) for activity quantification is crucial.

The second part of the thesis work concentrates on simulating realistic three-dimensional scintigraphic SPECT imaging using the GATE Monte Carlo toolkit. Validation of SPECT/CT image modelling was performed on anthropomorphic phantoms, following which clinical patient SPECT/CT images were generated.

c. Setting up of a virtual multicentric dosimetry trial

The last phase of the thesis aims to assess the uncertainty associated with each phase of the clinical dosimetry workflow using a virtual (simulated) dataset and propose standardised approaches to clinical dosimetry in molecular radiotherapy.

The thesis contains eight chapters.

- This chapter (1) introduces the general context and presents the work performed during the doctoral project.
- Chapter 2 outlines the different steps of the dosimetric chain starting from imaging systems, image acquisition, image reconstruction and associated corrections to estimate the radiopharmaceutical distribution in patients, assessment of pharmacokinetics and determination of time-integrated activity and absorbed dose calculation algorithms and approaches.
- Chapter 3 addresses the intercomparison of the dosimetry performed by various participants using the same patient dataset and following the same standard protocol and using identical software. This work was a part of a coordinated research project (CRP) initiated by the International Atomic Energy Agency (IAEA) in Vienna, Austria.

- Chapter 4 summarises the design and development of a benchmark dataset (consisting of time series of patient SPECT/CT images, a standard protocol, and the desired outcome at various stages of the dosimetry chain) that is required for training individuals on the dosimetry software (Planet[®] Dose) and evaluating their own mastery of the software.
- Chapter 5 discusses the modelling and validation of realistic phantom SPECT imaging using ^{177}Lu and ^{131}I . This work was a part of the MRTDosimetry project (MRTDosimetry 2016) within the European Metrology Programme for Innovation and Research (EMPIR).
- Chapter 6 presents the simulation of patient SPECT images derived from a clinical patient dataset of the IAEA CRP at various time points after activity administration, as well as the potential to integrate the simulated dataset into commercial dosimetry software.
- Chapter 7 explains the principle of the DosiTest project by demonstrating the setup of a virtual multicentric dosimetry trial, the generation of reference dosimetry, and the validation of the DosiTest project using an example of one centre.
- Chapter 8 presents a conclusion of the overall study emphasising the key results, underlines the contribution to the domain of molecular radiotherapy and discusses future perspectives on the enhancement of personalised dosimetry.

2

Background - Clinical dosimetry workflow

Contents

2.1 Introduction	22
2.2 Gamma camera: detector composition and image formation	25
2.2.1 Components of gamma camera	26
2.2.2 Signal processing	30
2.2.3 Image formation	31
2.3 Image Acquisition	32
2.3.1 Acquisition modes	32
2.3.2 Data acquisition settings	33
2.4 Image reconstruction	34
2.4.1 Filtered back projection (FBP)	35
2.4.2 Iterative reconstruction algorithm	35
2.5 Image degrading factors and their corrections	38
2.5.1 Attenuation	38
2.5.2 Scatter	39
2.5.3 Spatial resolution	41
2.5.4 Partial volume effect	42
2.5.5 Other image degrading factors and corrections	43
2.6 Absolute Quantification	44
2.7 Pharmacokinetics determination	45
2.7.1 Image Registration	45
2.7.2 Image Segmentation	47
2.7.3 Time-activity curves integration	50
2.8 Absorbed Dose calculations	52
2.8.1 Absorbed Dose Algorithms	53
2.8.2 Absorbed Dose Approaches	55
2.9 Assessment of variations in clinical dosimetry	57
2.9.1 Current status	57

2.9.2 Uncertainty assessment	58
2.9.3 The DosiTest project	59
2.10 Summary and presentation of the PhD work	61

2.1 Introduction

The absorbed dose (D) as defined by the International Commission on Radiation Units and Measurements is a measure of the energy $d\varepsilon$ imparted by ionising radiation per unit tissue mass dm (Equation 2.1).

$$D = \frac{d\varepsilon}{dm} \quad (2.1)$$

The mean absorbed dose $D(r_t)$ imparted to a target region (r_t) over a defined absorbed dose integration period T_D as defined by the Medical Internal Radiation Dose Committee (MIRD) (Bolch, Eckerman, et al. 2009) is given in (Equation 2.2).

$$D(r_t) = \frac{1}{M(r_t, t)} \sum_{r_s} \left[\int_0^{T_D} A(r_s, t) dt \sum_i \Delta_i \phi(r_t \leftarrow r_s, E_i, t) \right] \quad (2.2)$$

where, $A(r_s, t)$ is the activity in the particular source region r_s at time t . The time integral of activity represents the total number of decays in the particular source region from time zero to time T_D which is often up to infinity. This activity integral is termed as the *time-integrated activity* $\tilde{A}(r_s)$.

Δ_i is the product of E_i (mean energy of the i^{th} nuclear transition) and Y_i (number of i^{th} nuclear transitions per nuclear transformation). $\phi(r_t \leftarrow r_s, E_i, t)$ is the absorbed fraction i.e. fraction of emitted energy E_i at time t (in the source region r_s) that is absorbed in the target tissue r_t (Bolch, Eckerman, et al. 2009). The sum $\sum_i \Delta_i \phi(r_t \leftarrow r_s, E_i, t)$ represents the mean energy imparted per decay which is determined by the radionuclide's emission spectrum and the proportion of emitted energy deposited within the target region. This sum combined with the mass $M(r_t, t)$ term of the target region is referred to as the S-value and is summarised in Equation 2.3:

$$S(r_t \leftarrow r_s, t) = \frac{1}{M(r_t, t)} \sum_i \Delta_i \phi(r_t \leftarrow r_s, E_i, t) \quad (2.3)$$

The sum over r_s in Equation 2.2 describes the mean energy imparted to the target tissue r_t . Equation 2.2 can therefore be reduced to the following equation (Equation 2.4):

$$D(r_t) = \sum_{r_s} \tilde{A}(r_s) \cdot S(r_t \leftarrow r_s) \quad (2.4)$$

The S-value is a radionuclide and source-target combination specific quantity. It can be determined using whole-body “computational phantoms”, or models representing reference humans of a specific age, gender, total body mass, and standing height. Initially, analytical models described by equations were built to represent various anatomical structures (Cristy et al. 1987d). These models accounted for adult men, pregnant and non-pregnant women and children (Hindorf 2014). The second generation of models offered descriptive voxel based anatomical representation (Zaidi and Xu 2007) based on organ segmentation from tomographic images such as CT images (Menzel et al. 2009). Third generation non uniform rational spline (NURBS) models were generated using computer graphics to represent detailed surfaces of various geometries (Lee, Lodwick, et al. 2007; Xu et al. 2007; Segars et al. 2010), thereby allowing multiscale definition of human anatomy and a certain degree of flexibility that enabled breathing and cardiac cycle movements to be taken into account (Bailey, Humm, et al. 2014; Bolch, Jokisch, et al. 2016; Kim et al. 2018).

A first-order adaptation of these model-based dosimetry to patient-specific dosimetry includes the determination of the time-integrated activity for each patient and further adjustment of the corresponding S-values. Then, complete patient-specific dosimetry entails determining the activity distribution in the patient, integrating the kinetics data to establish the time-integrated activity and, eventually computing the absorbed doses. This is explained in detail in the following sections.

Equation 2.4 summarises the major components of absorbed dose calculations, the total number of decays in each source region $\tilde{A}(r_s)$, the radionuclide-specific emission data and their associated absorbed fractions $S(r_t \leftarrow r_s)$.

The calculation of the time-integrated activity $\tilde{A}(r_s)$ is a multi-step process starting from the determination of the spatial distribution of the radiopharmaceutical i.e. activity quantification via *quantitative scintigraphic imaging* in the patient as a function of time (*pharmacokinetic modelling*).

Quantitative imaging techniques use a gamma camera consisting of collimators, crystals, photomultiplier tubes and electronics to generate either 2D planar or 3D SPECT/PET images. In the case of SPECT imaging numerous projections, covering 360° around the patient, are acquired. To form a useful image these projections need to be reconstructed. These reconstructed images are not an accurate representation of the radionuclide distribution in the patient as they are

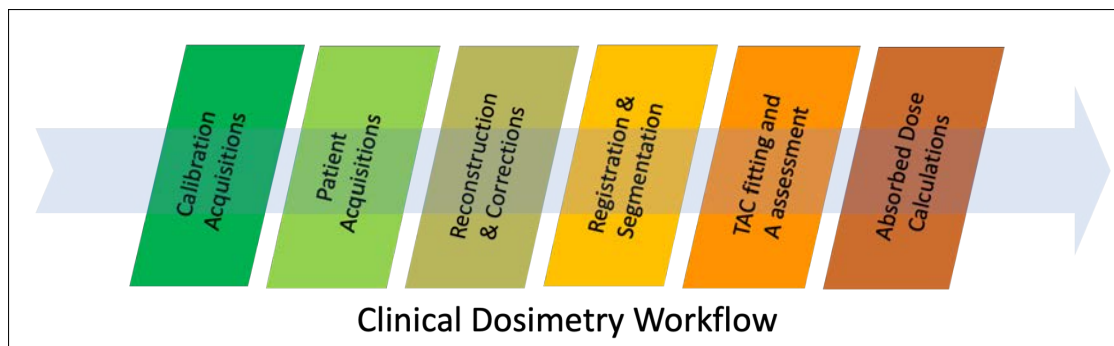


Figure 2.1: “Conventional” clinical radionuclide dosimetry workflow (Mora-Ramirez et al. 2020)

distorted by various physical effects (such as attenuation, scatter, etc.) originating either within the patient body or the gamma camera devices. Therefore, corrections need to be applied for accurate activity quantification. For the absolute quantification of the activity distribution in the patient, it is necessary to convert the reconstructed counts in the images to activity. This is done by using appropriate calibration factors.

The activity distributions obtained in the patient at various times post activity administration need to be registered or co-aligned. This is performed by applying appropriate geometrical transformations. Following this, the volumes of interest (VOI) are delineated on time-series images (or images at various time points). These VOIs can be propagated to all registered images. Alternatively, segmentation can be performed on each image in the registered time-series of images. This enables the quantification of activities in each volume of interest at each selected time post activity administration.

Following this, activities at various time points can be integrated to obtain the total number of radioactive disintegrations (time-integrated activity) in all source organs. This can be further multiplied by the corresponding S-value to obtain the absorbed doses in each target volume. This is the “classic” or “conventional” clinical dosimetry workflow.

Figure 2.1 shows the sequence of steps in this “conventional” clinical dosimetry workflow, each of which contributes a level of uncertainty. These steps are described in this chapter, as is the extent to which they are incorporated into (or excluded from) various commercial dosimetry software/toolkits.

Clinical dosimetry workflow may differ depending on the clinical centres especially when patient-specific absorbed dose calculations are concerned. After the calibration and patient acquisitions, reconstruction and corrections are performed

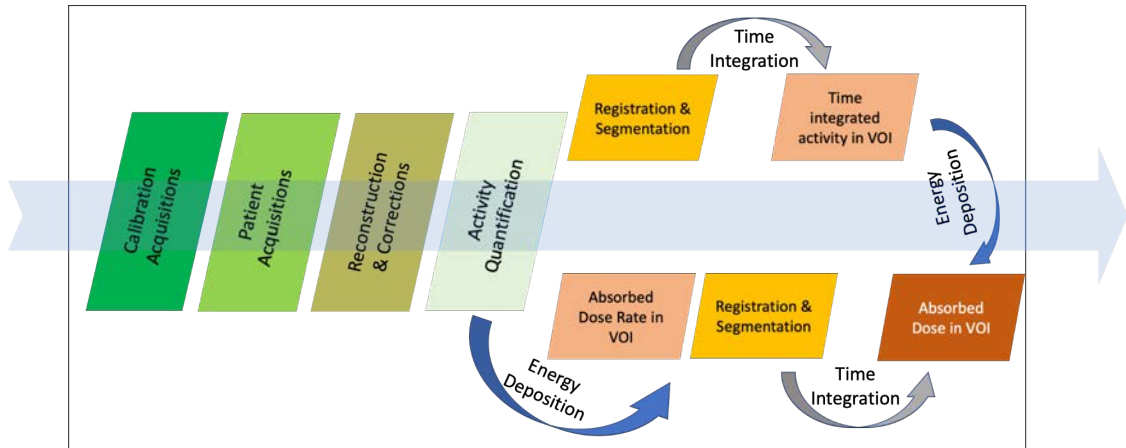


Figure 2.2: Alternative workflows for computing clinical dosimetry depending on the sequence of time integration and dosimetry step. This figure was partially derived from the work of Della Gala *et al.* (Della Gala *et al.* 2021)

so as to obtain the three dimensional activity distribution in the patient. From this stage on, an alternative approach for dosimetry calculations is to compute the absorbed dose rates. Following this, segmentation is performed, to obtain the different volumes of interest, and further propagated to time-series images. The absorbed dose rates can be further integrated over time to obtain the absorbed doses in each target volume. Different absorbed dose algorithms are detailed in the section on section 2.8. Figure 2.2 illustrates this alternative approach for computing the absorbed doses.

The following sections address each of the steps in the “conventional” clinical dosimetry workflow starting from how the *quantitative imaging* is performed (including the use of gamma camera, acquisition settings, image reconstruction and corrections followed by absolute quantification), *assessment of pharmacokinetics* (including image registration and segmentation and time integration of activities) till the computation of *absorbed doses*. At different stages, alternative dosimetry workflow has also been introduced.

2.2 Gamma camera: detector composition and image formation

Imaging in nuclear medicine is a major part of dosimetry aiming to provide information about the distribution of the radiopharmaceutical in the patient (Lassmann and Eberlein 2018). The detection and localisation of photons emitted during or after a radioactive decay of the administered radionuclides serves as the foundation for quantitative imaging.

Activity distribution in the patient can be imaged by planar (2D) or emission tomographic (3D) methods using gamma cameras (Ljungberg, Celler, et al. 2016). Planar imaging is two dimensional in nature, meaning that emitted photons, selected by the collimator, are detected in certain directions only. As a consequence, the depth dimension cannot be directly resolved from a single projection image. Although planar gamma imaging can be performed in fast acquisition and processing times (Jackson 1995), it compresses volumetric data to a single plane thereby causing the superimposition of the different structures of interest. This degrades the image contrast (Zanzonico 2012) and makes the quantification of volumes or activity within different organs and tumours difficult for dosimetric calculations (Ljungberg and Gleisner 2015).

3D SPECT tomographic images, where multiple projections can be acquired around the patient along different directions, can address these barriers. The basics of both imaging modalities are described in the following section.

2.2.1 Components of gamma camera

Gamma cameras are imaging systems capable of detecting photons and designed to be most sensitive to the gamma rays emitted by the radionuclide in the patient. These systems use scintillation detectors to generate 2D or 3D images by exploiting the excitation effect of gamma radiation on a scintillating material (crystal) and processing the electric signals to create functional images depicting the distribution of radiopharmaceuticals in the body.

The major components of a gamma camera, as shown in Figure 2.3, are a collimator, a scintillation crystal (detection medium for the photons transmitted through the collimator), a light guide, an array of photomultiplier tubes and electronics (to determine the position and energy of each interaction in the crystal). All these components are sealed in a lead shielding to minimise the incident background radiation. These are then connected to a computer for display of the 2D projection images of the activity distribution. For planar imaging, typically anterior and posterior projection views (i.e. one or two images) are acquired. In the case of SPECT imaging, a series of 2D projections are acquired from multiple angles around the patient and further processed (or reconstructed) to obtain three dimensional images.

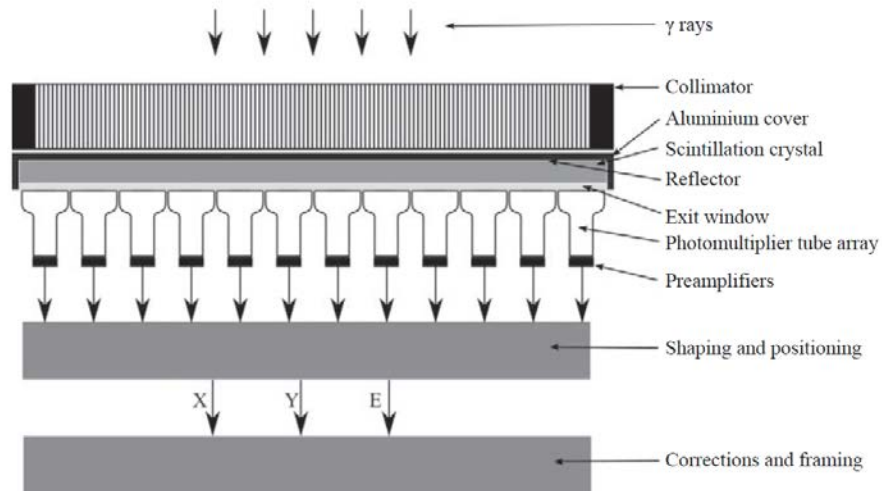


Figure 2.3: Schematic of a gamma camera (Jackson 1995)

2.2.1.1 Collimator

The collimator is the first processing layer of the gamma camera, consisting of a block of attenuating material (mostly lead) with an array of hexagonal holes. Gamma photons are emitted isotropically from the patient and may hit the detector in various locations. A collimator acts as a filter to allow only the photons travelling perpendicular, or close to perpendicular to the detector surface to pass through. This helps to localise the origin of the radionuclide within the patient body, thereby enabling image formation. These ‘acceptable’ photons are less than 1% of the photons emitted by the radiopharmaceutical while the rest are ‘wasted’ and not recorded by the gamma camera (Mettler et al. 2012). Therefore, the collimator can be considered as a limiting component in the gamma camera (Mettler et al. 2012) system, limiting the count rate (i.e. sensitivity).

Depending on the imaged isotope characteristics, collimators vary with respect to thickness, number, direction and diameter of the holes. The most commonly used collimator in gamma camera systems is the parallel hole collimator consisting of parallel holes with its long axis perpendicular to the crystal surface. The lead walls between these holes are called septa and these absorb most of the obliquely angled (unwanted) gamma photons. The length of the collimator holes and septal width controls the properties of the generated projections - longer septa indicate better spatial resolution but decreased sensitivity, while shorter septa decrease resolution and increase the detector count rates - this effect is often referred to as the resolution-sensitivity trade off (Van Audenhaege et al. 2015). The choice of collimators also depends on the energy of the radionuclide imaged.

Camera	Collimator	Hole size ^a	Septal thickness ^a	Length	Spatial resolution ^a	System sensitivity ^b
		(mm)	(mm)	(mm)	(mm)	(cps/MBq) \pm s.d.
Discovery (GE)	LEHR	1.5	0.2	35	7.4	96.6 \pm 1.7
	MEGP	3	1.05	58	9.4	70.3 \pm 1.2
Skylight (Philips)	LEHR	1.4	0.15	32.8	7.4	109.3 \pm 2.1
	LEGP	1.4	0.18	24.7	8.8	204.3 \pm 3.9
	MEGP	2.95	1.14	48	11.3	101.1 \pm 1.9
Intevo (Siemens)	LEHR	1.11	0.16	24.05	7.5	185.9 \pm 0.9
	LEAP	1.45	0.2	24.05	9.4	225.9 \pm 1.0
	MELP	2.94	1.14	40.64	12.5	115.6 \pm 0.5

Table 2.1: Characteristics of various collimators from the different manufacturers (Gregory, Murray, Gear, Aldridge, et al. 2017)

LEGP/AP/HR refers to low-energy general purpose/all purpose/high-resolution while MEGP/LP refers to medium-energy general purpose/low penetration collimators.

^aThe spatial resolution of collimated photons is specified in the manufacturer's specification as the FWHM at 10 cm from the collimator external surface for a $\frac{3}{8}$ " crystal. The thicker ($\frac{5}{8}$ ") Skylight crystal will have a lower spatial resolution, however this value is not specified by the manufacturer.

^bs.d. is the error propagated from the uncertainty in measured activity and the square root of the counts in the region of interest, as used in the NEMA sensitivity calculation

For ^{99m}Tc imaging (140 keV gamma energy), low energy collimators characterised by relatively large holes are used and termed as low energy all purpose (LEAP) collimators. Smaller holes and longer septa collimators are referred to as low energy high resolution collimators (LEHR) and are typically used to image small structures in diagnostics. Medium energy collimators are preferred for imaging ^{177}Lu with 113 and 208 keV gamma peaks (Huizing, Sinaasappel, et al. 2020). Higher energy radionuclides like ^{131}I (main gamma energy of 364 keV) require thicker septa and fewer holes to prevent the penetration of non-perpendicular gamma photons through the septa therefore, high energy collimators are best suited in that context. Table 2.1 presents a variety of collimators from different manufacturers and their characteristics.

2.2.1.2 Scintillation crystal

The incident gamma photons that are not attenuated in the patient and pass through the collimator are detected by a scintillation crystal, where they are converted into scintillation light photons. When the gamma rays strike the crystal, they lose energy through photoelectric and Compton interactions thus producing one or more secondary electrons with high kinetic energy. These secondary electrons travel through the crystal causing ionisations and excitations. De-excitation

of the electrons occurs further via the emission of the scintillation photons. The amount of scintillation light produced is directly proportional to the energy of the gamma photons deposited in the crystal during its interaction with the crystal medium (Smith et al. 2010).

Sodium iodide (doped with thallium) crystals are most widely used in commercial gamma cameras because of various reasons. This crystal has a reasonably high atomic number (Z_{eff} of 50.11) and density (3.67 g/cm^3) (Singh, Singh, et al. 2020) with a high linear attenuation coefficient of 2.22 cm^{-1} at 140 keV. NaI(Tl) being an inorganic scintillator has a light decay time of 230 ns and a peak light emission of 415 nm, the wavelength that corresponds closely to the optimal performance of the conventional photomultiplier tubes (PMTs) (Smith et al. 2010).

To ensure that the light photons collected by the PMT array are exclusively attributed to the scintillation events occurring in the crystal, the crystal is hermetically encapsulated in a metal casing to restrict any external sources of light. Furthermore, due to the crystal's hygroscopic nature, it is protected from any moisture that can limit transmission.

The light output of the scintillator is transferred to an array of PMTs through a light guide, an optical window placed at the back of the crystal. This reduces the light losses to PMTs as the guides are made of transparent plastic having a refractive index of 1.85, similar to the refractive index of NaI(Tl) (Singh, Singh, et al. 2020) and are carefully shaped to match the shape of photomultiplier cathode. Additionally, the thickness and the masking of the light guide are designed in such a way that scintillation light from a single gamma-photon event is dispersed among the PMTs in a fashion that enables the accurate determination of all the interaction sites in the crystal (Zeng et al. 2004).

2.2.1.3 PMTs

A photomultiplier tube (PMT) placed behind the NaI(Tl) crystal converts the light from the crystal to an electric signal of measurable magnitude.

Figure 2.4 shows the different components of a PMT. The interior surface of the entrance window of the PMT is covered with a photocathode coated with caesium antimony CsSb (Cherry et al. 2012c) where the incident photons interact and convert to photoelectrons. These photoelectrons are focused onto the first metallic plate called dynode held at a higher voltage with respect to the photocathode. Electrons are released via secondary emission for every incident electron that strikes the dynode: a typical amplification factor is between 3 and 6 (Smith et al. 2010). These electrons are directed onto the next dynode where secondary electrons are

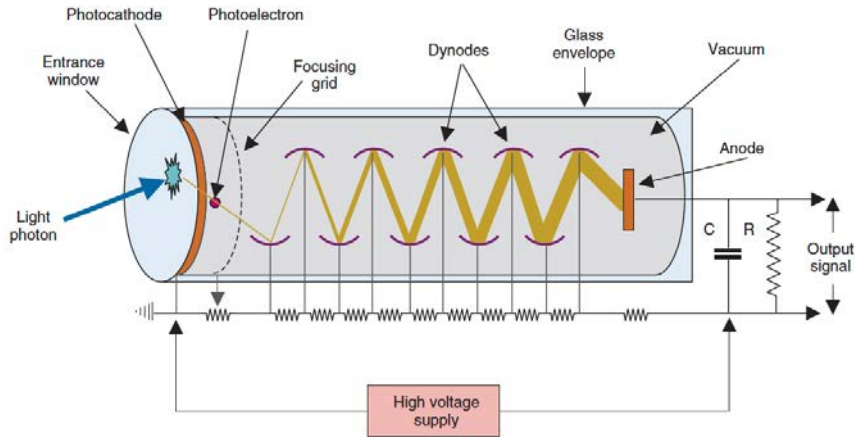


Figure 2.4: Schematic of a photomultiplier tube (Cherry et al. 2012d)

produced and the process is repeated at subsequent dynodes until the electrons are sufficiently amplified. The number of dynodes vary between 8 and 12 (Bailey and Humm 2014). The voltage at each dynode controls the multiplication factor. The resulting electrons are collected at the last electrode i.e. the anode. The PMTs are sealed in glass and are evacuated to reduce electron attenuation between dynodes. As they can be affected by external magnetic fields, these PM tubes are often wrapped in metal foil (Cherry et al. 2012d).

2.2.2 Signal processing

The photons emitted within the crystal will be detected and amplified by one or more PMTs positioned around the interaction site. The amount of light sensed by a single PMT is inversely related to the distance between the scintillation event and the centre of the PMT. The location of the gamma ray interaction in the crystal can be determined using the equations and calculations described by Cherry *et al.* (Cherry et al. 2012c) (Figure 2.5) and the computer algorithms used within the camera software to perform these positional estimations. The summation of all the signals from the PMTs gives the total electrical signal and this is proportional to the energy of the incident gamma ray.

The summed signals are sent to a pulse height analyzer (PHA) where discrimination of the photons occurs based on the energy deposited by a scintillating event in the crystal. The PHA retains the recorded events corresponding to the primary photons originating from the photopeak of the isotope and discards the scattered photons from the background radiation or from the Compton scattering in the patient. (Mettler et al. 2012). PHA can discriminate between photons due to the fact that the energy deposited by the event in the crystal is directly proportional

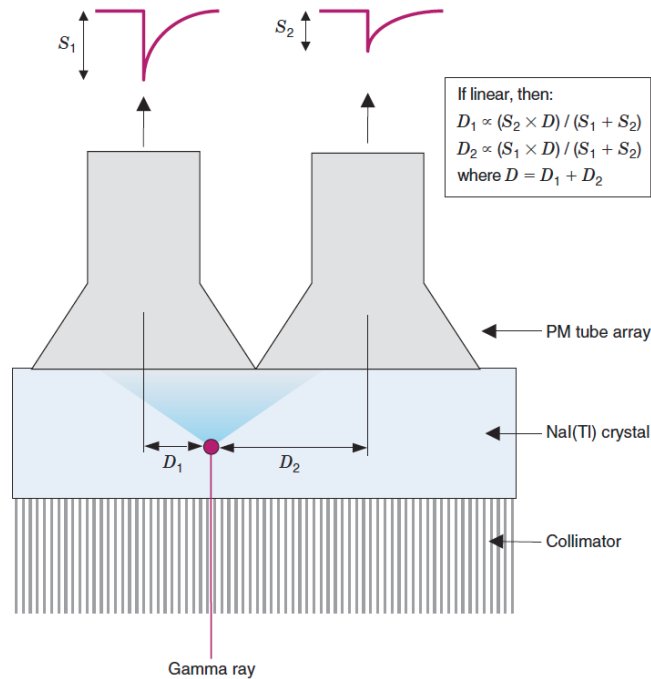


Figure 2.5: Signal processing in gamma camera (Cherry et al. 2012d)

to the PMT voltage signal. A multi-channel analyzer (MCA) employing an analog to digital converter digitises these signals for a specific energy range and produces a pulse height spectrum. Typically, energy windows of $\pm 10\%$ of the photopeak energy are set. Some radionuclides like ^{177}Lu have multiple photopeaks (113 keV and 208 keV) and images can be acquired considering either each or all of the photopeak energies.

2.2.3 Image formation

The final step in the gamma camera imaging is the image framing i.e. forming spatial histograms of the counts as a function of position and/or possibly other variables (Bailey and Humm 2014). Each element in a 2-D matrix of pixels or histogram corresponds to the location of the event in the scintillation crystal determined using positioning logic. All the recorded events are processed and added to this two-dimensional histogram which is further stored in computer memory. Framing software often enables the framing of multiple images from different energy windows into different images or summing of photons from different energy windows into a single image.

Projection images are generated by binning photons into images depending on the time period from the start of the acquisition or the preset number of counts. These projections can then be viewed or stored on a computer and/or further

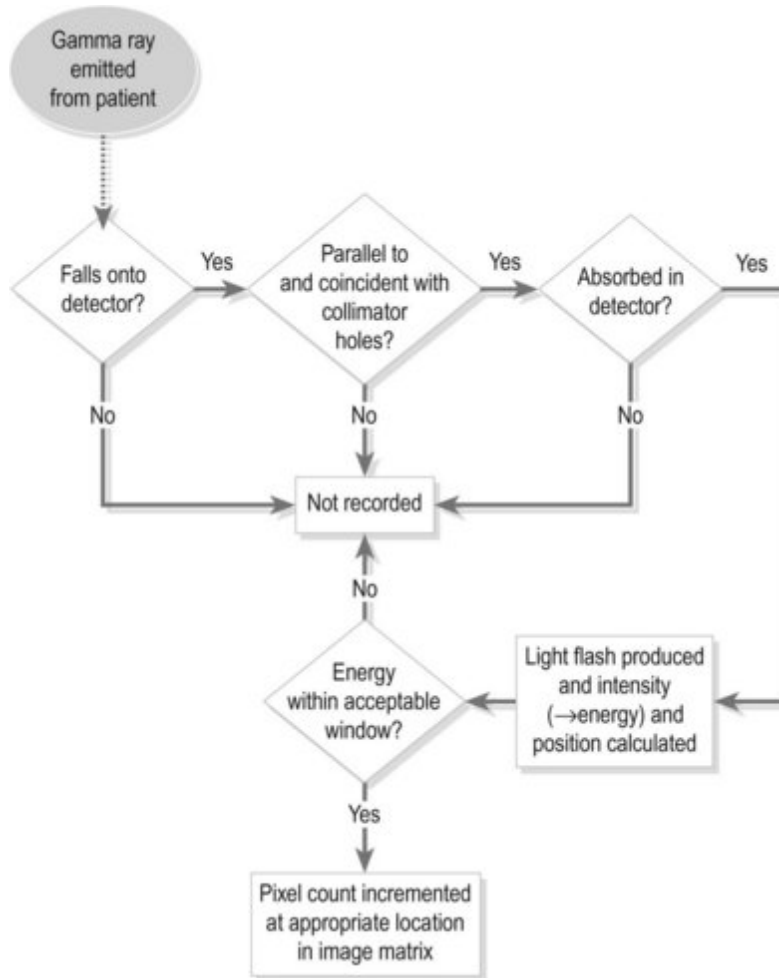


Figure 2.6: The process from the emission of gamma photons to the image formation (Themes 2016)

reconstructed to obtain 3D images. Figure 2.6 highlights the process from the time the gamma ray is emitted from the patient until it is recorded in an image.

The photons detected by the camera which contribute to the image formation are not an exact representation of the source distribution in the object (phantom/patient). This is due to the noise and physical factors like attenuation and scatter which degrades the image quality.

2.3 Image Acquisition

2.3.1 Acquisition modes

A SPECT scanner consists of a rotating gantry with an engineered radiation detection system. These scanners are equipped with one or multiple detector heads each with a collimator, crystal and associated electronics as described above. 2D

planar images are acquired with the gamma camera as single projection using a fixed incidence during the time of acquisition. However, for SPECT images, the gamma camera rotates around the patient to acquire two dimensional projections from multiple angles. These projections are further reconstructed to obtain three dimensional images.

Planar imaging fails to provide the depth (and therefore volume) information, thereby making it difficult to quantify activity (Assié, Dieudonné, et al. 2008) except at the whole body level. The hybrid imaging approach considers various whole body scans along with one or more tomographic scan(s) (Dewaraja, Frey, et al. 2012).

Current SPECT gamma cameras are often hybrid systems that include a computed tomography (CT) component, permitting several anatomical imaging modes to be acquired without moving the patient. The CT acquired can range from a low dose to full multislice diagnostic CT depending on the purpose. This provides various advantages:

- *Image fusion*: CT images have high spatial resolution and provide anatomical information. SPECT images on the other hand provide functional information of the specific uptake of the radiopharmaceuticals but with limited spatial resolution. Fusing the SPECT images onto the corresponding CT images improves the anatomical localisation and diagnostic certainty for various clinical studies (Jacene et al. 2008).
- *Attenuation correction*: The detected photons do not accurately represent the activity distribution in the body, as gamma rays emitted from the patient are attenuated in different regions before being detected by the gamma camera. A transmission image via CT allows the user to obtain an attenuation map which can be used to correct attenuation during the reconstruction process (Refer Section 2.5).

In what follows, we will focus on SPECT/CT as its current state of the art in terms of absolute quantification. However, many of the phenomena described below apply equally to planar and SPECT imaging.

2.3.2 Data acquisition settings

There are several data acquisition settings that can impact the quality or quantitative content of the final image. Some of the important parameters are listed below (Flower 2012):

- type of orbit of detector head(s)
- radius of rotation

- matrix size of the projections
- number of projections
- frame duration per projection
- angular range or angular step of the projections

The trajectory of the detector head(s) around the patient can be circular/continuous motion ie. with a fixed radius of rotation or can be auto-contour/step and shoot motion where the detector head moves as close as possible to the patient, thereby following the patient contours (variable radius of rotation). The step and shoot mode is considered as the default for SPECT imaging nowadays (Dewaraja, Frey, et al. 2012) as it minimises the depth-dependent spatial resolution and improves uniformity (Gottschalk et al. 1983; Heller et al. 1987). The matrix size of the projections specifies the dimensions of the 2D histogram from the projection. The typical matrix size is in the power of 2 and can range from 32×32 to 1024×1024 . The standard matrix size of 64×64 or 128×128 is used for patient SPECT scans, while 256×1024 is used typically for whole body imaging. Total number of projections collected around the patient is an important parameter since angular undersampling can lead to image blurring and artefacts. By increasing the number of projections, it is possible to improve angular sampling but at the expense of reduced counts per projection, unless the acquisition time can be extended (Flower 2012). The time duration per projection determines the number of the counts and therefore the noise in the projections. Projections can be obtained over a range of 180 degrees or 360 degrees, however 360° is less susceptible to image distortion when considering larger or deeper organs.

2.4 Image reconstruction

SPECT data are a series of two dimensional projections acquired by the detector(s) at multiple angles. A common way to represent this projection dataset is in the form of a 2-D matrix, often referred to as sinograms (due to the formation of the sinusoidal pattern by each point in the projection). Sinograms represent the acquired data for a particular axial position in one image. Each row in the sinogram can be mapped to each projection angle. First row corresponds to the first projection angle of the gamma camera while the last row is analogous to the last projection angle. The value along the rows is the sum of the intensity in each projection. Figure 2.7 shows the stack of projection profiles or sinograms. Sinograms can be quite useful for detecting artefacts (like the ones related to motion during acquisition) in SPECT images (Cherry et al. 2012c).

These sinograms are reconstructed to obtain a 3D estimate of the radiopharmaceutical distribution in the patient. There are numerous algorithms that reconstruct the images analytically or iteratively (Bruyant 2002). Analytical reconstruction algorithms use direct mathematical solutions for image formation while the iterative algorithm is a more complex mathematical solution necessitating several iterations to obtain the final reconstructed image (Asl et al. 2013).

The choice between algorithms is determined by the clinical situation to be studied and the computational capabilities provided by the workstation manufacturers.

2.4.1 Filtered back projection (FBP)

The analytical projection profiles $p(r, \Phi_i)$ are acquired at discrete angles Φ_i and are sampled at discrete intervals along r . This process is often referred to as forward projection (as seen in Figure 2.7). The images are reconstructed on a 2D matrix containing pixels in the (x,y) coordinate system. The main concept of backprojection is to project back each element in a profile to the image grid. The counts are evenly distributed in all the voxels along the line of response. When all the backprojections for all profiles are summed, an approximate source distribution is obtained. This gives rise to blurry images as counts are not projected in the true location (Cherry et al. 2012d).

Filtered back projection (FBP) utilises a ramp filter to correct for the blurring before acquisitions are back projected into the image space. This allows the suppression of lower spatial frequencies and enhancement of higher spatial frequencies. However, as a consequence, high frequency noise is also amplified. This algorithm has been widely used due to its speed and ease of implementation. However, it does not compensate for image degrading factors like photon scatter and depth dependent spatial resolution, even though an approximate attenuation correction proposed by Chang, assuming homogeneous density in the whole volume, can be applied (Flower 2012). Smoothing filters can be used to reduce the noise but at the cost of degraded spatial resolution. More advanced algorithms that accurately account for the image degrading factors should be employed for dosimetry purposes when accurate activity determination is required.

2.4.2 Iterative reconstruction algorithm

Iterative methods have gained popularity in the reconstruction of images and have advantages over the FBP including accurate modelling of the physical effects that degrade the image quality. The general schematic for iterative reconstruction is

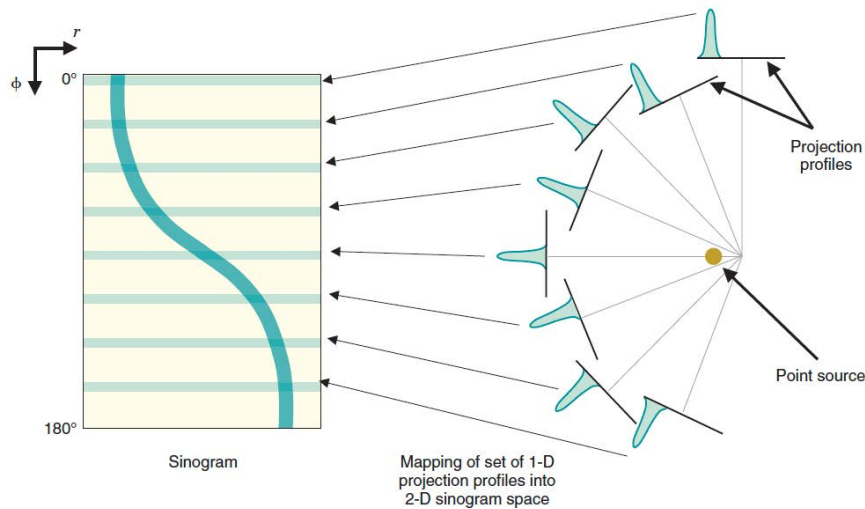


Figure 2.7: 2-D projection profiles of a radioactive point source displayed as sinograms. Each row in the sinogram represents the projection profile at each angle (Cherry et al. 2012d)

shown in Figure 2.8. It starts with an initial image estimate which can be a simple geometrical shape or uniform image $f^*(x,y)$. The projections from the estimated image are computed via forward projection and a sinogram is formed. The sinogram or a stack of projections is compared with the actual projections. Differences or sum of squares difference between the actual and estimated sinogram can be calculated pixel by pixel or by weighing the sinogram areas with high signal intensity (Zeng 2001; Knoll et al. 2012). This can be used to adjust the estimated image for better agreement. The update and compare process is repeated until there is a convergence i.e. the difference between the estimated and the true sinogram becomes significantly small. Although iterative reconstruction produces higher quality images than FBP, the approach is computationally demanding (Vandenberghe et al. 2001).

The most commonly used iterative algorithm is the maximum likelihood expectation maximisation (ML-EM) (Shepp et al. 1982). The MLEM algorithm is derived by maximising the likelihood of a reconstructed image generating a true projection set in accordance with Poisson statistics. The images reconstructed using this approach exhibit better noise characteristics than those reconstructed using FBP. However, for satisfactory convergence, many tens to hundred iterations may be required (Bailey and Humm 2014). A number of methods have been suggested to speed up the convergence.

The most widely used method is the ordered subset expectation maximisation (OS-EM) where the projection dataset is split into subsets. It follows the equation (Equation 2.5):

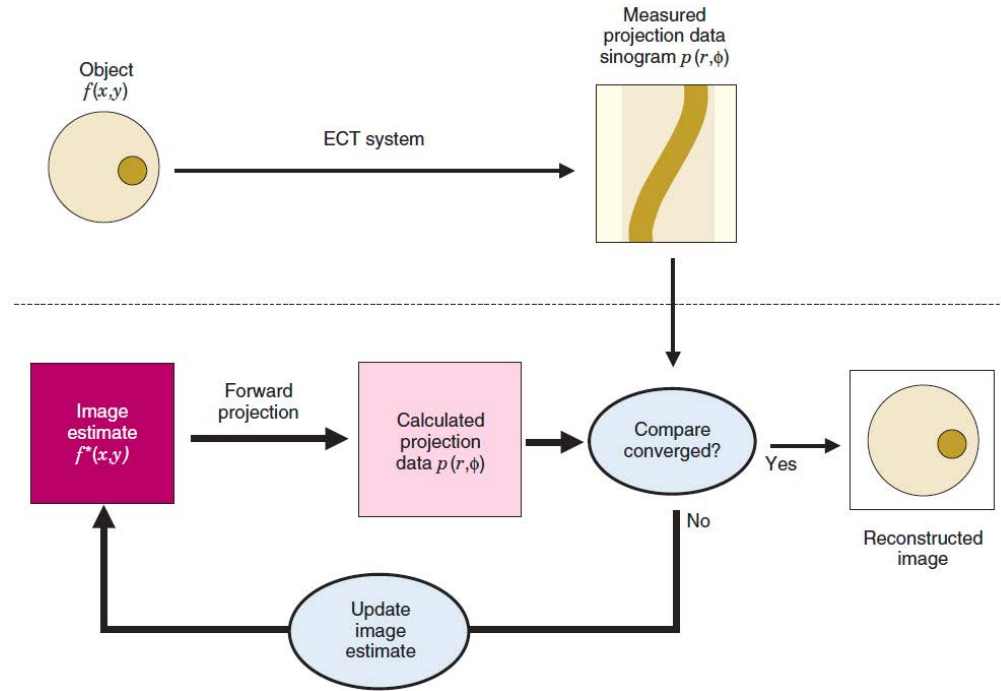


Figure 2.8: Schematic of iterative reconstruction (Cherry et al. 2012d)

$$X_i^{S+1} = \frac{X_i^S}{\sum_{j \in S} C_{ji}} \sum_{j \in S} \frac{C_{ji} T_j}{\sum_i C_{ji} X_i^S} \quad (2.5)$$

where, T_j is the j^{th} true projection, X_i^S is the i^{th} voxel of the estimated image for the S^{th} iteration. C_{ji} represents the j, i element of the system transfer matrix or system model. This matrix represents the probability of an emission of a photon from voxel i contributing to a count in the j^{th} pixel of the projection. This matrix can also contain information related to physical effects such as the attenuation and scatter. X_i^{S+1} is the new $(S + 1)^{th}$ estimate of the 3D image (Hutton 2011). S represents the number of subsets on which the iterations are performed. For example, if 30 projections are acquired, this can be divided into 3 subsets with 10 projections per subset. One subset at a time is used to update the image and one iteration is only completed after all the subsets are used. Following the example, therefore, the image is updated 3 times within one iteration for a set of 30 projections. In this way, OSEM accelerates the MLEM by a factor equivalent to the number of subsets used. After all the iterations, the result is a reconstructed 3D image of the activity distribution in the patient.

Iterative algorithms are now a part of commercial SPECT software packages and being used in a range of clinical applications.

2.5 Image degrading factors and their corrections

2.5.1 Attenuation

Many gamma rays pass through different structures within the patient and are attenuated before they are detected. The probability of a photon travelling through a material is described by an exponential function of the linear attenuation coefficient and its path length. It is given by the equation [Equation 2.6](#):

$$I(x) = I_0 e^{-\mu x} \quad (2.6)$$

where $I(x)$ is the photon intensity transmitted through a thickness x of the material and μ is the linear attenuation coefficient (proportional to the material density).

Depth dependent attenuation is one of the most important physical effects that degrades the quality of SPECT images. This is most severe in parts of the body containing bones with higher attenuation coefficients. This results in a reduction of counts and the absolute quantification of activity can be underestimated by a factor of 5-20 when the images are not corrected for attenuation (International Atomic Energy Agency [2014](#)). There are several methodologies to correct for this effect. Chang's post-reconstruction algorithm multiplies a single value of effective linear attenuation (μ_{eff}), assuming constant density variation, to each pixel in reconstructed images. Chang's attenuation correction method (Chang [1978](#)) is therefore one of the well-established techniques for tissues with a uniform attenuation coefficient. Several other fast analytic and computationally intensive iterative corrective techniques are discussed in the literature by various authors (Bellini et al. [1979](#); van Elmbt et al. [1993](#); Welch et al. [1997](#); Berker et al. [2016](#)).

The most commonly used technique to account for attenuation correction is the use of an accurate 2D attenuation map ($\mu(x, y)$ for each projection). This map can be obtained from a CT scan or from a transmission scan using a radioisotope source. For a transmission scan, an external source of radiation is used to acquire transmission profiles reflecting the linear attenuation coefficient of tissues for the reconstruction of images (attenuation maps). Compared with those obtained from a X-ray CT, attenuation maps obtained from transmission scans suffer from poorer image quality (due to the poor gamma camera resolution) and low photon flux in transmission scan acquisitions (Cherry et al. [2012c](#)). In case of CT imaging, the CT Hounsfield numbers (HU) are converted to the linear attenuation coefficient $\mu(E)$ at the corresponding photon emission energy E of the radionuclide to obtain

the attenuation map. This is then included in the forward projection step of the iterative reconstruction algorithm.

The major concern when using the CT attenuation maps is that they must be well aligned with the emission data from the gamma camera. When the CT is acquired on an independent CT scanner, variations may arise due to differences in patient positioning during scans and may require registration (International Atomic Energy Agency 2014). Even with the recent SPECT/CT scanners where both scans are acquired during the same imaging session, patient movement between emission and CT scans or misregistration due to imaging table or breathing motion can cause artefacts in attenuated images (Goetze et al. 2007; Lee, Alessio, et al. 2016). Despite the ability to acquire SPECT and CT without moving the patient, there are still differences between the two imaging modalities due to the time required for acquisition. CT images are acquired within seconds whereas SPECT projections take many minutes to acquire. Although these factors need to be considered, the high statistical CT image quality based attenuation correction surpasses these concerns (Ritt et al. 2014).

2.5.2 Scatter

Photons can be deflected on interaction with the patient tissues with or without loss of energy (Compton and Rayleigh scattering, respectively). To reduce the detection of these scattered photons, energy windows are defined. However, some scattered photons will always be detected in the same window as the unscattered or primary photons. These photons impart incorrect spatial information of their emitted origin, thereby degrading the image quality and overestimating activity in each image matrix pixel. Various authors in literature report an activity overestimation in the order of 20 - 50% depending on the position, object size and scattering angles (Rahmim et al. 2008; Hutton et al. 2011; Cherry et al. 2012c; International Atomic Energy Agency 2014). With the energy resolution of NaI(Tl) based gamma cameras of around 10% FWHM, an energy window of $\pm 10\%$ centred around the photopeak is typically considered (Ljungberg, Celler, et al. 2016). Due to the low energy resolution, narrower energy windows would lead to a reduction in count statistics, which is undesirable. (Kadrmas et al. 1998; Zaidi and Sgouros 2002).

Therefore, several methods to correct for scatter have been employed over the years (Zaidi 2006). The energy window method makes use of narrow energy windows adjacent to the photopeak window to estimate the scatter in the main window. The dual energy window (DEW) method proposed by Jaszczak *et al.* (Jaszczak et al. 1984) assumes that the scattered counts in a photopeak window is

proportional to the total counts acquired in a lower adjacent scatter window. The value of the proportionality factor k depends on the radionuclide used, the camera characteristics and the energy window settings (Lagerburg et al. 2012). However, the drawback of this method is that the spatial distribution of photons in the scatter window (greater angle scatter events) differs from the scattered photons (smaller angle scatter events) in the photopeak window. Therefore, it can lead to a misleading activity quantification and limits the accuracy of the applied method (Lu n.d.; Zaidi and Koral 2004).

The triple energy window (TEW) method uses two narrow energy windows around the main energy photopeak window for the estimation of scatter in the main window (Ogawa et al. 1991) as represented in Figure 2.9. The scattered counts C_{scat} are estimated from the counts in the lower C_{lower} and upper C_{upper} scatter windows using the equation (Equation 2.7):

$$C_{scat} = \left(\frac{C_{lower}}{W_{lower}} + \frac{C_{upper}}{W_{upper}} \right) \times \frac{W_{main}}{2} \quad (2.7)$$

where W_{main} is the width of the main energy window (photopeak) while W_{lower} and W_{upper} represents the width of the lower and upper scatter energy windows, respectively. This scatter contribution for each projection is added to the forward projection in the iterative reconstruction algorithm. However, due to the narrower scatter windows, the TEW method induces noisy images and filtering of the scatter window projection data is required (King, deVries, et al. 1997; King and Farncombe 2003). Despite this, the TEW correction has resulted in a reasonable activity quantification accuracy (Dewaraja, Li, et al. 1997).

Other scatter correction techniques include effective scatter source estimation technique (ESSE) where the scatter profile is calculated from an attenuation map and the activity distribution map of the patient. This method uses the precalculated scatter kernels computed from convolution (Frey and Tsui 2002) or variance reduced Monte Carlo simulation (Bippus et al. 2010).

Monte Carlo simulation based methods are another scatter correction technique which allows the modelling of all the possible interactions within the patient to estimate scatter without the need for empirical approximations and multi-energy window acquisitions (Dewaraja, Ljungberg, and Fessler 2006). Even though it is computationally challenging, it is becoming more popular recently and is used in some commercial workstations with the increase of computational capabilities (Beekman et al. 2002; Xiao et al. 2007).

Even though different corrections are available, the choice of the method applied largely depends on the equipment or workstation installed in the department of the

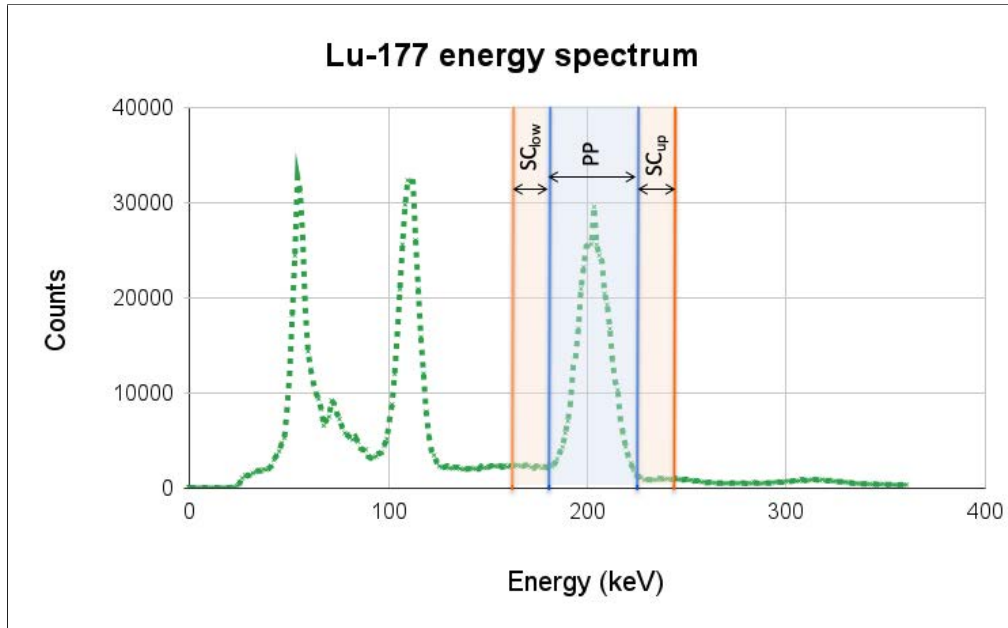


Figure 2.9: Energy spectrum of ^{177}Lu representing the triple energy windows (TEW). PP, SC (low) and SC (up) represent the main photopeak, lower scatter and upper scatter windows respectively

user. Among the various scatter correction techniques available (based on energy or spatial distributions) (King and Farncombe 2003), only double or triple energy window-based scatter correction and effective scatter source estimation (ESSE) have been commercially implemented (Dewaraja, Frey, et al. 2012).

A form of DEW scatter correction technique is incorporated within the iterative reconstruction methods in GE and Siemens systems, while Philips implemented a version of ESSE (Ljungberg and Pretorius 2018). Hermes, a vendor neutral workstation considers the Monte Carlo based scatter correction during the forward projection stage of iterative reconstruction (Bexelius et al. 2018).

2.5.3 Spatial resolution

Spatial resolution refers to the ability of the imaging system to display discrete yet contiguous sources of activity distribution. It is characterised by the full width half maximum (FWHM) of the profile drawn through the centre of a point source image, often referred to as point-spread function (PSF). Collimator response is a key contributor to the poor spatial resolution in SPECT imaging and it becomes worse with increasing source-to-collimator distance.

Moreover, the intrinsic detector response, characterised by photon interactions in the detector without collimation, including the photon scattering and statistical

uncertainty in position estimation, contributes to spatial resolution. The collimator and the intrinsic detector response collectively forms the collimator-detector response (CDR) and consists of the intrinsic, geometric, septal scatter and septal penetration components (Dewaraja, Frey, et al. 2012). Photon scatter and septal penetration correspond to the photons that scatter in the septa and penetrate the septa, respectively, but are still detected (Ghaly et al. 2016), thereby degrading the spatial resolution. The effect of septal scatter and penetration is more significant when radionuclides emitting medium or high photon energies are imaged.

Depth-dependent CDR can be modelled by a Gaussian function approximation, only when septal penetration and collimator scatter is not significant or by Monte Carlo methods for all source-collimator distances (Chun et al. 2013).

The corrections for resolution (often referred to as the resolution recovery (RR) or point spread function (PSF) modelling) is generally performed within the reconstruction algorithm (Ljungberg and Pretorius 2018). Knoll *et al.* (Knoll et al. 2012) reported an improvement in spatial resolution and decreased noise when implementing resolution recovery in three major SPECT/CT vendors - General Electric (Infinia), Siemens (Symbia T6) and Philips (BrightView). Contrast improvement for small structures using the resolution recovery method for the same systems, along with a GE Discovery 670 was reported by Seret *et al.* (Seret et al. 2012) with the additional need for a partial volume correction for more accurate quantification. Other authors (Hippeläinen et al. 2016; Van Gils et al. 2016) also showed that the collimator detector response correction improved activity quantification (either for ^{99m}Tc or ^{131}I).

2.5.4 Partial volume effect

Partial volume effect (PVE) is a consequence of limited spatial resolution in SPECT images. SPECT images have a characteristic ‘resolution volume’ that is determined by their PSF. Objects with a diameter smaller than two or three times the FWHM of their PSF partially occupy the resolution volume. Therefore, counts in the region only partially reflect the object as it comprises a contribution from structures beyond the object. Larger objects will have distorted concentrations at their borders caused by the partial volume effect and will be blurred out into the surrounding region (Cherry et al. 2012c). This causes an underestimation (due to spill out of counts) or overestimation (due to spill in of counts) of activity concentration thereby affecting the accuracy of the quantification of activity. The main goal to perform PVC is to improve activity quantification in all volumes of interest.

As PVE is a result of limited spatial resolution, this effect can be reduced by including resolution recovery in the iterative reconstruction algorithm. However, as mentioned by some authors including Seret *et al.* (Seret *et al.* 2012), partial volume correction (PVC) is essential especially for small objects along with CDR compensation for accurate quantification.

Several techniques for partial volume correction have been used over the years (Rousset *et al.* 2006). One of the traditional ways to correct for partial volume effects is based on the use of recovery coefficients (RC). A recovery coefficient is the ratio of measured activity concentration in SPECT images to the true activity concentration. Physical phantoms consisting of perfect spheres with variable sizes and known activity concentration can be used to obtain RCs and can be applied to spherical objects in SPECT images (Rousset *et al.* 2006). However, not all irregularly shaped anatomical structures in non-homogeneous background activity can be well approximated by simple geometrical shapes surrounded by uniform background activity. Various authors performed PVC during or after reconstruction (Livieratos *et al.* 2009; Erlandsson, Thomas, *et al.* 2011; Hesz *et al.* 2013). Erlandsson *et al.* (Erlandsson, Buvat, *et al.* 2012) summarised the different PVE corrections available that can be implemented.

2.5.5 Other image degrading factors and corrections

Other image degrading factors include patient movement, deadtime losses, noise and background activity.

SPECT/CT acquisition times vary and can last for around 30 minutes (Devaraja, Frey, *et al.* 2012). In this time span, movement of patients can occur and this affects the spatial resolution, inducing image artefacts. All manufacturers provide some form of motion corrections for SPECT acquisitions.

Counts are lost if new events occur too close in time to the previous event, thereby decreasing the count rate and sensitivity. There are mathematical models available to correct for count rate losses (International Atomic Energy Agency 2014).

Increased activity or longer acquisition periods may help minimise noise. The latter, however, is a trade-off, since a longer acquisition time increases the potential of patient movement and necessitates camera availability at clinical centres.

Additionally, for appropriate activity quantification, background activity in the patient must be subtracted from the measurements (Pereira *et al.* 2010; Shanei *et al.* 2015).

2.6 Absolute Quantification

SPECT imaging is used to visualise the distribution of activity across the body. When dosimetry is a concern, absolute quantification is required to determine the absolute activity distribution in the volume of interest in the patient. This is obtained by converting the total counts in the reconstructed image to activity using a calibration factor that is specific to the gamma camera, radionuclide, and reconstruction settings.

Calibration factors are derived by performing measurements with a source of known activity of the radionuclide to be used. The simplest method of obtaining a calibration factor is to acquire a planar image of a point-like source to determine the in-air camera sensitivity, with no attenuation or scatter corrections involved. (Shcherbinin et al. 2008). However, perfect correction is challenging to implement for patient SPECT data. Consequently, a source geometry such as a water-filled tank with uniform activity or with hot spheres in uniform background activity is desirable as it better reflects the scatter and attenuation effects in patient imaging (Zeintl et al. 2010; Dewaraja, Frey, et al. 2012). It is recommended to acquire the calibration images, to perform the reconstruction and apply corrections for degrading factors in the same way as would be done in patient studies. The calibration factor can be derived according to the equation Equation 2.8:

$$\text{Calibration factor } (k) = \frac{\text{Total Counts}}{\text{Activity} \times \text{Time}} \quad (2.8)$$

Calibration factors are generally denoted in counts per second (cps)/MBq or cps/MBq/ml (when activity concentration is used) or counts per minute (cpm)/kBq.

More and more personalised approaches to obtain the calibration factor for accurate activity quantification are available in literature. D'Arienzo *et al.* (D'Arienzo et al. 2016) recommended the use of a hot Jaszczak sphere in a non-radioactive water anthropomorphic phantom replicating a patient geometry for calibration of a SPECT system. The IAEA Human Health Report 9 (International Atomic Energy Agency 2014) suggested acquiring SPECT images of a phantom mimicking the patient in order to obtain the calibration factor. Similarly, Mezzenga *et al.* (Mezzenga et al. 2017) and Frey *et al.* (Frey, Humm, et al. 2012) also emphasised the use of large uniform phantom tomographic acquisitions with frequent sensitivity measurements as an optimal approach. Zhao *et al.* (Zhao et al. 2018) and Uribe *et al.* (Uribe et al. 2017) showed that the calibration factor obtained for a point-like source with planar acquisitions (with scatter correction) was similar to that obtained for a phantom filled with uniform activity with tomographic images. They

reported an overestimation of the calibration or camera normalisation factor when the scatter correction was not performed in planar acquisitions.

Lassmann *et al.* (Lassmann, Eberlein, and Tran-Gia 2021) recently summarised the various multicentric calibration efforts, therefore making it evident that there is currently no agreement on the best approach or a standardised approach for the calculation of calibration factor.

2.7 Pharmacokinetics determination

Quantitative imaging, as presented in the previous paragraph, will lead to an activity-indexed image (2D or 3D maps). According to the conventional clinical dosimetry workflow (CDW) presented in Figure 2.1, several steps have to be considered in order to derive the number of decays within each volume of interest in the patient: registration, segmentation and time-integrated activity determination.

In 3D imaging, volumes of interest (VOIs) can be defined on the images at each time point. Alternatively, one image is used for reference VOI definition, and VOIs are propagated further to images at different times. This is done in order to keep the same volume for the corresponding organs or tumours across the different time points. Whichever solution is selected, images acquired at various times along the pharmacokinetics have to be registered.

2.7.1 Image Registration

Co-registration is a process in which geometrical transformations are applied to images to spatially align the corresponding anatomical locations. Image registration can be classified into different categories depending on the dimensionality, nature of registration, nature and domain of transformation applied, and the modalities involved. Maintz *et al.* (Maintz et al. 1998), Crum *et al.* (Crum et al. 2004) and others explained a range of different registration methods. However, the most common registration techniques performed in clinical workstations nowadays are rigid registration or elastic registration. These registrations are named by the nature of the transformations applied to the images. While registering images, one dataset is assumed to be stationary and one or more datasets are considered to have moved. Figure 2.10 shows the flowchart of the registration process. A geometric transformation (T) is applied to the moving image such that it aligns with the stationary image. A similarity metric is employed to measure the non-correspondence between images. By using iterative optimisation, the algorithm finds the best results of this metric for the image registration process.

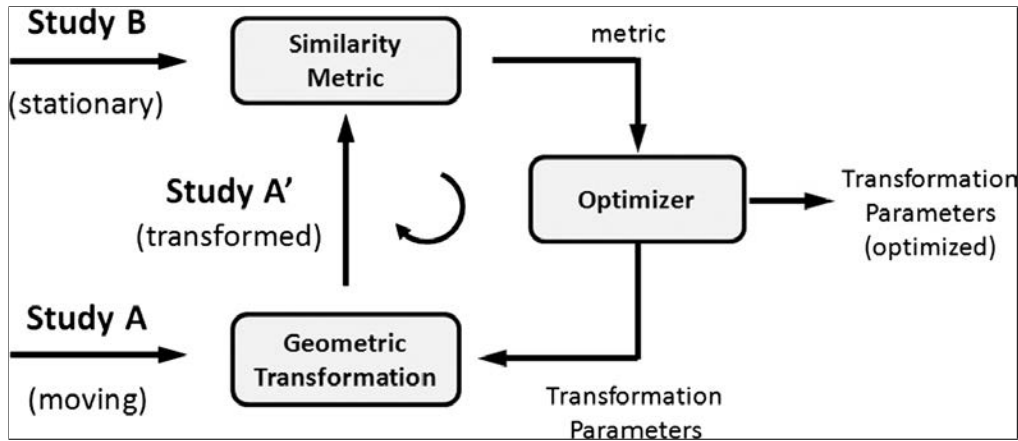


Figure 2.10: Image registration mechanism (Brock et al. 2017)

Rigid registration involves linear transformations i.e. translations in three directions and rotations around three axes. Therefore the maximum degrees of freedom or dimensionality of transformation is six. Rigid registration can be further expanded to nine or twelve degrees of freedom to account for scaling, shearing and plane reflection. This is often referred to as affine registration (Brock et al. 2017).

Non-rigid (or elastic or deformable) registration comprises transformations ranging from smooth dense displacement described with few parameters to dense displacement fields defined at voxel level (Crum et al. 2004). Here the degrees of freedom can be as large as three times the number of voxels in the stationary image (Brock et al. 2017). Elastic registration can be performed using B-splines or thin plate splines and physical or diffeomorphic models (Zhang et al. 2020). Even though the application of rigid registration is limited, due to the deformable nature of soft tissues, care must also be taken when using elastic registration as it can also result in substantial deformation of organs and tissues (Brock et al. 2017). Development of new and/or better image registration algorithms is now an active domain of research, including the use of deep learning techniques (Balakrishnan et al. 2019).

One drawback of nuclear medicine imaging is that SPECT images lack anatomical features, making it difficult to identify structures, even more so when quantitative accuracy is compromised by attenuation, scatter, and collimator blurring, resulting in low image resolution (Tang et al. 2006). This is why hybrid SPECT/CT imaging has now become the default in most quantitative imaging, dosimetry-oriented studies. Registering anatomical CT images with SPECT functional images aids the better localisation of volumes of interest. Additionally, the transformed CT enables the generation of transformed attenuation coefficient maps which in turn make it easier to perform attenuation corrections on SPECT images.

SPECT/CT hybrid systems in principle allow simultaneous emission-transmission acquisitions to be obtained. However, multi-modality images can still be misregistered if the patient moves between acquisitions as the scans are sequential (Keidar et al. 2003). In case of significant misregistration, manual registration has to be performed based on visual comparison (Dewaraja, Frey, et al. 2012). Software-based automatic registration is further desirable to avoid misregistration. Automatic and voxel intensity based registration has been suggested by some authors (Brinkmann et al. 1999; Lee, Huang, et al. 2007; Marinelli et al. 2012), but should be performed with proper care. Li *et al.* (Li, Zhu, et al. 2020) proposed organ-based non-rigid image registration keeping in mind that a whole body non-rigid registration can be computationally intensive. Most of the time, the choice of registration depends on the options provided by the available workstation. Mora-Ramirez *et al.* (Mora-Ramirez et al. 2020) compared various dosimetric software platforms including Dosimetric Toolkit (DTK) from GE Healthcare, Hybrid dosimetry module (HDM) from Hermes, Stratos from Philips, Planet OncoDose (PDOSE) from DOSIsoft and SurePlan MRT from MIM and stated that most of the tested commercial software propose a rigid registration, even though elastic (non-rigid or deformable) registration is sometimes available.

2.7.2 Image Segmentation

Activity information is extracted from each image in the registered time-series of images as it naturally changes with time. However, to quantify this activity over time and to determine the biokinetics of the associated radiopharmaceutical, image segmentation is required.

Segmentation is a process of outlining the volumes of interest (i.e. the organs and/or tumours) to quantify the counts or activity in the regions along with their masses.

Segmentation may be performed on images at a single time point and propagated to registered images if the organs or tumour do not change considerably (rigid propagation). However, if necessary, multiple segmentations of the volumes at each time point may be performed. The segmentation step is widely recognised as the step which introduces substantial variability into the dosimetry chain due to inter-operator (between operators) and intra-operator (same operator at different times) variability (Renard et al. 2020).

Various segmentation approaches have been employed and they can be classified into the following categories:

2.7.2.1 Manual segmentation

The most common method of segmentation is manual delineation (Gustafsson et al. 2017), a method which depends largely on the operator. The poor resolution of the SPECT images makes it difficult to segment volumes of interest, therefore high resolution CT images may be used alone or in conjunction with SPECT images for segmentation (King, Long, et al. 1991; Cheimariotis et al. 2018).

2.7.2.2 Threshold based segmentation

Another method commonly used for segmentation is the thresholding method on functional images. A fixed percentage of the maximum reconstructed counts is preselected within a region of interest. These fixed threshold values may vary from 25-70% but for large objects (diameter \geq two times the FWHM) these values converge to 43-46% (Erdi, Wessels, et al. 1995). An important limitation of this method is that, due to the activity spill out from the object to the background (i.e. the partial volume effect), blurring in the reconstructed images makes it difficult to delineate the true volume of the concerned region (Grimes et al. 2012).

Various adaptive thresholding techniques have been proposed in the literature where the threshold considers the source-to-background ratio of activity concentrations, image acquisition and processing methods and the size of the object concerned (Erdi, Mawlawi, et al. 1997; Daisne et al. 2003).

On the other hand, the iterative thresholding technique uses iterative methods to determine the appropriate threshold, most often determined from precalculated calibration curves from phantom experiments. Grimes *et al.* (Grimes et al. 2012) highlighted an important feature of their proposed iterative thresholding technique, which is the use of semi automatic selection of background regions thereby excluding the regions affected by spill out and effectively determining the background activity concentration. This method is also suggested by various authors (Mortelmans et al. 1986; Fleming et al. 1998; Jentzen et al. 2007; Pacilio, Basile, et al. 2011) for accurately estimating the organ (large object) and tumour (small object) volumes and activities.

Nevertheless, most thresholding methods are sensitive to noise in the image and they perform poorly in heterogeneous activity distributions, thereby underestimating the (tumour) volume.

2.7.2.3 Segmentation based on Machine Learning methods

Two arguments in favour of automatic segmentation would be the need for a reduction of the time required for delineation and improved reproducibility.

Image segmentation using the increasingly sophisticated computerised methods that are based on machine learning has gained a lot of attention in recent years (Roy et al. 2014; Litjens et al. 2017; Ker et al. 2018; Anwar et al. 2018; Cheplygina et al. 2019; Singh, Wang, et al. 2020). The reason behind the great success of deep learning models is the advancement in neural networks which incrementally learn high-level features from data, eliminating the requirement for domain expertise and laborious feature extraction (Zhou et al. 2019).

These techniques can be broadly divided into supervised methods which enable the development and optimisation of a given algorithm using an existing training dataset and unsupervised methods that perform the same function without the use of training dataset (Sharma et al. 2010). Some of these supervised methods include pattern recognition techniques (like classifiers) and artificial neural network based algorithms (ANN) (Boudraa et al. 2006) while clustering algorithms like K-means with or without the incorporation of Markov random field models (Pham et al. 2000) and fuzzy c-means algorithm (Chen, Jha, et al. 2019) fall under unsupervised methods (Chen and Frey 2020).

While many of the studies cited above affirm that automatic segmentation methods based on machine learning and thereafter deep learning are more accurate and efficient than manual/threshold segmentation methods, they are constrained by the technical skills required to develop and implement artificial intelligence software for use in various clinical dosimetric workstations. Additionally, the substantial effort needed to acquire sufficient training datasets persists.

Some clinical software like the GE Dosimetry toolkit[®] and Planet[®] Dose offer various choices for segmentation: manual, semi-automatic, or automatic using the initial images (NM or CT) with rigid propagation (assuming constant volumes) (Santoro et al. 2021). However, only a few commercial dosimetric platforms that provide artificial intelligence based auto-segmentation models are available, for example, MIM Maestro (Cleveland, OH, USA) (Urago et al. 2021) that is based on neural networks for automatic delineation on CT and MR images.

2.7.3 Time-activity curves integration

Once images are registered and segmented, and activity is quantified at different time points, the time-activity curve (TAC) can be generated following the “conventional” dosimetry workflow. The area under this TAC represents the time-integrated activity (TIA) (or cumulated activity) and is a measure of the number of radioactive decays in the source from time 0 (i.e. activity administration time) to infinity. The time-integrated activity coefficient (TIAC) (often represented as τ) can be computed as a ratio of TIA or total decays (represented as \tilde{A}) and the administered activity (represented as A_0 or simply A_{Adm}).

The area under the time-activity curve reflecting the time-integrated activity may be computed numerically by using the discrete activity values over time (for e.g. trapezoidal method) or analytically by fitting the observed data to a summation of exponential terms or another analytically integrated mathematical function.

The trapezoidal method includes the integration of activity from time t_0 to the last time point by adding the areas of trapezoids created by each pair of data points. Even though it is easy to implement, two problems are associated with this method, as can be seen from [Figure 2.11](#) i.e. the estimation of activity at time $t = 0$ and the estimation of activity beyond the last time point (Della Gala et al. [2021](#)).

[Figure 2.11](#) presents an example of “well-sampled” TAC, where the extrapolation from zero to t_1 and that from t_5 to infinity will probably not matter much to the total TIA. However, there may be situations where the extrapolated portion of the total TIA is more than the interpolated portion (from t_1 to t_5 in [Figure 2.11](#)). The quantification of the extrapolated fraction of the TIA is always an informative parameter that contributes to the evaluation of the goodness of time sampling for a given TAC (Hindorf et al. [2010](#)).

A solution for how to extrapolate activity after the last acquired image is to assume physical decay from the last time point to infinity. This can however lead to an overestimation of the time-integrated activity (McParland [2010](#)).

A more robust approach to obtaining the TIA is to fit the time activity data using mono-, bi- or multi-exponential functions, depending on the available data points. For fitting a mono-exponential function, three data points are required. A bi-exponential fitting function would need at least five or six data points, to account for uptake and clearance phases (Siegel et al. [1999](#)). Along with the number of time points, it is critical to consider the accurate time sampling in order to improve the accuracy of the TACs (Glatting [2022](#)). Siegel *et al.* (Siegel et al. [1999](#)) suggested to use one or two time points around some fraction of effective half-life, another near the effective half-life, and one or two at three or five times the effective half-life.

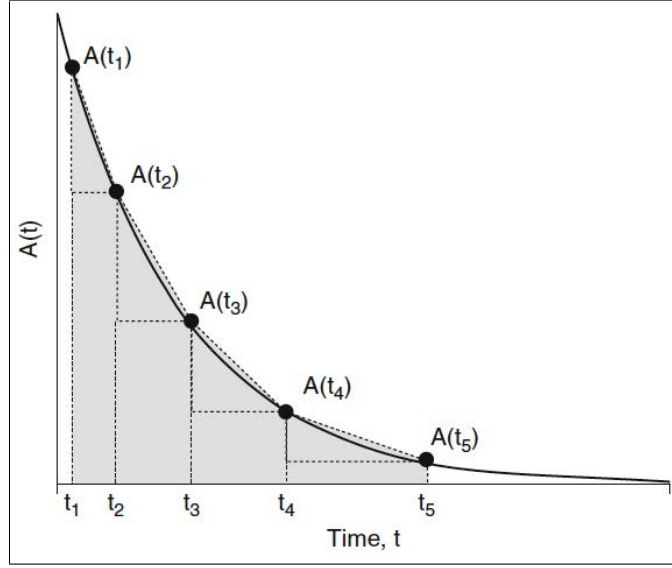


Figure 2.11: Computation of time-integrated activity using trapezoidal method

Analytical integration of the function characterising the curve yields the time-integrated activity from the fitted curve parameters. A sum of exponential functions of activity $A(t)$ as a function of time can be written as the follows (Equation 2.9):

$$A(t) = \sum_j A_j e^{-(\lambda_{phy} + \lambda_{bio,j}) \times t} \quad (2.9)$$

where, λ_{phy} and $\lambda_{bio,j}$ are the physical and biological rate constant of the j^{th} exponential respectively, t represents the time and A_j is the fitting curve parameter (dependent on the initial activity A_0). The effective rate constant is used to compute the effective half-life t_{eff} and is obtained using Equation 2.10 and Equation 2.11.

$$\lambda_{eff} = \lambda_{phy} + \lambda_{bio} \quad (2.10)$$

$$T_{eff} = \frac{\ln(2)}{\lambda_{eff}} \quad (2.11)$$

So, the parameters A_j and λ_{eff} are curve fitting parameters. By integrating the $A_h(t)$ from time zero to infinity, the time-integrated activity in the source region (r_s) can be obtained (Equation 2.12).

$$\tilde{A}(r_s, \infty) = \int_0^{\infty} A(t) dt = \sum_j \frac{A_j}{\lambda_{phy} + \lambda_{bio,j}} \quad (2.12)$$

The goal of curve fitting is to estimate the unknown parameters A_j and λ_{bio} such that the curve reflects the temporal variation of the measured data points.

A least squares estimate is a frequently used technique for determining the most optimal parameter values (McParland 2010) that minimises the sum of offsets or residuals of points from the plotted curve. The coefficient of determination R^2 is then used to determine the goodness of fit (Sarrut, Halty, et al. 2017). While it is often used, some authors (Kletting et al. 2009; Spiess et al. 2010) remarked that it may not be adequate. Other methods used include the F-test, Imbimbos I_P proposed in the pharmacokinetic context, Bayesian information criterion (BIC) and Akaike information criterion (AIC) (Motulsky et al. 2004). Glatting *et al.* (Glatting, Kletting, et al. 2007) emphasised the use of AIC based model selection over F-test as model selection criterion for the selection of the best function.

More and more commercial dosimetric platforms enable mono-, bi-, tri- or even x-exponential TIA fitting along with trapezoidal methods (with wide choices of interpolation methods) such as Planet[®] Dose (Mora-Ramirez et al. 2020; Huizing, Peters, et al. 2020; Santoro et al. 2021), while only mono-exponential fitting is available in the GE Dosimetry Toolkit[®] (Mora-Ramirez et al. 2020; Santoro et al. 2021). Hermes Hybrid Viewer Dosimetry Module incorporates mono- and bi-exponential fitting with at least three or four time points, respectively (with some extrapolation and interpolation options) (Mora-Ramirez et al. 2020; Huizing, Peters, et al. 2020). On the other hand, Stratos Imaytics from Philips (no longer distributed) enabled voxel-level TIAC computation, using trapezoidal integration and a mono-exponential function to account for physical decay (Mora-Ramirez et al. 2020).

2.8 Absorbed Dose calculations

Calculations of absorbed doses may be performed in two ways: from time-integrated activities, or from the integration of absorbed dose rates obtained at each time point (Figure 2.2). Passing from activity to absorbed dose rates, or from cumulated activity to absorbed doses requires the integration of imaging data in conjunction with information related to the characteristics of the radionuclide and patient-specific anatomy.

Different algorithms of absorbed dose computation are available, such as local energy deposition (LED), Convolution or Monte Carlo (MC) and each of these algorithms will affect the accuracy and computation time in a different way.

2.8.1 Absorbed Dose Algorithms

2.8.1.1 Local energy deposition (LED)

The local energy deposition method is an analytical method based on the assumption that the emitted radiation is non-penetrating, i.e. all the energy released is absorbed locally. This approach is computationally fast since it only requires multiplying SPECT-derived values (activity or TIA) by the energy emitted per decay, and then dividing the VOI by its mass.

The absorbed fraction from source to target region is 1 (Equation 2.13) if source and target regions are the same, while it is 0 (Equation 2.14) for source regions different from target regions (Budinger et al. 1991). The Equation 2.3 can then be simplified as:

$$S(r_t \leftarrow r_s, t) = \frac{\Delta}{M(r_t, t)} \quad \text{when } \phi(r_t \leftarrow r_s, t) = 1 \quad (2.13)$$

$$S(r_t \leftarrow r_s, t) = 0 \quad \text{when } \phi(r_t \leftarrow r_s, t) = 0 \quad (2.14)$$

where, Δ represents the total emitted energy per decay.

This makes the absorbed dose calculation a simple multiplication of time-integrated activity and the S-value (notice that in that case the S value may not need to be calculated explicitly).

$$D(r_t) = \tilde{A}(r_s) \cdot \frac{\Delta}{M(r_t, t)} \quad \text{when source} = \text{target} \quad (2.15)$$

$$D(r_t) = 0 \quad \text{when source} \neq \text{target} \quad (2.16)$$

This fast LED algorithm can be implemented at the organ level or even voxel level, provided that the voxel dimensions are larger than the radiation range and that non-penetrating radiation conditions can be assumed.

2.8.1.2 Dose point kernel convolution method

Convolution is considered in scenarios where non-penetrating contribution to the irradiation is substantial and cannot be disregarded. In these cases, it is vital to compute the amount of energy absorbed from the emission at a certain distance. For isotropic emission in a homogeneous medium, energy deposition depends only on the distance to the emission point. This justifies using absorbed dose point kernels (DPK). DPKs may be obtained analytically, experimentally, or by Monte

Carlo radiation transport modelling. Generation of DPKs from Monte Carlo radiation transport modelling was addressed by various authors (Janicki et al. 2004; Strigari et al. 2006; Ferrer, Chouin, et al. 2007; Botta, Mairani, Battistoni, et al. 2011; Papadimitroulas et al. 2012; Wu et al. 2012).

Generated DPKs in a homogenous medium can be further convolved with the activity or time-integrated activity distribution to obtain the absorbed dose rates or absorbed dose, respectively. Fast Fourier Transform techniques may be used to accelerate the convolution process. With voxel-based activity distributions, it is possible to compute absorbed dose rates at a voxel scale but this requires voxel-based S values (VSVs) sampled at the scale of activity map (Bolch, Bouchet, et al. 1999). Some years back, Lanconelli *et al.* (Lanconelli et al. 2012) provided a free database of VSV for seven radionuclides at thirteen different voxel sizes computed using the EGSnrc based Monte Carlo simulation code. Other studies in the same context included the comparison of VSVs between different Monte Carlo codes and evaluated the impact on resulting absorbed doses (Pacilio, Lanconelli, et al. 2009), computation of VSVs at variable voxel size using MCNPX Monte Carlo code (Dieudonné et al. 2010), proposition of methods to rescale these voxel S values for arbitrary voxel sizes (Fernández et al. 2013), determination of VSVs for monoenergetic electrons and photons analytically (Amato et al. 2012).

Convolution of these VSVs is relatively easy to implement and not computationally challenging (Dieudonné et al. 2010). Moreover, it allows the computation of the absorbed dose (rate) at voxel level. Nonetheless, the convolution approach is constrained in principle by the inability to accommodate tissue inhomogeneities even though several approaches have been proposed (Cross et al. 1992; Foox et al. 2021; Ahnesjö 1989).

2.8.1.3 Monte Carlo simulation approach

The use of Monte Carlo (MC) simulations for absorbed dose calculations is one of the most advanced and robust techniques capable of modelling radiation transport at any scale (macroscopic/microscopic) and in any media (homogeneous/heterogeneous) (Zaidi and Andreo 2002). This approach simulates all the probable interactions of emitted particles as they travel across a medium. It can be used to generate S values for organs or even VSVs, but also to calculate absorbed dose rates or absorbed doses directly (Bardiès and Myers 1996). The latter may use voxel-based patient geometry and activity distribution (for example from quantitative SPECT/CT imaging) as an input for the simulation of radiation transport and calculation of the absorbed dose rates (Ljungberg, Strand, et al. 2012).

A full MC simulation is computationally intensive, however, with the growing computational power, it is possible to obtain the absorbed doses in a reasonable timeframe.

There is a wide availability of MC codes today that are able to compute absorbed doses in most nuclear medicine scenarios, at least at tissue level. Some of these codes include MCNPX (Waters et al. 2007), EGS5 (Hirayama et al. 2005), EGSnrc (Kawrakow 2001), FLUKA (Botta, Mairani, Hobbs, et al. 2013), Geant4 (Agostinelli et al. 2003) and GATE (Sarrut, Bardès, et al. 2014) and PENELOPE (Issy-les-Moulineaux 2001).

2.8.1.4 Selection of the relevant approach for absorbed dose calculations

The preceding section discusses several methods for calculating absorbed doses with varying degrees of precision and computation time. The selection of the relevant approach can be characterised by two parameters: first, the type of radiation concerned and secondly, the medium for radiation transport.

The LED technique is favoured for non-penetrating radiation. If penetrating radiation is involved, it is necessary to determine whether the radiation is transported in homogeneous or heterogeneous media. Convolution should be employed for homogeneous media and complete MC simulation for heterogeneous media.

2.8.2 Absorbed Dose Approaches

There are two major approaches to dosimetry: model-based or reference dosimetry and patient-specific dosimetry.

2.8.2.1 Reference dosimetry

The purpose of reference dosimetry is to establish reference values for a particular procedure or a radiopharmaceutical, most often for diagnostic radiopharmaceuticals (Ljungberg 2022). According to ICRP recommendations, dosimetry data for a given radiopharmaceutical can be obtained by combining averaged pharmacokinetic parameters (TIAC) from patient or healthy volunteer cohorts, or even extrapolated from animal data, with reference anthropomorphic models that describe human anatomy. The objective is to generate fully described and traceable reference absorbed dose values (Menzel et al. 2009).

Some of the first reference models included adult mathematical models as used in MIRD pamphlet 11 (Snyder 1975), mathematical paediatric models from

Christy and Eckerman (Cristy et al. 1987g; Cristy et al. 1987a; Cristy et al. 1987e; Cristy et al. 1987b; Cristy et al. 1987f; Cristy et al. 1987c; Cristy et al. 1987d) and pregnant women models at different stages of pregnancy from Stabin (Stabin, Xu, et al. 2012). S values generated from these models were integrated in MIRDOSE and Organ Level Internal Dose Assessment with Exponential Modelling (OLINDA/EXM) software (up to the first version) (Stabin, Sparks, et al. 2005) and used for model-based dosimetry.

The evolution of the reference models towards polygon mesh descriptions of the geometry, resulting in more realistic models, considering different sizes, gender and ethnicity, along with the incorporation of breathing/cardiac motions at organ and voxel level has been summarised extensively by Xu *et al.* (Xu 2014).

Model-based dosimetry is essentially designed to document the absorbed dose imparted by a (diagnostic) radiopharmaceutical for standard examinations, and should not be employed for patient-specific dosimetry (Zanzonico 2002).

2.8.2.2 Patient-specific dosimetry

The transition from reference dosimetry to patient-specific dosimetry is particularly relevant in the context of molecular radiotherapy. Patient-specific dosimetry encompasses a range of steps, starting from the determination of activity or time-integrated activity distributions, the definition of volumes of interest and the selection of methods for absorbed dose computation. Patient-specific pharmacokinetic parameter assessment is a prerequisite for patient-specific dosimetry.

Regarding absorbed dose calculation, one possibility, while applying the MIRDOSE scheme, is to scale the S values from the model to that of the patient. Typically, the masses of the organs may be determined with a CT or MRI. These mass adjustments are proposed in Olinda (v1 and v2) (Stabin, Sparks, et al. 2005; Stabin and Siegel 2018) and iDAC-Dose2.1 (Andersson et al. 2017).

Using patient-specific pharmacokinetics and adjusted model-based dosimetry is a step in the direction of patient-specific dosimetry.

However, real patient-specific dosimetry entails using both the patient's anatomy and spatial distribution of the radioactivity as a function of time to derive the spatial distribution of absorbed dose in the specific patient. With exact knowledge of the distribution of density and composition of tissues (from the associated CT) and activity distribution (from the SPECT), absorbed dose rates for each voxel or user-defined collection of voxels can be obtained which can be further integrated to obtain the absorbed doses at organ or voxel level (Sgouros and Hobbs 2012). In this case, explicit computation of S values is not required and the absorbed dose rates

Context	Pharmacokinetics assessment (A)	Absorbed dose calculation (S)	Purpose
Diagnostics	Group-based representing a population	Model-based	Model-based reference dosimetry: ICRP / MIRD dose estimate reports
Therapy (1)	Patient-specific	Model-based \pm adjusted for organ mass	“adjusted” model-based dosimetry
Therapy (2)	Patient-specific	Patient-specific	Full patient-specific dosimetry

Table 2.2: Summary of dosimetric approaches in radionuclide therapy (used with the permission of Manuel Bardiès)

or even absorbed doses can be determined for the individual patient. Methods for this computation include convolution in homogeneous media or explicit radiation transport modelling with Monte Carlo techniques.

Table 2.2 summarises the different global approaches for dosimetry in radionuclide therapy, highlighting the context in which calculations are performed.

2.9 Assessment of variations in clinical dosimetry

2.9.1 Current status

Currently, dosimetry is not widely implemented in clinical facilities since it is argued to be a time-consuming, costly and complex process, due to the unavailability of proper resources and expertise (Haug 2020; Sgouros, Bodei, et al. 2020). Moreover, between the centres where dosimetry is considered, the procedures developed differ in approach and sophistication (Sjögreen Gleisner et al. 2017). As a result, there is a large heterogeneity in the implemented dosimetric approaches. *The main issue within clinical dosimetry is that no standard operating procedures currently exist.* Numerous multicentric clinical trials and multicentric studies including dosimetry have been established with the goal of standardising different facets of the dosimetric chain. Zimmerman *et al.* (Zimmerman et al. 2017) addressed an international multi-centric study to assess the accuracy and variability in activity quantification for planar and SPECT images with an IAEA phantom study using ^{133}Ba for the standardisation and harmonisation of image quantification for dosimetric purposes. Peters *et al.* (Peters et al. 2019) investigated the quantitative accuracy of several SPECT/CT systems with simple phantom measurements in order to standardise absolute SPECT quantification. Wevrett *et al.* (Wevrett, Fenwick, Scuffham, Johansson, et al. 2018) performed an inter-comparison study with a simple geometry set-up to demonstrate the variability of quantitative SPECT/CT imaging for ^{177}Lu in current clinical practice. Recently, Tran-Gia *et al.* (Tran-Gia et al. 2021) detailed a quantitative imaging intercomparison exercise to evaluate the accuracy of ^{177}Lu

SPECT/CT imaging using both a Jaszczak and anthropomorphic phantom. It was ascertained in this research that harmonisation of activity measurement is possible if a standardised protocol is employed across centres.

In the context of radioiodine treatment, the first multi-centric phase II trial (SEL-I-METRY) was set up to examine the prognostic significance of ^{123}I and ^{131}I SPECT/CT-based tumour dosimetry (Gregory, Murray, Gear, Leek, et al. 2019). In the same domain, Taprogge *et al.* (Taprogge et al. 2020) addressed the setting up of a quantitative SPECT imaging network for the standardisation of radioiodine activity quantification as a part of the H2020 European MEDIRAD project.

In the framework of absorbed dose calculations, Chauvin *et al.* (Chauvin et al. 2020) addressed the production and comparison of specific absorbed fractions (SAF), and the S values (computed from monoenergetic SAFs) for up to 1252 radionuclides with various available Monte Carlo codes in the OpenDose project (OpenDose 2018) thereby creating an open-access database for nuclear medicine dosimetry.

Various other authors (Finocchiaro, Berenato, et al. 2020; Mora-Ramirez et al. 2020; Huizing, Peters, et al. 2020; Della Gala et al. 2021; Capala et al. 2021) studied the different CDW available in the literature, thereby highlighting the wide heterogeneity in current clinical dosimetry practice.

Despite these various attempts to standardise and harmonise various steps of the dosimetry chain individually, one of the major challenges is how to determine the uncertainty of the whole dosimetric process, from scintigraphic imaging through absorbed dose calculation.

2.9.2 Uncertainty assessment

In clinical dosimetry, assessing the total uncertainty on the absorbed dose calculations is critical. How can variabilities in the different steps of the dosimetric chain among different centres (in same or different countries) be quantified for better and more standardised absorbed dose calculations? Recently, Gear *et al.* (Gear et al. 2018) published the EANM practical guidelines on the uncertainty analysis for absorbed dose calculations within TRT, describing the framework of total uncertainty determination based on the application of propagation of uncertainty. Finocchiaro *et al.* (Finocchiaro, Gear, et al. 2020) demonstrated the typical uncertainties that can be expected in the realisation of a tumour dosimetric study by evaluating results for a sample of patients with the abovementioned EANM practical guidelines. However, these uncertainties are difficult to assess *in-situ* and therefore ignored commonly in clinical routine.

One approach could be to distribute many identical phantoms to various centres, with each centre performing dosimetry. This has been addressed by different authors as mentioned above, however a phantom cannot always accommodate for patient heterogeneities, movement (respiratory or cardiac) and more. An alternative is to send an acquired dataset (say a series of planar/SPECT/PET with or without anatomical images like CT/MRI) from a patient to various centres for the evaluation of dosimetric variability across different facilities. This has been recently addressed in the Society of Nuclear Medicine & Molecular Imaging (SNMMI) challenge for the treatment of NETs with Lutathera (“SNMMI 177Lu Dosimetry Challenge 2021” [2021]). It can provide insights about the variability of absorbed dose estimates and allow the identification of several significant contributors to the variability in absorbed doses, as well as suggestions for future impediments. However, circulation of a patient dataset acquired on a single gamma camera allows only a partial uncertainty assessment in activity quantification.

2.9.3 The DosiTest project

A more comprehensive approach has been suggested through the initiation of the DosiTest project in 2008 (*Home - Dositest* [2021]). The global idea is, for a specific chosen therapy, to generate multi-modal patient projections (planar/SPECT/PET) of a reference patient (via Monte Carlo modelling) considering multiple gamma cameras. This modelled data would then be circulated to various clinical centres for them to perform dosimetry according to their local protocol and resources. It is hypothesised that the set-up of such a ‘*virtual*’ multicentric dosimetry trial based on Monte Carlo modelling will enable the evaluation of the variability introduced at each stage of the dosimetric chain. A significant amount of research has highlighted the potential of Monte Carlo modelling in image generation, even more in recent times due to increased computational capabilities (Zubal et al. [1992]; Furhang et al. [1997]; Zaidi and Sgouros [2002]; Ljungberg, Sjögren, et al. [2002]; Dewaraja, Wilderman, et al. [2005]; Botta, Mairani, Battistoni, et al. [2011]; Ljungberg, Strand, et al. [2012]; Sarrut, Bardiès, et al. [2014]; Seco et al. [2016]; Sarrut, Bała, et al. [2021]; Shin et al. [2021]; Seco et al. [2021]). **Figure 2.12** displays the schematic of the Dositest project.

A reference patient model with a reference radiopharmaceutical pharmacokinetics is considered. With the complete and thorough knowledge of anatomy (density distribution) and activity distribution at different time points, absorbed doses can be directly computed based on Monte Carlo simulations. This is the ‘ground truth’ and acts as reference dosimetry (1). Then, each participating centre

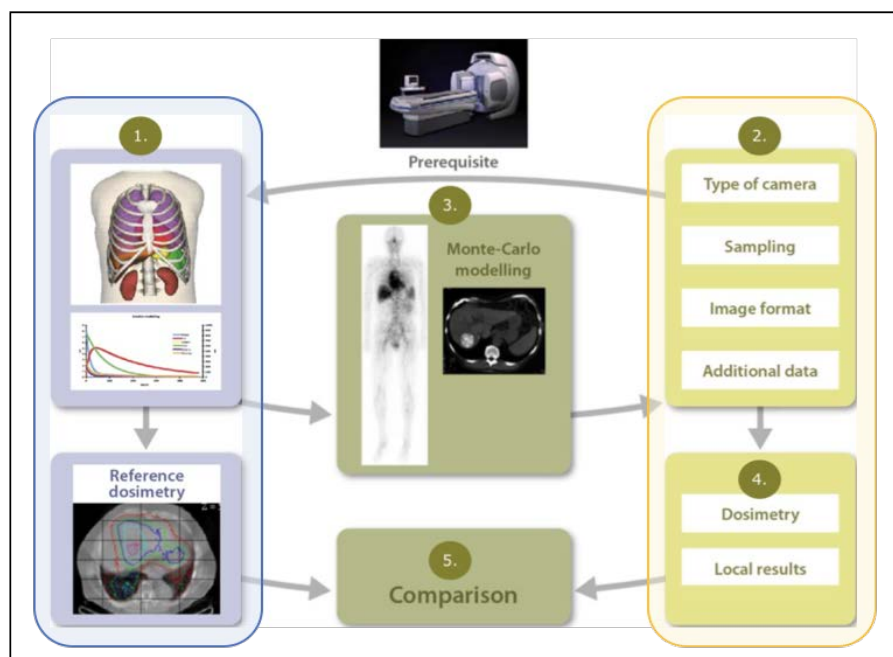


Figure 2.12: Schematic overview of the DosiTest project (www.dositest.org)

willing to participate in this multi-centric trial is enrolled. Each centre determines the data type needed to perform the dosimetric study as how they would do it locally and provide this information such as the number of, and timings of acquisitions, spatial sampling, gamma camera type and so on (2). The specific gamma camera is modelled and validated then both calibration and patient images based on GATE Monte Carlo modelling (Sarrut, Bardiès, et al. 2014; Sarrut, Bała, et al. 2021) are generated according to their local acquisition protocol. In this way, a dataset equivalent to what would have been acquired locally on a real patient is obtained (3). These simulated scintigraphic images are provided to the respective centre to perform activity quantification and a dosimetry study using their local protocol and resources (4). These results are further benchmarked against the reference dosimetry generated from the reference model (5). This enables the assessment of the variability introduced by the variously implemented dosimetric methodologies and also highlights the critical steps in the dosimetry process that are more susceptible to uncertainty.

The DosiTest project derives from QuantiTest (Hapdey et al. 2004). The first presentation of DosiTest was given by Ferrer *et al.* (Ferrer, McKay, et al. 2009) at the Society of Nuclear Medicine & Molecular Imaging (SNMMI) meeting in 2009. A preliminary phase of DosiTest included the design of TestDose, a custom computing platform developed to answer the needs of the DosiTest multicentric virtual dosimetry trial (McKay et al. 2009; Garcia et al. 2015). It was primarily

designed using an analytic imaging simulator and was subsequently updated to incorporate full Monte Carlo modelling ie. the generation of scintigraphic images (planar or SPECT) and absorbed dose calculations using the GATE simulation toolkit. This system was employed with ICRP 110 female adult model (ICRP, 2009) and NURBS-based whole-body XCAT phantom (Segars et al. 2010) for Octreoscan™ (^{111}In -pentetretotide) therapeutic treatment with six-compartment pharmacokinetic models derived from literature.

Further, the computation of absorbed dose at the clinical scale using the ICRP female reference computational model based on GATE Monte Carlo modelling was addressed by Villoing *et al.* (Villoing et al. 2017). The fraction of emitted energy from the source organs absorbed by the target organs per unit mass of each target organ (S-values) were generated with GATE for twelve regions of interest in the female ICRP 110 model thereby leading to 144 source/target combinations. The absorbed dose estimates from GATE were benchmarked against MCNPX, an established reference Monte Carlo code for dosimetric calculations. In the framework of the DosiTest project, it was proven that GATE could be safely used for radiopharmaceutical voxel-based dosimetry along with modelling scintigraphic images.

Following this, Costa *et al.* (Costa, Bonifácio, et al. 2017) illustrated the feasibility of generating realistic 2D planar whole-body images of an anthropomorphic XCAT phantom with hypothetical ^{177}Lu -DOTATATE pharmacokinetics with GATE. Since these imaging-based simulations are computationally intensive, they demonstrated techniques to accelerate the simulation time in order to obtain images that are sufficiently realistic when compared with real acquisitions.

In the beta phase of the project, four clinical centres were enrolled to simulate the context of clinical 2D planar dosimetry (sequential planar whole-body imaging) with the clinical situation of Peptide Receptor Radiotherapy (PRRT) and ^{177}Lu -DOTATATE.

2.10 Summary and presentation of the PhD work

This chapter described the different steps contributing to the calculation of absorbed doses starting from the *quantitative scintigraphic images* (i.e. calibration and patient image acquisitions, image reconstruction methods and correction of the image degrading factors for accurate activity quantification) to the *pharmacokinetics*, dealing with image registration, segmentation at various time points and time-integration of activity, followed by *absorbed dose calculations*.

SPECT imaging is used extensively in this work to determine the *in vivo* activity distributions in radionuclide therapy. Clearly, SPECT acquisitions are superior to planar images for three dimensional activity quantification. Even though a limited anatomical region can be covered by the SPECT images due to its limited axial field of view and whole body SPECT imaging would require impractical long acquisitions times, SPECT images are still preferred for accurate dosimetry in radionuclide therapy (Ljungberg and Gleisner 2015).

The evolution of integrated SPECT/CT systems and their availability in clinics to provide both anatomical and functional information has been proven to be beneficial in various steps of the dosimetric chain such as i) the determination of non-uniform attenuation coefficient maps for attenuation correction during reconstruction of SPECT images (Ljungberg, Celler, et al. 2016), ii) the possibility of proper co-registration of SPECT and CT images, thereby preventing misalignment of the patient images acquired on separate systems; iii) the CT enables good definition of the volumes of interest (except for low dose CT) due to its higher spatial resolution and improved contrast with respect to SPECT images, iv) the possibility to obtain voxel-wise CT-based density distribution for performing voxel-based patient-specific dosimetry using Monte Carlo radiation transport simulations (St James et al. 2021).

Since absorbed dose computation is a sequence of steps, its accuracy relies on the accuracy of each of the steps in the dosimetry chain. Because the uncertainties in each individual step are difficult to quantify empirically, a virtual multicentric clinical trial was proposed and established for Lutathera treatments based on Monte Carlo modelling (DosiTest). This doctoral project contributes to a better assessment of uncertainties in the clinical dosimetry workflow. It combines the analysis of clinical dosimetry performed on experimental (clinical) datasets with the further development of DosiTest.

Chapter 3 discusses the dosimetry performed on a *clinical* patient SPECT/CT dataset by different centres, using one specific workstation. This helped define the relevant indices to consider in the comparison of clinical dosimetric approaches.

Following this, the generation of a benchmark dosimetry dataset designed for the training of individuals on a specific clinical dosimetry software is presented in Chapter 4.

The next chapters present our contribution to DosiTest.

Chapter 5 presents the generation of realistic ^{177}Lu SPECT imaging of phantom models using GATE Monte Carlo modelling.

The successful generation of simulated patient datasets using the pharmacokinetics and geometry derived from a real patient receiving Lutathera treatment is presented in Chapter 6. This demonstrates the feasibility of the generation of realistic SPECT/CT projections using Monte Carlo modelling in a context to molecular radiotherapy.

Finally, the practical feasibility of the DosiTest project is presented in Chapter 7.

The conclusions and future possibilities for development are then discussed in Chapter 8.

3

Pitfalls in dosimetry analysis on a patient SPECT/CT dataset using Planet[®] Dose - An IAEA study

Contents

3.1 Introduction	65
3.2 Materials & Methods	66
3.2.1 Participants	66
3.2.2 Clinical patient SPECT/CT dataset	67
3.2.3 Definition of clinical workflow	68
3.2.4 Statistical analysis	70
3.2.5 Iterations	72
3.3 Results	74
3.3.1 Activity quantification	74
3.3.2 Absorbed Dose Rate (ADR)	78
3.3.3 Absorbed dose computation (AD)	81
3.4 Discussion	83
3.5 Conclusion	88

3.1 Introduction

The evaluation of uncertainties associated with clinical dosimetry is a very real problem in MRT dosimetry. In that context, a coordinated research project (CRP) E2.30.05 “Dosimetry in radiopharmaceutical therapy for personalized patient treatment”, initiated by the International Atomic Energy Agency (IAEA) was ini-

tiated in 2017 for a 3 year duration (further extended to 4 years due to the COVID situation).

This CRP aimed to investigate the standardisation of dosimetric methods in nuclear medicine and as such assist Member States to develop and implement harmonised dosimetric procedures, as well as to assess the global accuracy of dosimetry in NM practice. Participants were recruited from research institutions in Colombia, Croatia, Cuba, France, India, Indonesia, South Africa, and the United States of America.

As part of this project, a **reconstructed** clinical SPECT/CT patient dataset with the associated calibration factor at various time points was circulated to the participating centres to perform dosimetry using a standard protocol on one workstation - Planet[®] Dose from DOSIsoft.

The aim of the CRP project is to participate to the assessment of user-dependent variability introduced in the clinical dosimetry workflow. Since participants in this project performed the dosimetric analysis according to a standardised step by step protocol, using a single clinical workstation, not all sources of variation could be considered. Yet this work can be considered as a step in the direction of the DosiTest project, and, as will be seen, helped a lot in the developments presented in subsequent chapters of this manuscript.

This chapter focuses on the performance and training of different clinical centres on the dosimetric analysis with the **'clinical'** SPECT/CT patient dataset using Planet[®] Dose from DOSIsoft.

3.2 Materials & Methods

3.2.1 Participants

The nine different participating centres from different countries performing dosimetric analysis include Instituto Nacional de Cancerología ESE, Bogotá, *Colombia*; Clinical Department of Nuclear Medicine and Radiation Protection, University Hospital Centre Zagreb, *Croatia*; Oncology and Radiobiology Institute, La Havana, *Cuba*; DosiSOFT SA, Cachan, *France*; Centre de Recherches en Cancérologie de Toulouse, *France*; Fortis Memorial Research Institute in Gurgaon, *India*; Center for Technology of Radiation Safety and Metrology, Jakarta, *Indonesia*; Tygerberg Academic Hospital/Stellenbosch University, Medical Physics-Nuclear Medicine Department, Cape Town, *South Africa* and John Hopkins University, School of Medicine, Baltimore, *USA*.

3.2.2 Clinical patient SPECT/CT dataset

3.2.2.1 Patient images acquisition

The clinical dataset was derived from the dosimetric study of a patient treated with Lutathera[®] (¹⁷⁷Lu-DOTATATE) in the Tygerberg Hospital, South Africa. Activity was administered in four cycles with an interval of 11 weeks between cycles. However, only the first three cycles were employed in this study since the data quality of the fourth image dataset was deemed unsatisfactory. The amount of activity administered for cycle 1, cycle 2 and cycle 3 were 6243 MBq, 6672 MBq and 6848 MBq respectively.

Patient SPECT/CT images were acquired at various time points post activity administration (1 hour, 4 hours, 24 hours, 48 hours and 96 hours) on a dual-headed Infinia Hawkeye 4 SPECT/CT system (GEHC, Milwaukee, USA) with a medium energy (ME) collimator and a 9.5 mm (³/₈") NaI crystal for each cycle. Step and shoot SPECT acquisitions were performed with an energy window of 208 keV \pm 10% (187.2 - 228.2 keV), matrix size of 128 \times 128 (4.418 \times 4.418 mm²) with 15 seconds per projection.

The helically rotating 4-slice detector array CT system revolves at 2.6 revolutions per minute with a fixed pitch of 1.9 mm per revolution. Other CT specifications include a voltage of 140 kVp, tube current of 2.5mA and slice thickness of 10 mm. CT slices were acquired in a 256 \times 256 matrix with pixel size of 2.209 \times 2.209 mm².

3.2.2.2 Calibration acquisition

Along with patient acquisitions, SPECT/CT images of a NEMA-IEC calibration phantom with three hollow spheres (inner diameters: 12 mm, 28 mm, and 37 mm) were acquired. The background and three spheres had activity concentrations of 32.26 kBq/ml and 250 kBq/ml, respectively.

3.2.2.3 Reconstruction and derivation of a calibration factor

Calibration phantom and patient SPECT/CT images were reconstructed using the OSEM algorithm on a HybridRecon-Oncology version v3.0.1 in Hermes[™] GOLD workstation v4.15 Dicom (HROD) from Hermes[™] workstation (Hermes Medical Solutions, Stockholm, Sweden) (3 iterations, 15 subsets, 0.8 cm FWHM 3D Gaussian post filter). During reconstruction, attenuation correction based on CT images was applied, as well as built-in Monte Carlo scatter correction.

The reconstructed calibration images yielded a calibration factor of 122.6 Bq/counts. A VOI was drawn to include the whole phantom image in order to attain the total counts with a 1800 seconds calibration time.

The patient data set was anonymised and sent to each participant for dosimetric analysis.

3.2.3 Definition of clinical workflow

A standard dosimetric protocol was defined and Planet[®] Dose v3.1.1 (DOSIsoft SA, Cachan, France), from now on called ‘Planet’, was installed in each participating clinical centre to perform the dosimetric analysis of the three treatment cycles on the aforesaid clinical patient dataset.

Each participant received reconstructed images along with the associated calibration factor. A very well-defined processing protocol was defined, and specific training with Planet was given to each participant, including specific ad hoc training sessions during the duration of the CRP.

The patient images were uploaded in the DOSIsoft DICOM List (network mode). These images were then uploaded to Planet and the SPECT and CT images were grouped, which resulted in the creation of a Planet onco study. The SPECT and CT images were superimposed to allow for their fused visualisation.

3.2.3.1 Registration

Automatic rigid registration for all time points were performed taking the first CT as reference. The registration volume box was adjusted to include the whole liver and the two kidneys. These registered images were saved in the ‘registered space’ in ‘Regis mode’.

3.2.3.2 Segmentation

The volumes of interest (VOI) to be segmented included organs such as the liver and the two kidneys and four liver lesions named 1-Anterior, 2-Lateral, 3-Posterior, and 4-Inferior. Since the lesions were present in the liver, absorbed dose calculations of the whole liver and normal liver (liver without the lesions) were performed.

Organ Segmentation: The normal organs (kidneys and whole liver) were contoured semi-manually on the first CT using an interactive brush tool set-up with adequate HU thresholds defined upon each center and potentially with an interpolation process depending on the participants. Once defined in the first CT, the structures were propagated in a rigid way through all the registered CTs. Some

variation between centres is expected, but this should be limited as the contrast in the anatomical images (CT) is good enough to allow clear identification of the structures.

Lesion Segmentation: The lesions considered were defined in each SPECT. First a one click automatic detection method was used to select the four liver lesions (named anterior, lateral, posterior, and inferior) and to track them over the time. Next, a 40% threshold of the maximum uptake for each lesion and SPECT was applied to perform the segmentation. The VOIs were propagated in a rigid way between modalities. Even though this step is operator dependent, it should provide the same result for each participating centre.

To define the normal liver, a 4D boolean operation between the whole liver (defined on the CT) and the four lesions (transformed from functional image sampling to anatomical one) was performed. Total counts were obtained in each volume of interest and further activity was quantified using the appropriate calibration factor.

3.2.3.3 Absorbed dose rate (ADR)

Following activity determination, absorbed dose rates (ADR) can be obtained using the local energy deposition (LDM) method or convolution (with or without density correction) for each time point, for each VOI, in each cycle within Planet. At this stage, some additional input, including the selection of radionuclides (¹⁷⁷Lu), calibration factor (122.6 Bq/counts considering 1800 seconds of acquisition time), administered activity are required.

In the ‘standard dosimetry protocol’ defined in this comparison work, a *convolution algorithm with density correction* was chosen.

3.2.3.4 Absorbed dose computation (AD)

Planet allows computing absorbed doses in two ways:

With the activity at each time point for each VOI, a time-activity curve (TAC) can be fitted and time-integrated activity (TIA) can be obtained in each VOI to compute the absorbed dose. This corresponds to the conventional CDW presented in Chapter 2.

Besides the integration of activity, it is also possible to integrate the absorbed dose rate in time, a CDW variant presented in Chapter 2 and implemented by default in Planet.

Different fitting methods are available in Planet[®] Dose such as mono-, bi- or tri-exponential fitting, trapezoidal fitting etc. A bi-exponential fit includes one

uptake and one decay coefficient (positive and negative parameters), while a tri-exponential fit includes one uptake and two decay exponentials. The ‘Origin’ can be chosen to include the (0,0) point or a continuous fit can be chosen by extrapolating the fitting curve to zero. The goodness of fit can be evaluated using mean square deviation and Spearman’s rank correlation coefficient. Each centre chooses the fit that best suited the data.

In this work, absorbed doses were obtained from the integration of ADR in time. Absorbed dose rate at each time point and VOI, after the appropriate fitting was exported together with the fitting model used.

3.2.3.5 Data exportation

The capability to export intermediary results is of paramount importance for analysing the causes for any inter-operator variations. The following paragraph outlines the different variables accessible in Planet throughout the dosimetry processing process.

Segmentation: Once all the VOIs are defined, segmented and propagated to all time points in anatomical or functional mode, the volume in cm³ and total voxels of each VOI were exported as a text file. The anatomical contouring results table was used to get information about the normal organs, whilst the functional contouring results table was used to gain insights about the lesions. The text file also included the total counts in each VOI.

Activity: Using the calibration factor and administered activity, the activity in all the VOIs and each time point were exported as a csv file from the software.

ADR & AD: After the completion of the absorbed dose calculation, a file containing the absorbed dose rate (in µGy/s), the fitting parameters i.e. the equation, mean square deviation (MSD), Spearman’s rank correlation coefficients (with the native number of points and one variant with additional ones generated) along with the absorbed doses (in Gy) in each VOI was obtained in a csv file format.

3.2.4 Statistical analysis

Median and its associated uncertainties: To quantify the variations among participants for different parameters (or checkpoints), the median along with its uncertainties were computed using Equation 3.1 and Equation 3.2 according to Müller *et al.* (Müller 2000).

$$MAD = median\{x_i - \tilde{m}\}, \text{ for } i = 1, 2, \dots, n \quad (3.1)$$

$$s(\tilde{m}) = \frac{1.858}{\sqrt{n-1}} \cdot MAD \quad (3.2)$$

where, MAD is the median of the absolute deviations; x_i denotes the sample of n ordered variables x_1, x_2, \dots, x_n ; \tilde{m} and $s(\tilde{m})$ represents the median and the uncertainty on the median, respectively and n is the number of data points in the sample.

t-Test: The t-test was performed in conjunction with the median for the absorbed dose computation to examine the significance of the difference between the fitting techniques used among participants. The results of participants who used the same fitting technique were grouped together, and each fitting group was considered as an independent set following the normal distribution. For this comparison, a 95% confidence level was required, or, $p \leq 0.05$ (Meyers et al. 2020; Cicone et al. 2020).

The following quantity t is computed to determine if the difference between the means of independent fitting sets of measurements is substantially different from zero (Equation 3.3).

$$t = \frac{|\bar{X}_1 - \bar{X}_2|}{\sqrt{[(n_1 - 1)SD_1^2 + (n_2 - 1)SD_2^2]/(n_1 + n_2 - 2)}} \times \frac{1}{\sqrt{(1/n_1) + (1/n_2)}} \quad (3.3)$$

where \bar{X}_1 and \bar{X}_2 are the means of two fitting datasets, SD_1 and SD_2 are their respective standard deviations and n_1 and n_2 are the number of data values in each set respectively (Cherry et al. 2012a).

The computed value of t is then compared against the critical values of the t-distribution for the specified degree of freedom $df = n_1 + n_2 - 2$.

Several plots that were used to analyse the data are listed below:

- Scatter plots:

These were plotted to illustrate the correlations between variables (time points, volumes of interest, and parameters) and the clustering caused by the enormous amount of data collected from participants. For several plots, line plots with scatter markers were used to quantify the data trend from each centre and to find potential sources of variation.

- Box plots:

These were used to obtain a good indication of the distribution and skewness (measure of asymmetry of the probability distribution) of the numerical data (checkpoints within the dosimetry chain) among different centres for each VOI and time point. The boxplots are often a standardised way of displaying the distribution of data based on a five number summary - minimum (0th percentile or the smallest value), first quartile Q1 (25% percentile of data), median Q2 (50% percentile or midpoint of data), third quartile Q3 (75% percentile of data) and maximum (100th percentile or the largest value) (Williamson et al. 1989). The difference between Q3 and Q1 is considered as the interquartile range. The advantage of using box plots is that it is not affected by outliers since it does not take into account the data points below Q1 and above Q3 (Cooksey 2020).

For all phases within the dosimetry analysis, the same statistical methods and plots were employed.

3.2.5 Iterations

As previously stated, the goal of this IAEA-CRP work is to contribute to the standardisation of dosimetric methods in nuclear medicine, as well as to assist Member States in developing and implementing harmonised dosimetric processes and assessing the worldwide accuracy of dosimetry in NM practice.

Therefore, after each brainstorming session, the results were discussed and further training was provided to the participants. This was followed by a next iteration in the dosimetry calculation by the various clinical centres. Even though the results obtained by each centre were not available to all, the procedure was not that of a blind intercomparison, but rather evolved to an elaborate training procedure, with the objective to decrease multi-centric variations. The identification of outliers led participants to evaluate the integrity of their results. Other variations observed consistently throughout the data necessitated the inclusion of additional checkpoints in the dosimetric procedure and subsequently a new set of results was generated (Figure 3.1). The number of iterations ranged from 1 - 4 and 2 - 3 iterations for the first and second therapy cycles, respectively depending on the feasibility of the different clinical centres. However, for the third therapy cycle a minimum of four iterations was made by each clinical centre. The analysis was performed to identify remaining outliers at each level of iteration for the third therapy cycle. The results presented here are therefore the best that could be obtained after extensive training and iterations.

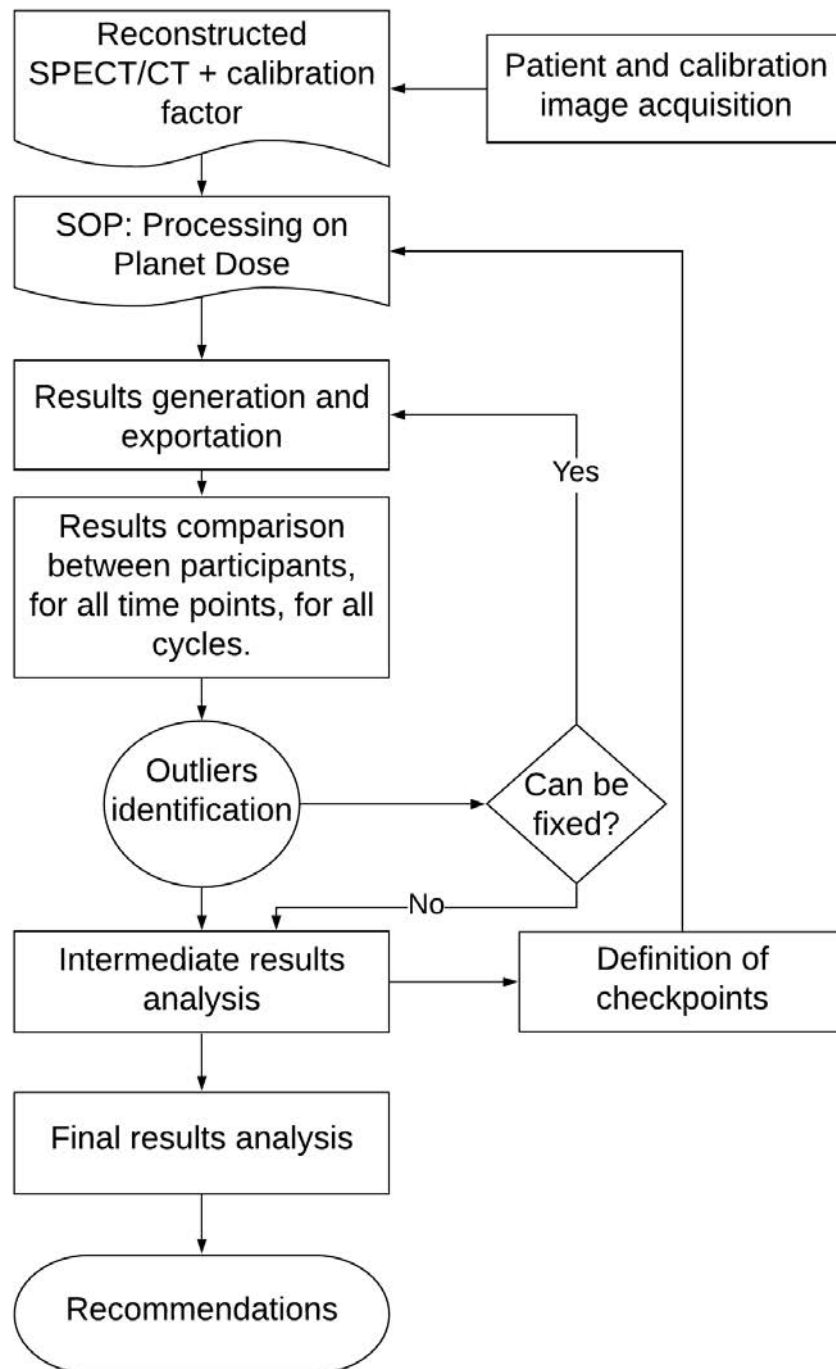


Figure 3.1: Workflow used for analysing the data and computing the final results and recommendations

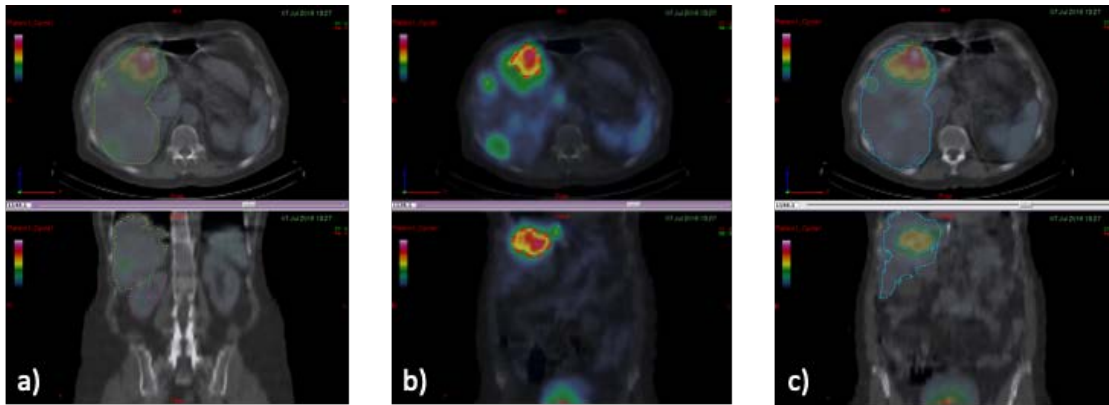


Figure 3.2: a) Anatomical segmentation (for whole liver and kidneys); b) Functional segmentation; c) Normal liver defined as a boolean operation between the whole liver and the lesions

3.3 Results

Results were obtained for each time point and segmented volumes of interest corresponding to each of the three treatment cycles. However, only the most exemplary results are shown here.

3.3.1 Activity quantification

3.3.1.1 Volume segmentation

The volumes contoured in the patient SPECT/CT can be seen in [Figure 3.2](#) for one cycle. As can be seen, the liver and the kidneys were segmented along with the four lesions in the liver. Similarly, segmentation was performed for all the following cycles.

The volumes obtained for each region at various time points (T1 - T5) for the first treatment cycle by the nine different centres (C1 to C9) are plotted in [Figure 3.3](#). The variations in volumes from the median among participants account for 5.9% and 6.2% for whole and normal liver respectively; 9.0% and 12.3% for left and right kidney, respectively. Each of the variations shown above is the average deviations of the three treatment cycles, since there were no significant differences between treatment cycles. However, for lesions, higher variations were observed among time points and treatment cycles, 0.6% - 7.3% for anterior, 7.8% -58.6% for lateral, 4.9% -20.1% for posterior and 5.1% -21.8% for the inferior lesion.

[Table 3.1](#) contains the median values with associated uncertainty for each cycle and volume of interest, as well as the range of values obtained by each participant. From these results, it can be observed that the two smallest lesions exhibit the largest variability.

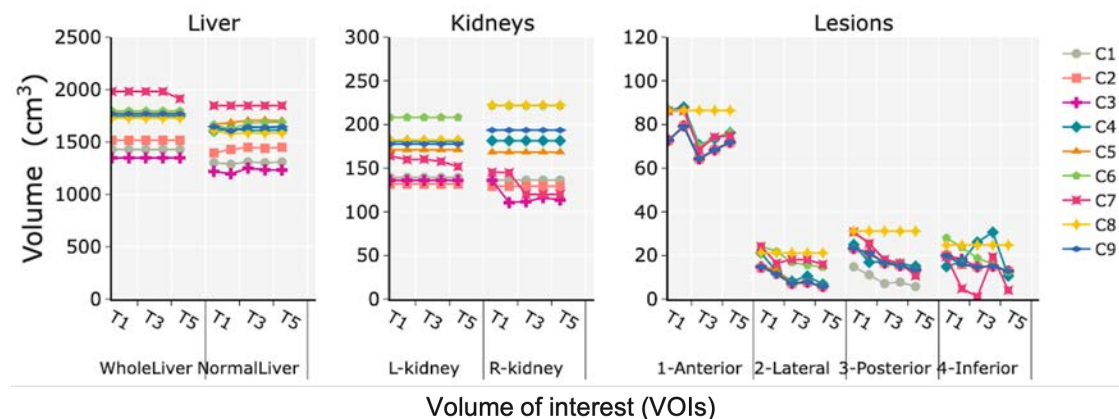


Figure 3.3: Volumes (in cm^3) segmented for each volume of interest (organs and lesions) in the first treatment cycle. All the graphs contain the information for all time points post injection (T1 to T5). Each colour on the graph denotes a participating centre (C1 - C9)

3.3.1.2 Derivation of counts and activity

The total counts and activity in each volume of interest was obtained by each participant and for each treatment cycle. [Figure 3.4](#) and [Figure 3.5](#) illustrate the counts and activities, respectively in liver, kidneys and lesions obtained for each time point post activity administration for the third treatment cycle since the most intriguing variations were observed in the processing of this treatment cycle. It is important to keep in mind that since all time points on the x-axis are equidistant, these graphs do not accurately depict the time-activity/count curves. As can be observed, the counts and activities within each volume of interest tend to follow a similar trend for most of the time intervals and participants, an expected behaviour as counts are converted to activity using a constant calibration factor (122.6 Bq/counts).

The largest VOI, i.e. the whole liver, demonstrated significantly lower variations in volume and measured activity, ranging from 5.1% to 5.49% and 2.95% to 5.49% respectively, at each time point and cycle analysed. On the other hand, the smallest VOI, the lateral lesion, had the widest range in volume, ranging between 7.8% and 58.6%, and activity varying between 10.17% and 49.22%. Surprisingly, the other smaller lesions had relatively smaller activity fluctuations (1.59% to 14.9%) like that in kidneys ([Table 3.2](#)).

Nonetheless, certain outlier data are observable. In [Figure 3.4](#), the counts from the sixth participating centre, C6, are significantly higher in the lateral lesion when compared to those from other centres. The activity plot ([Figure 3.5](#))

VOIs	Treatment cycle	Median	Min	Max	s(m)	IQR
		(cm ³)				
Whole Liver	Cycle 1	1747.56	1349.00	1981.98	109.85	255.75
	Cycle 2	1634.59	1415.00	2023.27	103.51	226.57
	Cycle 3	1698.11	1413.68	1859.26	86.64	261.46
Normal Liver	Cycle 1	1610.09	1196.43	1847.11	105.96	270.98
	Cycle 2	1538.26	1151.83	1893.17	100.76	185.36
	Cycle 3	1541.48	1272.75	1719.35	80.94	234.16
L-kidney	Cycle 1	171.04	131.80	208.22	14.01	41.38
	Cycle 2	162.30	137.12	236.28	15.91	35.18
	Cycle 3	169.53	124.53	231.06	15.36	21.47
R-kidney	Cycle 1	168.35	110.62	222.13	24.26	64.26
	Cycle 2	156.06	105.79	243.01	20.36	47.63
	Cycle 3	162.84	123.46	223.2	16.98	38.20
A_Lesion	Cycle 1	71.84	64.25	86.42	2.87	13.46
	Cycle 2	74.08	31.96	94.96	2.07	77.10
	Cycle 3	82.96	53.98	92.18	1.41	2.76
L_Lesion	Cycle 1	7.85	5.78	24.2	2.98	10.06
	Cycle 2	10.78	5.61	25.52	1.07	5.67
	Cycle 3	8.62	7.68	27.08	1.43	3.67
P_Lesion	Cycle 1	16.56	5.78	31.18	2.58	8.25
	Cycle 2	20.96	14.3	33.38	1.10	7.06
	Cycle 3	21.73	7.42	28.69	1.22	2.66
I_Lesion	Cycle 1	15.09	4.1	28.03	2.43	5.26
	Cycle 2	16.47	11.8	32.16	1.81	7.16
	Cycle 3	16.21	12.88	29.32	1.04	4.40

Table 3.1: Volumes of each volume of interest (VOIs) for each cycle. The median was obtained among participants and for each time point along with the associated uncertainties. The interquartile range (IQR) is also specified

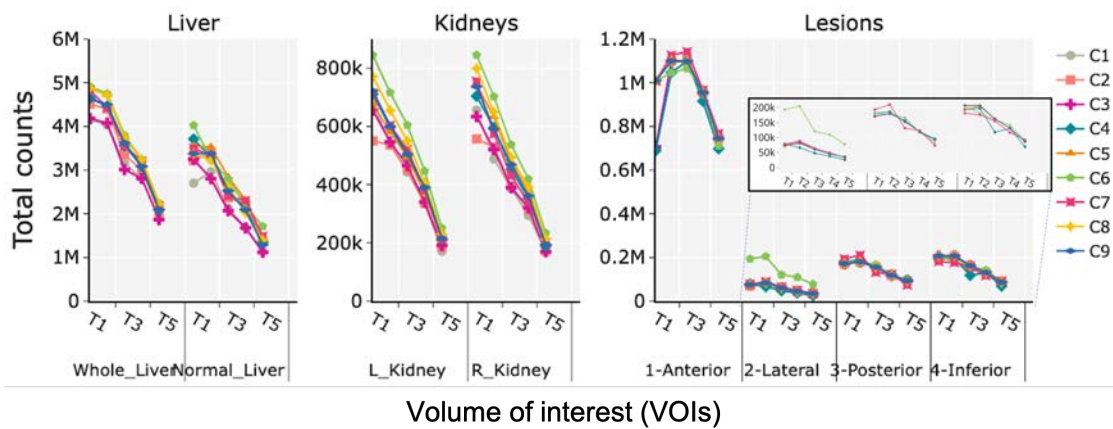


Figure 3.4: Total counts for each volume of interest (organs and lesions) in the third treatment cycle. All the graphs contain the information for all time points post injection. Each colour on the graph denotes a participating centre (C1 - C9)

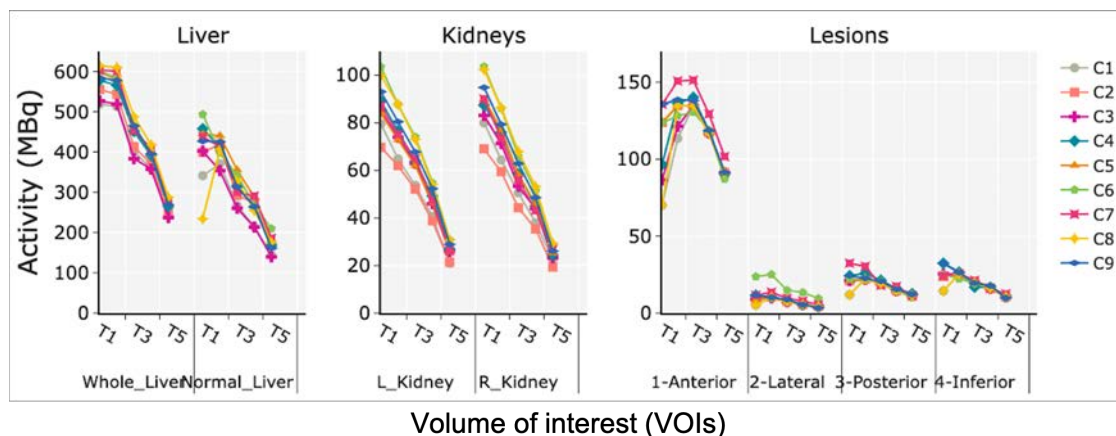


Figure 3.5: Activity in MBq for each volume of interest (organs and lesions) in the third treatment cycle. All the graphs contain the information for all time points post injection. Each colour on the graph denotes a participating centre (C1 - C9)

VOIs	Treatment Cycle	Variation in Volume		Variation in Activity	
		Minimum	Maximum	Minimum	Maximum
Whole Liver	Cycle 1	6.1%	6.3%	3.5%	4.0%
	Cycle 2	6.3%	6.3%	3.9%	5.5%
	Cycle 3	5.1%	5.3%	2.9%	4.3%
Normal Liver	Cycle 1	6.3%	6.8%	4.8%	10.1%
	Cycle 2	6.5%	7.3%	4.8%	6.4%
	Cycle 3	5.2%	5.6%	3.3%	8.4%
L-kidney	Cycle 1	8.0%	8.6%	6.2%	7.3%
	Cycle 2	9.3%	10.0%	5.4%	6.8%
	Cycle 3	8.1%	9.2%	5.7%	6.5%
R-kidney	Cycle 1	12.1%	14.4%	7.7%	12.3%
	Cycle 2	12.7%	13.3%	9.4%	12.6%
	Cycle 3	8.7%	11.2%	6.0%	6.6%
A_Lesion	Cycle 1	3.1%	6.2%	0.9%	6.5%
	Cycle 2	1.1%	7.2%	1.2%	3.9%
	Cycle 3	0.6%	7.3%	1.3%	12.8%
L_Lesion	Cycle 1	17.4%	58.6%	10.2%	17.0%
	Cycle 2	7.8%	21.2%	27.2%	49.2%
	Cycle 3	11.0%	22.1%	13.9%	26.2%
P_Lesion	Cycle 1	11.2%	20.1%	1.6%	4.9%
	Cycle 2	4.9%	6.2%	2.9%	9.9%
	Cycle 3	5.4%	9.3%	2.2%	13.2%
I_Lesion	Cycle 1	8.4%	21.8%	4.2%	6.4%
	Cycle 2	7.0%	11.7%	10.8%	14.6%
	Cycle 3	5.1%	10.3%	2.0%	12.1%

Table 3.2: Minimum and maximum variation of volume and activity in volume of interest for each cycle among participants

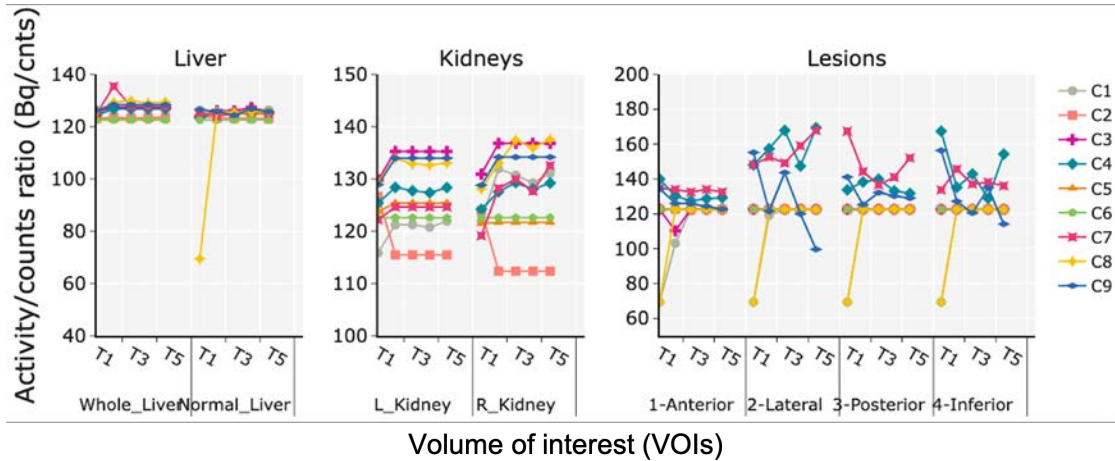


Figure 3.6: Derivation of activity and counts ratio (in Bq/counts) for each volume of interest (organs and lesions) in the third treatment cycle. All the graphs contain the information for all time points post injection. Each colour on the graph denotes a participating centre (C1 - C9)

exhibits a similar trend, which can be attributed to this centre's segmentation of a larger lateral lesion.

On the other hand, a significantly lower activity is seen in the lesions and hence also in the normal liver at the first time point for the eighth centre, C8. Considering that the activity is derived from the number of counts, a similar trend in counts was expected; however, this is not observed. *This necessitated the inclusion of a new checkpoint, namely the ratio of activity to counts, to identify and evaluate the cause of variation.*

Figure 3.6 demonstrates the computation of the activity-to-count ratio for each volume of interest at each time point for the third therapy cycle among participants. The above-mentioned variation in activity (for C8) can be attributed to various reasons (for example, incorrect calibration factor input or a specific software flaw linked with a particular time-point) and hence requires further investigation.

There is also considerable variability in the activity-to-count ratio for lesions for centres C4, C7, and C9. This can be ascribed to the discrepancies found at certain time points in the activity and counts plots for these centres.

3.3.2 Absorbed Dose Rate (ADR)

Each participating centre computed the absorbed dose rate (ADR) from the activity quantification for all treatment cycles and all volumes of interest. Even though all treatment cycles were processed analogously, several remarkable anomalies are observed for the third treatment cycle and hence are presented in Figure 3.7. Except

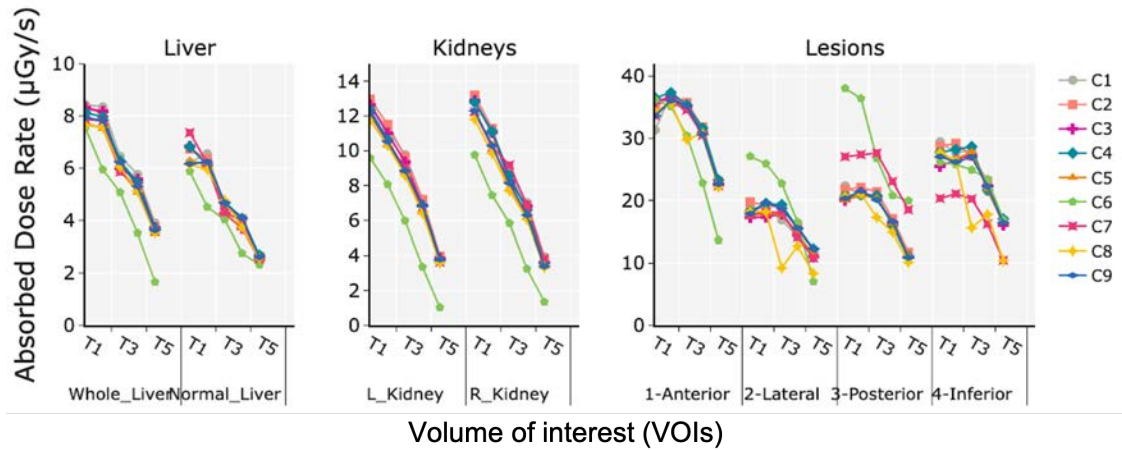


Figure 3.7: Absorbed Dose Rate (ADR) in Gy/s for each volume of interest (organs and lesions) in the third treatment cycle. All the graphs contain the information for all time points post injection. Each colour on the graph denotes a participating centre (C1 - C9)

for results from centre C6, the ADRs for each organ are reasonably consistent between time points and participants. This is anticipated, given that all centres use the same software and follow the same standard protocol (convolution method with density correction for ADR) while processing the same patient dataset. On the other hand, lesions exhibit a higher degree of variability in ADR amongst participants, the majority of which have no obvious justification. *This resulted in the definition of new checkpoints, such as determined activity concentration and the ratio of absorbed dose rate to activity concentration in order to better understand the source of disparity.* Owing to the fact that absorbed dose rate is globally proportional to activity concentration (for self-dose contributions to the absorbed dose, which will dominate in regions of high uptake), it is hypothesised that the ADR-to-activity concentration ratio will be relatively constant for each volume of interest at each time point.

Figure 3.8 shows the activity concentration for the organs and lesions at each time point for the third treatment cycle. As can be seen, all centres, including C6, have fairly consistent activity concentrations for the liver (both whole and normal) and kidneys. As a result, the deviation in absorbed dose rate between centre C6 and the mean/median of other participants in the liver and kidneys (varying between 6% and 73% across time points) cannot be attributed directly to volume segmentation or activity derivation but is most likely due to a transcriptional error (either incorrectly typed input/output or other unknown non-scientific errors). Moreover, the activity concentration calculation suggested that centre C8 overlooked some

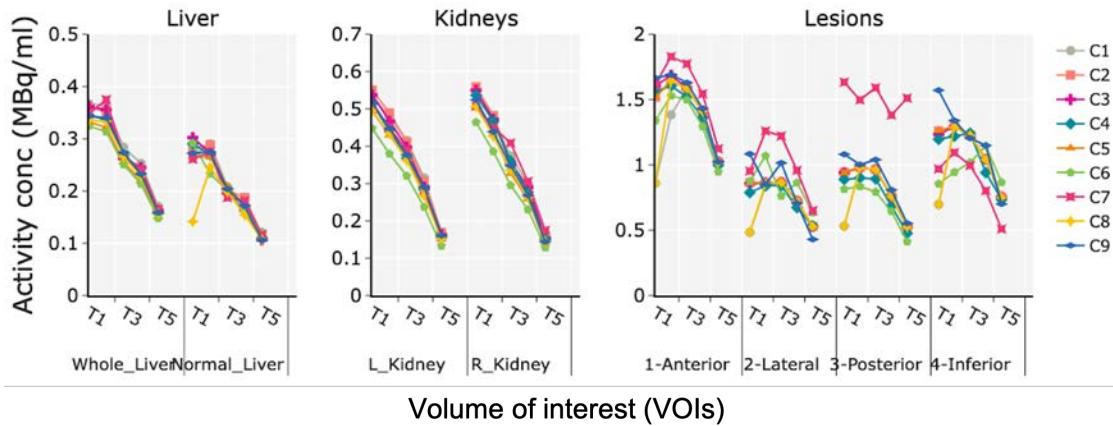


Figure 3.8: Activity concentration (Act. Conc.) in MBq/ml for each volume of interest (organs and lesions) in the third treatment cycle. All the graphs contain the information for all time points post injection. Each colour on the graph denotes a participating centre (C1 - C9)

systematic errors at the first time point (the exact source of error is unclear, however it can be asserted that it is not scientific).

The higher absorbed dose rate in the posterior lesion obtained by centre C7 can be intrinsically linked to the aberrant trend in activity concentration observed for the same centre, especially considering that the activity is significantly higher for the first two time points and lower for the third time point. For the anterior and lateral lesion, while the activity concentration values are higher in comparison to other centres, their effect on the absorbed dose rates is negligible. However, absorbed dose rate is in line with the activity concentration in the inferior lesion.

The computation of absorbed dose rate-to-activity concentration ratio (ADR/AC ratio) is demonstrated in [Figure 3.9](#). Nearly constant values were achieved for the organs despite the presence of few outliers. However, even though for each volume of interest defined and at each time point, this ratio was deemed to yield a constant value, this did not hold true for the lesions. Due to the incoherent absorbed dose rate and activity concentration of centre C6, their ADR/AC ratio varied significantly. Variability in this ratio for lesions at the first time point in centre C8 seems to be a result of error propagation from the activity quantification step (low activity noticed at this time point). However, for the same centre, lower ADR/AC ratio for lesions from the third time point is associated with some unexpected transcriptional inaccuracy in the estimation of absorbed dose rate.

Centre C1 mirrors the same concerns as C8 related to the greater ADR/AC ratio for the lesions at the initial time point. This appears to be the consequence of a poor calibration factor or a bug in the software.

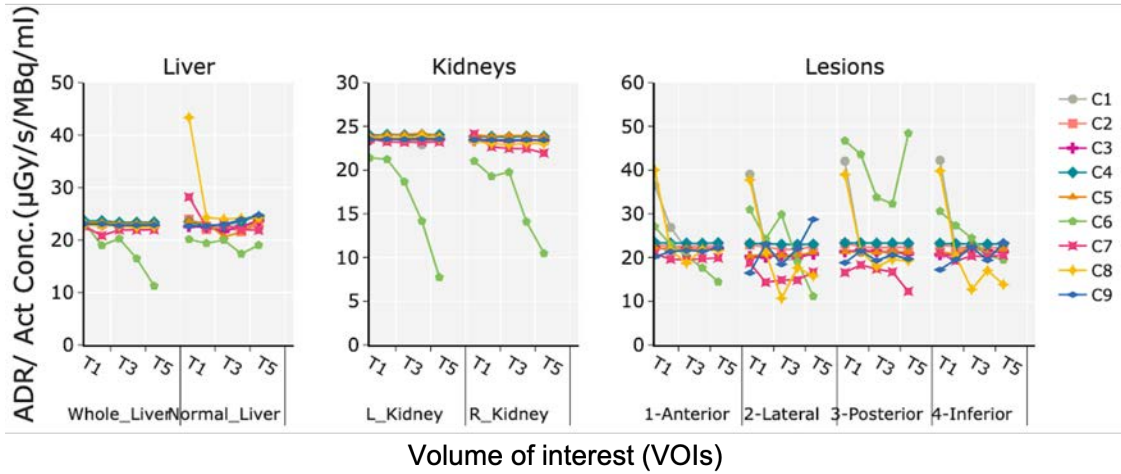


Figure 3.9: Computation of the ratio of the ADR and Act. Conc. in (Gy/s)/(MBq/ml) for each volume of interest (organs and lesions) in the third treatment cycle. All the graphs contain the information for all time points post injection. Each colour on the graph denotes a participating centre (C1 - C9)

Treatment cycle	VOIs	No. of centres	
		Mono-exp	Bi-exp
Cycle 1	Organs	6	3
	Ant. Lesion	3	6
	Other lesions	1	8
Cycle 2	Organs	6	3
	Ant. Lesion*	3	5
	Other lesions	4	5
Cycle 3	Organs	5	3
	Ant. Lesion	3	6
	Other lesions	4	5

Table 3.3: Fitting chosen by the different centres to obtain ADR for each VOI. * represents the absence of fitting parameters from clinical centre(s)

3.3.3 Absorbed dose computation (AD)

The absorbed dose rates were integrated using either mono- or bi-exponential fitting models to obtain the absorbed doses (AD) in each volume of interest and each treatment cycle. The fitting chosen by different centres for different VOIs are stated in [Table 3.3](#).

Absorbed doses for the first treatment cycle are plotted in [Figure 3.10](#). Liver and the kidneys exhibit low absorbed doses (in the range of 2 - 4 Gy) while lesions have absorbed doses up to 41 Gy. It was determined that when mono-exponential fitting was used, the absorbed dose was substantially higher in the whole liver than when bi-exponential fitting was used (3.76 ± 0.15 Gy vs 3.21 ± 0.24 Gy with $p < 0.01$). The normal liver demonstrated the same behaviour (2.82 ± 0.26

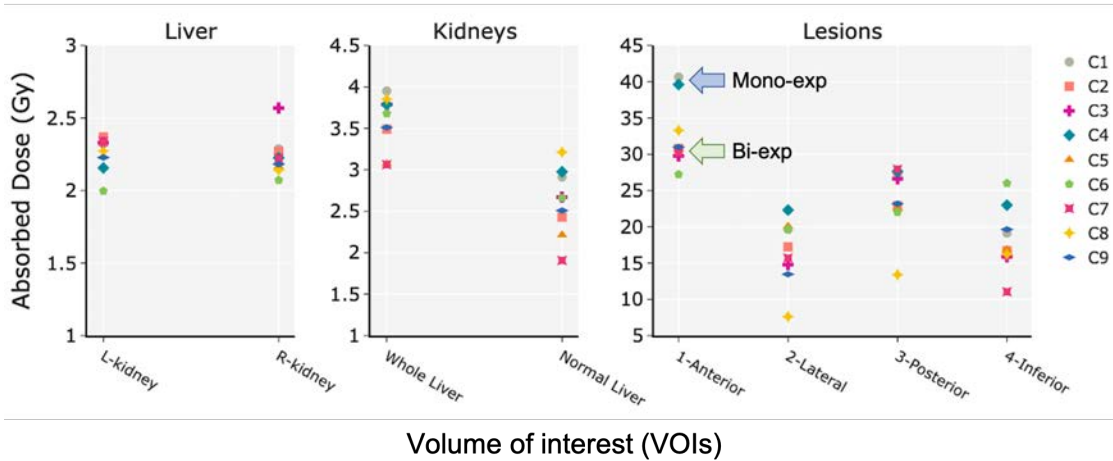


Figure 3.10: Absorbed Doses (in Gy) for each volume of interest (organs and lesions) in the first treatment cycle. Each colour on the graph denotes a participating centre (C1 - C9)

Gy vs 2.18 ± 0.26 Gy; $p < 0.01$), as did the anterior lesion (37.85 ± 3.98 Gy vs 29.97 ± 1.42 Gy; $p < 0.01$).

Significant variations in cycle 3 results between fitting methods (mono- and bi-exponential) were seen only in the whole liver (3.43 ± 0.13 Gy vs 3.18 ± 0.09 Gy; $p < 0.01$), and the anterior lesion (27.07 ± 1.19 Gy vs 23.37 ± 0.59 Gy; $p < 0.01$).

Absorbed doses for the third treatment cycle are also plotted in [Figure 3.11](#). For the organs, variation in absorbed doses is rather comparable across participants, despite the fact that results from one centre (C6) drifted away by up to 73% in the calculation of absorbed dose rates. For lesions, several outliers in the absorbed dose assessment are identified. The high and low outliers in AD calculations in lateral lesion corresponding to C6 and C8, the high outlier in posterior lesion aligning to C7, and the lower AD value in inferior lesion corresponding to C7 and C8 is associated to their respective high or low absorbed dose rate. While ADR is higher for centre C6 in the posterior lesion, it is not apparent in AD, presumably because it is compensated during its mono-exponential ADR integration. The high absorbed dose in the inferior lesion from centre C6 is not plausible given the reduced absorbed dose rates and activity concentrations in comparison to other participants. As a result, a high AD value is perhaps likely a consequence of a transcriptional error or mishandling of the software.

Variations in the absorbed dose calculation for each cycle in each volume of interest can be seen in [Figure 3.12](#) where Cy1, Cy2 and Cy3 represent the first, second and third treatment cycle, respectively. Some of the outliers in this figure are intrinsically linked to the fitting models employed (in whole and normal liver

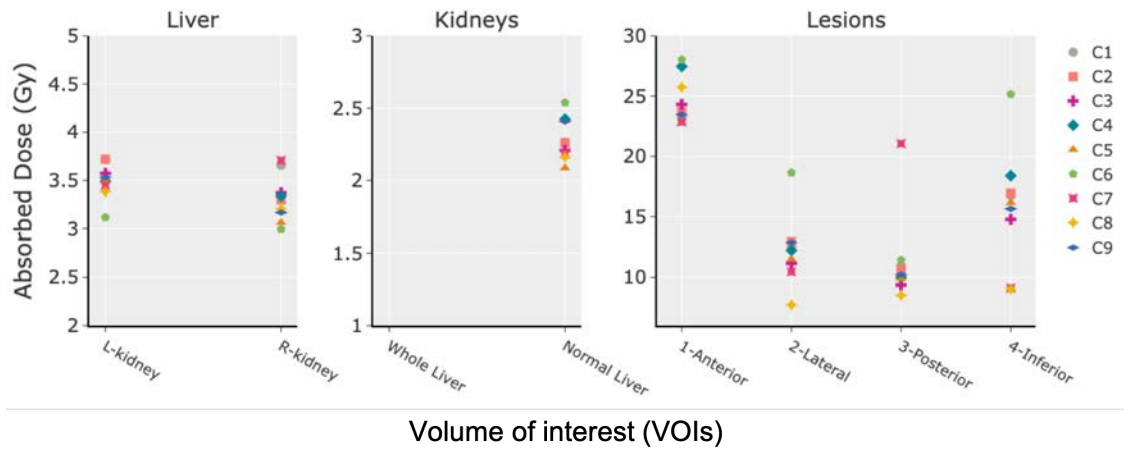


Figure 3.11: Absorbed Doses (in Gy) for each volume of interest (organs and lesions) in the third treatment cycle. Each colour on the graph denotes a participating centre (C1 - C9)

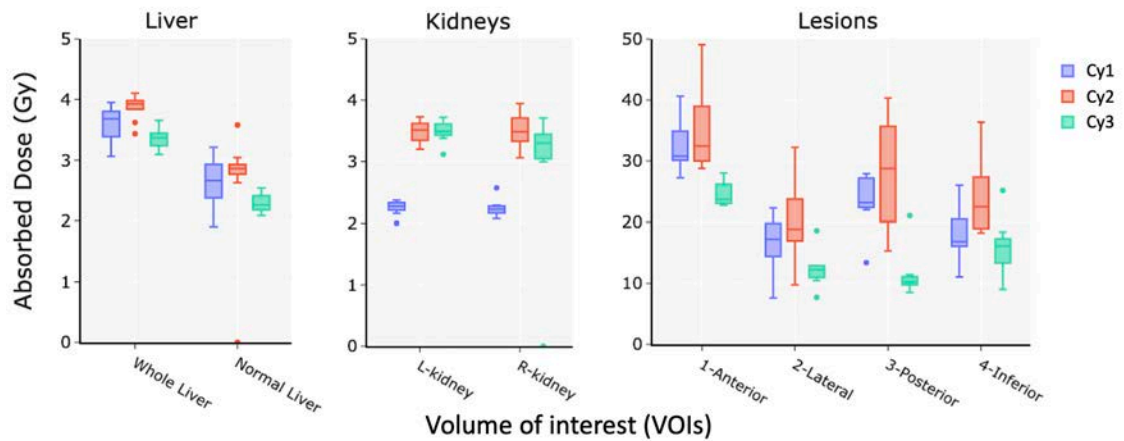


Figure 3.12: Absorbed Doses (in Gy) for each volume of interest (organs and lesions) for each treatment cycle

for cycle 2), while others are due to absorbed dose rate variations (in left kidney for cycle 1, in lesions for cycle 3). The higher outlier in the right kidney for cycle 1 is a consequence of segmentation of a lower volume (Table 3.4).

3.4 Discussion

This work presents the dosimetry analysis performed on a 3D SPECT/CT patient dataset acquired at five distinct time points in three therapy cycle(s) using a single version of Planet[®] Dose from DOSIsoft by nine participants from eight countries. To the best of our knowledge, this is the first time that such a multi-centric

VOIs	Cycle 1		Cycle 2		Cycle 3	
	Median (Gy)	CoV	Median (Gy)	CoV	Median (Gy)	CoV
R-kidney	2.2	4.3%	3.5	3.9%	3.3	4.6%
L-kidney	2.3	2.8%	3.5	2.3%	3.5	2.1%
Whole Liver	3.7	2.5%	3.9	2.7%	3.4	4.2%
Normal Liver	2.7	4.2%	2.9	3.5%	2.3	5.3%
1-Anterior	30.8	11.0%	32.5	4.7%	23.7	12.7%
2-Lateral	17.2	17.4%	18.9	9.8%	12.2	33.3%
3-Posterior	23.2	17.7%	28.8	14.3%	10.2	16.7%
4-Inferior	16.9	14.6%	22.5	13.4%	16.1	47.4%

Table 3.4: Absorbed doses in each volume of interest for each treatment cycle. Coefficient of variation (CoV) is computed as the ratio of the uncertainty to median value

dosimetry comparison has been conducted on a single clinical patient dataset using the same protocol and software by various centres across the globe.

The clinical dataset used for this comparison was a series of reconstructed patient images dataset along with the associated calibration factor. Although considerable variations have been documented in the reconstruction and calibration phases (Zimmerman et al. 2017), their impact on the dosimetry chain has not been considered in this work, since a single calibration factor was provided as a true value to all participants.

A standard procedure for performing each step of the dosimetry chain was defined starting from the registration of SPECT/CT images to the calculation of absorbed doses, based on a pre-established consensus between the participants at the start of the project. Rigid registration was preferred so as to not affect the voxel size and to minimise the variability between the participants. The organs were contoured on the anatomical images, while the lesions were delineated on the functional images, due to the limited contrast resolution of the low-dose CT and to minimise additional variability between physicists outlining lesions on the anatomical images. Even though manual definition of organ volumes on CT images was considered a possibility in well contrasted images, more methods (such as automated or semi-automatic algorithms) could have been investigated. Convolution algorithms and density correction were agreed upon by participants at the beginning of the project. A unique version of the Planet was preselected and circulated to each participant for dosimetry analysis. Multiple training and vendor support were provided to all participants.

Along with the generation of absorbed doses in each VOI, numerous intermediate results that were exportable from the software were then entered in an excel

sheet, including volumes, total counts and activities, absorbed dose rates, and fitting models for each time point and volume of interest. This facilitated the assessment of variations in the dosimetry chain at each possible step.

For this *independent dosimetry analysis*, each participant generated the results for each attribute, which were then extensively investigated. Multiple iterations were conducted owing to the existence of important discrepancies among participants. Several issues were remediated until the last iteration in order to obtain scientifically significant results. The Results section illustrates various examples of these aberrations spanning multiple therapeutic cycles. The sources of inaccuracies observed throughout this process can be summarised in two categories as follows:

1. *Software related:*

- (a) *Missing or NaN values:* this indicates that the software exported no values at all or had undefined values. The NaN value was often noticed in the exported results when absorbed dose rates or fitting parameters were being determined. Nevertheless, the absorbed doses were still computed by the software. This could be a result of a hidden software bug or the misuse of the software.
- (b) *Data exportation:* Several files containing varying amounts of information on the related but different parameters were exported by the software. This resulted in participants being unclear about what to report.

2. *Operator related:*

- (a) *Unit conversion:* Relates to improper unit conversions that resulted in a factor of 10 or 100 difference in the results
- (b) *Non-standardisation of decimal representation worldwide:* Implies the use of a dot or comma or sometimes a combination of the two to represent decimals.
- (c) *Data input/output:* this refers to the error in copy/pasting exported data from software (output) in the excel sheets (input) between time points or among lesions.
- (d) *Variability in volume segmentation:* The use of a smaller bounding box when segmenting lesions (in this case, the anterior lesion) using the thresholding approach ([Figure 3.13](#)) led to a high variability in lesion volume. This is an example of a typical error that may arise in clinical

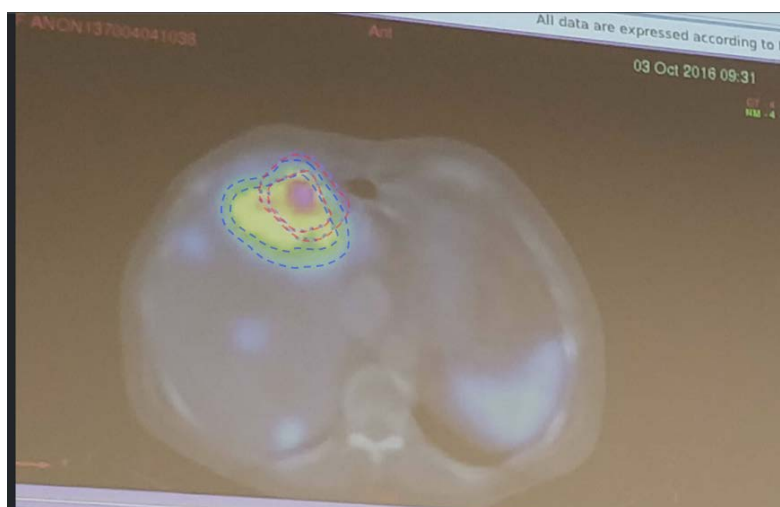


Figure 3.13: A typical error illustrating the selection of a small bounding box (in red) for anterior lesion (in this example) while performing threshold-based segmentation. The blue contouring represents the corrected segmentation

routine, therefore it is important to verify each slice of the SPECT/CT images after performing thresholding-based segmentation in order to facilitate accurate dosimetry.

- (e) *Scientifically illogical results:* This refers to either extremely low or zero values for say activity when segmented lesions have high counts; or a substantial increase in activity at the third or fourth time points, and sporadically even higher than the first or second time points, and so on. This might be due to any of the aforementioned aberrations, or a combination of them.

Numerous examples also highlighted the relationship between two attributes or the influence of one on the other; for example, smaller volume segmentation leading to lower total counts when compared to the median values, or higher counts resulting in higher activity in a particular VOI. Indeed, total counts and activity are proportionate and should reflect similar trends across multiple volumes of interest and time points, but this was not always the case. This necessitated the definition of a checkpoint derived from the exported data i.e. the *activity-to-count ratio*.

Similarly, for the volume-activity relationship, a smaller volume generating lower activity in comparison to the respective median values is possibly due to user-dependent segmentation and each participant's clinical experience. In this scenario, the participant's results cannot be undermined. Computing an intermediate checkpoint, namely the *activity concentration*, enables for the assessment of its impact on absorbed doses. First, activity concentration should be less segmentation

dependent, since a smaller segmented volume may yield lower activity yet maintain a consistent activity concentration. Then, the absorbed dose rate is expected to follow the activity concentration linearly for a given volume. Thus, an intermediate checkpoint associated with the *ratio of absorbed dose rate to activity concentration* was devised to determine whether this constant ratio is attained.

These two specified extra checkpoints could be included into the software to evaluate the internal consistency (sanity checks) of the computations.

Our initial hypothesis was that the same patient data with the same processing workflow in the same software would yield the same or at least very close results; yet this assumption proved to be wrong.

The large number of iterations needed to increase the proficiency of each user in the software and globally in the clinical dosimetry process has highlighted the importance of training. Basically, to our knowledge, the training delivered after the acquisition of the relatively new software packages extends rarely beyond a couple of days. This is clearly insufficient in a context of an emerging field where the professional experience is quite often lacking.

Obviously, the results were obtained within the framework of an exercise that had no direct impact on patient management. One can make the hypothesis that a computation performed in a clinical environment with real clinical consequences would have been more intensely checked by each participant.

Yet a major conclusion of our study is the observation of the absence of quality assurance in clinical nuclear medicine dosimetry, and the need to develop quality control procedures.

While dosimetry is gaining significant attention in the area of nuclear medicine, best practises should be adopted to ensure that results are reliable, traceable and reproducible.

This comprises (but is not limited to) double processing verification, using independent software and cross-validation across physicists, as is current practice in external beam radiotherapy. The fact is that in many nuclear medicine centres, only one physicist is performing clinical dosimetry, and therefore cannot rely on cross verification of their results by a colleague. In addition, quite often only one software is used to perform clinical dosimetry. In that context, it can be stressed that checking the results via an independent computation tool would certainly increase the degree of confidence in the obtained results.

The use of a standardised list of processing steps that can be verified, as well as the long-term archiving of the studies for traceability should be conducted. In that respect, it is crucial to integrate multiple input/output possibilities, to allow

parallel processing and verification. Most current commercial clinical dosimetry software (Della Gala et al. 2021) do not allow the extraction of intermediary results. As could be seen in this study, the possibility offered by Planet to import/export intermediary results helped a lot in identifying the sources of errors. Yet, giving too many processing options is also potentially increasing the chances to deviate from the intended procedure. In that respect, designing and enforcing preset clinical workflows would certainly help in decreasing the sources of errors. In addition, built-in sanity checks at various stages in the procedure should be integrated directly in the dosimetry software, to report aberrant behaviour.

Then, coming back to training, it was clearly demonstrated how practical training could increase proficiency in clinical dosimetry. Yet, having access to a benchmark clinical dataset that comes with a set of expected results, or at least a range of “acceptable” results, would be an invaluable component of the training.

3.5 Conclusion

This chapter illustrates how dosimetric analysis performed by numerous operators using the same technique and software on the same patient dataset may result in large inconsistencies for multiple volumes of interest and time points. This is more pronounced for smaller lesions than compared to the large organ volumes. There is a necessity to integrate the following aspects for performing ‘good’ dosimetry:

- *Establishing checkpoints:* Since dosimetry has several facets, it is important to establish checkpoints at almost every step to verify the integrity of the data.
- *Sanity checks in the dosimetry packages:* It is vital to implement sanity checks internally inside the program to minimise human mistakes. In the ideal case, the user should see a warning message if a substantial disparity or illogical output is observed in the prior phase.
- *Validation of results:* Cross validation of results among physicists / clinicians or professionals can aid to minimise transcriptional errors.
- *Benchmarked dataset:* There is a fundamental necessity for a benchmarking dataset, which enables each user to examine his or her proficiency with the software and get an insight on how precisely their findings resemble those of their peers.

Nonetheless, this CRP project represented a stepping stone towards the definition of good dosimetry procedures. Our results allowed highlighting some aspects that should be included in a clinical dosimetry quality assurance procedure.

Amongst other aspects, this research sparked the need for the creation of a benchmark dosimetry dataset. Chapter 4 addresses the creation of this benchmark dataset to allow individuals to assess their ability to work with a dosimetry software and to investigate the potential variations induced by varying the processing.

4

Creation of a benchmarking dataset on clinical patient images using Planet[®] Dose

Contents

4.1 Introduction	91
4.2 Materials & Methods	92
4.2.1 Participants	92
4.2.2 Clinical patient SPECT/CT dataset	93
4.2.3 Definition of clinical workflow	94
4.2.4 Statistical analysis	95
4.3 Results	95
4.3.1 Activity quantification	95
4.3.2 Absorbed dose rate (ADR)	99
4.3.3 Absorbed Dose calculations (AD)	101
4.4 Discussion	102
4.5 Conclusion	105

4.1 Introduction

The comparison of various steps of the dosimetry chain across different centres was performed as a part of coordinated research project (CRP) E2.30.05 “Dosimetry in radiopharmaceutical therapy for personalized patient treatment” initiated by the International Atomic Energy Agency (IAEA). Despite the fact that the same patient dataset was processed using the same software and a standard protocol, substantial variability in the absorbed dose results was observed. While some of

the anomalies could be related to or associated with transcriptional errors and data management, there were still certain irregularities in the results that were/could not be explained. This spurred the need to establish multiple intermediary checkpoints, to cross-validate the produced results and to conduct training and brainstorming sessions. This was reported in the previous chapter. A conclusion was drawn, that in order to improve training and to enable self-assessment of the obtained results, it would be desirable to generate a benchmark dataset specifically for that purpose, which would include not only input data (patient images and associated calibration factor), but also intermediate and final results, as well as a procedure for the training physicist to follow.

This chapter discusses the design and development of a benchmark dataset that can be used by individuals to assess their knowledge of the software and get a perspective of the consistency of their results to those obtained by peers. As a part of the IAEA inter-comparison exercise, participants used the same *reconstructed* clinical SPECT/CT patient dataset and *associated calibration factor* to perform dosimetry on Planet[®] Dose from DOSIsoft at the same time during a ‘*face-to-face*’ work session organised at the headquarters of International Atomic Energy Agency (IAEA) in Vienna during the last CRP meeting in November 2021.

This round-table dosimetry analysis enabled the identification and assessment of the sources of variability introduced during each step in real time, as well as the generation of training material for individuals for a specific software package.

4.2 Materials & Methods

4.2.1 Participants

The eight participating clinical centres from various nations are Instituto Nacional de Cancerología ESE, Bogotá, *Colombia*; Clinical Department of Nuclear Medicine and Radiation Protection, University Hospital Centre Zagreb, *Croatia*; Oncology and Radiobiology Institute, La Havana, *Cuba*; DosiSOFT SA, Cachan, *France*; ICO René Gauducheau, Nantes, *France*; Center for Technology of Radiation Safety and Metrology, Jakarta, *Indonesia*; Tygerberg Academic Hospital/Stellenbosch University, Medical Physics-Nuclear Medicine Department, Cape Town, *South Africa* and John Hopkins University, School of Medicine, Baltimore, *USA*.

4.2.2 Clinical patient SPECT/CT dataset

4.2.2.1 Patient & calibration image(s) acquisition

For this part of the doctoral project, one therapy cycle dataset from the same patient considered in Chapter 3 was selected.

As a reminder, a patient administered with 6672 MBq Lutathera[®] (¹⁷⁷Lu - DOTATATE) in the Tygerberg Hospital, South Africa was considered for this work. This activity corresponds to the patient's second therapeutic cycle. Patient SPECT/CT images were acquired at 1 hour, 4 hours, 24 hours, 48 hours and 96 hours post activity administration on a dual-headed Infinia Hawkeye 4 SPECT/CT system (GEHC, Milwaukee, USA) with a medium energy (ME) collimator and a 9.5 mm (³/₈") NaI crystal for each cycle. Step and shoot SPECT acquisitions were performed with an energy window of 208 keV \pm 10% (187.2 - 228.2 keV), matrix size of 128 \times 128 (4.418 \times 4.418 mm²) with 15 seconds per projection.

Low dose CT scans were obtained on a helically rotating 4-slice detector array CT system at 2.6 revolutions per minute with a fixed pitch of 1.9 mm per revolution. Other CT specifications include a voltage of 140 kVp, tube current of 2.5mA and slice thickness of 10 mm. CT slices were acquired in a 256 \times 256 matrix with pixel size of 2.209 \times 2.209 mm².

SPECT/CT images of the NEMA-IEC calibration phantom were obtained in the same way as explained in the previous chapter.

4.2.2.2 Reconstruction and derivation of calibration factor

Calibration phantom and patient SPECT/CT images were reconstructed in the same way as explained before on a HybridRecon-Oncology version v3.0.1 in Hermes[™] GOLD workstation v4.15 Dicom (HROD) from Hermes[™] workstation (Hermes Medical Solutions, Stockholm, Sweden) (OSEM algorithm, 3 iterations, 15 subsets, 0.8 cm FWHM 3D Gaussian post filter). Attenuation based on CT images and built-in Monte Carlo scatter correction was applied.

A calibration factor of 122.6 Bq/counts was derived considering the whole field of view as the VOI in order to attain the total counts with an 1800 seconds calibration time. Anonymized patient data were sent to each participant for dosimetric analysis.

4.2.3 Definition of clinical workflow

The clinical workflow was similar to that described in Chapter 3 for the independent dosimetry analysis. Due to the fact that the reconstructed dataset served as an input or baseline dataset with the calibration factor, this round-table dosimetry analysis began with registration and segmentation. The five SPECT/CT images corresponding to the second treatment cycle were uploaded on DOSIsoft DICOM List in Planet[®] Dose, software that was installed in each participant's clinical centre as a part of the CRP project.

Registration & Segmentation: Using the first CT image as a reference, SPECT/CT images at all time points were automatically registered rigidly by the medical physicists at each centre. The liver and two kidneys along with the four lesions labelled 1-Anterior, 2-Lateral, 3-Posterior, and 4-Inferior were segmented. Due to the presence of lesions in the liver, absorbed dose calculations were done on the whole liver and normal liver, which is the whole liver without lesions.

Segmentation of organs at risk was accomplished by each participant defining Hounsfield unit (HU) thresholds on the initial CT image and then propagating them across all registered CTs. However, the four lesions were segmented using a 40% threshold of maximal uptake on functional SPECT images. Then, the VOIs were rigidly propagated across modalities (i.e. from SPECT to CT). Normal liver was then obtained as a result of a 4D boolean operation between the whole liver (in anatomical mode) and the four lesions (transformed from functional to anatomical mode).

Absorbed dose rate: Following the activity quantification, by converting the total counts in the segmented VOIs with the calibration factor to activity, the absorbed dose rate (ADR) for each VOI and time point was determined by convolving the activity distribution with density correction.

Absorbed doses: Using the available fitting models and equations, temporal integration of the ADR resulted in the generation of absorbed doses for each VOI. Planet[®] Dose supports a variety of fitting techniques, including mono-, bi-, or tri-exponential fitting, trapezoidal fitting, and so on. While the bi-exponential fit considered one uptake and one decay exponential, the triexponential fitting included the same but with an additional decay exponential. The Spearman's coefficient may then be used to determine the goodness of fit. Each centre was responsible for selecting the best fit.

Data exportation: The data was exported from the program in a consistent manner like explained in the previous chapter to minimise the possibility of transcriptional inaccuracies at this stage. The Appendix A contains a sample Google spreadsheet used for data collection.

Established checkpoints: Numerous intermediate checkpoints were established to facilitate the analysis of critical aspects in clinical dosimetry. This comprises the direct intermediary results from the software such as the volumes and voxels within each volume of interest, the total counts and activity associated with each VOI, absorbed dose rates, and absorbed doses. The additional checkpoints included the activity-volume ratio (activity concentration), the activity-to-count ratio and the ratio of absorbed dose rate to activity concentration. Each checkpoint sheds light on the specific phases of the clinical dosimetric procedure that are most susceptible to anomalies. Additionally, it facilitates the understanding of the critical stage in the absorbed dose calculation.

4.2.4 Statistical analysis

Mean, standard deviation and coefficient of variation: The mean or average of each parameter, as well as the standard deviation, were determined in this chapter, since the majority of the data followed a normal distribution. Additionally, the coefficient of variation (CoV) was calculated as the ratio of the standard deviation to the mean. The median and its uncertainty were also calculated, but are not reported as they converged significantly on the mean value.

t-Test: For determining the significance of the difference between the means of the absorbed dose computed using different fitting methods, the t-Test was used assuming a normal distribution. For comparison between the absorbed doses a 95% confidence level was required, or, $p \leq 0.05$ (Cherry et al. 2012b; Cicone et al. 2020; Meyers et al. 2020).

Scatter and box plots: Scatter plots were utilised to analyse the results from participants and the clustering that resulted from the enormous quantity of data collected from participants. To help in visualising the pattern of each participant's results, trendlines were added to these plots. In the case of absorbed doses, box plots were used in conjunction with scatter plots to illustrate outliers in the results.

4.3 Results

4.3.1 Activity quantification

4.3.1.1 Volume segmentation

The volumes defined for each volume of interest during face-to-face analysis is shown in Figure 4.1.

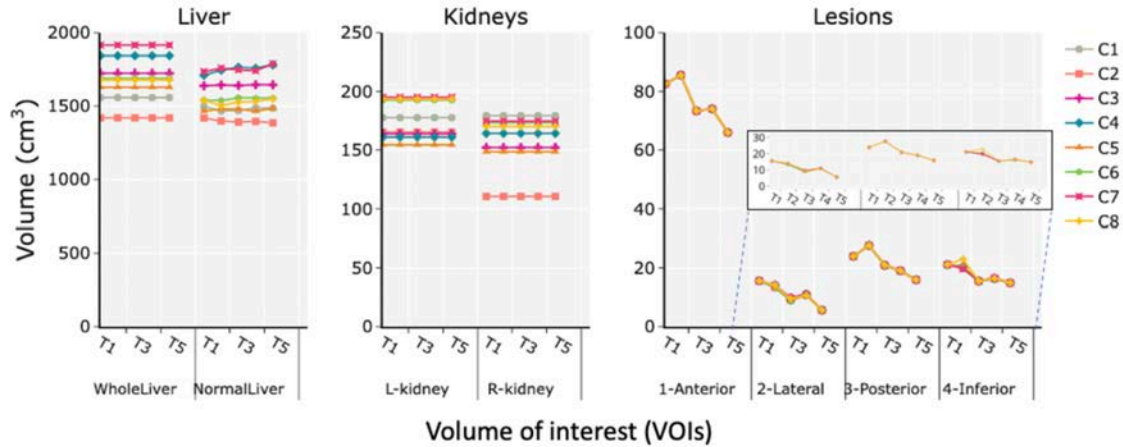


Figure 4.1: Volumes (in cm^3) segmented for organs and lesions in the second treatment cycle. All the graphs contain the information for all time points post injection. Each colour on the graph denotes a participating centre (C1 - C8)

As can be seen from the figure, the volumes of the whole liver and kidneys remained constant throughout all time points and there was essentially no difference in their volume segmentation from one time point to the next for each participant. According to its clinical expertise, participant C2 contoured a smaller volume for the right kidney. The variations for these healthy organs are reported in [Table 4.1](#). The volumes of the four lesions decreased with time, as would be anticipated given that the therapies are aimed at tumour cells, and were nearly similar amongst individuals (*variations* $\leq 5.1\%$).

Fluctuations between time points for normal liver amongst participants can be observed and this resulted from the effect of decreasing lesion volumes since a boolean operation between whole liver and lesion volumes is used to determine the normal liver volume. However, the variations of normal liver volume between time points for each participant were less than 1.5% and therefore mean and standard deviation along with the minimum and maximum values were stated in [Table 4.1](#).

4.3.1.2 Determination of counts and activity

Counts and activity for the second therapy cycle was obtained for each volume of interest. [Figure 4.2](#) illustrates the activities in organs and lesions. The graph of total counts is consistent with the activity and is thus not displayed here. Variation in counts for whole and normal liver, left and right kidneys was 6.9% and 10.3%, 7.5% and 12.3%, respectively among time points and participants. Due to lower volume segmentation by participant C2, lower total counts ($\sim 30\%$ lower than the mean total counts computed among other participants) were obtained, increasing

VOIs	Time point	Mean	Min	Max	Std. dev.	CoV (%)
		(cm ³)				
Whole Liver	T1-T5	1681.91	1419.59	1915.91	155.70	9.3
Normal Liver	T1-T5	1572.49	1385.62	1788.35	131.73	8.38
L-kidney	T1-T5	175.41	154.40	195.00	16.46	9.4
R-kidney	T1-T5	159.09	110.43	179.33	22.44	14.1
1 - Anterior Lesion	T1	82.53	82.53	82.53	0.00	0.0
	T2	85.55	85.55	85.55	0.00	0.0
	T3	73.31	73.30	73.39	0.03	0.0
	T4	74.08	74.08	74.08	0.00	0.0
	T5	65.97	65.97	65.97	0.00	0.0
2 - Lateral Lesion	T1	15.61	15.60	15.61	0.00	0.0
	T2	13.79	13.19	14.14	0.40	2.9
	T3	9.26	8.62	9.83	0.44	4.7
	T4	10.88	10.69	10.95	0.11	1.0
	T5	5.61	5.61	5.61	0.00	0.0
3 - Posterior Lesion	T1	23.97	23.97	23.97	0.00	0.0
	T2	27.68	27.68	27.68	0.00	0.0
	T3	20.96	20.96	20.96	0.00	0.0
	T4	19.06	19.06	19.06	0.00	0.0
	T5	15.95	15.95	15.95	0.00	0.0
4 - Inferior Lesion	T1	21.13	21.13	21.13	0.00	0.0
	T2	20.54	19.66	23.03	1.04	5.1
	T3	15.51	15.44	15.52	0.03	0.2
	T4	16.44	16.30	16.56	0.12	0.7
	T5	14.92	14.92	14.92	0.00	0.0

Table 4.1: Volumes for each volume of interest (VOIs) for each time point. The mean was obtained among participants along with the associated standard deviation. The min-max range is also specified.

the variation in the right kidney. Variations in total counts for the anterior, lateral, posterior and inferior lesion accounted for 0%, 1.5%, 1.4% and 2.1%, respectively.

Quantification of activity followed a similar pattern to that of total counts. Variations in activity were less than 10% for the whole and normal liver and the left kidney while a slight increase to 11.3% was observed for the right kidney. The lesions exhibited very consistent results with a maximum variation of 4.2% among various lesions, time points and participants. A larger deviation (10.8% from the mean value) for participant C8 was observed at the second time point in the inferior lesion. A similar pattern for C8 was observed in the volume segmentation, and is logically propagated to total counts and activity quantification for this participant.

At time point T1, for the anterior lesion, participant C3 had 10% larger activity than the mean value. Due to the fact that there is no discrepancy in the segmented volume and total counts from their respective mean values, this disparity may be attributable solely to a transcriptional error.

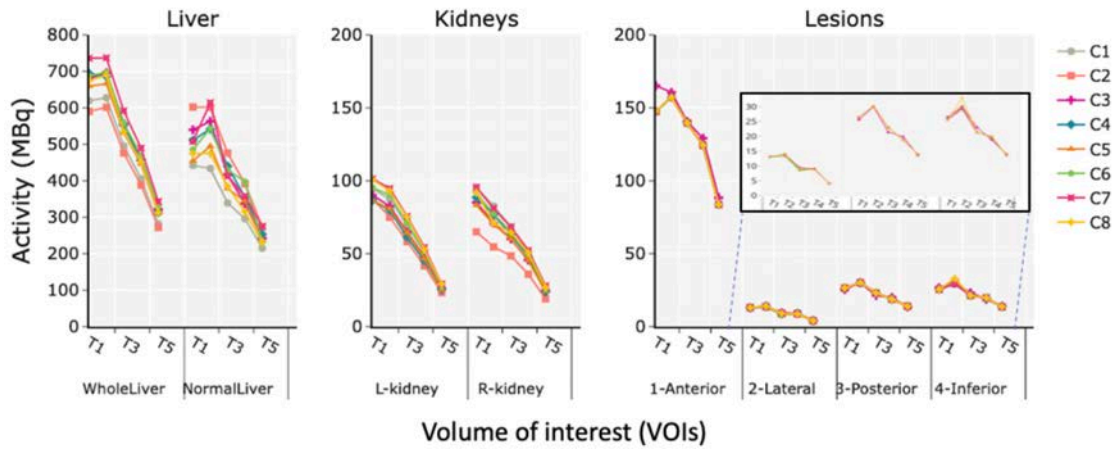


Figure 4.2: Activity in MBq for organs and lesions in the second treatment cycle. All the graphs contain the information for all time points post injection. Each colour on the graph denotes a participating centre (C1 - C8)

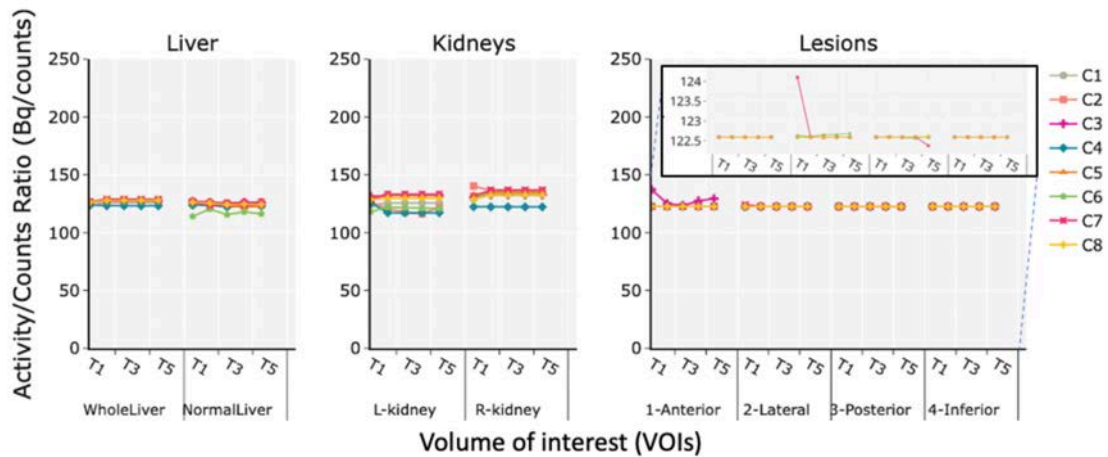


Figure 4.3: Deviation of activity-to-counts ratio (Bq/counts) for organs and lesions in the second treatment cycle. All the graphs contain the information for all time points post injection. Each colour on the graph denotes a participating centre (C1 - C8)

This can be proven from [Figure 4.3](#) where the activity-to-count ratio for the anterior lesion acquired by participant C3 is not linear among time points. For the participant C6, some variations are observed for normal liver among time points due to the variation in the lesion volumes. A small spike is seen in the first time point in the lateral lesion (1.2% from the mean) and the final time point in the posterior lesion (0.18% from the mean) from participant C7, but is only evident in the enlarged region of the figure.

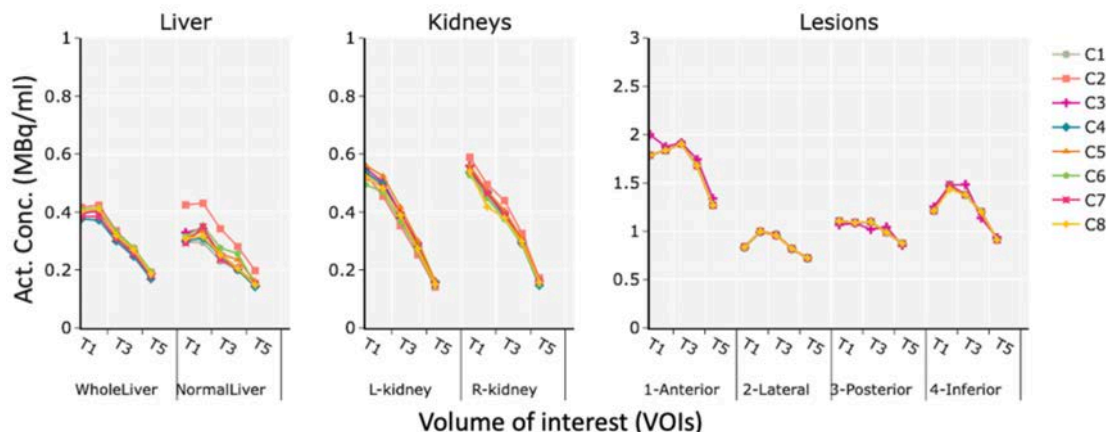


Figure 4.4: Computation of activity concentration (MBq/ml) for organs and lesions in the second treatment cycle. All the graphs contain the information for all time points post injection. Each colour on the graph denotes a participating centre (C1 - C8)

4.3.1.3 Determination of activity concentration

The concentration of activity is remarkably consistent among participants for various volumes of interest (Figure 4.4). As originally envisioned, the variations in volume and activity in the right kidney from a participant (C2) are proportional, thereby resulting in activity concentrations coherent with other participants (max variation among time points is 5.3%). However, some fluctuations in the activity concentration of the normal liver is seen from the same participant. This is due to 11 - 14% lower volume segmentation and 14 - 23 % higher activity quantification among time points therefore resulting in 30 - 38% of higher activity concentration.

The variation among participants and time points is less than 2% in lesions and less than 5% for the healthy organs. However, due to the aforementioned discrepancy in the normal liver, the variation increased to 12.8%.

4.3.2 Absorbed dose rate (ADR)

The absorbed dose rate plotted in Figure 4.5 closely relates to the activity concentration. After rectifying several transcriptional inconsistencies throughout the process, a consistent degree of variability amongst participants was obtained. Except for the normal liver, the variation in ADR among participants and time points was not significant (< 5% for healthy organs and < 3% among the four lesions).

To ensure that the correlation of absorbed dose rate to activity concentration is constant, the ADR/AC ratio was calculated and is displayed in Figure 4.6. Despite the heterogeneity of variables (ADR and AC individually) from participant C2, the ADR/AC ratio remained constant in the normal liver. However, a variation of

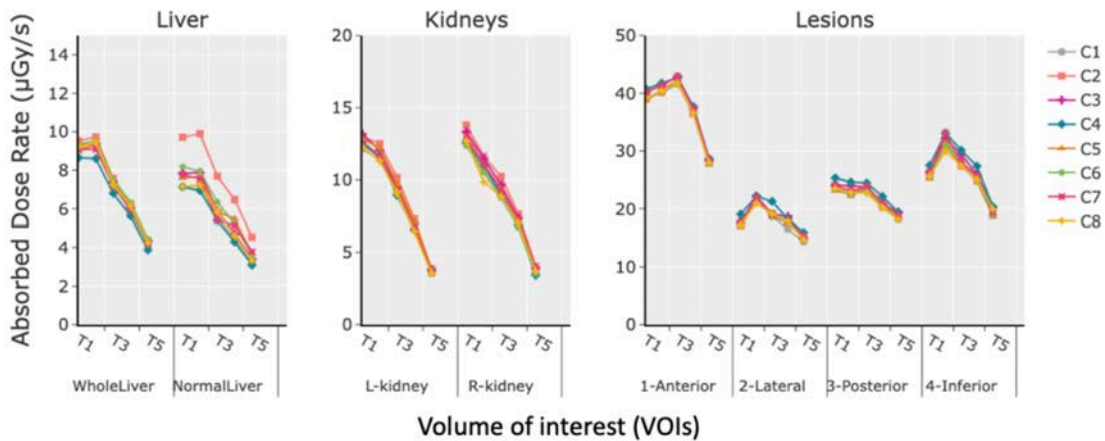


Figure 4.5: Absorbed dose rate ($\mu Gy/s$) for organs and lesions in the second treatment cycle. All the graphs contain the information for all time points post injection. Each colour on the graph denotes a participating centre (C1 - C8)

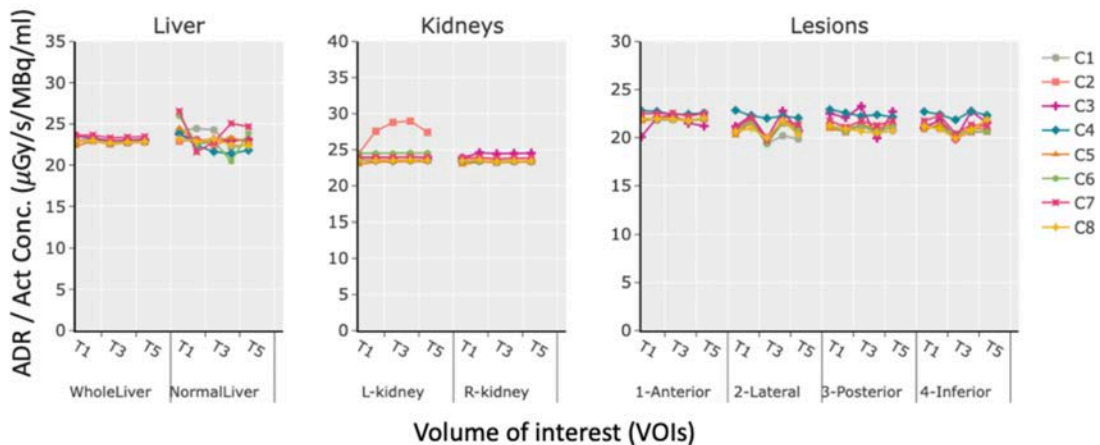


Figure 4.6: Derivation of absorbed dose rate to activity concentration ratio ($\mu Gy/s$)/(MBq/ml) for organs and lesions in the second treatment cycle. All the graphs contain the information for all time points post injection. Each colour on the graph denotes a participating centre (C1 - C8).

2% to 8% (from the mean values across time points) in the left kidney from the same participant was identified when no substantial variation in the ADR or AC was observed. Fluctuations in the normal liver are induced by fluctuations in the lesions although the mean variation among time points is less than 5%. A small dip in the ADR/AC ratio at the third time point can be noticed in lateral and posterior lesions, however, these variations are less than 5% from the mean values computed for this ratio among the other time points.

VOIs	No. of centres	
	Mono-exp	Bi-exp
Organs	7	1
1-Anterior Lesion	3	5
2-Lateral Lesion	4	4
3-Posterior Lesion	6	2
4-Inferior Lesion	3	5

Table 4.2: Fitting chosen by the different centres to obtain ADR for each VOI

4.3.3 Absorbed Dose calculations (AD)

Absorbed doses obtained for organs and lesions are plotted in [Figure 4.7](#) after integration of the absorbed dose rates over time. The fitting models chosen by different participants are listed in [Table 4.2](#).

Due to the higher absorbed dose rates, participant C2 had a larger absorbed dose for the normal liver than the mean AD of the other participants. The lower absorbed dose for liver from participant C4 is largely attributable to the selection of bi-exponential fitting.

Mono- and bi-exponential fitted absorbed dose rates yielded a mean absorbed dose of 4.01 ± 0.12 Gy and 3.49 ± 0.0 Gy respectively ($p \leq 0.01$) for the whole liver while 3.42 ± 0.50 Gy and 2.64 ± 0.0 Gy respectively with $p \leq 0.02$ for normal liver. For the liver, all the centres fitted the ADR mono-exponentially with one centre as an exception employing bi-exponential fit ([Table 4.2](#)). Therefore, the uncertainty in absorbed doses among participants using bi-exponential ADR fit was 0 Gy. In the case of the kidneys, the mean absorbed doses were 3.5 ± 0.13 Gy and 3.6 ± 0.16 Gy for the left and right kidney, respectively and the influence of ADR fitting models on absorbed doses was marginal (less than 5%).

In case of anterior and lateral lesion, a clear distinction can be seen between participants using mono- or bi-exponential fitting (blue or green boxes respectively in [Figure 4.7](#)) for obtaining absorbed doses. The difference in mean absorbed doses with respect to fitting models is 22.5% (mono-exp: 39.48 ± 0.59 Gy vs bi-exp: 30.61 ± 1.56 Gy with $p \leq 0.01$) for anterior lesions and 36.9% (mono-exp: 27.43 ± 1.67 Gy vs bi-exp: 17.32 ± 1.12 Gy with $p \leq 0.01$) for lateral lesions.

In posterior and inferior lesions, the mean absorbed doses are 35.12 ± 3.72 Gy and 21.86 ± 2.70 Gy respectively. The range of absorbed doses among participants are shown in [Table 4.3](#) along with the mean and standard deviation. The minimum and maximum AD values of lesions shown in this table are from the participants employing mono-exponential and bi-exponential ADR fittings, respectively.

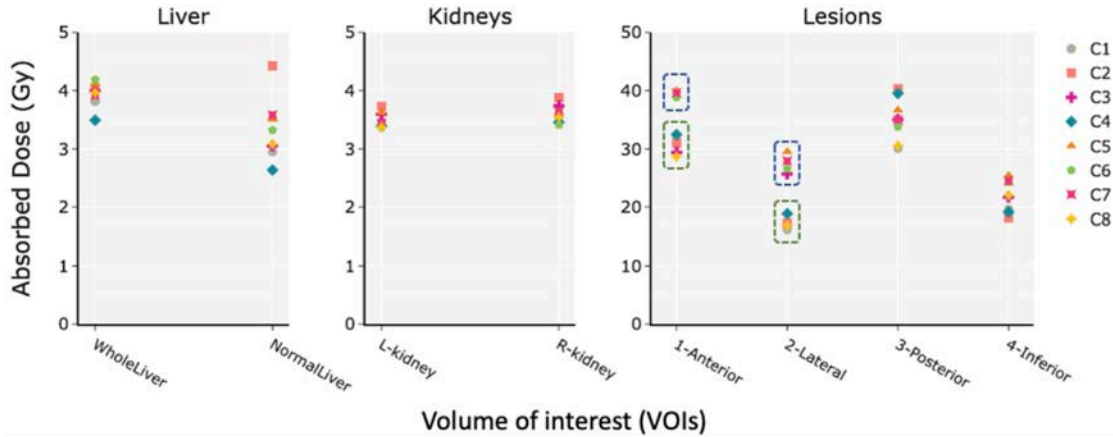


Figure 4.7: Absorbed dose (in Gy) for organs and lesions in the second treatment cycle. Each colour on the graph denotes a participating centre (C1 - C8). The blue and green dotted boxes represent the use of mono- and bi- exponential ADR fitting respectively to obtain absorbed doses

VOIs	Mean	Min	Max	CoV
		(Gy)		(%)
R-kidney	3.60	3.41	3.88	4.44
L-kidney	3.50	3.37	3.73	3.71
Whole Liver	3.94	3.49	4.19	5.58
Normal Liver	3.32	2.64	4.43	16.27
1-Anterior	33.93	28.66	39.98	14.00
2-Lateral	22.38	16.21	29.53	24.84
3-Posterior	35.12	30.08	40.34	10.59
4-Inferior	21.86	18.25	25.41	12.35

Table 4.3: Mean absorbed doses in each volume of interest (in Gy) along with the related CoV and range

These absorbed dose variations can also be seen in the box plots displayed in [Figure 4.8](#). Outliers in the complete liver relate to the use of bi-exponential fitting by one participant, while those in the normal liver result from the contouring of a smaller volume by another participant.

4.4 Discussion

This work presents for the first time a multi-centre dosimetry comparison performed in ‘*real time*’ at a round-table discussion on a single patient SPECT/CT dataset receiving Lutathera[®] therapy, using a single version of Planet[®] Dose from DOSISoft by eight participants from seven nations.

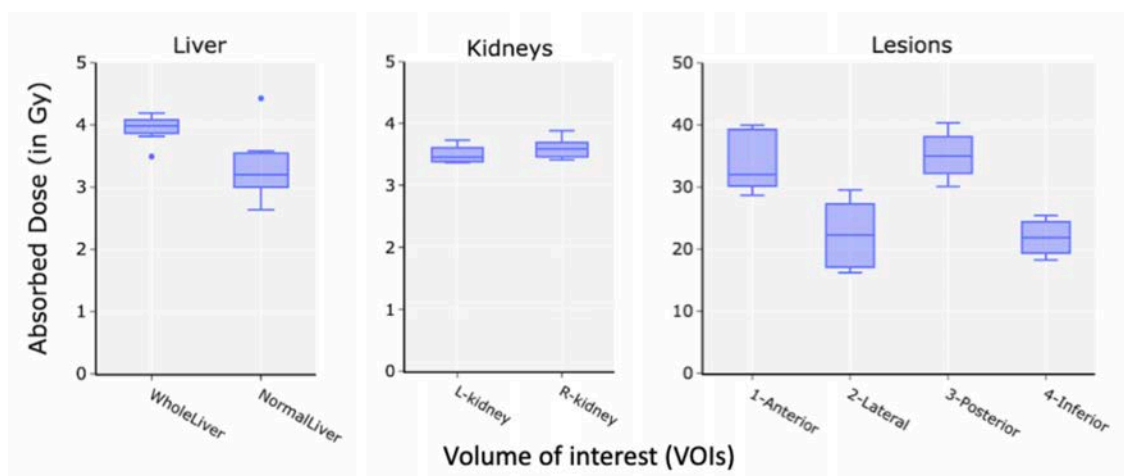


Figure 4.8: Variation in absorbed doses (in Gy) for each volume of interest (organs and lesions) for the second treatment cycle

As a series of reconstructed patient images and the corresponding calibration factor was provided, the impact of reconstruction and calibration methodology was not included in the evaluation of absorbed dose calculations. A specific clinical workflow including some user-dependent tasks (such as segmentation or fitting models) were defined in order to investigate inter-operator variability across participants using the same patient dataset and software. The checkpoints were used to identify and understand the source of variability for different parameters.

In contrast to previous independent dosimetry analysis, variability in the lesion volumes were substantially lower than that of organs, with some cases demonstrating an absolute 0% variability, as seen in [Figure 4.9](#). Additionally, the variability in volume contouring of organs at risk across time points was remarkably low for each participant, as expected given the rigid registration approach utilised. It was observed that the participants were more at ease and confident when each step was assessed and compared with their colleagues, resulting in less variations and anomalies throughout this face-to-face training session. The fact that everyone's results were assessed during live sessions possibly enhanced the involvement of each participant.

The use of an activity-to-count ratio checkpoint, showed a similar correlation across time points between activity quantification and number of counts among participants. It was demonstrated that the use of a single calibration factor would not necessarily result in similar activity values from the number of counts among the different participants. This checkpoint helped to identify a transcriptional error for the activity quantification for the anterior lesion by one participant.

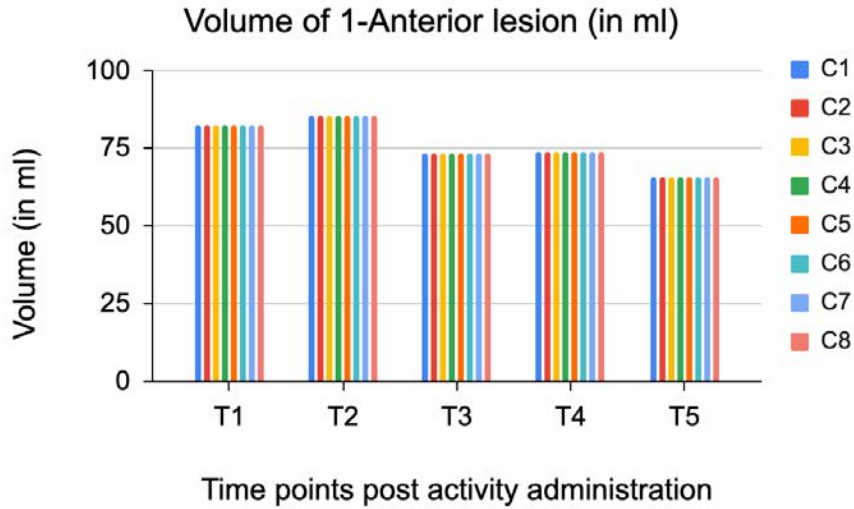


Figure 4.9: Volume of anterior lesion (in ml) obtained by each participant at various times post activity administration

Yet, this transcriptional error had no direct consequence on the absorbed dose calculation within Planet.

The absorbed dose rates for various volumes of interest were strikingly similar among participants (coefficient of variation $\leq 5\%$ for the healthy organs and lesions). However, this variation increased to around 12.5% for normal liver as one of the participants obtained a higher ADR value for normal liver. If this is considered to be an outlier and excluded from the analysis, the inter-participant variation in ADR for normal liver decreased to 6.5%. However, the high ADR values from the participant are consistent with high activity concentrations as can be seen in the ADR/AC ratio plot and in turn can be attributed to a lower volume segmentation. As a result, this is not considered as an anomaly but rather as a user-dependent step within routine clinical dosimetry practice.

The absorbed dose values obtained from participants differ substantially according to the fitting model chosen. The variation between mono- and bi-exponential fitting was not significant for kidneys (5%), but increased to 29%, 58%, 16%, and 23% for anterior, lateral, posterior, and inferior lesions, respectively; and 15% and 30% for whole and normal liver, respectively. While the goodness of fit for each centre was not systematically assessed, the mean squared displacement (MSD) remained similar among individuals in their respective fitting groups.

4.5 Conclusion

A ‘*real time*’ multi-centric dosimetry comparison was performed on the 3D SPECT/CT patient dataset administered with Lutathera[®]. This *round-table dosimetry analysis* made use of the predefined checkpoints to understand the source of variation among participants. Exemplary and comprehensive results were achieved for the predefined checkpoints, and the sources of variation were identified in the majority of cases after extensive training and brainstorming sessions.

This work resulted in the generation of a ‘*benchmark dataset*’ consisting of:

- reconstructed patient SPECT/CT data at five time points
- an associated calibration factor
- a standard workflow to be followed in Planet[®] Dose
- Step-by-step dosimetry results (with mean and percentage of variation for each established checkpoint)

The complete benchmark dataset is available in [Appendix B](#). The dissemination of this dataset is ongoing by the IAEA.

One limitation of the study is that it only applies to a given clinical dosimetry workflow. It would be interesting to see how, from the same dataset, one could obtain variable results either by varying the processing within Planet (considering alternative segmentation/registration, absorbed dose algorithm, etc.), or by using a different dosimetry software. Yet we have a range of results obtained that represent inter-operator variability and can probably be accepted as valid. This will enable an individual to train oneself on the software (Planet[®] Dose) with a realistic dataset and to assess their own capability of working with the software.

This study focused on the *precision* of the dosimetry analysis done on a single patient dataset using a standard protocol and a specific software in order to generate a *benchmark dataset*. It can be seen that since we had no idea of the true result, more work is required to assess the accuracy of the CDW.

In this context, the DosiTest project may play a pivotal role, since in principle using simulated datasets provides an a priori knowledge of the ground truth. The rest of the doctoral work contributes directly to the development of DosiTest. Chapter [5](#) presents the modelling and validation of *anthropomorphic phantom* SPECT imaging whereas the development of *realistic patient* SPECT/CT dataset is presented in Chapter [6](#).

5

Modelling SPECT auto-contouring acquisitions using new developments in GATE

Contents

5.1 Introduction	107
5.2 Materials & Methods	109
5.2.1 Experimental acquisitions and development of NCO modelling	110
5.2.2 CO vs NCO comparison: ^{177}Lu and ^{131}I SPECT modelling	121
5.2.3 Image comparison metrics	122
5.3 Results	124
5.3.1 Validation of gamma camera models	124
5.3.2 Simulation time	130
5.3.3 Auto-contouring motion vs. circular camera motion using ^{177}Lu and ^{131}I	130
5.4 Discussion	132
5.5 Conclusion	135

5.1 Introduction

The starting phase of setting up DosiTest requires the generation of multi-modal patient projections (planar/SPECT/PET) of a reference patient (via Monte Carlo modelling). The generation of 2D planar whole-body images of an anthropomorphic XCAT phantom with hypothetical ^{177}Lu -DOTATATE pharmacokinetics has been

addressed previously by Costa *et al.* (Costa, Bonifácio, et al. 2017) using GATE Monte Carlo modelling. This chapter addresses the realistic modelling of 3D SPECT imaging using GATE for simple anthropomorphic phantoms.

SPECT images are acquired using a detector or gamma camera rotating around the patient, either in a circular motion (with a fixed radius) or in auto-contour motion (following the contour of the patient as close as possible). The trajectory of the detector around the patient influences the source-to-detector distance, which in turn impacts the image spatial resolution and sensitivity (Cherry et al. 2012d), a major impediment to quantitative imaging (Li, Liang, et al. 1998; Benedetto 1987; van Elmbt et al. 1993). In clinical centres, there is no predetermined distance between the collimator and the patient (Sayed 2020). However, to improve the image quality, the non-circular detector orbit is nowadays considered the default for SPECT imaging (Dewaraja, Frey, et al. 2012; Sanders et al. 2015).

Modelling SPECT imaging in GATE has been widely addressed in the literature (Buvat and Castiglioni 2002; Santin et al. 2003; Strulab et al. 2003; Staelens et al. 2003; Jan et al. 2004; Assié, Breton, et al. 2004; Autret et al. 2005; Buvat and Lazaro 2006; Stute et al. 2011; Garcia et al. 2015; Costa, Bonifácio, et al. 2017; Sarrut, Bała, et al. 2021). This is because GATE is an open source platform that allows the easy design of different medical imaging devices for emission tomography. Additionally, it enables the simulation of time-dependent phenomena such as detector motion, activity distribution across time, radioactive decay and patient movements in order to generate realistic acquisition conditions.

Until date, SPECT acquisition modelling with GATE has only considered a circular orbit (CO) detector movement around the patient, i.e. the detector's rotation around the patient is accomplished with a fixed radius for each step angulation, large enough to prevent a detector/patient collision. Within this context, despite the fact that non-circular orbit (NCO) is the standard SPECT acquisition mode in clinical practice, it was not considered in the simulation. The impact of that simplification is difficult to assess *a priori*. It is likely to be more important in conditions where septal penetration occurs, for energetic emitters such as ^{131}I . For less energetic emitters like ^{177}Lu , the impact of implementing circular rather than non circular orbit needs to be evaluated. This chapter discusses the implementation of the auto-contouring motion in SPECT imaging with GATE, and its influence on simulated projections.

5.2 Materials & Methods

Gamma camera modelling in GATE requires the explicit modelling of the collimator (low, medium or high energy) and the NaI(Tl) crystal according to the manufacturer's specifications. In addition, further consideration of a back-scatter compartment and of the detector lead shield may be required to better model the detector response. The back-scatter compartment is designed to "represent" the light guide, photomultiplier tubes (PMTs) and associated electronics, but in fact is actually meant to optimise detector performance by accounting for back-scatter that may rebound from that compartment and be detected in the crystal. It is important to describe the number of detector heads and their movement around the patient or phantom. After these components are defined, it is essential to simulate the electronic behaviour (digitization) based on spatial and energy resolution, and the selected spectrometric windows.

SPECT image modelling not only requires the development of a gamma camera model (detector), but also a model of the imaged object, which is based on a patient or a phantom (physical test object) used in experimental acquisitions. In GATE, the detector and phantom/patient are defined as two independent volumes (spaces). This allows for the implementation of the detector head movement around the patient without the need to create various input files for each SPECT projection, which represents a major asset of GATE. However, the two (virtual) volumes cannot overlap. This means that auto-contour acquisition modes cannot be simulated in GATE at the moment. This may be of no importance for low energy gamma emission imaging, but may have an impact for high energy emitters as ^{131}I . In the frame of this doctoral work, and to improve SPECT modelling with GATE, we decided to implement and evaluate the impact of explicit non-circular orbit acquisition modelling in GATE.

SPECT images were acquired experimentally for two isotopes (^{177}Lu and ^{131}I) on different gamma cameras at different institutions using different phantoms, thereby covering a range of applications. These experimental acquisitions were simulated in GATE and the simulated SPECT projections were validated against the experimentally acquired projections.

Next, to assess the relevance of modelling auto-contouring motion, SPECT images were generated for each gamma camera model using more complex realistic phantoms with both CO and NCO motion.

This chapter is separated into two main parts. The first section discusses the validation of the simulation of two gamma camera models while the second section

emphasises on the necessity of modelling the NCO motion by comparing SPECT projections with NCO and CO detector motion for each radionuclide. To allow for the comparison of the images generated in the first and second sections, a metric and/or specific estimators had to be established.

5.2.1 Experimental acquisitions and development of NCO modelling

Experimental acquisitions with ^{177}Lu were performed on a Siemens Symbia T2 camera, using a 2-organ physical phantom developed during the joint research European project “Metrology for clinical implementation of dosimetry in molecular radiotherapy (MRTDosimetry)” (Robinson 2021; MRTDosimetry 2016). Experimental acquisitions with ^{131}I were performed on a GE Discovery 670 camera, using an anthropomorphic SPECT torso phantom or lung spine phantom (ANT) (Anthropomorphic SPECT phantom 2021).

5.2.1.1 Experimental setup

a. Phantoms

Experimental acquisitions were performed on 2 anthropomorphic phantoms. The first one is a 3D printed phantom generated by The Christie NHS Foundation Trust in the United Kingdom as part of the MRTDosimetry project (MRTD) (MRTDosimetry 2016; Tran-Gia et al. 2021). Two 3D-printed realistically-shaped abdominal organs, specifically a spleen and a two-compartment right kidney, are positioned inside a cylindrical Jaszczak phantom (with a diameter of 21.6 cm and height of 18.6 cm for the active volume) (Figure 5.1). The kidney is composed of two compartments: the medulla and the cortex. To complete the phantom, base plates, screws, and supports are included.

The second phantom considered is the anthropomorphic lung and spine torso phantom (model ECT/TOR/P), a large, body-shaped cylinder with inserts for the lungs, liver, and spine (Figure 5.1). In the liver, a spherical “tumour” insert is incorporated. The phantom resembles an average-to-big male patient’s upper body. The dimensions of the anterior-posterior and lateral outside phantoms are 26 cm \times 38 cm, whereas the inner dimensions are 24 cm \times 36 cm with 9.5 mm wall thickness (Anthropomorphic SPECT phantom 2021).

b. Acquisition setup

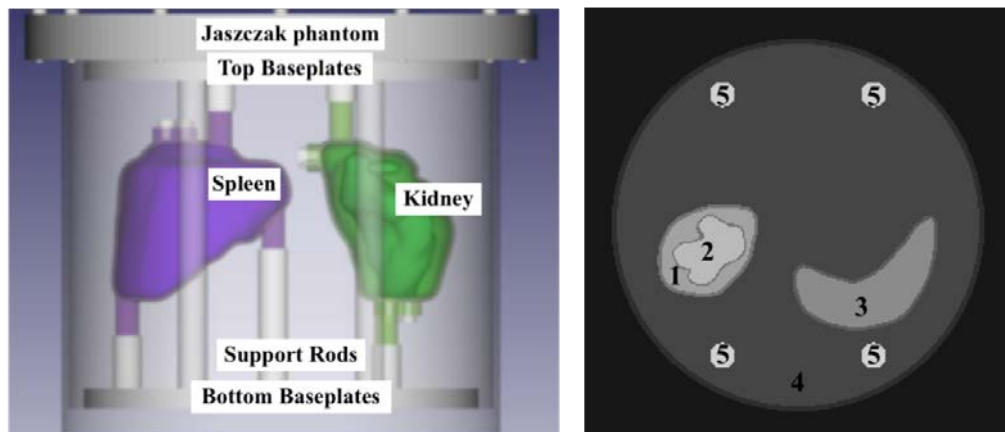


Figure 5.1: The MRTdosimetry 2-organ (spleen and right kidney) phantom: (a) and its transaxial CT cross section (b)
 1= Right Kidney Cortex; 2= Right Kidney Medulla; 3 = Spleen, 4= Phantom; 5 = Support Poles

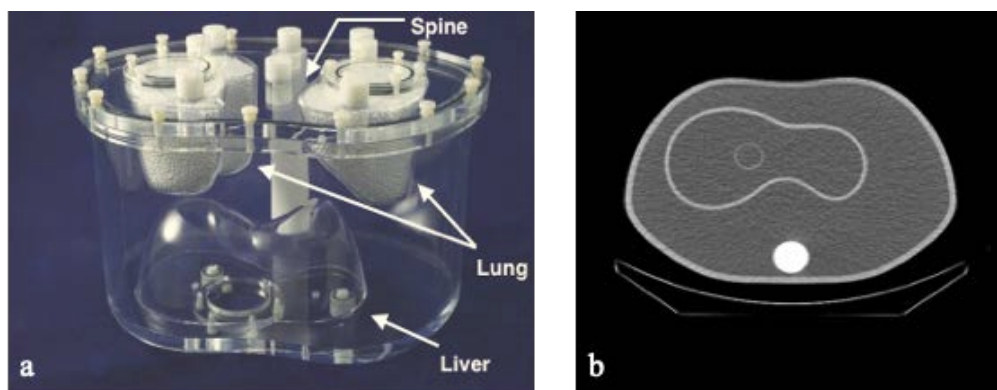


Figure 5.2: ANT (anthropomorphic torso phantom, model ECT/TOR/P) with lungs, liver and cylindrical spine inserts (Data Spectrum CorporationTM) (a) and its transaxial CT cross section (b)

^{177}Lu SPECT NCO projections were acquired with the MRTD 2-organ phantom at the University Hospital Würzburg (UKW), Germany on a dual-head Symbia T2 gamma camera (Siemens Healthineers, Germany) equipped with a medium energy (ME) collimator and a 15.8 mm ($\frac{5}{8}$ ") crystal. Additionally, a low-dose CT scan (130 kVp, $512 \times 512 \times 78$ matrix, $0.98 \times 0.98 \times 5$ mm resolution) was obtained to compensate for attenuation and to serve as the basis for geometry design in Monte Carlo simulations.

Experimental ^{131}I SPECT/CT NCO projections of the lung and spine ANT phantom were obtained at The Christie (Manchester, UK) on a GE Discovery 670 (GE Healthcare, USA) equipped with a high energy (HE) collimator and a thinner 9.5 mm ($\frac{3}{8}$ ") crystal. The associated low-dose CT dataset was obtained at a voltage

<i>UKW (Siemens Symbia T2 gamma camera with ^{177}Lu)</i>				
<i>Phantom</i>	<i>Acquisition parameters</i>			
	<i>Matrix size</i>	<i>Pixel size (mm²)</i>	<i>Time per proj. (seconds)</i>	<i>Energy windows</i>
2-organ MRTD	128 × 128	4.795 × 4.795	20	SC: 178 keV (166.14 - 186.9 keV) PP: 208 keV (186.9 - 228.44 keV) SC: 238 keV (228.44 - 249.2 keV)

Table 5.1: Acquisition parameters for experiments at UKW
SC: scatter window; PP: photopeak or main window

<i>The Christie (GE Discovery 670 gamma camera with ^{131}I)</i>				
<i>Phantom</i>	<i>Acquisition parameters</i>			
	<i>Matrix size</i>	<i>Pixel size (mm²)</i>	<i>Time per proj. (seconds)</i>	<i>Energy windows</i>
Lung and spine ANT phantom	128 × 128	4.418 × 4.418	30	SC: 317 keV (307.6 - 326.62 keV) PP: 364 keV (328.05 - 400.95 keV) SC: 414 keV (401.47 - 426.31 keV)

Table 5.2: Acquisition parameters for experiments at The Christie
SC: scatter window; PP: photopeak or main window

of 120 kVp, with a matrix of $512 \times 512 \times 161$ and a resolution of $0.98 \times 0.98 \times 2.5$ mm.

The acquisition settings for each phantom and gamma camera at UKW and The Christie are shown in [Table 5.1](#) and [Table 5.2](#), respectively. In both cases, sixty SPECT projections per head were obtained in step-and-shoot mode with a 3° angular step (for a total of 180° per head). Each clinical centre defined the energy windows (photopeak and scatter) and their width based on what is currently employed in their clinical acquisition protocols.

c. Activity distribution in different phantoms

[Table 5.3](#) summarises the activities (^{177}Lu /UKW) in the spleen, right kidney cortex (RKC), and right kidney medulla (RKM) of the 2-organ phantom, as well as the overall activity in the phantom. These values were obtained from the activity concentrations of the stock solutions and were determined using a VDC-405 radionuclide calibrator in conjunction with a VIK-202 ionisation chamber (Comcer SpA). This was cross-calibrated to a high-purity germanium detector (Canberra Industries Inc.) whose energy-dependent efficiency was calibrated using several NIST and National Physical Laboratory traceable standards over the energy range considered.

Centre	Phantom	Isotope	Liver	Spleen	RKC	RKM	Tumour	BG	Total
UKW	MRTD 2-organ	¹⁷⁷ Lu	-	178.6	108.7	16.1	-	-	303.4
The Christie	ANT Lung & Spine	¹³¹ I	51.6	-	-	-	5.06	186.76	243.42

Table 5.3: Activities (MBq) in the 2-organ MRTD phantom and the lung & spine ANT phantom
RKC = Right Kidney Cortex; RKM = Right Kidney Medulla; BG = Background; Total = Total activity in the entire phantom

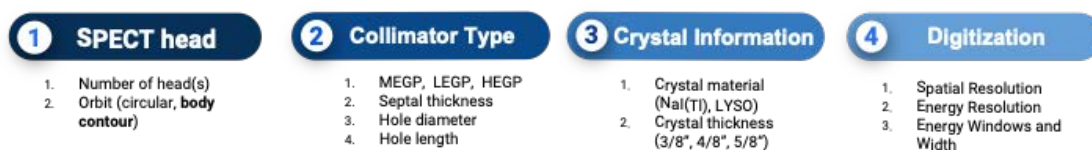


Figure 5.3: Schematic of modelling the gamma camera components and its response

Table 5.3 additionally includes activities (¹³¹I/The Christie) for the lung and spine ANT phantoms. These values are derived from the activity concentrations of the stock solutions and the pre- and post-fill weights of the compartments. The activities were determined using a Capintec55t radionuclide calibrator with calibration factors calibrated to National Physical Laboratory standards and a Fidelis secondary standard calibrator. The weights/volumes of the background and the cylinder were obtained on a scale calibrated to 1 ml.

5.2.1.2 Simulation setup in GATE

a. Modelling the motion of the gamma camera head

As mentioned earlier, modelling the gamma camera requires modelling each component of the detector head independently (collimator, crystal, electronics), followed by modelling the detector response (digitization). The major components of the SPECT head modelling are shown in Figure 5.3.

In this work, the models of the Siemens Symbia T2 gamma camera and the GE Discovery 670 were derived from the previous work of Costa *et al.* (Costa, Bonifácio, et al. 2017) and Autret *et al.* (Autret et al. 2005) respectively.

To model the circular motion of the detector head around the phantom/patient in GATE, a fixed translation (radius) for the detector head is set and rotation is performed using the ‘orbiting’ class by specifying a speed in degrees per second Figure 5.4. However, to model auto-contour motion, a fixed distance between the

2.5.3. Orbiting

Rotating a volume around any axis during a simulation is possible using the orbiting motion. This motion is needed to model the camera head rotation in SPECT. To rotate the *Name_Volume* volume around the X axis with a speed of N degrees per second, the commands are:

```
/gate/SPECThead/moves/insert orbiting
/gate/SPECThead/orbiting/setSpeed N. deg/s
/gate/SPECThead/orbiting/setPoint1 0 0 0 cm
/gate/SPECThead/orbiting/setPoint2 1 0 0 cm
```

The last two commands define the rotation axis.

Figure 5.4: Implementation of circular detector motion in GATE ([GATE documentation 2018](#))

2.5.7. Generic repeater move

You can combine generic repeater and generic move to allow different repeated configurations according to time. This is for example useful to describe multi-leaf collimator from a single leaf which is repeated at different positions, and which move according to each beam:

```
/gate/myvolume/moves/insert genericRepeaterMove
/gate/myvolume/genericRepeaterMove/setPlacementsFilename data/myvolume.place
/gate/myvolume/genericRepeaterMove/useRelativeTranslation 1

##### List of placement (translation and rotation)
##### Column 1 is rotationAngle in degree
##### Columns 2,3,4 are rotation axis
##### Columns 5,6,7 are translation in mm
Time s
NumberOfPlacements 3
Rotation deg
Translation mm
#Time # Placement 1 # Placement 2 # Placement 3
0 10 0 1 0 20 0 0 10 0 1 0 80 0 0 10 0 1 0 -60 0
1 20 0 1 0 20 10 0 20 0 1 0 80 10 0 20 0 1 0 -60 10
2 30 1 1 0 20 0 0 30 1 1 0 80 0 0 30 1 1 0 -60 0
4 40 0 1 1 20 0 40 40 0 1 1 80 0 40 40 0 1 1 -60 0 4
```

The 'NumberOfPlacements' is needed to indicate how many different repetition are performed at each motion.

Figure 5.5: Implementation of auto-contouring detector motion in GATE ([GATE documentation 2018](#))

centre of rotation and the detector cannot be employed. Therefore, the 'Generic repeater move' class in GATE allowing for the movement of repeated geometric configurations (in this example, detector heads) in time using a set of transformations (translations and associated rotations) was considered ([Figure 5.5](#)).

To this end, information such as radial position (radial distance of the detector from the centre of rotation), start angle (position of the detector around the patient at the start of the acquisition), and angular step (angular scan arc step between projections) must be extracted from the experimental SPECT projection DICOM headers. Extraction of this information from the DICOM header varies according to the gamma camera model and manufacturer.

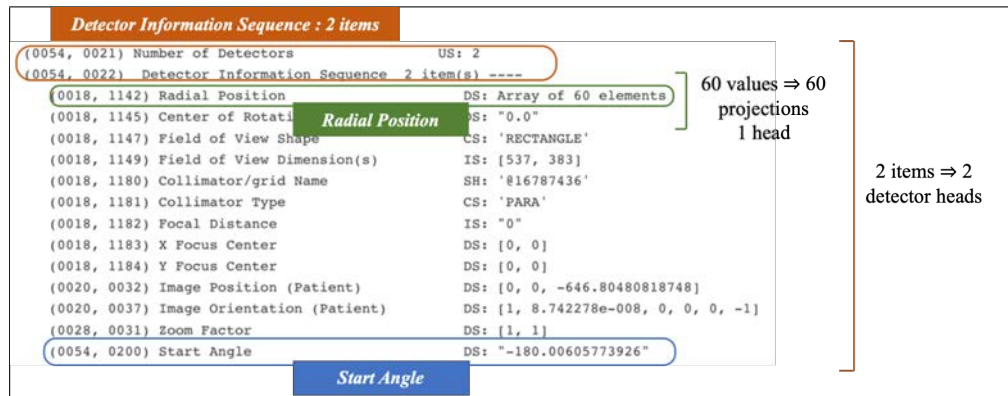


Figure 5.6: Extraction of auto-contour mode information from Siemens Symbia T2 DICOM header

For the *Siemens Symbia T2* gamma camera, auto-contour motion information for each head has to be extracted from the ‘Detector Information Sequence’. In this sequence, the DICOM tag [0018, 1142] corresponding to ‘Radial position’ has as many values as the number of projections per head and the associated start angle for the detector head. For this dual-headed gamma camera, 60 projections per head were acquired, hence ‘Detector Information Sequence’ contains two items and 60 values for ‘Radial position’ (Figure 5.6).

However, when acquisitions are made with the same number of projections and detector heads on a *GE Discovery 670* gamma camera, the ‘Radial position’ tag in the DICOM header does not contain 60 values, as can be seen in Figure 5.7. This field has a single value (in polar coordinates). This is because the gamma camera calculates the radial distance between the centre of rotation and the detector head using an additional DICOM tag [0013,101e], corresponding to ‘Tomo View Offset’. This tag contains three values for each projection, namely the x, y, and z coordinates (therefore in cartesian coordinates). With a total of 120 projections, this tag therefore has $120 \times 3 = 360$ values (Figure 5.8). To derive the ‘actual radial position’, the offset value for each projection in polar coordinates is calculated and combined with the single value of the radial position DICOM tag.

This yields a set of radial positions for each gamma camera. These radial positions (in polar coordinates) with the appropriate angular step and start angles are then transformed to cartesian coordinates with a script in Python 3 (Van Rossum et al. 2009) to obtain the x, y, and z positions of the detector head so as to generate a list of translations and rotations for the implementation of NCO acquisitions. The positions of each detector head, as well as the rotation angle, rotation axis,

(0054, 0052) Rotation Information Sequence 1 item(s) ----		
(0018, 1130) Table Height		DS: "79.5"
(0018, 1131) Table Traverse		DS: "860.0"
(0018, 1140) Rotation Direction		CS: 'CC'
(0018, 1142) Radial Position		DS: "226.533"
(0018, 1143) Scan Arc	Radial Position	DS: "360.0"
(0018, 1144) Angular Step		DS: "3.0"
(0018, 1242) Actual Frame Duration		IS: "30000"
(0054, 0053) Number of Frames in Rotation		US: 120
(0054, 0200) Start Angle	Start Angle	DS: "359.58"

} 1 value only

Figure 5.7: Radial position information from GE Discovery 670 DICOM header

(0055, 1022) [Xeleris Detector Information Sequence] 1 item(s) ----		
(0011, 0010) Private Creator		LO: 'GEMS_GENIE_1'
(0011, 1023) [Use FOV Mask]		SL: 0
(0011, 1024) [FOV Mask Y Cutoff Distance]		SL: 0
(0011, 1025) [FOV Mask Cutoff Angle]		SL: 0
(0011, 1029) [Uniformity Mean]		SL: 0
(0011, 103e) [FOV Shape]		SL: 13
(0013, 0010) Private Creator		LO: 'GEMS_GENIE_1'
(0013, 1018) [Transmission Scan Time]		FD: 0.0
(0013, 1019) [Transmission Mask Width]		FD: 0.0
(0013, 101a) [Copper Attenuator]	Tomo View Offset	FD: 0.0
(0013, 101e) [Tomo View Offset]		FD: Array of 360 elements
(0035, 0010) Private Creator		LO: 'GEMS_GENIE_1'
(0035, 1001) [Start Angle]	Start Angle	FD: 179.57999999999998

120 × 3 (x, y, z) offsets
⇒ 120 projections

*Tomo View Offset (0013,101e): Table of offsets from COR during acquisition
[GE DICOM Conformance Statement]*

$$\text{Actual Radial Position} = \text{Radial Position (0018, 1142)} + \text{Tomo View Offset (0013,101e)}$$

Figure 5.8: Extraction of auto-contour mode information from GE Discovery 670 DICOM header

and corresponding times were then saved in a file format readable by the ‘Generic Repeater Move’ class.

The patient table was not modelled in the simulations; nevertheless, the distances between the phantom and the camera head were determined based on experimental settings wherein the patient table was present.

b. Phantom modelling and NCO implementation in GATE

In Monte Carlo codes, labelled voxelised models of the phantoms created from the acquired CT scans are employed. They shall be referred to as “phantom models” in the following to distinguish them from real phantoms (Figure 5.1b) (Petoussi-Henss et al. 2014).

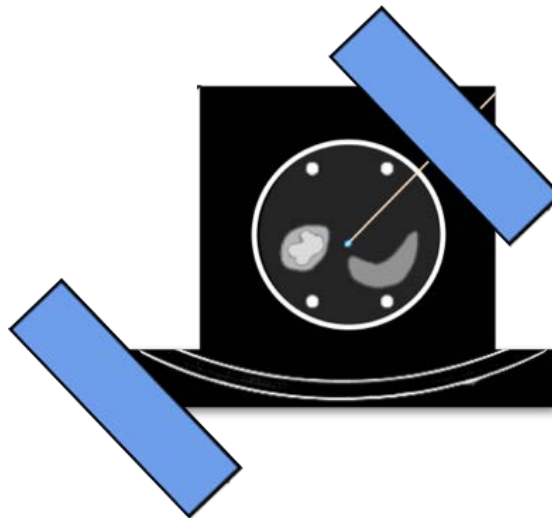


Figure 5.9: Illustration of the geometry modelling issue in GATE: For some camera positions, the gamma camera head model overlaps the phantom model volume

By default, a phantom volume is a three-dimensional square voxelized matrix with air around it, as seen in [Figure 5.9](#). As a result, when the virtual gamma camera head approaches the phantom model, the two volumes may collide ([Figure 5.9](#)). This is inconsistent with Geant4/GATE standards, as distinct independent geometries can neither intersect or overlap.

The development of a specific NCO acquisition mode required the conversion of the voxelized geometry to a tessellated mesh phantom model. Tessellation is a mathematical operation that enables the subdivision of a geometry into smaller meshes by the use of triangle primitives or tetrahedral surfaces (Renze [1995](#)). With this, the labelled regions of interest in the phantom model can be extracted individually as meshes, thereby eliminating the air region outside the ‘real’ phantom boundaries. This allows the gamma camera head to approach as close as possible to the phantom model within the virtual GATE environment without colliding or overlapping.

To comply with GATE standards, this approach prioritised triangular primitives over tetrahedral mesh structures. Triangular primitives were constructed by first selecting the coordinates of each segmented and labelled compartment of interest in the phantom model. Following that, a list of vertices and faces was generated to produce meshes for each compartment using Python scripts using the NumPy (Harris et al. [2020](#)) and SimpleITK libraries (Yaniv et al. [2018](#)).

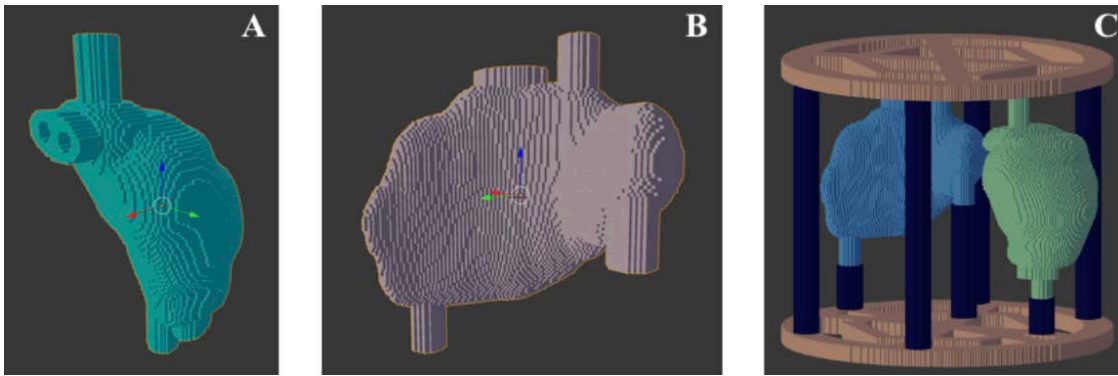


Figure 5.10: Creation of tessellated volumes with right kidney and spleen followed by the representation of the 2-organ phantom model with the two organs, support poles and baseplates (without the phantom model wall)

The object files (.obj) produced by this Python script were then uploaded in Blender, an open source 3D image software (Bücking et al. 2017), for the purpose of merging triangles on planar faces and linear edges. This was performed by dissolving the interior vertices and edges of the compartment, while retaining its outside mesh surface. All faces were triangulated further and exported as stereolithographic (.stl) files, a triangular representation of three-dimensional surface geometry. Triangulation mesh surfaces of the two organs and the constructed phantom model are shown in Figure 5.10. The Geant4 G4TessellatedSolid class was used to transform these individual compartmental mesh surfaces into unique volumes with individual materials in GATE. Based on the phantom CT, each volume was ascribed a specific material.

c. Radionuclide emission modelling and data output

Two radionuclides were used in this work: ^{177}Lu and ^{131}I .

^{177}Lu (half-life of 6.64 days) is a beta/gamma emitter with a growing number of indications (including neuroendocrine or prostate cancers). In addition to some low-energy X-rays, major photon emissions of 112.9 keV (6.2%) and 208.4 keV (10.4%) are employed for diagnostic evaluation and dosimetry.

^{131}I has a half-life of 8.02 days and emits beta and gamma radiation. It is the most often used radioisotope in MRT, mainly for the treatment of thyroid disorders. The major photon emissions of 284.3 keV (6.1%), 364.5 keV (81.5%), 637 keV (7.2%) and 722.9 keV (1.77%) (MIRD 2021; Dewaraja, Ljungberg, and Koral 2000) makes it possible to perform scintigraphic imaging. The presence of high energy photons necessitates the use of a high energy collimator. Even then, septal penetration artefacts in scintigraphic images may occur.

¹⁷⁷ Lu		¹³¹ I	
Energy (keV)	Yield	Energy(keV)	Yield
0.019	1.281	0.017	0.763
1.639	0.004	4.097	0.002
6.982	0.001	4.413	0.001
7.833	0.001	29.452	0.014
7.890	0.013	29.781	0.026
9.038	0.012	33.567	0.002
9.34	0.002	33.63	0.005
10.54	0.002	34.39	0.001
54.72	0.016	80.18	0.026
55.92	0.029	177.21	0.003
63.12	0.003	272.50	0.001
63.38	0.006	284.30	0.061
65.05	0.001	318.09	0.001
65.11	0.001	325.79	0.003
71.64	0.002	364.49	0.817
112.95	0.062	404.81	0.001
136.72	0.000	503.00	0.004
208.37	0.104	636.99	0.072
249.67	0.002	642.72	0.002
321.32	0.002	722.91	0.018
Total	1.543	Total	1.821
Gamma	0.172	Gamma	1.007
X-rays	1.372	X-rays	0.814

Table 5.4: Energy of the gamma photons for ¹⁷⁷Lu and ¹³¹I with their respective yields used in simulations

Due to the fact that only gamma and X-ray photons contribute to the production of SPECT images, the simulations considered only photon emissions. For ¹⁷⁷Lu and ¹³¹I, this means a total of 1.543 and 1.821 emissions respectively per disintegration (Table 5.4).

To model the transportation of radiation and related physical processes, a pre-built physics list '*emstandard_option3*' encompassing the various electromagnetic interactions of particles and matter was used. A range cut-off of 1 mm was applied to all volumes (and corresponding materials) to avoid the production of secondary particles in order to optimise the simulation time. This was done utilising the *production cuts* in GATE which internally converts range to energy for relevant

Phantom	Activity (MBq)	Radio-isotope	Yield (emission/decay)	Primaries (particles)
2-organ	303.4	^{177}Lu	1.546	5.63×10^{11}
ANT	243.42	^{131}I	1.825	8.00×10^{11}

Table 5.5: Conversion of activity to primaries

materials. This implies that for example, secondary photons with an energy level of < 100 keV will not be produced in lead.

GATE allows for several output formats. The most suitable output format for acquisition protocols using a multi-headed rotating gamma camera is an inter-file/projection output (*.hdr/.sin*). The header file (*.hdr*) includes all acquisition-related data, while the *.sin* file contains the binary data of the image. Projections for each energy window may be generated individually if they are defined in the input files (macros) prior to initiating the simulation.

GATE facilitates the storage of hits and singles (output pulses) as ROOT files (*.root*) for post-processing of the generated simulated data. This file provides information on the position (in x, y, and z), the direction (dx, dy, dz), the time, the energy deposition and the location of the interaction, as well as the type of particle associated with each hit (Brun et al. 1997). This enables building projections for any energy window and width for scatter correction or further analysis even after the simulation is completed.

In this work, projections corresponding to energy windows considered in experimental acquisitions as specified in Table 5.1 and Table 5.2 were simulated for ^{177}Lu and ^{131}I , respectively.

d. Computation of the primaries / particles

The total number of primaries used in the simulations for each phantom were computed using the total activity in each phantom, 60 projections per head, 20 seconds or 30 seconds each projection (2-organ or ANT phantom, respectively), and 1.546 or 1.825 emissions per decay (^{177}Lu or ^{131}I , respectively). These are reported in Table 5.5.

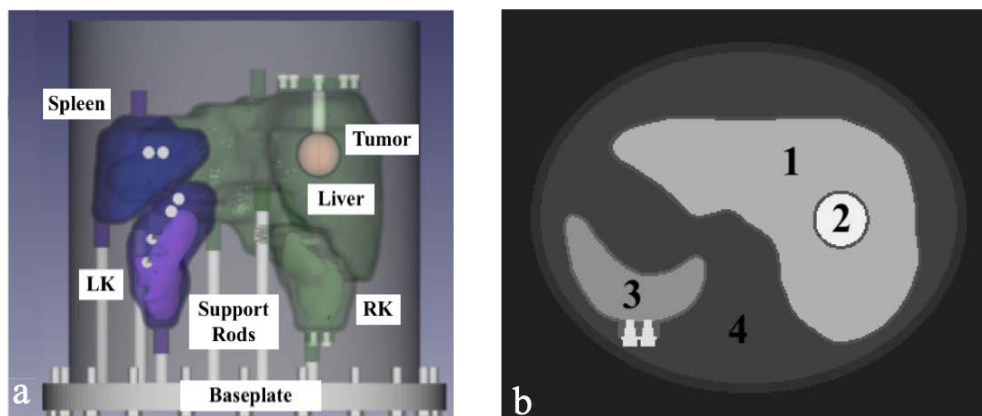


Figure 5.11: Elliptical phantom with 4-organs (spleen, liver, left (LK) and right kidney (RK)) with the spherical tumour in the liver (a) and transaxial CT cross section of the phantom (b)

1= Liver; 2= Spherical tumour; 3 = Spleen, 4= Phantom

5.2.2 CO vs NCO comparison: ^{177}Lu and ^{131}I SPECT modelling

For the comparison of circular detector motion and non-circular or auto-contouring detector motion, it is crucial to consider phantoms that sufficiently resemble a patient geometry. Clearly, a cylindrical section phantom model is counterproductive for this scenario. Thus, instead of using the cylindrical two-organ phantom, an elliptical four-organ phantom was employed to generate ^{177}Lu NCO and CO SPECT projections using the Siemens Symbia T2 gamma camera model. This 4-organ phantom (also developed within the framework of the MRTD project) comprises a spleen, kidneys, and liver inserted into an ellipsoid phantom (with short radii, long radii and height of 10.6 cm, 13.55 cm and 31.2 cm, respectively). A spherical tumour is present in the liver. Features such as base plates, screws and supports are added to complete the phantom (Figure 5.11).

The activity distribution for each compartment at various times post activity administration in the 4-organ phantom was derived from the compartmental pharmacokinetic model of Brodin *et al.* (Brodin *et al.* 2015) assuming an administered activity of 7.4 GBq. A full set of time-activity curves (TAC) was generated for this realistic 4-organ phantom. However, for the purpose of NCO vs CO comparison, the activity distribution at 40 hours post activity administration was simulated due to adequate statistics Table 5.6. Acquisition parameters similar to that for the 2-organ phantom were used except for the time per projection which was set to 30 seconds. The number of primaries used for the 4-organ phantom is reported in Table 5.7.

Activity distribution in the 4-organ MRTD phantom corresponding to ^{177}Lu pharmacokinetics at different times post injection									
Time (h)	Liver	Spleen	RK C	RK M	LK C	LK M	Tumour	BG	Total
1	149.16	47.14	48.28	7.60	57.97	9.12	30.62	840.43	1190.32
24	180.55	63.28	39.34	6.19	47.24	7.43	30.11	108.25	482.39
40	145.41	54.60	31.91	5.02	38.32	6.03	27.38	79.44	388.11
72	109.90	39.55	20.80	3.27	24.98	3.93	22.27	57.64	282.34
144	61.23	19.11	8.07	1.27	9.69	1.53	13.84	29.02	143.76

Table 5.6: Activity (in MBq) in 4-organ phantom model corresponding to ^{177}Lu pharmacokinetics

RKC = Right Kidney Cortex; RKM = Right Kidney Medulla; LKC = Left Kidney Cortex; LKM = Left Kidney Medulla; BG = Background;
Total = Total activity in the phantom

Phantom	Radioisotope	Activity (MBq)	Yield (emissions/decay)	Primaries (particles)
4-organ MRTD	^{177}Lu	388.11	1.546	1.08×10^{12}

Table 5.7: Computation of primaries for the 4-organ phantom with ^{177}Lu

For ^{131}I , simulated NCO and CO SPECT acquisitions were modelled with the same lung and spine phantom on a GE Discovery 670 model, as presented in part A, as the phantom is realistic enough.

In the context of NCO acquisitions, head position information was extracted from experimental acquisitions performed at The Christie on both the 4-organ phantom and the ANT phantom to generate detector positions at varying projection angles (radial distance from centre of rotation to surface of the gamma camera). For CO acquisitions, the largest distance between the centre of rotation and the surface of the gamma camera during experimental acquisitions was selected.

For both CO and NCO acquisition modes, the exact thickness of each gamma camera head was considered to prevent phantom model and detector volume overlaps or collisions.

5.2.3 Image comparison metrics

The comparison of the results obtained involved the validation of the modelling (experimental vs. simulated projections for various camera/phantom/isotope combinations) and the analysis of the impact of incorporating NCO acquisitions in GATE SPECT modelling (comparison between modelled projections, for different phantom models, gamma cameras and isotopes).

The metrics used for image comparison include the difference in profile magnitudes and the gamma index.

Magnitude difference in profiles: For the purpose of comparing the series of 2D SPECT projections, flattened 1D profiles on the x-axis were constructed by aggregating all the counts along the y-axis. Then, for each projection, the relative difference between experimental and simulated profiles was determined, and a mean relative difference was generated over all projections.

Gamma index: Gamma evaluation techniques are often employed in intensity modulated radiotherapy (IMRT) to compare absorbed dose distributions quantitatively. This evaluation approach compares two absorbed dose distributions using the absorbed dose difference (DD) criteria in conjunction with the distance to agreement (DTA) criterion (namely reference or measured and evaluated or simulated absorbed doses). These criteria complement each other, thereby allowing evaluation of the absorbed dose distribution calculation quality (Low et al. 1998; Hussein et al. 2013). The gamma index of the reference $\gamma(\vec{r}_r)$ is defined as the minimum of generalised functions as represented in Equation 5.1, Equation 5.2, Equation 5.3, Equation 5.4 (Wendling et al. 2007):

$$\gamma(\vec{r}_r) = \min\{\Gamma(\vec{r}_e, \vec{r}_r)\} \forall (\vec{r}_e) \quad (5.1)$$

$$\Gamma(\vec{r}_e, \vec{r}_r) = \sqrt{\frac{\delta^2(\vec{r}_e, \vec{r}_r)}{\Delta D^2} + \frac{r^2(\vec{r}_e, \vec{r}_r)}{\Delta d^2}} \quad (5.2)$$

$$\delta(\vec{r}_e, \vec{r}_r) = D_e(\vec{r}_e) - D_r(\vec{r}_r) \quad (5.3)$$

$$r(\vec{r}_e, \vec{r}_r) = |\vec{r}_e - \vec{r}_r| \quad (5.4)$$

$D_e(\vec{r}_e)$ and $D_r(\vec{r}_r)$ represent the evaluated and reference absorbed doses respectively, \vec{r}_e and \vec{r}_r are the vector positions of the evaluated and reference points respectively, and ΔD and Δd are the DD and DTA criteria respectively.

As a result, the gamma index is defined as the minimum distance between two distributions in a renormalized absorbed dose-distance space. Only if $\gamma(\vec{r}_r) \leq 1$, the evaluated distribution is accepted. This implies that each point in the evaluated distribution is reviewed to see if both criteria meet or exceed the tolerances chosen (for e.g. 2 % DD and 2 mm DTA). The gamma index pass rate (GIPR) specifies a percentage of $\gamma(\vec{r}_r) \leq 1$ (indicating the points lying within the given DD/DTA acceptance criteria) (Low 2010). This gamma index approach was used to compare 2D SPECT projections using the difference in counts as the DD criteria and the spatial difference as the DTA criterion.

To validate the NCO implementation (i.e., experimental versus simulated ^{177}Lu SPECT images of the 2-organ MRTD phantom), DTA was set to the maximal difference in pixels between experimental and simulated images, and DD was set to 2% (i.e., the maximum permissible difference in counts in this context).

To validate ^{131}I SPECT images of the lung and spine ANT phantom, DD, DTA criteria of 2%, 1 pixel were considered.

Then, to analyse the impact of NCO detector motion (i.e. CO versus NCO simulated SPECT projections for ^{177}Lu and ^{131}I), the DTA was set to one pixel (the maximum attainable shift) and the DD criterion to 2%. In all cases, 2% was selected for the DD criterion since results above this value converge.

5.3 Results

5.3.1 Validation of gamma camera models

5.3.1.1 Siemens Symbia T2 for ^{177}Lu with 2-organ MRTD phantom

SPECT projections for the two-organ phantom model considering the auto-contouring motion were simulated. [Figure 5.12](#) illustrates the movement of the gamma camera model around the phantom model consisting of the collimator and crystal, as well as the PMTs and electronics. One detector head moves from 0° to 45° and 90° while the other turns from 180° to 225° to 270° (from [Figure 5.12a](#) to [Figure 5.12c](#)). Each detector head moves independently, approaching to or stepping away from the phantom model. As can be seen in [Figure 5.12b](#), the camera heads are not equidistant from the centre of rotation, thus showing the auto-contouring acquisition mode (or non-circular movement) of the gamma camera in simulations. Additionally, the distance between the two detector heads in [Figure 5.12a](#) is shorter than the distance between the two detector heads in [Figure 5.12c](#), thereby exemplifying that the detector heads do not move in a fixed radius.

Simulated SPECT projections for the 2-organ phantom model (containing the spleen and the right kidney) are shown in [Figure 5.13](#). These projections were modelled from 0° to 360° with a 3° angular step, resulting in a total of 120 projections (60 projections per head). However, just a few projections from [Figure 5.13a](#) to [Figure 5.13d](#) are illustrated here, which correspond to 0° , 90° , 180° , and 270° , respectively. The projections of 0° and 180° correspond to the positions of the gamma camera head below and above the table, respectively. The gamma camera rotates clockwise, which explains why the right kidney appears in the second projection (at 90° detector head position) and the spleen in the final projection (at 270° detector head position) independently.

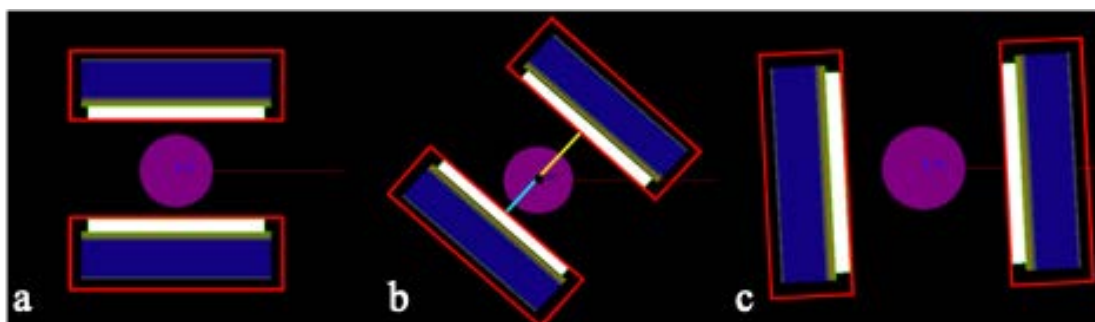


Figure 5.12: Auto-contouring motion of the gamma camera around the 2-organ phantom model. a) Detector heads at 0° and 180° , b) Detector heads at 45° and 225° , c) Detector heads at 90° and 270°
Collimator (white); Crystal (grey); PMT (blue); SPECT head (red); phantom model (purple)

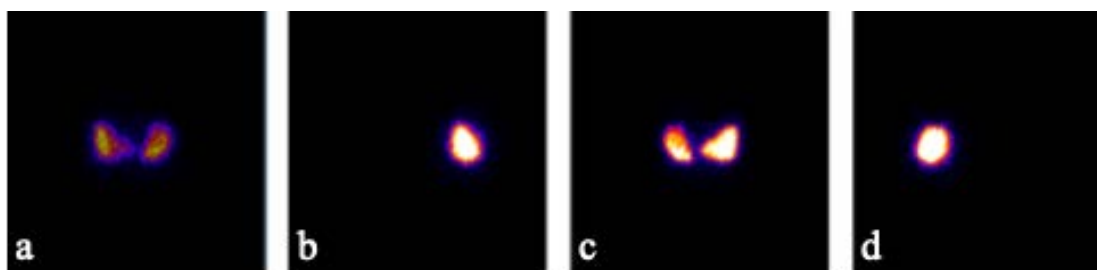


Figure 5.13: Simulated SPECT projections for the 2-organ phantom at different projection angles: a) 0° , b) 90° , c) 180° and d) 270° as the gamma camera in auto-contouring motion moves clockwise. a) spleen is on the left and the right kidney on the right, b) shows the right kidney, c) 180° shows the inverse of a) and d) highlights the spleen

The measured (at UKW, Germany) and simulated energy spectra of ^{177}Lu (with two major gamma peaks at 113 keV and 208 keV, a low energy X-ray peak around 50 keV and the Compton continuum) are shown in [Figure 5.14a](#), demonstrating the agreement between experiments and simulations, particularly within the energy windows considered for imaging (i.e. $208 \text{ keV} \pm 10\%$ photopeak energy). Some discrepancies between experiments and simulations are observed for lower energies, but this doesn't prevent using the model for the energy window selected. Simulated gamma cameras are always simplifications of real gamma cameras, which means that not all aspects of acquisitions may be considered (like electronics, exact material and densities, components used in building gamma cameras).

The simulated non-circular detector movement in [Figure 5.14b](#) depicts the camera heads rotating around the phantom, with each thin blue line indicating the gamma camera plane at its corresponding 3° angular step. As can be seen, the gamma camera follows a non-circular trajectory. When the detector head is

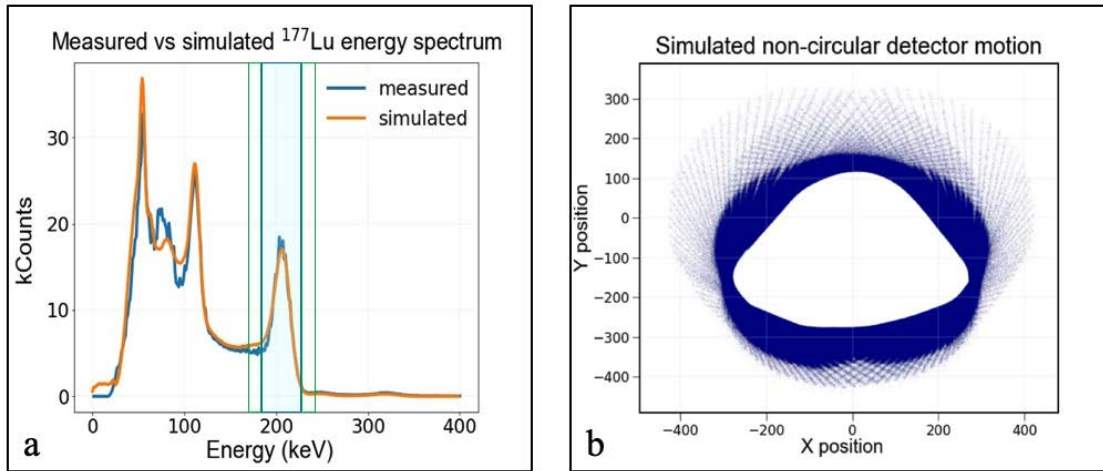


Figure 5.14: Simulated energy spectrum of ^{177}Lu (energy in keV). The blue and green windows highlight the photopeak (208 keV) and two scatter energy windows (lower scatter at 178 keV and upper scatter at 238 keV) respectively; b) Simulated non-circular orbit of detector head (from ROOT). The semi-circular section in the positive Y-axis and horizontal elongation in the negative Y-axis verifies the position of the phantom and presence of the table, respectively

above the phantom i.e. in the positive y axis, it is possible to get closer to the patient than when it is below the phantom (in negative y axis) due to the presence of the table. This explains the lower activity observed in [Figure 5.13a](#) for 0° , compared to [Figure 5.13c](#) for 180° .

The experimental projections and the simulated projections for the 2-organ phantom (model) are shown in [Figure 5.15](#). As can be seen visually, these projections are remarkably similar. To assess the similarities (or differences) between experiments and simulations, profiles were drawn for both sets of projections ([Figure 5.16](#)). The two peaks in the profiles ([Figure 5.16a](#) and [Figure 5.16c](#)) represent the spleen and right kidney, respectively. This difference in counts between spleen and right kidney arises due to higher spleen activity ([Table 5.3](#)). As the detector head advances from 0° to 90° , the right kidney is more prominently seen ([Figure 5.13b](#)), explaining why the projection at 90° ([Figure 5.16b](#)) has just one peak. Similarly, for the projection at 180° , a mirror image of the projection at 0° is seen, and as the camera advances from 180° to 270° , the spleen becomes increasingly apparent ([Figure 5.13d](#)), thereby explaining the single peak for the projection at 270° ([Figure 5.16d](#)).

When experimental and simulated profiles are evaluated, it is evident that not all simulated projection profiles resemble the experimental profiles perfectly. For example, although the profiles at 0° and 180° are relatively similar, the height of the peak at 0° corresponding to the spleen is considerably different. The reason for this

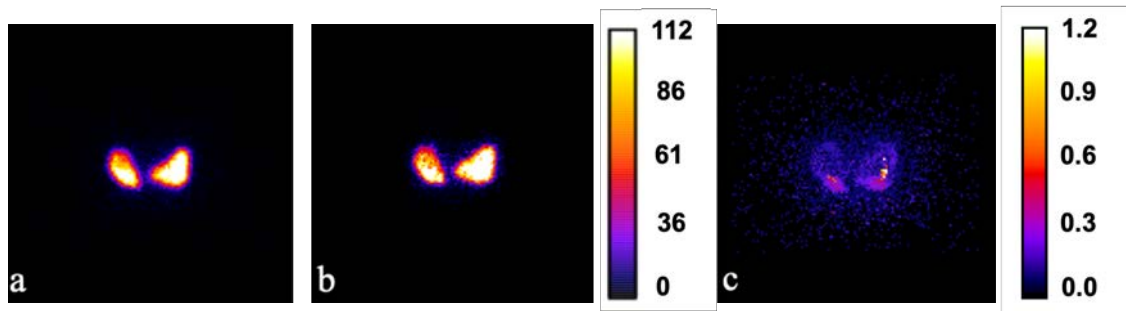


Figure 5.15: (a) Experimental and (b) simulated SPECT projection at 180° of the 2-organ phantom (model) acquired with auto-contouring gamma camera motion, (c) gamma index map (for the photopeak energy window at 208 keV)

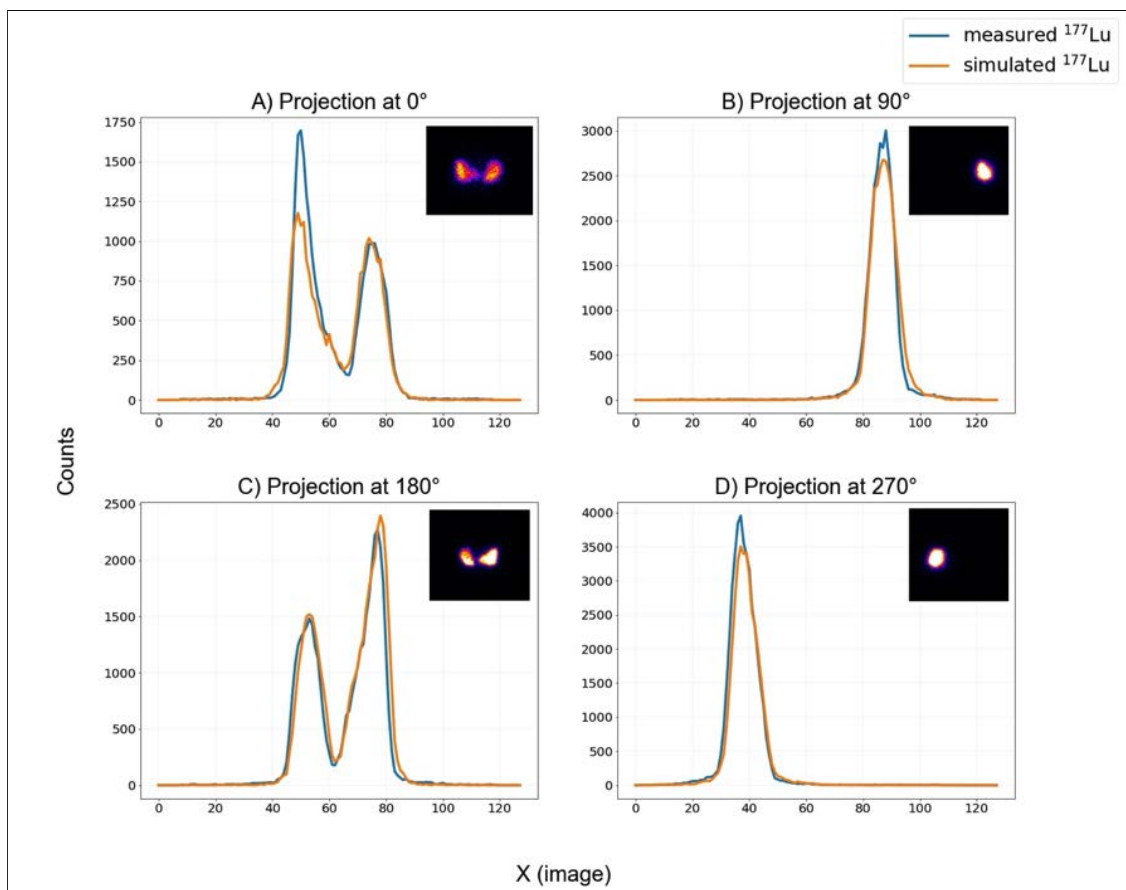


Figure 5.16: Profiles of experimental (blue) and simulated (orange) SPECT projections at different projection angles for ^{177}Lu

discrepancy was difficult to ascertain since the experimental projections included very little information about the precise geometry and positional uncertainties. Additionally, from a simulation standpoint, it is hard to master the detector response perfectly, which could have caused some variations, notably for projection at 0° . Nonetheless, a tilt in the phantom positioning along the table axis was observed in the phantom CT (resulting in an offset of 6 pixels) and was accounted for in the simulations. Therefore, in the case of 90° and 270° projections, the simulated profiles closely reflected the experimental profiles.

The distance to agreement (DTA) in the gamma index was adjusted to 6 pixels (corresponding to the maximal shift found in profiles) in order to better understand the effect of the shift when comparing experimental and simulated projections. The permissible difference in counts was 2% of the maximum count in the experimental image. The GIPR ($\gamma < 1$) value for the two-dimensional global gamma index of 2% - 6 pixels was 96.27% with a γ_{avg} of 0.242. [Figure 5.15c](#) shows the corresponding gamma index map. This demonstrates the significant degree of resemblance between the images, thus validating the simulation of our gamma camera model, including the newly developed implementations in GATE, such as non-circular detector movement and mesh-based phantom geometries.

5.3.1.2 GE Discovery 670 for ^{131}I with the lung and spine ANT phantom

As previously described for ^{177}Lu imaging, auto-contouring motion modelling for the GE Discovery 670 SPECT system using the lung and spine phantom was performed and compared against experimental projections, as shown in [Figure 5.17](#). In the liver, a tumour with a high activity concentration can be observed. The other regions with activity include liver and background.

As seen in [Figure 5.18](#), profiles were created for both sets of projections to determine their similarity. The projection profiles are fairly close at all angles. In the 180° profiles, a minor drop in counts is noticed along the centre x axis, which is explained by the existence of the cylinder representing the spine in the phantom.

The gamma index metric considered a 2%, 1 DD, DTA pixel criterion. The GIPR (gamma index passing rate) with $\gamma < 1$ for a 2D global gamma index of 2% - 1 pixel was 92.89% with an γ_{avg} of 0.36. The gamma index map in [Figure 5.17c](#) demonstrates close similarity, validating our model of the GE Discovery 670 gamma camera.

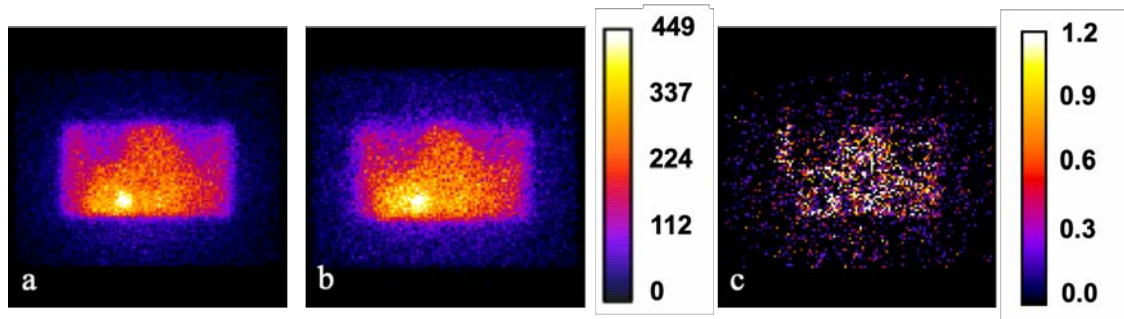


Figure 5.17: (a) Experimental and (b) simulated ^{131}I SPECT projection at 0° of the lung and spine ANT phantom acquired with auto-contouring gamma camera motion, (c) gamma index map (for photopeak energy window of 364 keV)

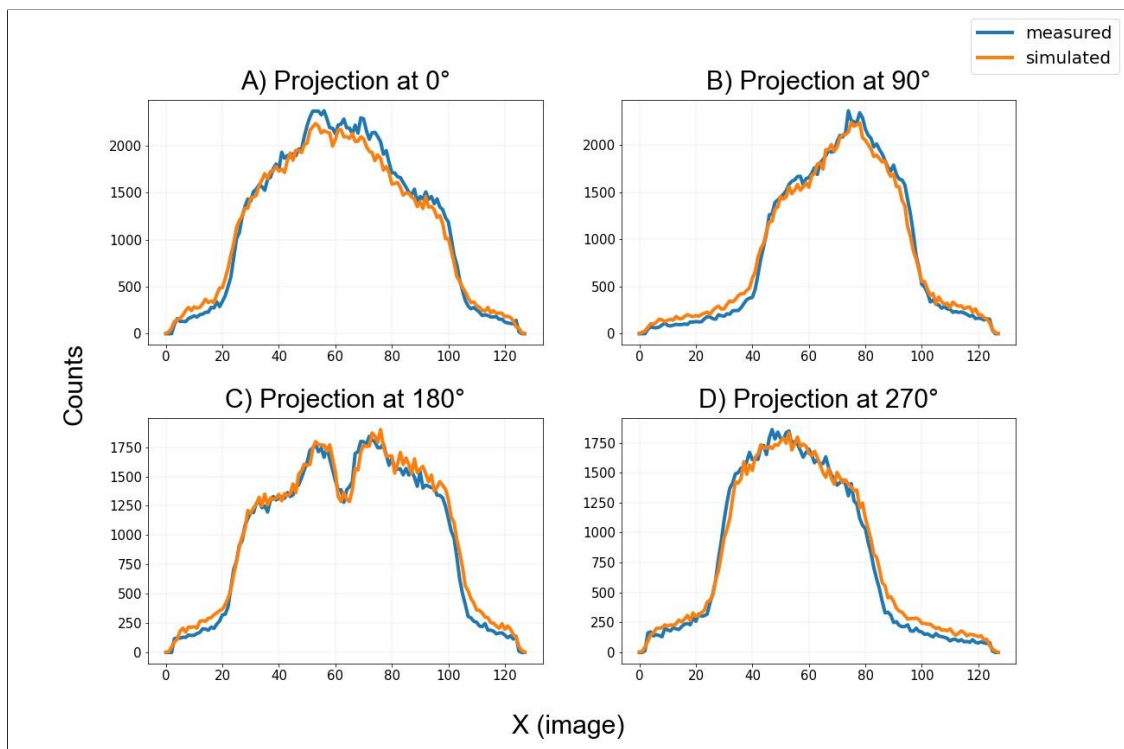


Figure 5.18: Profiles of experimental (blue) and simulated (orange) ^{131}I SPECT projections of the ANT phantom at different projection angles

5.3.2 Simulation time

The simulation time for modelling SPECT projections with the above mentioned activity and number of primaries was computed to be between 2.24 and 3.25 years on a single CPU core running at 2.6 GHz, 16 GB without the use of optimisation variance techniques. However, with access to a regional high-performance computing centre at CALMIP (Villeneuve et al. 2019), it was feasible to perform brute-force simulations in a reasonable time frame of 12 to 16 hours (using 1600 - 1800 cores) . The variation in simulation time is attributable to the availability of cluster cores.

5.3.3 Auto-contouring motion vs. circular camera motion using ^{177}Lu and ^{131}I

As illustrated in Figure 5.19, SPECT projections of the 4-organ phantom were simulated using non-circular camera motion for ^{177}Lu . The spherical tumour in the liver, which is visible in the figure, has the highest activity concentration. The other colored sections indicate the activities in the various organs and the background.

Similarly, SPECT projections for the 4-organ phantom (with ^{177}Lu) and for the ANT phantom (with ^{131}I) considering CO detector motion were also generated. The comparability between the two acquisition modes was then evaluated by drawing profiles for both the phantoms in CO and NCO acquisition mode.

For ^{177}Lu , the maximum and minimum distance between the centre of rotation (COR) to the surface of the detector (say the effective radius) for NCO detector motion are 325 mm and 197 mm, respectively. The maximum NCO effective radius is the same as the fixed radius for CO detector motion. CO and NCO detector motion profiles corresponding to the minimum and maximum effective radius i.e. at 0° and 60° , respectively, are shown in Figure 5.20. As anticipated, when the distance between the COR and detector surface is the same for both modes (i.e. 325 mm), the profiles for CO and NCO are fairly identical. However, with differing effective radii (197 mm for NCO and 325 mm for CO), the maximum difference in counts between CO and NCO profiles was roughly 2.6% (across all projections).

In case of ^{131}I , the minimum and maximum effective radius for NCO detector motion were respectively 271 mm and 434 mm and the fixed radius for CO detector motion was 434 mm. These effective radii of 271 mm and 434 mm represented 0° and 240° detector positions, respectively. When the profiles of NCO and CO detector motion were drawn at these two angles, the average difference in counts

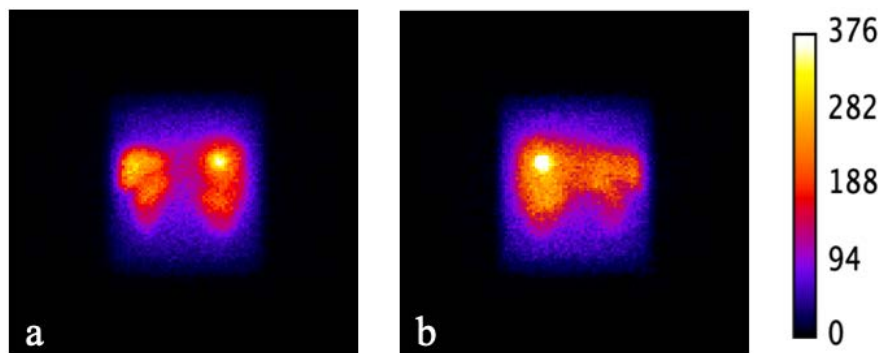


Figure 5.19: Simulated projections for the 4-organ phantom with ^{177}Lu considering auto-contouring motion (for photopeak energy window of 208 keV) at a) 0° and b) 180° detector head position

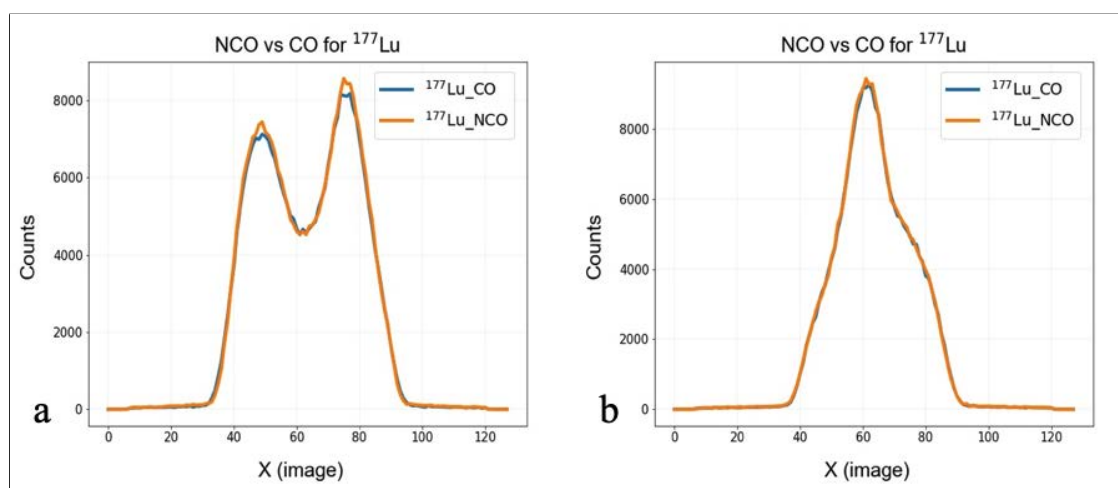


Figure 5.20: Profiles for comparison of circular vs. non-circular SPECT gamma camera motion for ^{177}Lu and the 4-organ MRTD phantom at gamma camera position 0° (a) and 60° (b)

between CO and NCO profiles increased to 13.13% (across all projections). This can also be seen in [Figure 5.21](#).

The gamma index metric was also computed with 2%, 1 pixel DD, DTA criteria for both ^{177}Lu and ^{131}I to highlight the importance of modelling NCO motion. The GIPR ($\gamma < 1$) in the case of ^{177}Lu was 99.85% with γ_{avg} of 0.108. However, a lower GIPR ($\gamma < 1$) of 75.58% and a higher γ_{avg} of 0.6 was obtained for ^{131}I . This demonstrates that the simulated ^{131}I SPECT images vary significantly depending on the acquisition mode considered (CO or NCO).

Knowing that the mean relative difference between counts from profiles for ^{131}I is roughly 13%, the gamma index was recomputed but with 13%, 1 pixel DD (maximum difference in counts), DTA criteria. The GIPR ($\gamma < 1$) increased to 96.79%, while γ_{avg} decreased to 0.35. This means that if a discrepancy in counts

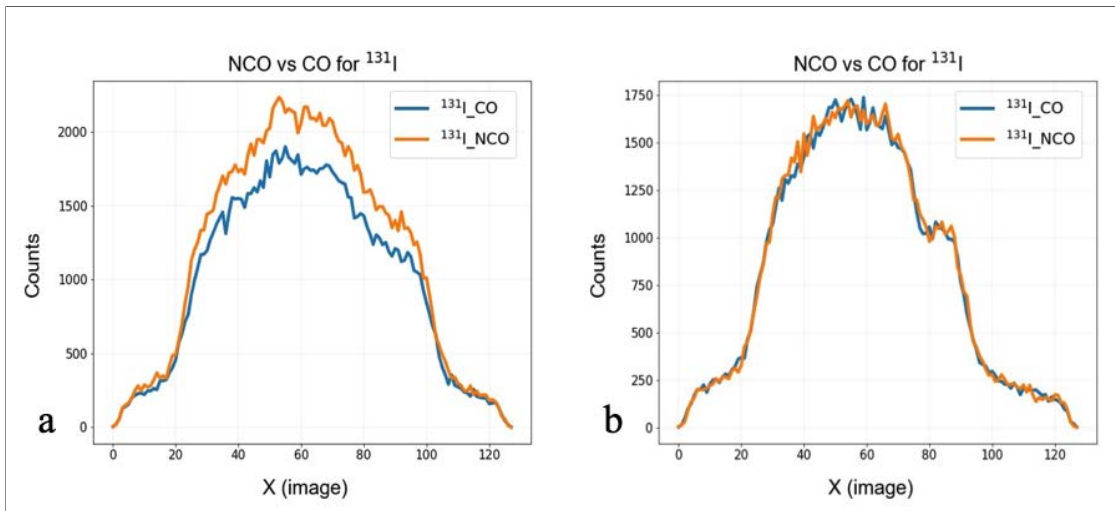


Figure 5.21: Profiles for comparison of circular vs. non-circular SPECT gamma camera motion for ^{131}I and the ANT phantom at gamma camera position 0° (a) and 240° (b)

of 13% between NCO and CO mode profiles are deemed acceptable, then 96.79% of points in the profiles will agree. As a result, it can be concluded that there is at least a 13% difference in counts between CO and NCO gamma camera motion.

5.4 Discussion

This work addresses the new developments in GATE for modelling the step-and-shoot auto-contouring motion of the gamma camera in SPECT imaging. The step-and-shoot data acquisition (static data collection) was chosen in this study since it is often used in clinical settings. Continuous acquisition mode (dynamic data acquisition) has been proposed in the literature (Cao et al. 1996) as a way to improve image quality and, with more research and validation, may be replicated in Geant4/GATE as well.

Information from the experimental DICOM projections were extracted for modelling the NCO detector motion. Since the same tag may not relate to the same property across manufacturers, extracting this for modelling the movement of the gamma camera around an object (phantom or patient) proved quite a stumbling block. For example: detector heads rotating at 3° angular step and producing 60 projections per head have 60 locations per head in terms of radial rotation. However, one manufacturer's 'Radial position' tag may have 60 values whereas the same tag for another manufacturer's DICOM file can contain just one value (which has to be adjusted with another tag containing 60 offset values). As

a result, decoding DICOM headers from a variety of vendors needs meticulous observation and analysis.

This study suggested the use of tessellated meshes rather than voxelized phantom geometry to allow the detector head to approach the phantom model without colliding, hence permitting the modelling of the auto-contouring detector motion. It is often stressed that mesh modelling of individual regions of interest, and hence the whole phantom, is a time-consuming and cumbersome approach when compared to the implementation of voxelized phantoms. However, as computational techniques evolve, this procedure can now be readily automated (using a python script for example). Also, to prevent the degradation of simulation performance, each mesh compartment was optimised in Blender by reducing the number of internal vertices, faces, and edges to ensure rapid geometry initialisation in GATE.

In simulations, the patient table was not modelled, therefore any attenuation caused by the patient table was disregarded. This is believed not to have a substantial impact on the results in this study, but it can be incorporated in the future if required.

The ^{177}Lu simulated energy spectrum was compared to the experimentally measured energy spectrum and was found to be substantially consistent. Following this, simulated ^{177}Lu SPECT projections were validated against experimental projections for the primary energy window only i.e. $208 \text{ keV} \pm 10\%$. Nonetheless, the projections for the scatter energy windows, namely the $178 \text{ keV} \pm 5\%$ and $238 \text{ keV} \pm 5\%$ in [Table 5.1](#), were also simulated to account for scatter during reconstruction (when it is performed in a later stage).

The experimental energy spectrum was not available for ^{131}I SPECT imaging. Despite the fact that a simulated ^{131}I energy spectrum was generated, this work is limited by the absence of a measured spectrum, offering only a limited validation for the primary photopeak energy window ($364 \text{ keV} \pm 10\%$). Yet, the whole energy spectrum comparison for collimated and uncollimated detector heads was published in the work of Autret *et al.* (Autret et al. [2005](#)), from which the gamma camera model was derived.

The simulations used scatter energy window settings of $\pm 5\%$ for ^{177}Lu and $\pm 3\%$ for ^{131}I as given by nuclear medicine departments in line with their local clinical protocols. The simulations were carried out with free computational hours provided by the regional high-performance computing facility CALMIP. This permitted the rapid generation of simulated datasets. However, if necessary, variance reduction methods such as splitting, Russian roulette, or fixed forced detection, all of which are accessible in GATE may be used to speed-up the simulations.

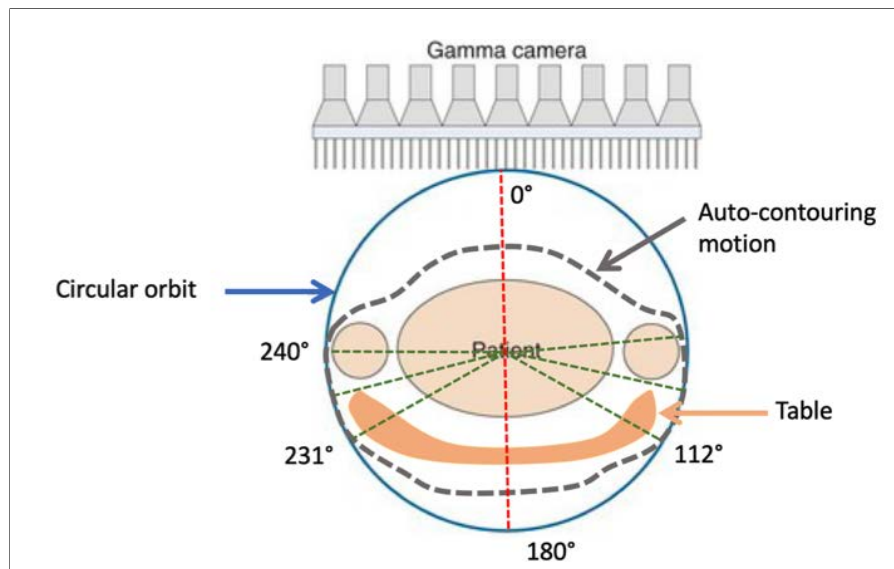


Figure 5.22: Circular (CO) vs non-circular orbits (NCO) acquisitions

To demonstrate the importance of modelling this acquisition mode, a CO versus NCO detector motion comparison was performed for both radionuclides. Activity distribution in the 4-organ phantom was derived from that described by Brodin *et al.* (Brodin *et al.* 2015) and adapted to account for the volume differences between the compartments. Time activity distributions depicting the activity in each organ and tumour as a function of time were then generated as a part of the MRT Dosimetry project. The 40-hour post-injection activity distribution was chosen for simulations since it offered sufficient statistics. The variations in activity in the different regions of interest in the phantom model as a function of time is not expected to have a substantial influence on the results presented.

While the comparison of CO vs NCO acquisition modelling yields equivalent results for ^{177}Lu , substantial discrepancies were observed for ^{131}I . Additionally, the differences observed are more significant for certain angles. This can be explained in Figure 5.22. The blue circle depicts the detector's circular motion, while the dark grey circle represents the auto-contouring orbit. The patient (in this case phantom) is lying on the table.

At angles 231° , 240° , or 112° (in green radii), it is evident that the distance between the centre of rotation and the detector head is nearly identical for CO and NCO, and hence the projections at these angles are very similar. However, for 0° (or 180°) projections, the distance between the centre of rotation and the detector head is largely different for CO and NCO, and hence the projections will be affected by septal penetration. As was mentioned, ^{177}Lu has main photon emission peaks at 113 keV ($\sim 6\%$) and 208 keV ($\sim 10.4\%$), and a maximum gamma energy of 321.3

keV ($\sim 0.2\%$) while ^{131}I emits photons at 364 keV ($\sim 81.7\%$), 637 keV ($\sim 7.2\%$) and 723 keV ($\sim 1.8\%$). While the production of ^{131}I high energy photons is fairly modest, these photons have the potential to penetrate through the collimator septa, thereby degrading the image resolution and thus the image quality (Lewis et al. 1998). This may elucidate why the impact of varying source-detector distance is more pronounced on ^{131}I compared to ^{177}Lu .

5.5 Conclusion

This chapter addresses the modelling of auto-contour step-and-shoot acquisition mode for SPECT imaging in GATE. Two gamma camera models namely the Siemens Symbia T2 (with $\frac{5}{8}$ " crystal thickness and ME collimator for ^{177}Lu imaging) and the GE Discovery 670 (with $\frac{3}{8}$ " crystal thickness and HE collimator for ^{131}I imaging) were validated.

Comparison of counts between CO vs NCO acquisition modes revealed differences of 2.6% in case of ^{177}Lu and roughly 13% for ^{131}I thus emphasising the need of using NCO acquisition mode in simulations particularly for radionuclides featuring high septal penetration. In the context of MRT dosimetry, this means that a possible underestimation of quantified activity by using a CO acquisition mode may have an influence on the determination of the absorbed dose.

SPECT images for three anthropomorphic phantoms were successfully modelled in GATE. The next chapter discusses how to employ auto-contouring motion to simulate SPECT images for more complicated scenarios, such as actual patient geometry.

6

Generation of patient SPECT/CT dataset for DosiTest

Contents

6.1 Introduction	137
6.2 Materials & Methods	138
6.2.1 Gamma camera model	139
6.2.2 Generation of the calibration factor (simulations)	140
6.2.3 Patient model	141
6.2.4 Source modelling	145
6.2.5 Comparison metrics	147
6.2.6 Reconstruction	148
6.3 Results	148
6.3.1 Calibration images	148
6.3.2 Clinical images	149
6.3.3 Computation Time	153
6.3.4 Reconstruction	153
6.4 Discussion	155
6.5 Conclusion	157

6.1 Introduction

The beta phase of DosiTest focused on the generation of two-dimensional planar images of phantoms employing pharmacokinetics data from the literature. Taking a step further, SPECT imaging was modelled for basic anthropomorphic phantoms in GATE considering the step-and-shoot auto-contouring motion. However, one of

the primary challenges in setting up a virtual dosimetry trial is the generation of realistic patient images that can be incorporated into a clinical workstation “as if it were a real patient”. An essential asset for the development of such an approach is the implementation of Monte Carlo modelling to generate clinical images based on a virtual, fully characterised patient.

The generation of simulated *clinical* SPECT images at different time points post activity administration, based on a patient geometry and pharmacokinetics is addressed in this chapter. The clinical situation of Peptide Receptor Radionuclide Therapy (PRRT) using FDA and EMA approved radiopharmaceutical Lutathera[®] (Hennrich et al. 2019) was considered. Further, integration of the simulated projections into a SPECT/CT DICOM header file was carried out to enable the commercial image workstations to access the simulated datasets for reconstruction and dosimetry purposes.

6.2 Materials & Methods

SPECT/CT images of a *patient* undergoing Lutathera[®] treatments were acquired in Tygerberg Hospital, South Africa on a dual-headed Infinia Hawkeye 4 SPECT/CT (GEHC, Milwaukee, USA) with a medium energy (ME) collimator as a part of the coordinated research project (CRP) E2.30.05 “Dosimetry in radiopharmaceutical therapy for personalized patient treatment” initiated by the International Atomic Energy Agency (IAEA). These CT and SPECT projections of the patient were obtained at 1 hour, 4 hour, 24 hour, 48 hour and 96 hour post activity administration (injection) along with SPECT/CT images of a calibration phantom.

The CT system, consisting of four-slice detector arrays, rotates at a speed of 2.6 revolutions per minute. Additionally, a 140 kVp tube voltage, a 2.5 mA tube current, and a helical scan with a fixed pitch of 1.9 mm per rotation were included in the CT scan settings. CT slices with a pixel size of $2.209 \times 2.209 \text{ mm}^2$ and a slice thickness of 10 mm were acquired in a 256×256 matrix.

SPECT projections were acquired in auto-contour mode with a matrix size of 128×128 (pixel size $4.418 \times 4.418 \text{ mm}^2$), 60 projections per head with time per projection of 15 seconds, and a single energy window (photopeak at 208 keV with 20% energy window width i.e. 187.2 keV - 228.8 keV).

To facilitate quantitative analysis of patient images i.e. to convert the counts in patient images to activity, SPECT/CT images of a water-filled IEC NEMA calibration phantom were acquired. This calibration phantom contains six spheres of inner diameter 10 mm, 13 mm, 17 mm, 22 mm, 28 mm and 37 mm. A homogeneous

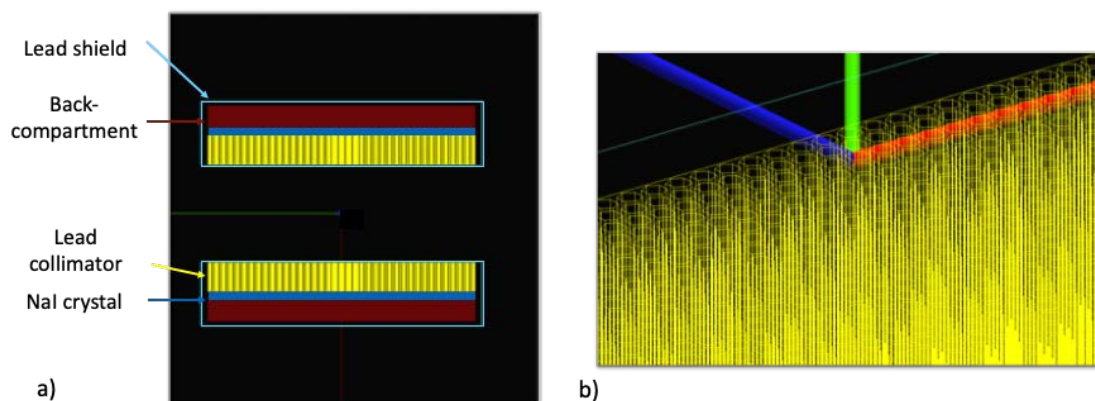


Figure 6.1: a) Schematic of the modelled gamma camera along with its components; b) Zoomed view of the collimators with hexagonal holes

^{177}Lu activity concentration of 250 kBq/ml in the three largest spheres and 32.26 kBq/ml in the phantom (total volume of 10200 ml) was used.

Additionally, reconstruction of both the calibration and patient SPECT/CT images were performed by the same centre on a HermesTM workstation (Hermes Medical Solutions, Stockholm, Sweden) v2.8.0.0 using the OSEM algorithm (3 iterations, 15 subsets) and 0.8 cm Gaussian post-filter. These images were corrected for attenuation using the low dose CT and for scatter using in-built Monte Carlo techniques. A calibration factor of 4.53 ± 0.22 cps/MBq was obtained for the activity quantification in reconstructed clinical patient images.

6.2.1 Gamma camera model

As mentioned in the previous chapter, SPECT image modelling requires the development of a gamma camera model along with the modelling of the patient (or phantom). Individual components of the gamma camera model i.e. the collimator (holes, septa and collimator cover), crystal and the glass back-compartment (light guide, photomultiplier tubes (PMTs) and associated electronics) with a lead shield were derived from the previous work of Autret *et al.* (Autret *et al.* 2005) and Garcia *et al.* (Garcia *et al.* 2015) for the GE Infinia Hawkeye SPECT/CT gamma camera model according to the manufacturer's specifications (shown in Figure 6.1). In this work, a crystal thickness of 9.5 mm ($3/8$ ") NaI crystal in an aluminium cover was simulated with a medium energy lead collimator as was used for acquiring the patient images.

The auto-contouring detector motion was simulated by extracting information from experimental acquisitions such as radial position, acquisition starting angle, and angular step with a python script. These parameters were then transcribed

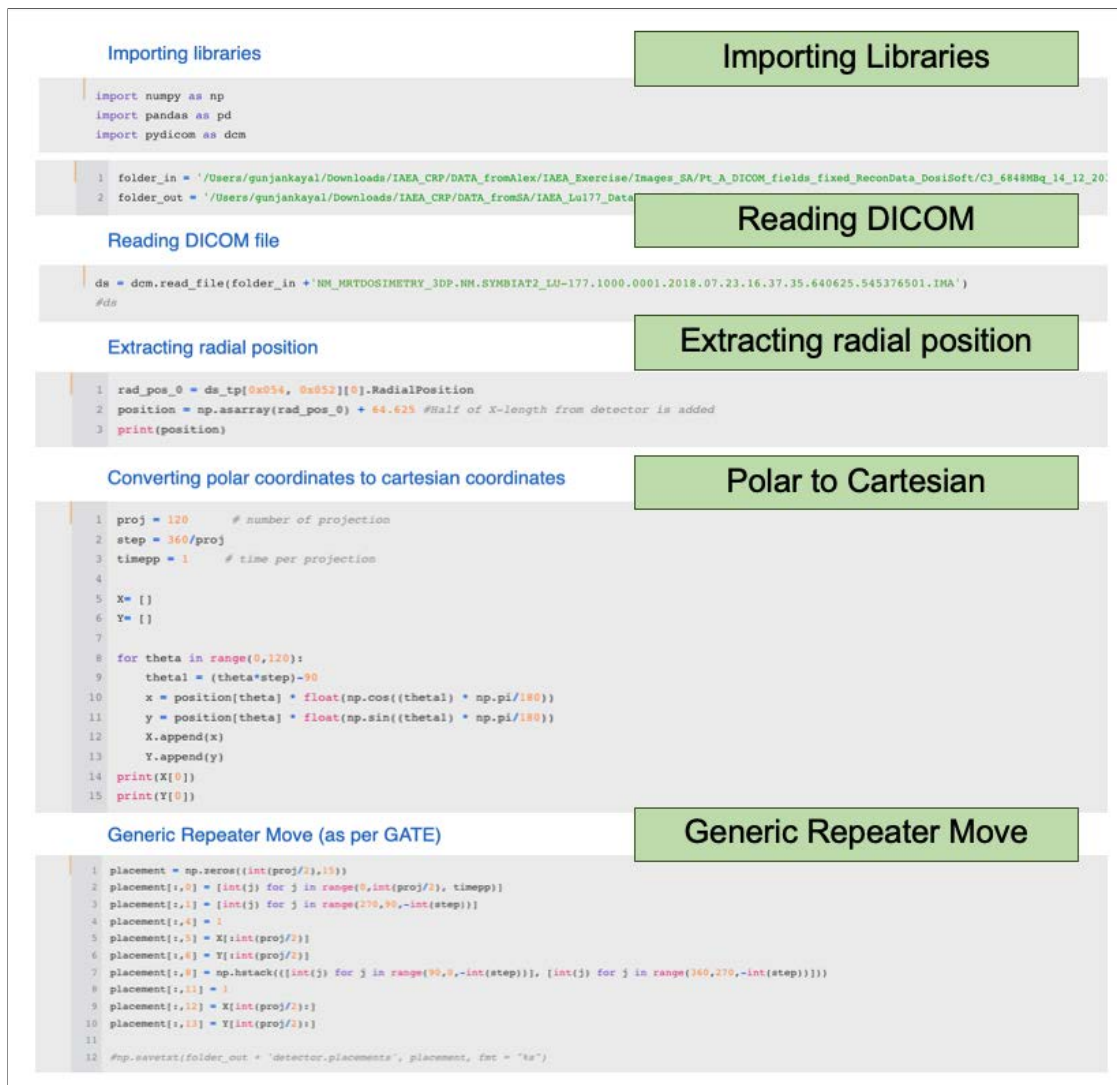


Figure 6.2: A sample of python script for extracting information from experimental DICOM headers for modelling auto-contour detector motion

to an ASCII file compatible with GATE through a sequence of translations and rotations in order to represent the independent movement of each gamma camera head around the patient. A sample of the python script is shown in [Figure 6.2](#).

6.2.2 Generation of the calibration factor (simulations)

Calibration factors determined experimentally cannot be directly used for quantifying activity in the simulated images, since the sensitivity of the gamma camera model is not always equal to that of the real gamma camera. To generate a simulated calibration factor, a virtual calibration study was designed.

The simulation employed a homogeneous NEMA IEC calibration phantom identical to the one used in the experiments but without spherical inserts. The

experimental acquisition parameters were used for simulating SPECT projections (matrix size, pixel size, time per projections, number of projections, energy window settings) in GATE. A uniform activity concentration of 11.12 kBq/ml was used in the entire phantom as was done by Zhao *et al.* (Zhao *et al.* 2018). This corresponded to a total activity of 107.83 MBq in the phantom.

For the derivation of the simulated calibration factor, the counts in the whole field of view (FOV) were considered.

6.2.3 Patient model

6.2.3.1 CRP patient

This work considered the third cycle of treatment where the patient was administered an activity of 6.85 ± 0.34 GBq Lutathera[®] in Tygerberg Hospital, South Africa. The associated acquisition setup and parameters were presented earlier. SPECT/CT images of the patient at various post activity injections (i.e. 1 hour, 4 hours, 24 hours, 48 hours and 96 hours) were acquired. Pre-processing of these images was considered necessary so that it could be used in simulations.

OpenDose3D (Gil *et al.* 2020), a specific clinical dosimetry module based on 3D Slicer (Fedorov *et al.* 2012; Pinter *et al.* 2012) was used for this purpose.

Reconstructed SPECT/ CT images were imported into the image database of OpenDose3D and the experimental calibration factor (4.53 ± 0.22 cps/MBq) along with the acquisition time (1800 seconds) were entered in the software. The CT images were resampled to the resolution of SPECT images using Lanczos interpolation (Meijering *et al.* 1999). Following that, the Hounsfield units (HU) in the CT were rescaled to density using the Schneider CT calibration curve and density matrices (at voxel scale) were generated for each time point.

The SPECT images were registered with the CT at the first time point as reference. Further, the segmentation of different volumes of interest (VOIs) was performed in OpenDose3D using the 3D Slicer Segment Editor tool. The organs including the lungs, bones, left and right kidneys, spleen and liver were contoured on the CT while the tumour present in the liver was segmented on the SPECT image. This process was performed for every time point. These segmentations are shown in Figure 6.3.

Each VOI was labelled further, and the labelled map was exported from the Slicer3D toolkit for use in modelling the patient geometry (Figure 6.4).

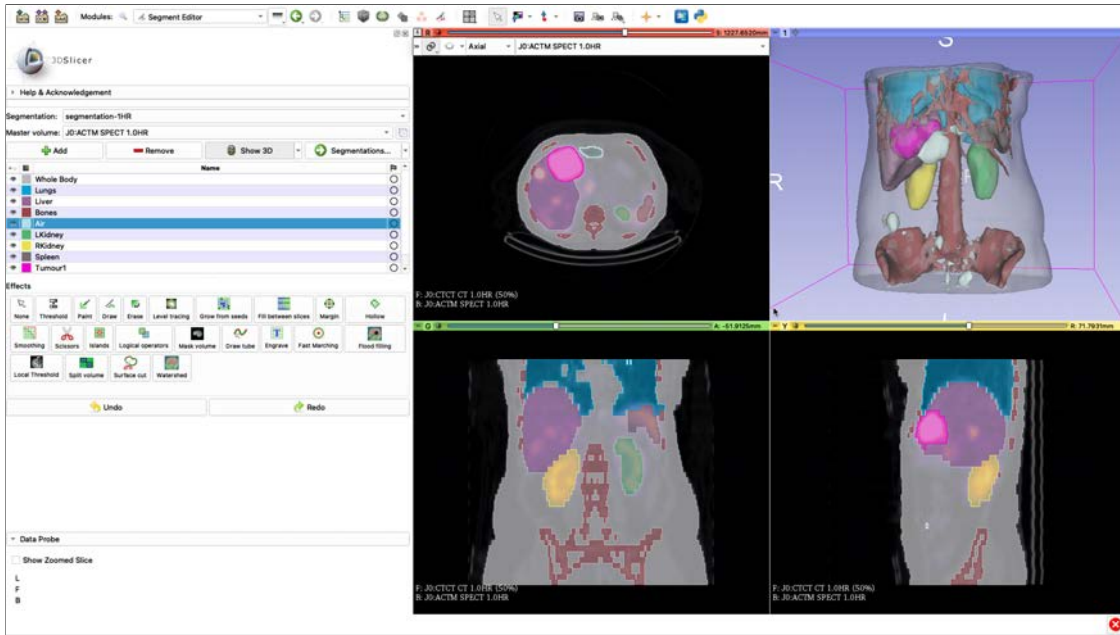


Figure 6.3: Segmentation of different volumes of interest in OpenDose3D Slicer module

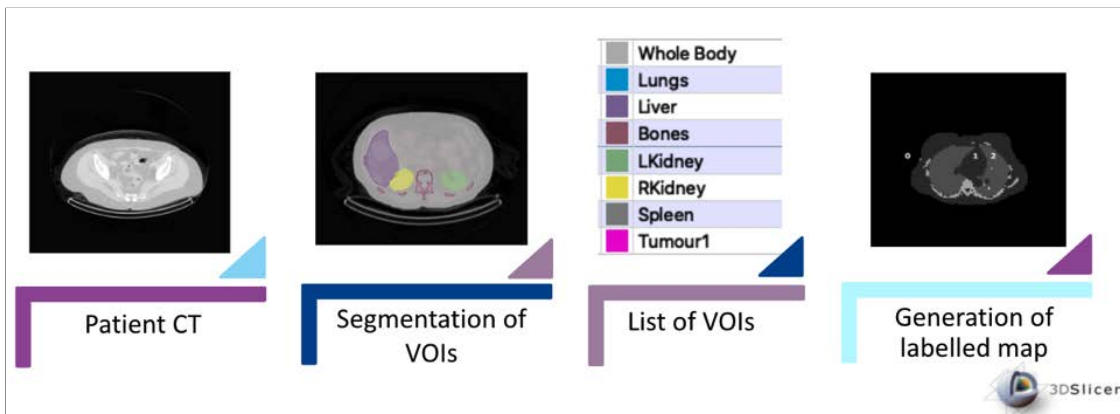


Figure 6.4: Generation of labelled maps from the patient CT images (after registration and segmentation) in OpenDose3D Slicer toolkit

6.2.3.2 From CRP patient to digital patient model

The segmented and labelled patient CT maps were used to characterise the geometry and composition of each volume of interest. The composition of each VOI was determined using the NIST material database, and the average densities were determined using the patient CT (Table 6.1). As a result, the modelled patient geometry is therefore a three-dimensional matrix of size $256 \times 256 \times 40$ ($565.5 \times 565.5 \times 400 \text{ mm}^3$).

As the detector head rotates around the patient geometry to acquire SPECT projections at every 3° angular step and follows the auto-contour mode, it ap-

Volume of interest (VOIs)	Volumes (cm ³)		Densities (g/cm ³)
	Mean	CoV (%)	
Lungs	1524.2	4.41	0.36
Liver	1326.6	2.43	1.02
Bones	1301.7	5.31	1.09
Left Kidney	183.0	5.30	1.05
Right Kidney	194.0	6.55	1.05
Spleen	121.0	3.39	0.99
Tumour	239.0	9.96	1.02
Remainder	19077.0	2.07	0.94

Table 6.1: Volumes and densities of each segmented region of interest in the patient *CoV* is coefficient of variation and is computed as the ratio of standard deviation and mean

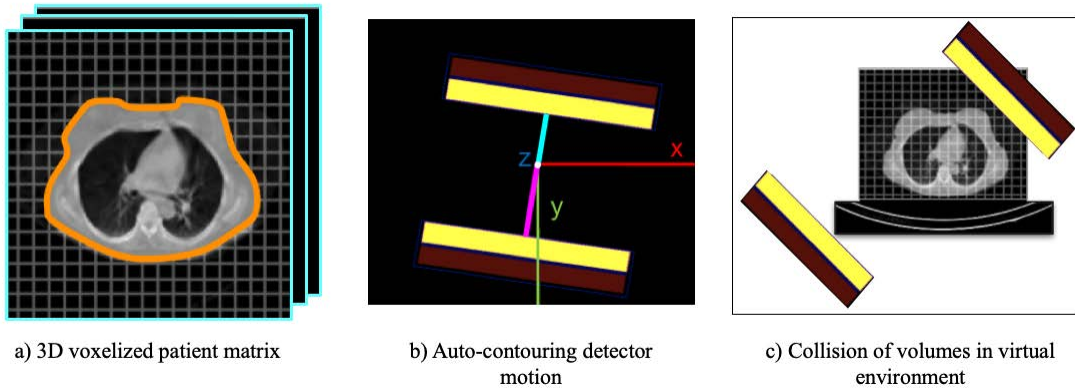


Figure 6.5: Collision of volumes (patient geometry and detector head) in virtual GATE environment

proaches the patient model as close as possible (Figure 6.5).

As previously stated, the concept of tessellation was introduced that enables the extraction of volumes of interest (VOI) in fine triangular meshes, hence obviating the virtual collisions due to the air around the patient. The labelled patient map was then used to extract mesh surfaces for each VOI independently using a dedicated Python script (Figure 6.6).

After refining and simplifying all of the individual meshes in the open source 3D image software Blender (Bücking et al. 2017), stereolithography (.stl) files for each volume were exported. This is shown in Figure 6.7. These mesh surfaces were then imported in GATE and materials were added to each volume in combination with the patient CT data.

Tessellated volumes were extracted for each time point from its associated voxelised labelled CT image in order to account for changes in patient posture, organ volume and position over time and therefore enhanced the realism of the simulated dataset.

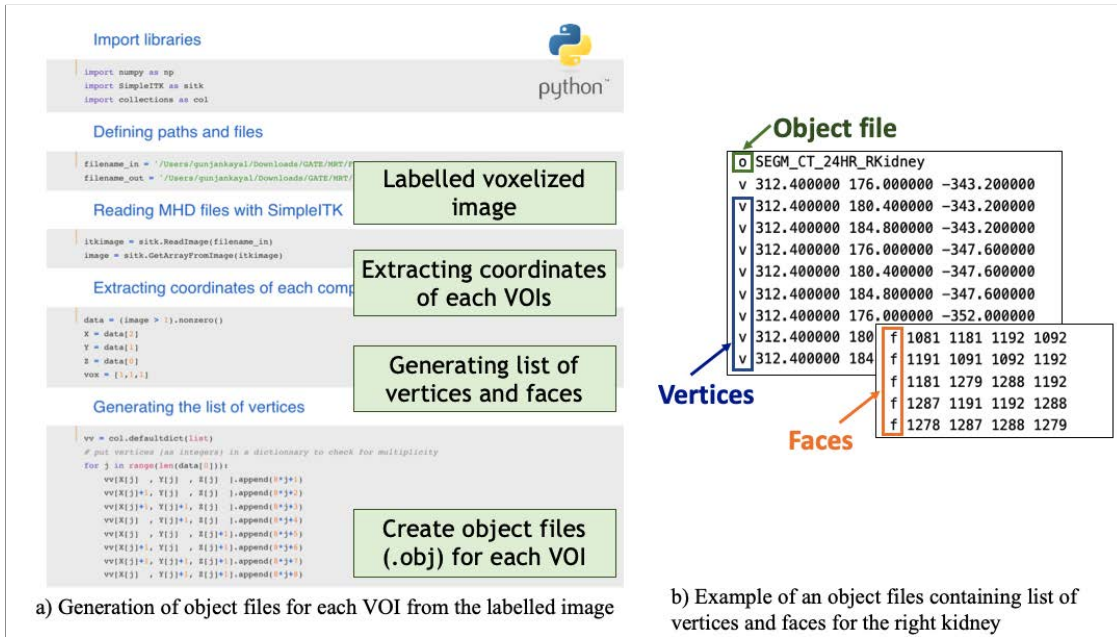


Figure 6.6: Generation of object files (.obj) from the labelled map of the patient geometry with python script

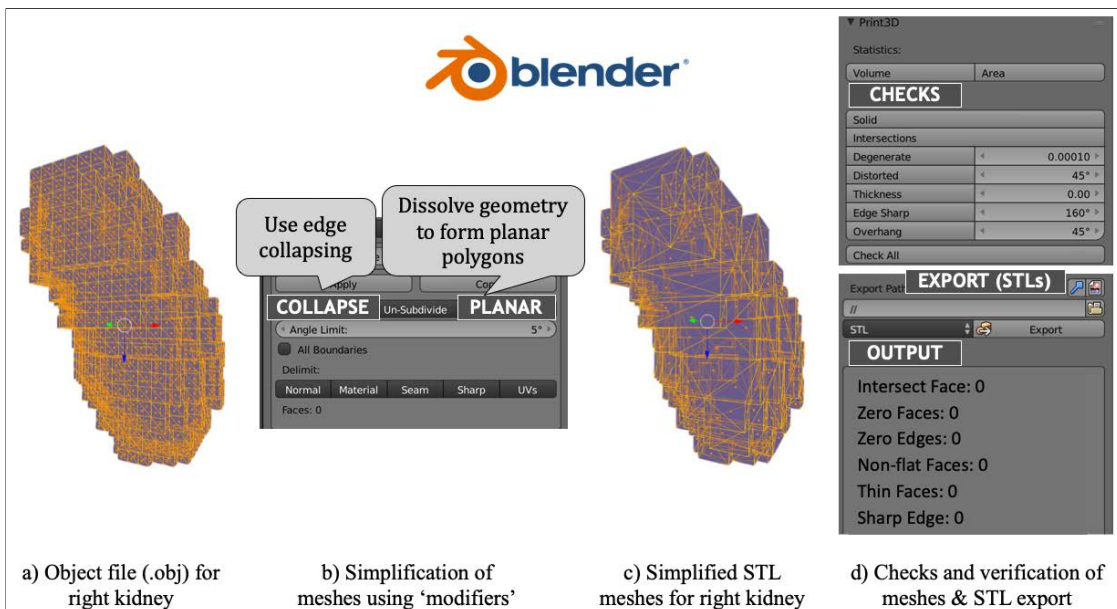


Figure 6.7: Simplification of meshes by reducing the number of vertices, faces and edges in Blender along with implemented checks and STL exportation for use in GATE

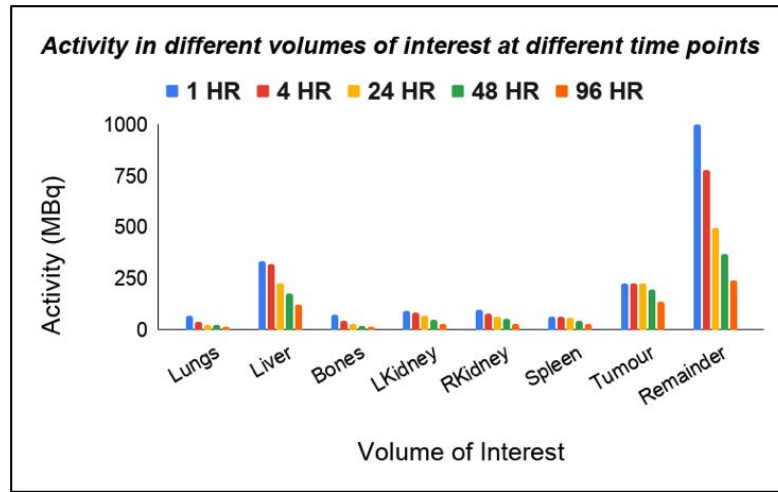


Figure 6.8: Activities (in MBq) at each time point (in hours) for the segmented volumes of interest

6.2.4 Source modelling

6.2.4.1 Definition of the activity map

The counts in the reconstructed experimental SPECT images were rescaled to activity using the calibration factor in OpenDose3D Slicer extension. The activity maps for each time point post activity administration were then extracted from the module after masking the patient volume and assigning zero activity to the regions outside the patient boundary.

The incorporation of calibrated SPECT/CT images in simulations allowed for the preservation of the heterogeneity in the activity distribution in the patient across time points. Next, these heterogeneous activity maps were aligned and oriented to conform to the geometry of the patient in the GATE environment.

The activity in each volume of interest obtained after registration and segmentation of experimental SPECT/CT images is plotted in [Figure 6.8](#) for each time point. The overall activity in the FOV was calculated by aggregating the activities in various VOIs at different time points. The total activities determined at each time point were 1.96, 1.69, 1.19, 0.93, and 0.61 GBq for 1 hour, 4 hours, 24 hours, 48 hours and 96 hours, respectively ([Figure 6.9](#)). This information was then used to determine the total number of primary (or particles) that would be simulated at each time point.

6.2.4.2 Source definition, physics list used for the simulations and output

^{177}Lu decays to ^{177}Hf through beta emissions, which produces a spectrum of gamma radiation with two main energy peaks at 112.9 keV (6.4%) and 208 keV (11%)

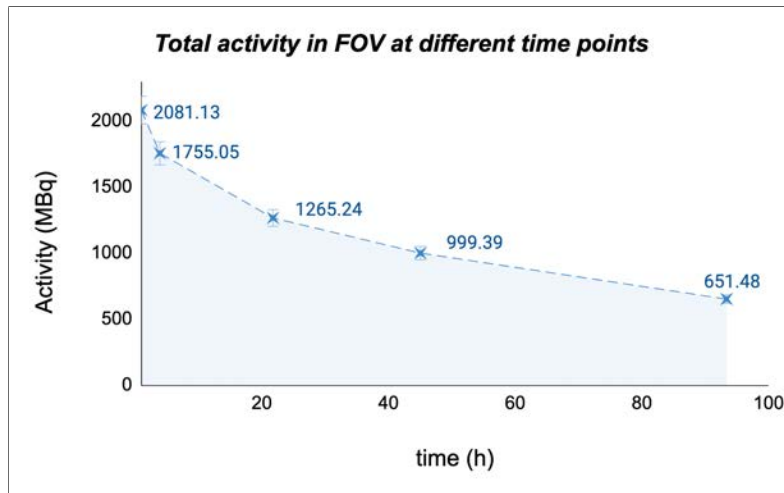


Figure 6.9: Total activities (in MBq) at each time point (in hours) in the whole field of view

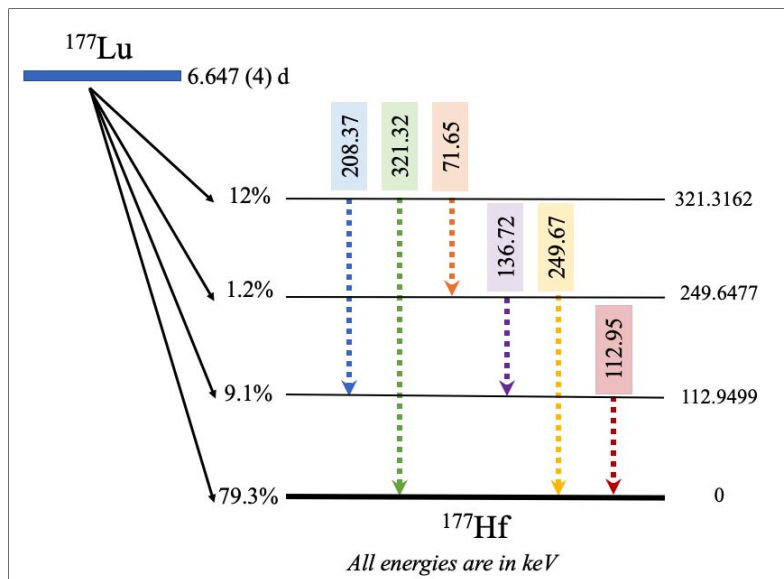


Figure 6.10: ^{177}Lu energy spectrum highlighting all the gamma emissions and their energies (in keV) that were used in simulations

(MIRD 2021). As only gamma photons contribute to image formation, the simulations used 0.18033 emissions per decay (Figure 6.10). The yield for each energy of gamma rays is shown in Table 6.3 (Eckerman et al. 2008).

This necessitated the generation of 17.50×10^9 primaries for the modelling of phantom images (corresponding to the activity of 107.83 MBq in the total phantom). Table 6.3 summarises the activity present in the field of view at each time point for patient images, along with the computed number of primaries (computed by multiplying the total activity, photon yield, number of projections per head and time per projection).

Energy (in keV)	Yield (in %)
71.6	0.15
112.9	6.40
136.7	0.05
208.4	11.00
249.7	0.21
321.3	0.22

Table 6.2: Energy of the gamma photons with their respective yields used in simulations

Time (in h)	Activity (MBq)	# Primaries
1	1960	318 x 10 ⁹
4	1687	274 x 10 ⁹
24	1193	194 x 10 ⁹
48	930	151 x 10 ⁹
96	613	99.6 x 10 ⁹

Table 6.3: Activities at different time points with the corresponding number of primaries used in the simulations

The electromagnetic Geant4 physics list used in GATE was *emstandard_opt3* (Jan et al. 2004; *EM Opt3* n.d.).

Along with the storage of projection files (header files accompanying the raw image format), the simulation output was also stored in ROOT files (Brun et al. 1997) containing information on the particle id, position, direction, and interaction type. This permitted the extraction of SPECT projections for any spectrometric energy windows relevant within the simulated energy range post-simulation.

6.2.5 Comparison metrics

Several criteria were used to compare the simulated SPECT projections to the experimental SPECT projections:

Flattened profiles:

To compare the slices of 2D SPECT projections, flattened 1D profiles on the x-axis were constructed (for each projection) by summing the counts along the y-axis using a Python script.

Gamma Index:

As described in the previous chapter, the gamma index was employed to evaluate images since it takes into account both count differences (Dose Difference

or DD criterion) and spatial differences (Distance to Agreement or DTA criteria) (Wendling et al. 2007; Low 2010).

Gamma index pass rate (GIPR), a pass/fail criterion, characterises a percentage of $\gamma < 1$ (i.e., the points that fall inside the specified DD/DTA acceptance criteria) (Hussein et al. 2013).

6.2.6 Reconstruction

Each clinical workstation utilises DICOM (Digital Imaging and Communications in Medicine) files, which are composed of a raw image (a 3D matrix representing the image) and a header file enclosing a standardised series of tags having information about the patient's demographics, acquisition parameters, image dimensions, matrix size, and colour space, and a host of additional information. The raw image or the pixel intensity data (single or multiple image frames) is attributed to a tag called 'Pixel Data' (7FE0, 0010) in the DICOM file (Bidgood et al. 1997; Varma 2021).

Simulated SPECT projections are raw images in interfile/projection format (.raw or .hdr/.sin extension). These simulated projections were integrated in the 'Pixel Data' tag of the patient DICOM file while keeping the header information regarding patient and acquisition parameters intact. This was done to assess the integration of the simulated projections in vendor-neutral and vendor-specific clinical workstations.

6.3 Results

6.3.1 Calibration images

Simulated SPECT projections were generated for the calibration phantom. Since the activity concentration used between the experiments and simulations was not the same, the comparison of the SPECT projections were not performed. However, both experimental and simulated calibration projections were reconstructed on a Hermes workstation (Hermes Medical Solutions, Sweden) using OSEM algorithm with 5 iterations, 16 subsets, 0.8 cm FWHM Gaussian post filter while correcting for attenuation (using CT), scatter (using in-built Monte Carlo scatter correction) and collimator-detector response (default). Calibration factors were derived using the expression considering the total counts in the whole field of view (Equation 6.1).

$$\text{Calibration factor } (CF) = \frac{\text{Counts}_{VOI}}{\text{Activity } (A_0) \times \text{time}_{acq}} \quad (6.1)$$

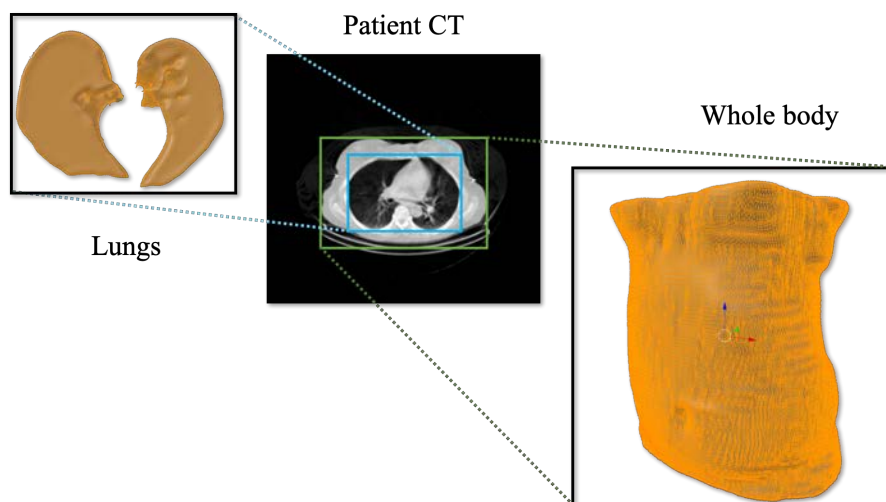


Figure 6.11: Visualisation of different tessellated volumes of interest from the voxelised patient CT

While the experimental calibration factor was 5.33 ± 0.27 cps/MBq, the calibration factor obtained from simulated images was 20% higher and was equal to 6.40 cps/MBq. This is entirely plausible, given that the sensitivity of the virtual gamma camera is often higher than that of the actual gamma camera. This demonstrates the pivotal role of determining a simulation-specific calibration factor in order to quantify the activity in simulated SPECT images. Additionally, this calibration factor ratio, also referred to as the sensitivity ratio, is used to calibrate the simulated patient images for its comparison against the experiments.

6.3.2 Clinical images

6.3.2.1 Simulated patient SPECT projections

Tessellated volumes of interest (such as lungs, remainder of the body, etc.) extracted from the voxelised patient CT image are displayed in [Figure 6.11](#).

The simulated projections of the patient model ([Figure 6.12a](#)) were generated with realistic activities by implementing the auto-contouring detector motion ([Figure 6.12b](#)). This can be seen in the illustrative example ([Figure 6.12c](#)) where the two detector heads are not equidistant from the centre of rotation (the unequal distance in orange and blue).

[Figure 6.13](#) demonstrates the SPECT projections at various gamma camera positions corresponding to the 208 keV photopeak energy. Additionally, projections for the upper and lower scatter energy windows (see [Figure 6.14](#)) were retrieved

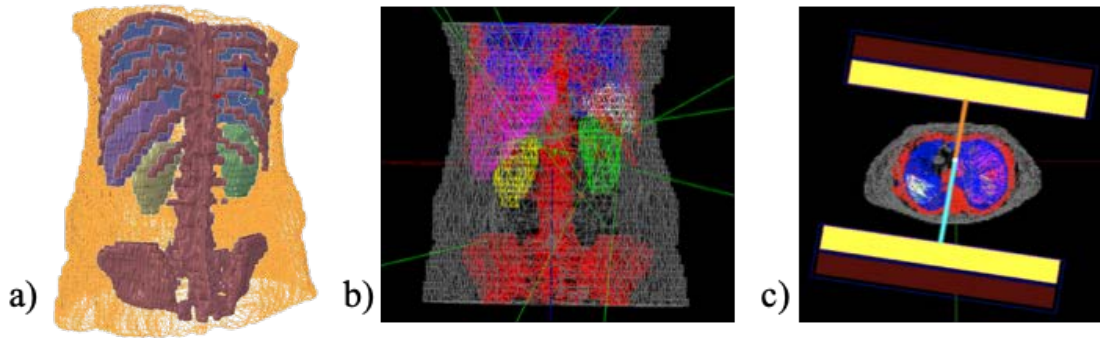


Figure 6.12: Visualisation of the patient mesh model with different volumes of interest - bones (in red), lungs (in blue), liver (in pink), spleen (in white), left and right kidney (in green and yellow respectively along with the remainder of the body (in grey) a) in Blender and b) in GATE. The green lines represent the photons emissions in GATE. c) Visualisation of the auto contouring GE Infinia gamma camera motion in GATE.

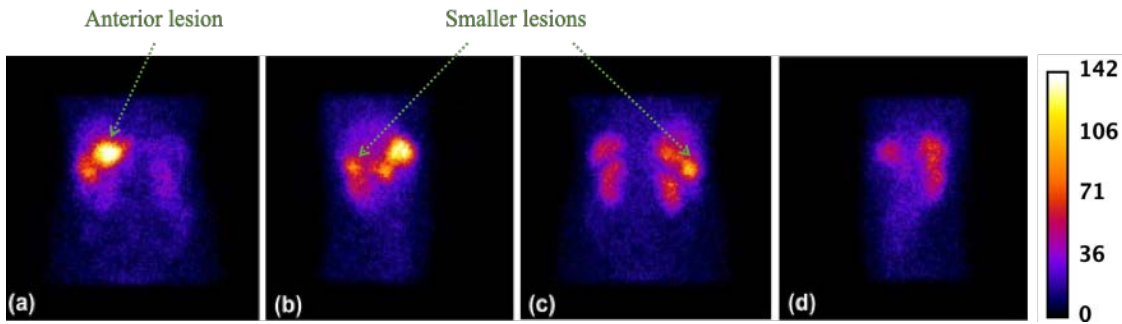


Figure 6.13: Simulated SPECT projections as the gamma camera rotates around the patient model - from left to right the angles are 0° , 90° , 180° , 270° respectively. The tumour in the liver having the highest activity can be seen in the projections along with lower activities in kidneys and spleen (corresponding to 1-hour post injection)

from the ROOT output and used to correct for scatter during reconstruction. Scatter images are shown in [Figure 6.15](#) (a and c).

6.3.2.2 Comparison of simulated and experimental patient images

The modelled SPECT projections were compared to the experimental patient projections. As seen in [Figure 6.16](#), the simulated projections closely reflect the experimental images.

To compare these images acquired at various gamma camera positions, flattened 1D profiles were constructed ([Figure 6.17](#)). These profiles between experiments and simulations exhibit the accurate placement and alignment of the patient and gamma camera with regard to the centre of rotation. This dataset was compared using a gamma index with a 2% - 1 pixel criterion. The gamma index passing rate (GIPR) was 95.5% with an γ_{avg} of 0.35 (for images obtained one hour post

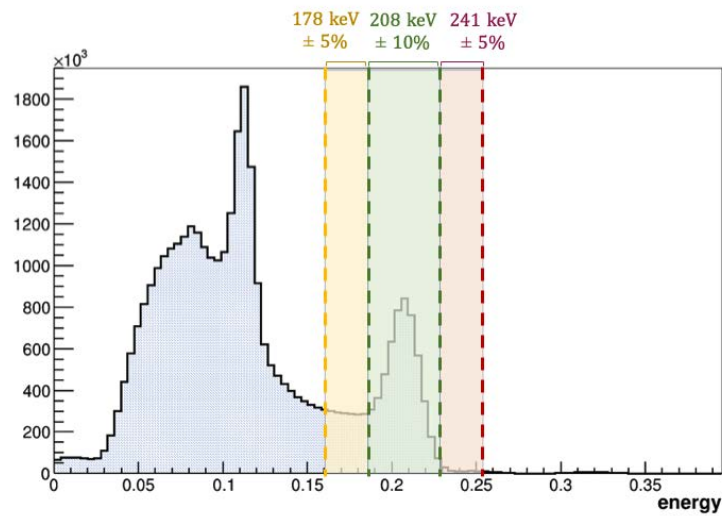


Figure 6.14: Simulated energy spectrum of ^{177}Lu . The three energy windows (yellow, green and orange) correspond to upper scatter of $178 \text{ keV} \pm 5\%$, photopeak of $208 \text{ keV} \pm 10\%$ and upper scatter of $241 \text{ keV} \pm 5\%$ respectively (corresponding to 1-hour post injection)

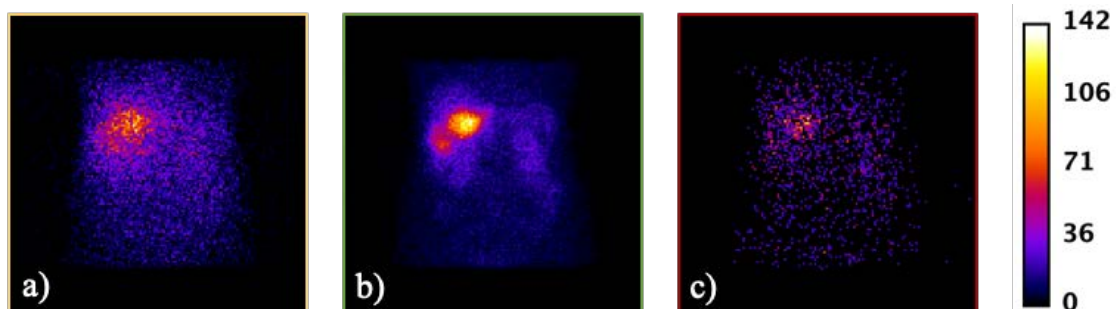


Figure 6.15: Simulated SPECT projections at 0° detector position for three energy windows: a) low scatter ($178 \text{ keV} \pm 5\%$), b) photopeak ($208 \text{ keV} \pm 10\%$) and c) upper scatter energy ($241 \text{ keV} \pm 5\%$) windows (corresponding to 1-hour post injection)

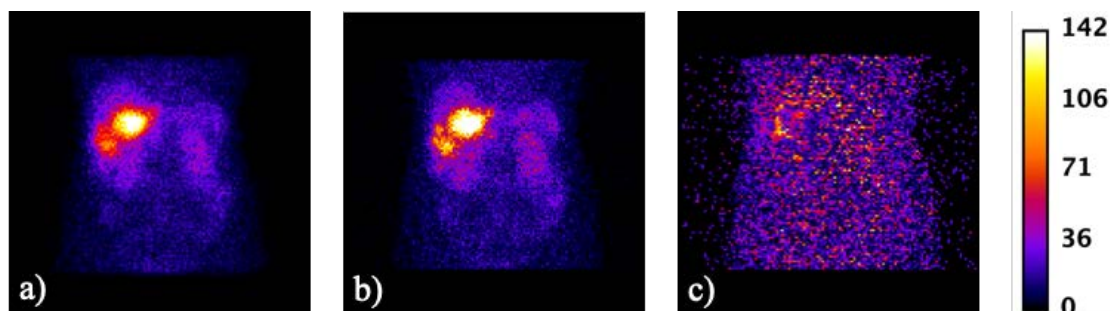


Figure 6.16: Simulated (a) and clinical (b) patient SPECT projections at 0° detector position corresponding to 1-hour post injection along with the gamma index map (with gamma index ranging from 0 to 0.1) (c)

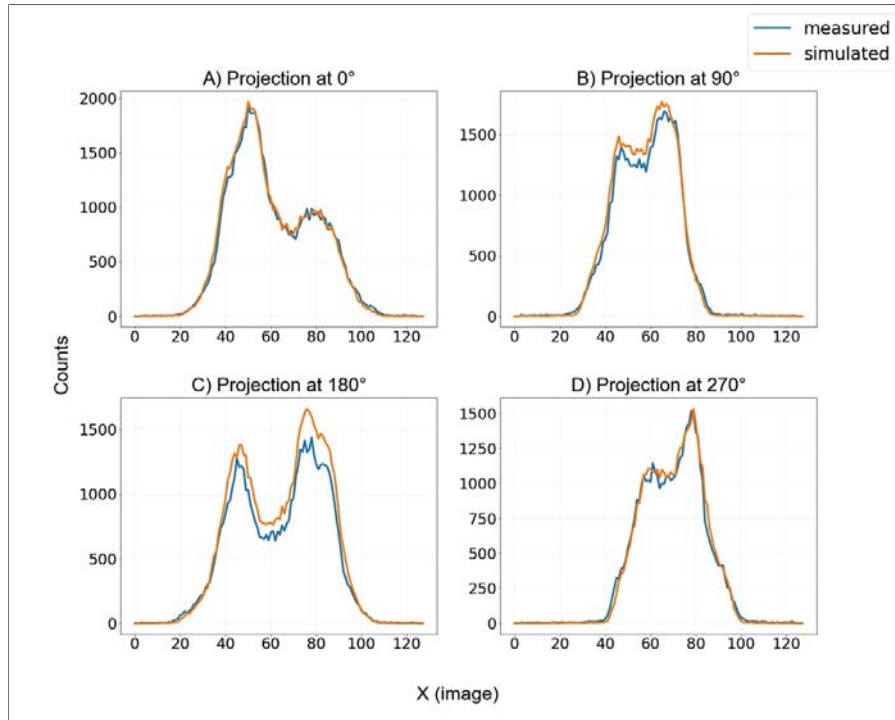


Figure 6.17: Flattened profiles on x-axis for comparison of clinical and simulated images at different projection angles - (A) 0° , (B) 90° , (C) 180° , (D) 270°

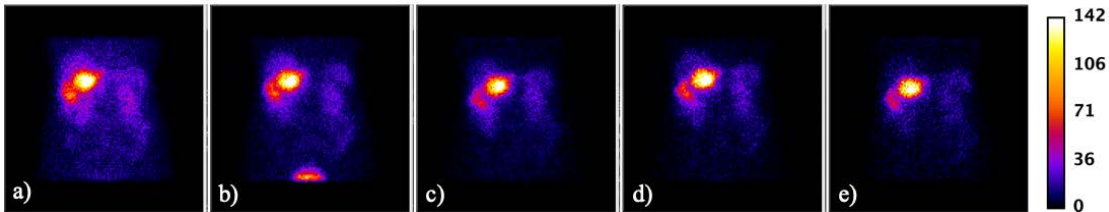


Figure 6.18: Simulated patient SPECT projections at different time points post injection (p.i.): a) 1 hour p.i., b) 4 hours p.i., c) 24 hours p.i., d) 48 hours p.i. and e) 96 hours p.i.

injection), showing a high degree of similarity between experimental and simulated images. At one hour post injection, the difference in total counts between experimental and simulated patient images was around 2% .

Additionally, simulated SPECT patient projections were generated for the subsequent time points (4h, 24h, 48h, and 96h post injection), allowing for the modelling of activity distribution inside the patient over time, the assessment of cumulated activity, and the computation of absorbed dose. The simulated SPECT projections at these time points are shown in [Figure 6.18](#).

These simulated projections at 4h, 24h, 48h, and 96h post-injection were also compared to the corresponding clinically obtained patient images using the same gamma index metric as for the 1-hour post-injection projections. The gamma

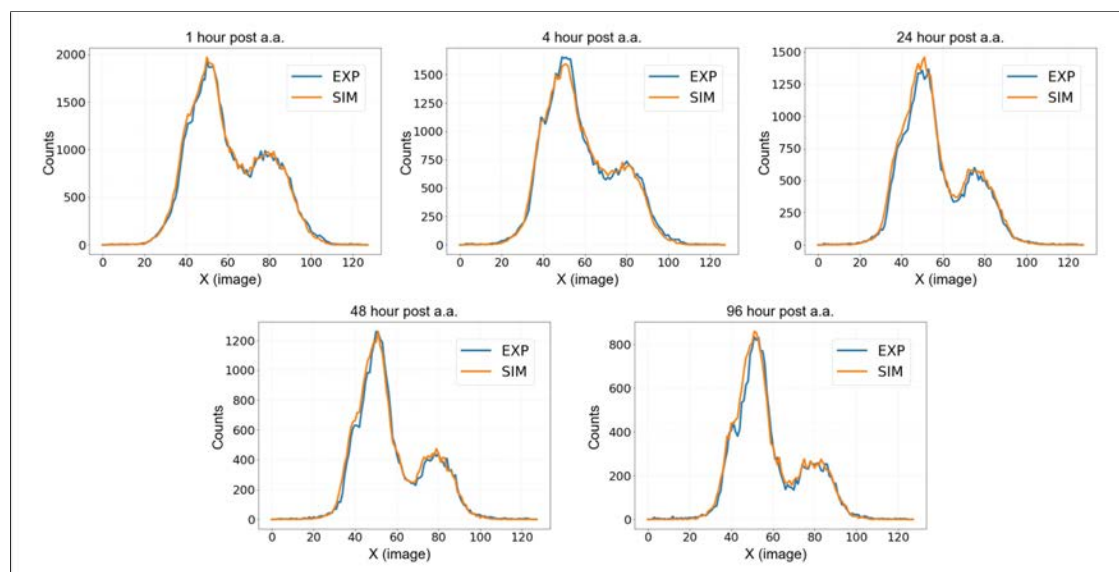


Figure 6.19: Comparison of clinical vs simulated SPECT projections at different time points post activity administration (a.a.) with flattened 1D profiles

index passing rate was between 95 and 98 percent, and the average gamma was between 0.28 and 0.35 across multiple time points, showing a striking similarity among images. Between different time points, the difference in total counts between experiments and simulations was less than 6%. The flattened profiles for each time point post injection were also compared between experiments and simulations and are shown for 0° detector position in [Figure 6.19](#).

6.3.3 Computation Time

Simulation of SPECT projections with realistic activities in a therapeutic context (1-hour post injection) took 11.5 hours to compute using 3560 CPU cores at the regional high-performance computing (HPC) centre CALMIP (Villeneuve et al. [2019](#)) (instead of 9.59 years with a single CPU core with 2.6GHz, 16 GB), thus making it feasible to generate simulated SPECT images for the virtual multicentric clinical dosimetry trial.

6.3.4 Reconstruction

6.3.4.1 Reconstruction with HermesTM

The simulated SPECT images included in experimental Infinia patient DICOM headers were successfully processed in the vendor-neutral HermesTM workstation. Together with the experimental patient CT, these simulated SPECT images (.dcm)

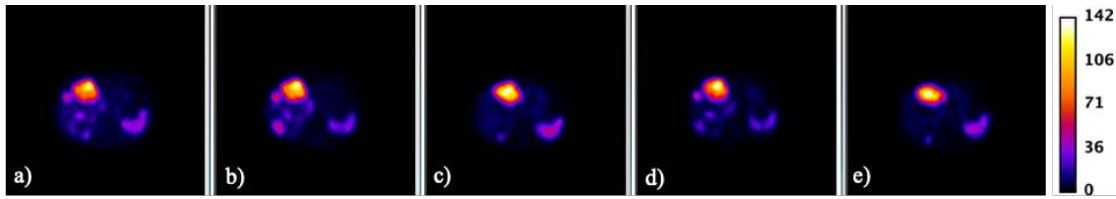


Figure 6.20: Reconstructed simulated SPECT images on Hermes at different time points post injection (p.i.) - a) 1 hour p.i., b) 4 hours p.i., c) 24 hours p.i., d) 48 hours p.i. and e) 96 hours p.i.

were employed as an input to the Hybrid dosimetry moduleTM (HDM) from HERMES Medical Solutions (v1.0). The dataset was reconstructed with HybridRecon-Oncology v1.3 DICOM (HROD) using a 208 keV main ^{177}Lu spectrometric energy window. All images were reconstructed using a 5-iteration OSEM reconstruction algorithm with 16 subsets and a Gaussian post filter set at 0.8 cm. Corrections were made, including those for attenuation based on CT images, scatter using in-built Monte Carlo scatter corrections, and collimator-detector response with default settings. At the time of this study, the workstation lacked the SPECT standard uptake value (SUV) option (Mora-Ramirez et al. 2020), which Hermes states is critical for comparing their reconstructed results to those of other manufacturers.

The matrix size of all SPECT reconstructed images is 128×128 with 120 slices and the voxel size is $4.42 \times 4.42 \times 4.42 \text{ mm}^3$. Figure 6.20 illustrates the reconstructed simulated SPECT images obtained at various time points after injection.

6.3.4.2 Reconstruction with XelerisTM

Simulated SPECT projections were successfully accepted by the vendor-specific Xeleris workstation for all time points post injection when incorporated into the experimental Infinia patient DICOM headers.

The reconstruction of the simulated SPECT images was performed at ICO, Nantes, France, using XelerisTM software (v3.0513) from GE Healthcare. The OSEM algorithm was used to reconstruct the images (5 iterations, 16 subsets). Correcting for attenuation was attained using suitable attenuation maps produced from the CT dataset. To account for the TEW scatter correction, projections corresponding to the lower scatter of ^{177}Lu i.e. $178 \text{ keV} \pm 5\%$ and an upper scatter of ^{177}Lu i.e. $241 \text{ keV} \pm 5\%$ were generated from the root file as discussed before and a subtractive method was applied (Ljungberg, Celler, et al. 2016).

The matrix size of all SPECT reconstructed images is 128×128 with 120 slices and the voxel size is $4.42 \times 4.42 \times 4.42 \text{ mm}^3$. Figure 6.21 depicts the reconstructed SPECT images in Xeleris at various time points post injection.

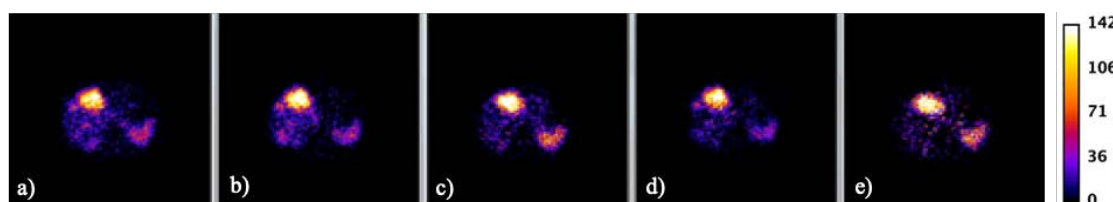


Figure 6.21: Reconstructed simulated SPECT images on Xeleris at different time points post injection (p.i.) - a) 1 hour p.i., b) 4 hours p.i., c) 24 hours p.i., d) 48 hours p.i. and e) 96 hours p.i.

6.4 Discussion

This study demonstrates how realistic patient SPECT projections may be modelled in GATE exploiting the previously developed auto-contouring detector motion. Along with the patient image modelling, calibration phantom images were also simulated in order to quantify the activity distributions in patients. Often, virtual or simulated gamma cameras have a greater sensitivity than real gamma cameras. This is because a modelled gamma camera (by Monte Carlo simulation) is typically more accurate than a real gamma camera, since not everything present in a real camera can or is addressed in modelling. Moreover, additional losses may occur inside a real camera owing to elements such as the gel linking the PMT and crystal that are camera- and time-dependent and hence impossible to model. Thus, it is critical to generate a calibration factor that corresponds to simulations in order to accurately quantify activity in simulated patient images.

Following that, patient images were simulated at various time points post injection using tessellated mesh models for patient geometry and heterogeneous activity maps derived from actual patient pharmacokinetics. The use of tessellated mesh to avoid collision of the patient model with detector head in the virtual GATE environment requires segmentation of the patient geometry, a user-dependent procedure to obtain individual mesh compartments. This is opposed to the usage of phantoms, which have a well-defined shape and are identical across studies and operators. Additionally, it limits the consideration of heterogeneous density distributions within a specific volume of interest. This may not pose a problem for critical organs that are soft tissue such as the kidneys or spleen, but it may have a profound impact on the activity quantification of bone and/or lung (where the density is variable). On the other hand, activity maps generated from actual patient pharmacokinetics were used to incorporate voxel-by-voxel heterogeneity in the activity distribution within the patient. This enabled the generation of clinically relevant patient SPECT images with realistic therapeutic activities.

Simulated SPECT projections were validated against those from experiments and were found to be in good agreement. While it is widely known that simulating SPECT imaging is computationally extensive, brute force simulations were possible using the freely accessible CALMIP resources.

The simulated projections were embedded in the DICOM header of the clinical images to ensure that they were recognised by the workstations. It is crucial to emphasise that DICOM tags can vary substantially between manufacturers. Therefore, this step can be relatively challenging and will require comprehensive knowledge to decipher and decode the DICOM tags appropriately.

Then, reconstruction of these simulated SPECT projections was performed on two workstations: a vendor-neutral Hermes workstation and a vendor-specific GE Xeleris workstation. Images reconstructed on Xeleris were noisier compared to those reconstructed on Hermes. This might be attributed to the fact that the reconstruction parameters were not identical between workstations.

Additionally, Hermes implements scatter correction using a Monte Carlo method with the primary energy window, but Xeleris employs a TEW subtractive technique with three energy windows, contributing to noise generation. Also, Xeleris was unable to account for the resolution recovery correction, which consequently led to the observed disparities in the reconstructed images. While the purpose of this study was not to compare the reconstruction methods implemented on different workstations, assessing the simulated projections on multiple workstations offered useful insights on how these toolkits are programmed. This is a huge asset for the DosiTest project, since the participating centres will conduct the same steps by harnessing locally available resources.

It should be emphasised that for a particular workstation, it is recommended to reconstruct both the experimental/simulated calibration phantom images and the patient experimental/simulated SPECT projections in the same manner. The calibration factor should then be determined for each workstation and used in conjunction with patient images to quantify activities in various volumes of interest. Eventually, activity quantification should yield comparable results across workstations. This is being studied further as part of the DosiTest project.

Yet, it should be underlined that the GATE produced simulated SPECT projections was successfully reconstructed in two commercial workstations (Hermes and Xeleris) after appropriate incorporation of the simulated image data into the DICOM headers supported by these workstations.

6.5 Conclusion

This chapter outlines the generation of realistic simulation of ^{177}Lu clinical datasets (patient SPECT images) with realistic activities in a therapeutic context. Additionally, it demonstrates how the simulated datasets can be integrated into clinical DICOM headers so that they can be accepted by clinical workstations. Further research is required to understand if and how simulated images can be generated for all gamma camera manufacturers (GE, Siemens, Philips or Mediso). At this point, it is unclear if the problem can be handled by transcoding the simulated data into another proprietary format or whether each gamma camera requires its own model. Nonetheless, the goal is to generate a series of modelled images (planar, SPECT/CT), at various time points, with various gamma cameras, for the *same* virtual patient and pharmacokinetics, enabling comparison of various dosimetric techniques.

7

Proof-of-concept of DosiTest, a virtual multicentric clinical trial for assessing uncertainties in Molecular Radiotherapy dosimetry

Contents

7.1 Introduction	159
7.2 Materials & Methods	161
7.2.1 Clinical dataset	161
7.2.2 Reference dosimetry generation	163
7.2.3 Monte Carlo based image generation	164
7.2.4 Validation procedure	168
7.3 Results	170
7.3.1 Reference dosimetry generation	170
7.3.2 Monte Carlo based image generation	170
7.3.3 Comparison of activities, absorbed dose rates and absorbed doses	173
7.4 Discussion	176
7.5 Conclusion	179

7.1 Introduction

The DosiTest project [Home - Dositest 2021](#) was initiated with the objective to assess the uncertainty associated with each phase of the clinical dosimetry workflow and

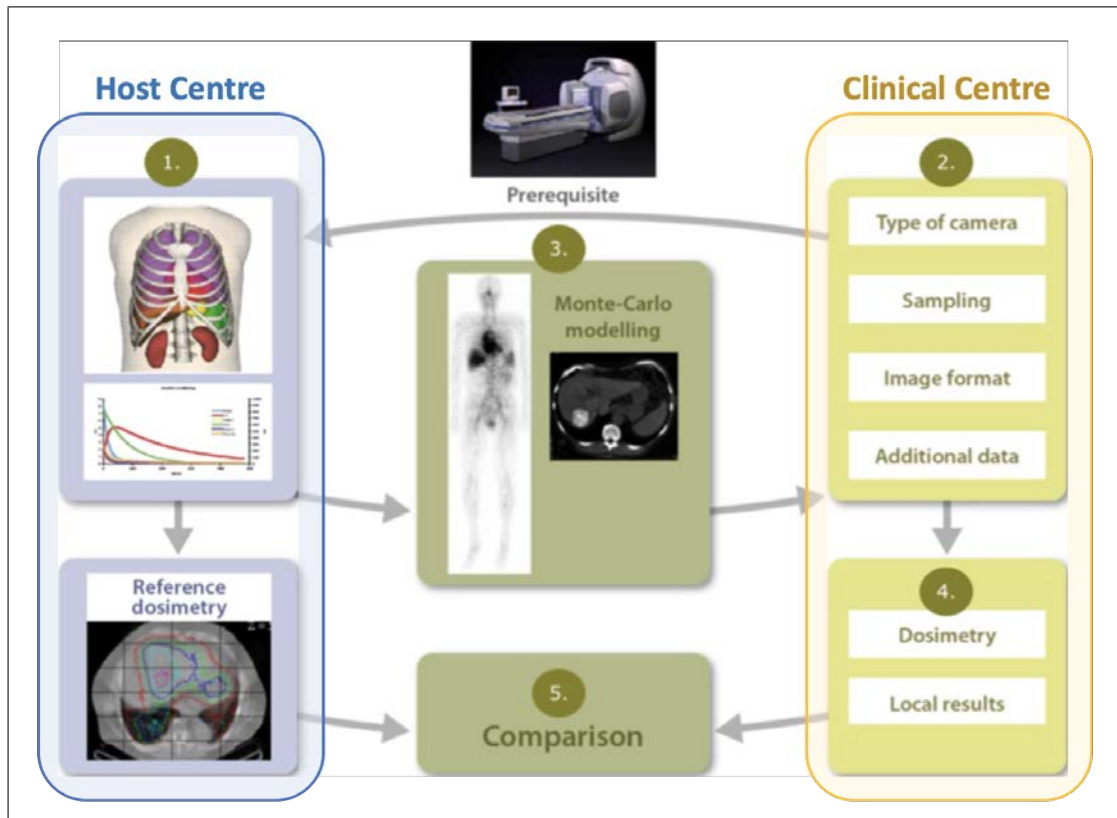


Figure 7.1: Schematic overview of the DosiTest project (www.dositest.org): (1) A reference patient geometry is used, with a reference activity distribution profile that allows generating direct reference dosimetry by the Host centre. (2) Each participating Clinical centre sends the list and structure of the data they would need to perform clinical dosimetry locally: number and times of acquisitions, acquisition mode, etc. (3) The gamma camera is modelled (and validated) and scintigraphic images and additional data are generated according to the local protocol, in order to obtain a dataset equivalent to what would have been acquired locally on a real patient. (4) The Clinical centre then performs image quantification and activity determination based on the simulated scintigraphic images, and the dosimetric study is performed using local resources. (5) The results are then benchmarked against the reference dosimetry.

to propose standardised approaches to clinical dosimetry in molecular radiotherapy. The overview of DosiTest was already presented in Chapter 2. Its description is given again here (Figure 7.1) to improve readability. The fundamental idea of this project is to circulate a virtual patient dataset across participating centres for them to perform dosimetry on this simulated dataset according to their local dosimetry protocols, as if it was a patient enrolled in their clinical centre. The participating centres and the centre providing the simulated dataset are referred to as the Clinical centre and Host centre, respectively throughout the text.

As outlined in Chapter 1, although it was technically doable to replicate a complex patient dataset, a significant barrier was the generation of realistic images

that could be read by a clinical workstation “as if it were a real patient” (due to proprietary tags in the image header). In a similar clinical setting, we recently provided a comprehensive overview of full SPECT/CT image generation (Kayal, Chauvin, Vergara-Gil, et al. 2021) for a patient model.

The current work illustrates the proof-of-concept of the overall DosiTest project, with a demonstrative example starting a virtual patient derived for a clinical dataset and associated activity distribution, the determination of the reference dosimetry and the generation of 3D patient SPECT/CT images tailored to image-based dosimetry. An evaluation of the goodness of the various modelling steps was performed.

7.2 Materials & Methods

7.2.1 Clinical dataset

The reference dataset stemmed from the dosimetric study of the patient receiving an activity of 6.85 ± 0.34 GBq of Lutathera[®] (¹⁷⁷Lu-DOTATATE) during the third therapy cycle in the Tygerberg Hospital (South Africa), as part of an IAEA-Coordinated Research Project (E23005) on “Dosimetry in Radiopharmaceutical therapy for personalised patient treatment” (presented in chapters 3 and 4).

The patient SPECT/CT image acquisition parameters are stated in Table 7.1.

Additionally, SPECT/CT images were acquired of a homogeneously water-filled NEMA-IEC calibration phantom. The ¹⁷⁷Lu activity concentration in the background was 32.26 kBq/ml and 250 kBq/ml in the three spheres (22 mm, 28 mm and 37 mm).

On a Hermes[™] workstation (Hermes Medical Solutions, Stockholm, Sweden), SPECT/CT images (both patient and phantom) were reconstructed using the OSEM algorithm (5 iterations, 16 subsets, 0.8 cm FWHM 3D Gaussian post filter) and corrections were performed (CT-based attenuation correction, built-in Monte Carlo-based scatter correction and default collimator-detector response). The matrix size of the reconstructed SPECT/CT images was $128 \times 128 \times 90$ ($4.418 \times 4.418 \times 4.418$ mm³). All reconstructions discussed in this article were performed using the aforementioned software and parameters. The experimental calibration images yielded a calibration factor of 5.33 ± 0.27 cps/MBq, which enabled the generation of activity-indexed images.

Gamma camera	
Model	Dual-headed GE Infinia Hawkeye 4 (GEHC, Milwaukee, USA)
Collimator type	Medium energy (ME)
Crystal information	9.5 mm (3/8") NaI crystal
Detector orbit	Auto-contour mode
Acquisition parameters	
Matrix (and pixel) size	128 × 128 (4.418 × 4.418 mm ²)
Time per projection	15 seconds
Time per projection	60
Energy window	208 keV ± 10% (187.2 - 228.2 keV)
CT system	
Technology	Four-slice detector arrays
Gantry rotation speed	2.6 revolutions per minute (rpm)
Pitch	1.9 mm per revolution
X-ray tube voltage and current	140 kVp and 2.5 mA
Matrix (pixel) size	256 × 256 (2.209 × 2.209 mm ²)
Slice thickness	10 mm

Table 7.1: SPECT/CT gamma camera characteristics and acquisition parameters

7.2.1.1 Patient model

A digital patient model was derived from the clinical dataset. Density and activity distributions were defined voxel by voxel, for each acquisition time point.

7.2.1.2 Description of patient geometry

The 3D geometry map was obtained by resampling the CT to the SPECT resolution using Lanczos interpolation (Meijering et al. 1999) and further rescaling to obtain density matrices. This was done for the CTs at all time points using OpenDose3D (Gil et al. 2020), a clinical dosimetry module developed by our team within the 3D Slicer environment (Pinter et al. 2012). The patient geometry model therefore consisted in a matrix of 128 × 128 × 90 with voxel dimensions of 4.418 × 4.418 × 4.418 mm³. This served as input for Monte Carlo modelling and will be referred to as ‘*geometry input*’.

7.2.1.3 Description of activity distribution

SPECT/CT images were acquired at 1 hour, 4 hours, 24 hours, 48 hours and 96 hours post injection. Voxel-based heterogeneous activity distribution maps were derived after reconstructing the acquired SPECT/CT images and converting the counts in the reconstructed images to activity with the associated calibration factor.

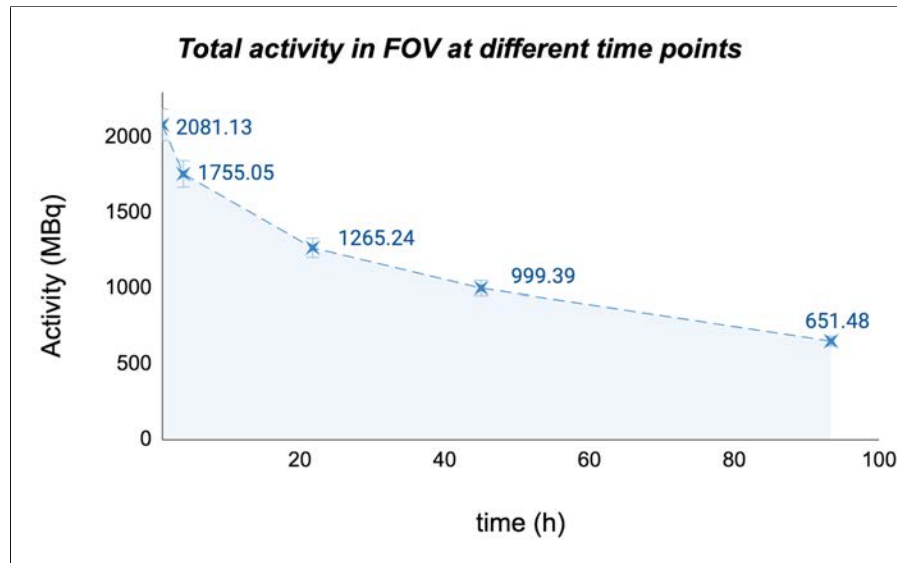


Figure 7.2: Total activity corresponding to each time point post injection (FOV - field of view)

These activity maps consist of matrices of $128 \times 128 \times 90$ with voxel dimensions of $4.418 \times 4.418 \times 4.418 \text{ mm}^3$. The activity present in the whole field of view corresponding to the above time points was 2.08 GBq, 1.76 GBq, 1.27 GBq, 1 GBq and 0.65 GBq, respectively (Figure 7.2). This served as ‘*activity input*’ for the corresponding geometry.

7.2.2 Reference dosimetry generation

Monte Carlo modelling using the Geant4-based GATE toolkit was used to determine the reference dosimetry or ‘ground truth’. Voxel-based absorbed dose rate map calculation requires the distribution of density as well as the activity distribution in the patient, at each time-point.

- The *geometry input* of each time point was used for that purpose. For each voxel, the Hounsfield units (HU) were converted to the material and density by the use of Schneider curve (Schneider et al. 2000) available as *HounsfieldMaterialGenerator* in GATE (GATE documentation 2018).
- In addition, voxelized activity maps i.e. *activity input* for each time point derived from clinical acquisitions was used in GATE as source definition. Since all emissions contribute to the absorbed dose rate calculation, the radioactive decay along with the atomic de-excitation was simulated by using a ^{177}Lu ion source defined by its atomic number ($Z = 71$), atomic weight ($A = 177$), ionic charge ($Q = 0$) and the excitation energy in keV ($E = 0$).

The *DoseActor* was used in GATE to calculate and store the absorbed dose rates in a given volume in a 3D matrix (Sarrut, Bardiès, et al. 2014) and was ‘attached to’ 3D patient volume. Since all particles were simulated, the number of simulated primaries was equal to the total activity present at each time point.

The generated dataset defines the ‘reference dosimetry’.

7.2.3 Monte Carlo based image generation

The participating clinical centre sends the host centre an image dataset (SPECT projections, corresponding CT, and reconstructed SPECT/CT) of a simple phantom (for example a uniform Jaszczak phantom, or an IEC phantom with or without spheres) acquired on their gamma camera. Along with this dataset, information regarding the gamma camera characteristics (such as crystal thickness, type of collimator, energy and spatial resolution), the activity settings (amount of activity in each compartment, date and time of activity calibration) and the acquisition protocol (acquisition time and duration, energy window information, type of orbit used, etc.) are required.

Following this, patient images are generated for each centre in accordance with their local acquisition protocols. The workflow adopted for image generation and data circulation is illustrated in Figure 7.3.

Centre-specific SPECT/CT images are generated using GATE. The x and y axis of each projection corresponds to the sagittal (left to right) and axial (top to bottom) axis respectively. The simulated raw SPECT projections are incorporated into the template of the clinical images, and necessary tags in the DICOM header (for example: *Largest Image Pixel Value*, *Smallest Image Pixel Value*, *CountsAccumulated*) are adapted to the simulated dataset (using pydicom library (Mason 2011) in a python3 script) so that they can be read by the clinical workstations present in the clinical centre.

Calibration images are modelled first. This has three potential advantages:

- It allows for the validation of the modelled gamma camera with a simple phantom,
- It validates the integration of a test image in the clinical centre image workstation,
- It enables the generation of a calibration factor corresponding to the simulated data set. This is important since the virtual gamma camera sensitivity is not necessarily strictly equal to that of a real gamma camera.

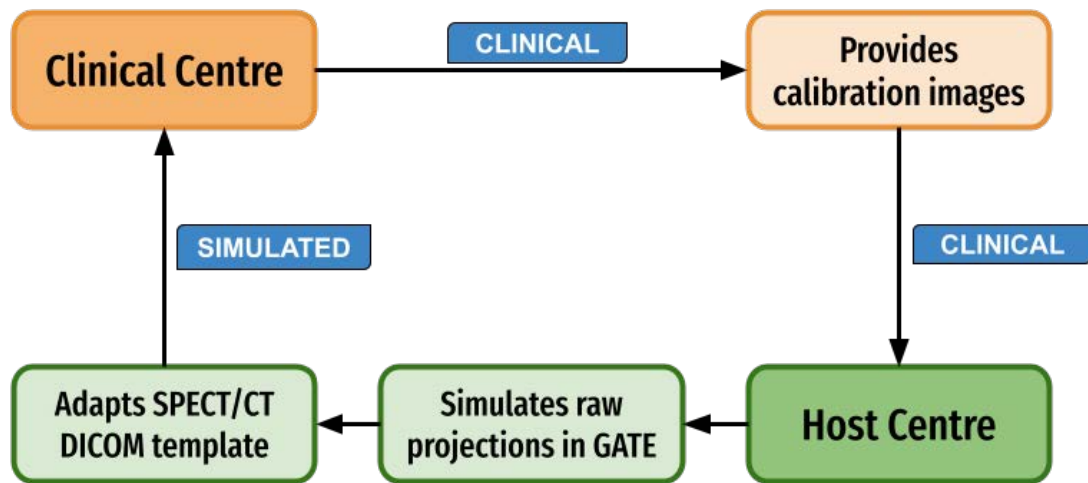


Figure 7.3: Workflow of Monte Carlo-based image generation: each participating Clinical centre provides a sample of experimental images (usually calibration phantoms). The Host centre can then simulate images based on the experimental geometry and camera characteristics. Simulated images are then imported to the clinical image workstation for verification

7.2.3.1 Calibration image modelling

a. Simulation of calibration SPECT projections in GATE

For the simulations, a model based on the NEMA IEC calibration phantom was designed, as used in clinical acquisitions. Also, information on activity concentration and background along with the acquisition settings was obtained from the clinical settings.

The GE Infinia gamma camera model was derived from the work of Garcia *et al.* (Garcia *et al.* 2015), and was adapted to the camera used for clinical acquisitions (3/8" NaI crystal size and medium energy collimator). The radial position, start angle and the angular step were extracted from the DICOM headers of clinical images, and used to simulate the gamma camera auto-contouring motion (Kayal, Chauvin, Mora-Ramirez, *et al.* 2020).

The water-filled NEMA IEC phantom with the spheres of inner diameter 22 mm, 28 mm and 37 mm was modelled. For image modelling, only gamma emissions need to be considered. Therefore, contrary to the absorbed dose modelling, a weighted sum of gamma emissions (yield) was considered: 71.6 keV (0.15%), 112.9 keV (6.4%), 136.7 keV (0.05%), 208.4 keV (11%), 249.7 keV (0.21%) and 321.3 keV (0.22%) (MIRD 2021). A total activity of 348.6 MBq was simulated and this corresponds to 5.66×10^{10} primaries obtained as a product of activity in Bq, time per projection, number of projections and the total percentage of gamma emissions.

b. Validation of simulated calibration projections

Two criteria have been used to compare simulated calibration projections to experimental projections:

Flattened profiles (2D image to 1D profile): 1D profiles were produced on the x-axis for each projection or 2D image by aggregating all the counts in the y-axis using a python script. This difference in magnitude was estimated to assess the goodness of the simulated images.

Gamma index (3D images): The Gamma index was used to compare the absorbed dose distributions between clinical and simulations, which is a vital determinant in external beam radiotherapy (Low et al. 1998). This technique requires the user to define two assessment criteria: the absorbed dose difference (DD), which is the maximum difference between three-dimensional absorbed dose distribution maps, and the distance to agreement (DTA), which is the maximum spatial difference between compared images. The gamma index passing rate (GIPR) and average gamma are computed from these criteria, i.e. the percentage and average number of points that meet the specified DD/DTA acceptance requirements, respectively.

Throughout the work, the same criteria were used to compare two data sets (SPECT projections, reconstructed SPECT/CT images and activity-indexed maps).

From the calibration projections, a ratio between the total counts in the measured and simulated projections was derived and utilised to adjust the patient projections. This is referred to as ‘normalisation’ in the Results section.

c. Reconstruction of calibration projections

For the sake of the validation, the simulated SPECT projections were reconstructed in the same manner as the clinical dataset.

The following equation (Equation 7.1) was used to derive a calibration factor for the simulated data set from the reconstructed SPECT/CT images:

$$\text{Calibration factor (CF)} = \frac{\text{Counts}_{VOI}}{\text{Activity}(A_o) \times t_{acq}} \quad (7.1)$$

where Counts_{VOI} , A_o , and t_{acq} denote the total number of counts inside the volume of interest (VOI), the initial activity, and the total acquisition time, respectively. The VOI was defined in this case as the whole field of view.

7.2.3.2 Patient image modelling

a. Simulation of patient SPECT projections in GATE

Patient image simulations were performed using the same gamma camera model as for the calibration images. Manual segmentation was performed on the registered CT for organs and on the SPECT for the lesion. The volumes of interest segmented include soft tissues (liver, kidneys, spleen, and tumour) as well as bones, lungs, and the rest of the field of view. The segmentation was stored as a .nrrd file (nearly raw raster data), a file format often used in Slicer for scientific visualisation and image processing involving N-dimensional data (Fedorov et al. 2012). For each volume of interest, tessellated mesh structures were created. The materials and the densities associated with each compartment or volume of interest were specified in GATE. Heterogeneous activity distribution maps were generated for each time point as explained in Kayal *et al.* (Kayal, Chauvin, Vergara-Gil, et al. 2021).

The ^{177}Lu spectrum presented above for calibration image modelling was used.

The number of primaries simulated from the first to the last time point ranged from 3.18×10^{11} to 1.0×10^{11} . The generation of patient SPECT images is described in more detail in the previous chapter.

b. Validation of simulated patient projections

The goodness of simulations was assessed using the same metrics previously indicated for the calibration images - flattened profiles and gamma index (by setting DD and DTA criteria as 2% and 1-pixel, respectively).

c. Reconstruction of patient projections

Simulated SPECT projections were inserted into the template of the clinical images and DICOM tags updated according to the approach chosen for calibration images. The simulated patient SPECT/CT images were reconstructed using the same software and the same reconstruction settings as the clinical dataset. These reconstructed SPECT/CT images have a dimension of $128 \times 128 \times 90$ and voxel size of $4.418 \times 4.418 \times 4.418 \text{ mm}^3$.

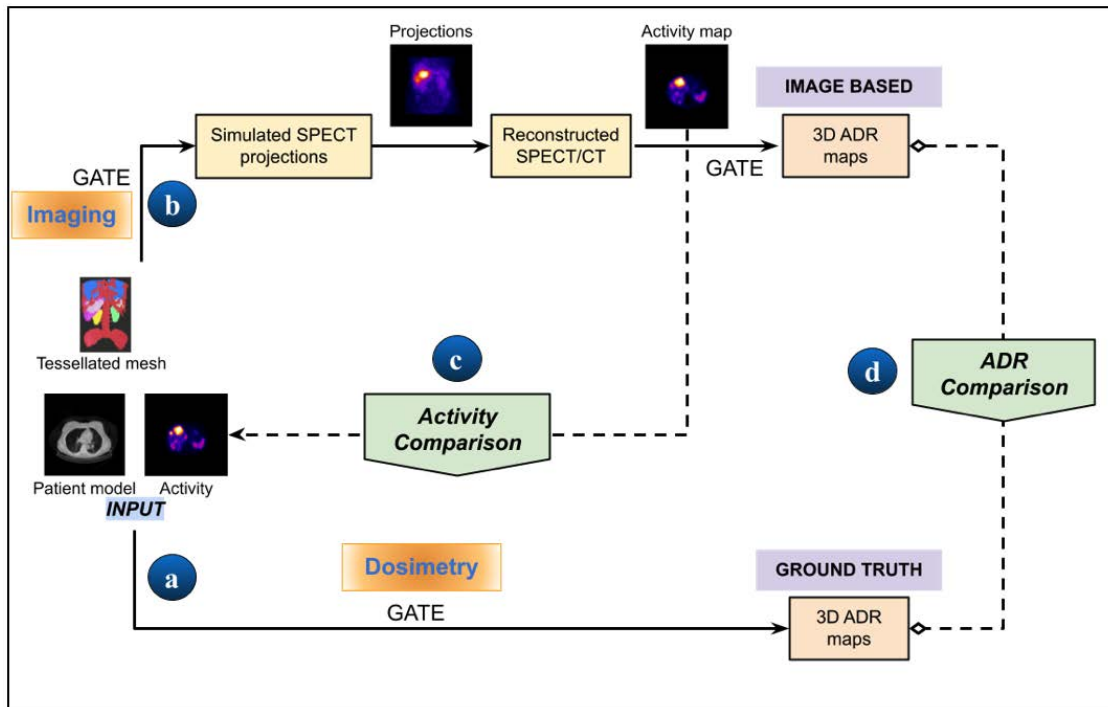


Figure 7.4: Schematic describing the workflow for assessing the feasibility of DosiTest.

The ‘input’ is the starting point. a) Reference absorbed dose rates are calculated directly from the ‘input’ in GATE without imaging (referred to as ‘Ground truth’). b)

From ‘input’, simulated SPECT projections are generated and activity maps are obtained after reconstruction. c) These derived activity maps are compared to the input (referred to as ‘Activity comparison’). d) Absorbed dose rates are computed from the simulated activity maps (referred to as ‘Image based’) and these are compared to the ‘Ground truth’ absorbed dose rates (referred to as ‘ADR comparison’).

(This figure was derived from the pioneer work of Dewaraja *et al.* Dewaraja, Wilderman, et al. 2005)

7.2.4 Validation procedure

7.2.4.1 Activity-indexed images

The workflow used for evaluating the feasibility of the DosiTest project is shown in Figure 7.4. The reference dosimetry or the absorbed dose at each time point is generated directly from GATE using the ‘input’ (*patient model input* and *activity input*). This step is indicated as ‘a’ in Figure 7.4. Following this, simulated image-based dosimetry is performed from the same ‘input’ (referred to as ‘b’ in Figure 7.4). Further, the activity-indexed map is compared to the ‘*activity input*’ and the absorbed dose rates derived from image-based clinical dosimetry are assessed against the reference dosimetry (referred to as ‘c’ and ‘d’ in Figure 7.4, respectively).

- a. Generation of simulated activity-indexed images

The reconstructed SPECT/CT images of the simulated patient were inserted into the OpenDose3D Slicer toolbox, together with the derived simulation calibration factor, the activity injected (6848 MBq), and the date/time of activity injection. For each time point, activity-indexed maps from the simulated data set were generated.

b. Activity comparison (Input vs generated activity images)

Activity input was compared to the simulated activity-indexed images derived after the reconstruction and calibration of the simulated dataset at each time point using the flattened profiles and gamma index. In [Figure 7.4](#), this is referred to as ‘Activity Comparison’.

7.2.4.2 Absorbed Dose Rate (ADR)

a. Generation of image-based ADR

GATE was used to generate 3D absorbed dose rate maps for each time point using the simulated activity-indexed maps and the resampled CT. This made use of the ‘*Generate Gate*’ functionality in the OpenDose3D Slicer module, which automatically generates the macros and data input files required by GATE.

The absorbed dose rates (ADR) generated by GATE were then imported into OpenDose3D (through the built-in capability ‘*Import Gate*’), which is capable of reading and interpreting the GATE-derived ADR for further dosimetric analysis.

b. ADR comparison (Ground truth vs image-based)

The ADR estimated directly from the input data (referred to as ‘ground truth’ ADR) was compared to the ADR calculated from simulated activity-indexed images (referred to as ‘image based’ ADR) using flattened profiles and the gamma index, as illustrated in [Figure 7.4](#).

7.2.4.3 Integration of absorbed dose rates in time

At each time point, absorbed dose rate maps (both reference and image-based ADRs) were imported into OpenDose3D (using the ‘*Import Gate*’). For the simulated datasets, the segmentation done on the clinical dataset and saved as .nrrd file format was imported to segment the corresponding VOIs.

From the start of injection (i.e. 0 hour) and the first time point (i.e. t_1 or 1 hour), activity was assumed to be constant (blue horizontal line in [Figure 7.5](#)), which implied that the origin (0,0) was excluded from the fitting and from the first time point to infinity, a mono-exponential fitting approach was employed. The same fitting technique was used both for reference and image-based datasets.

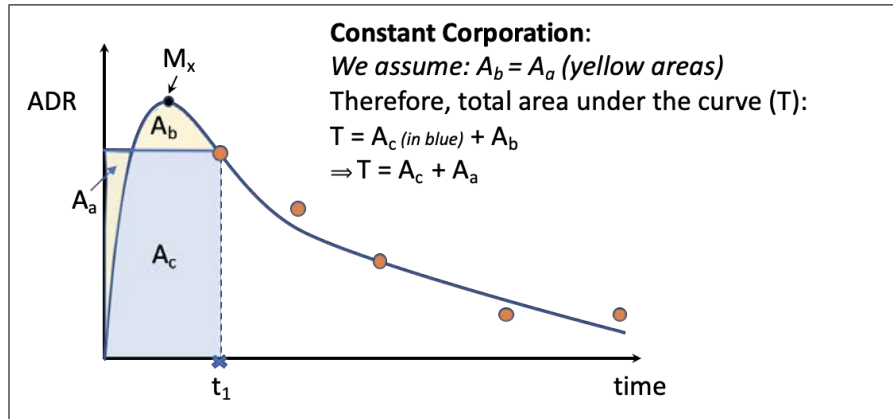


Figure 7.5: A basic representation displaying the constant incorporation of absorbed dose rate (ADR) from start of injection (0 hour) to first time point (1 hour)

7.2.4.4 Absorbed Dose (AD)

Following the integration of absorbed dose rates, the absorbed doses for each volume of interest was determined. The relative difference in absorbed doses between reference (AD_{ref}) and image-based (AD_{img}) approaches was calculated using the [Equation 7.2](#).

$$Relative\ difference\ (\%) = \frac{AD_{ref} - AD_{img}}{AD_{ref}} \quad (7.2)$$

7.3 Results

7.3.1 Reference dosimetry generation

As shown in [Figure 7.6](#), the absorbed dose map is illustrated with the *geometry input* and *activity input* at 1 hour after activity administration. Higher activity and hence higher absorbed dose rates are observed for the tumour present in the liver. [Figure 7.7](#) shows the reference absorbed dose rate maps for all time points.

7.3.2 Monte Carlo based image generation

7.3.2.1 Generation and validation of calibration images

Simulated calibration images for the IEC phantom were generated employing three hot spheres and homogeneous background activity ([Figure 7.8](#)).

Simulated calibration images were validated against the experimental calibration projections by generating flattened profiles ([Figure 7.9](#)). As can be observed, the biggest sphere (37 mm diameter) exhibits the highest activity, and a peak corresponding with this sphere can also be identified in the flattened profiles at the 0°

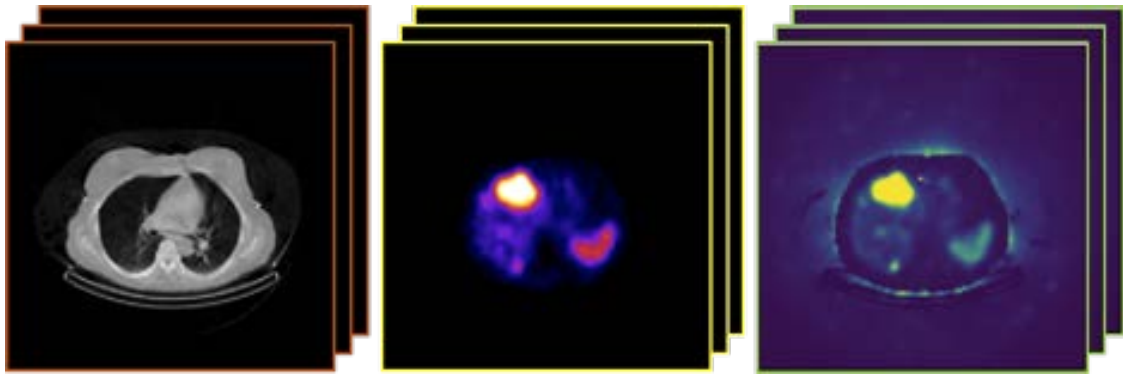


Figure 7.6: The geometry input (left), the activity input (centre) and the computation of the 3D absorbed dose rate map (right) for the first time point (1 hour post activity administration)

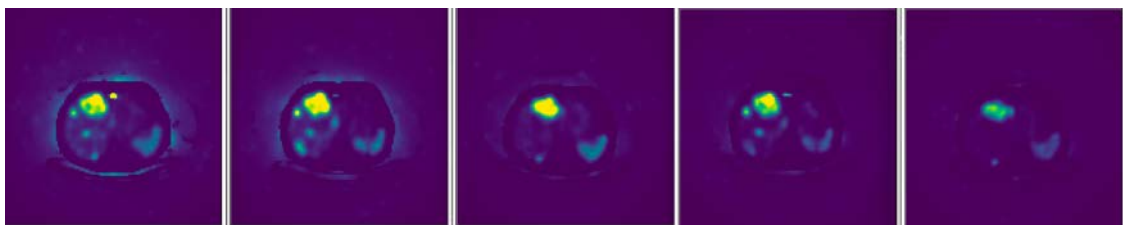


Figure 7.7: Absorbed dose rate for each time point post activity administration (from 1 hour on the left to 96 hours on the right)

gamma camera position (Figure 7.9a). Between clinical and simulated projections, the GIPR and average gamma (γ_{avg}) were 96.04% and 0.35, respectively.

The simulated calibration SPECT projections were embedded in the DICOM headers of clinical images and reconstructed using Hermes clinical software. Using Equation 7.1, a simulated calibration factor of 6.46 counts per second (cps)/MBq was derived. This factor was used to convert counts to activity in a simulated patient dataset.

A calibration factor of 5.33 ± 0.27 cps/MBq was determined for the clinical images. As is often seen, the simulated gamma camera has a higher sensitivity than a real gamma camera.

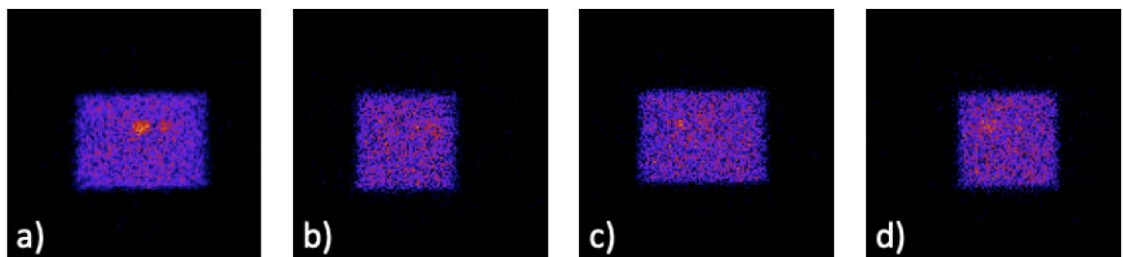


Figure 7.8: Simulated SPECT projections of the IEC calibration phantom with spheres at a) 0°, b) 90°, c) 180° and d) 270° gamma camera positions

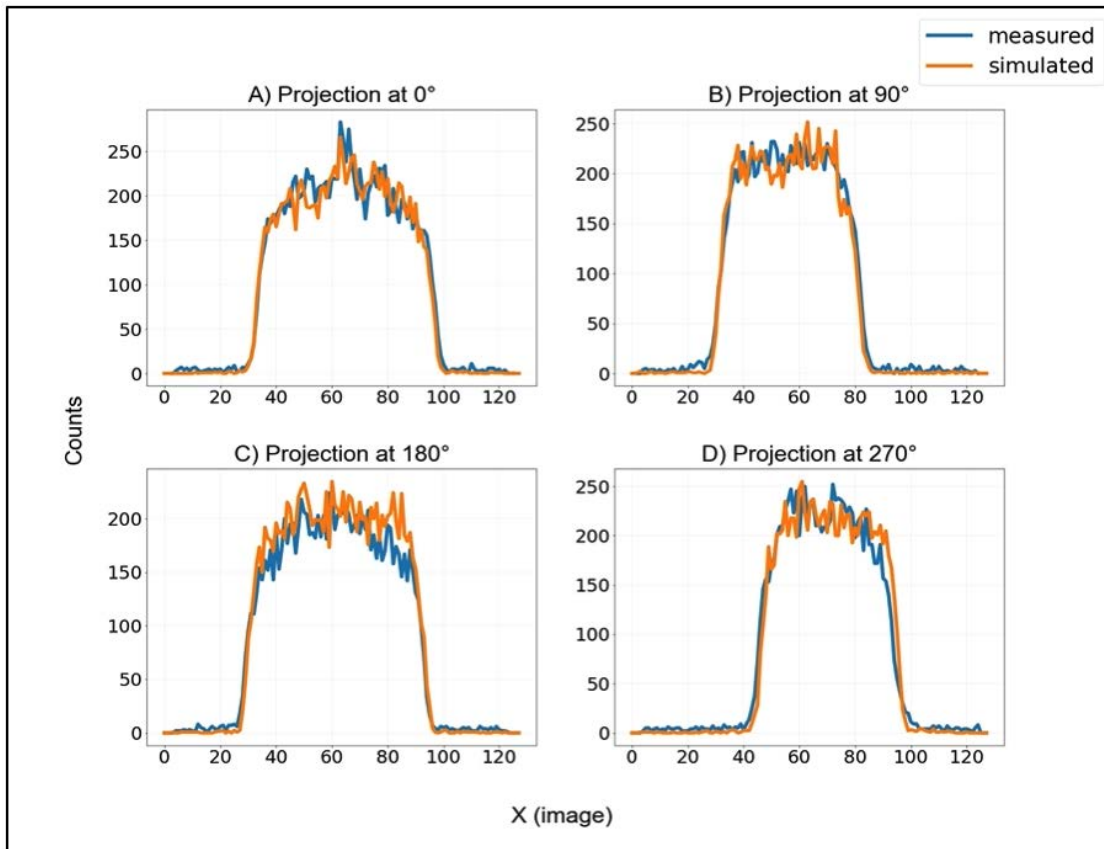


Figure 7.9: Comparison of experimental and simulated calibration SPECT projections profiles (normalisation based on image total counts)

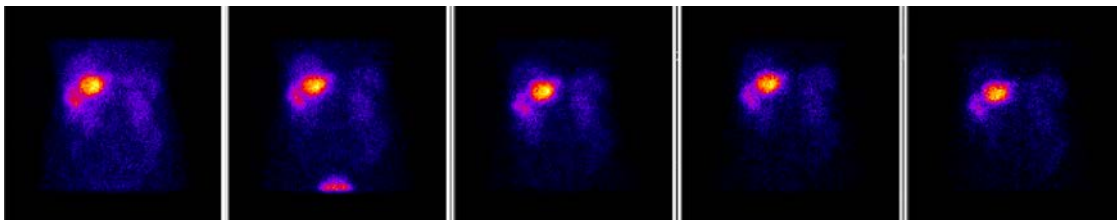


Figure 7.10: Simulated SPECT projections at different time points post activity administration (1 hour, 4 hours, 24 hours, 48 hours and 96 hours from left to right respectively)

7.3.2.2 Generation and validation of patient images

At 1 hour, 4 hours, 24 hours, 48 hours, and 96 hours post activity administration, simulated projections were generated in GATE using auto-contouring detector motion and a tessellated mesh phantom. [Figure 7.10](#) illustrates these projections at various time points after activity administration.

After normalisation ([Figure 7.11](#)), flattened profiles between experiments and simulations were compared for each projection angle from 0° to 360° with an angular step of 3° (hence 60 projections/head).

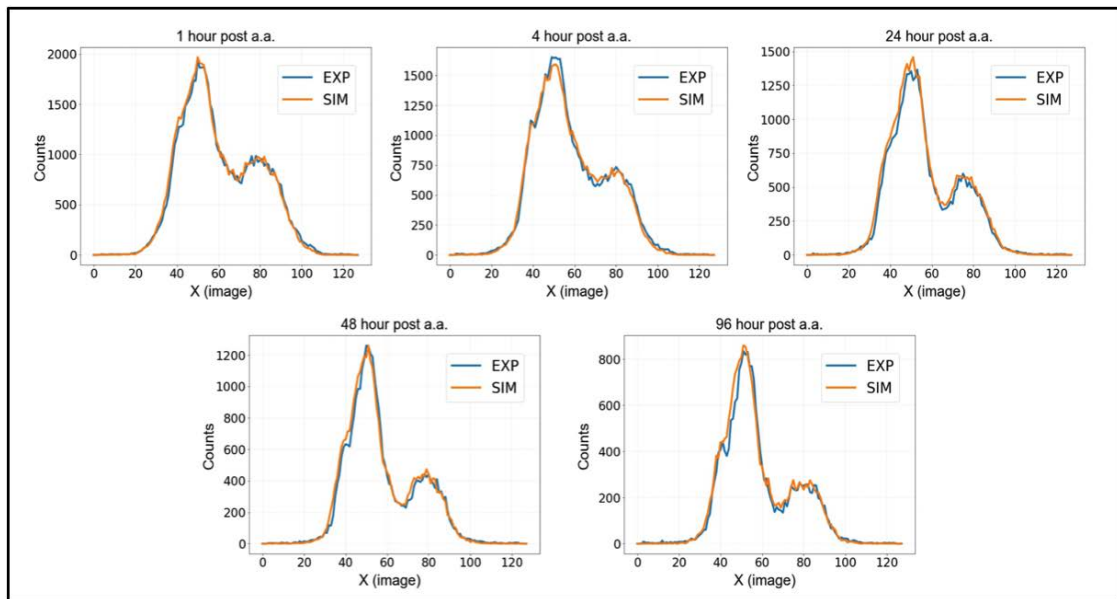


Figure 7.11: Comparison of clinical vs simulated SPECT patient projections at different time points post activity administration (a.a.). Profiles are drawn on the x axis for counts vs x-axis of the image

Comparing clinical and simulated projections, the GIPR and averaged gamma (γ_{avg}) values varied from 95% to 98 % and 0.28 to 0.35, respectively, demonstrating the goodness of simulated patient SPECT projections.

7.3.3 Comparison of activities, absorbed dose rates and absorbed doses

7.3.3.1 Activity-indexed images

- a. Generation of simulated activity-indexed images

Using a simulated calibration factor of 6.46 cps/MBq, counts were translated in reconstructed simulated SPECT projections to 3D activity-indexed maps. These simulated activity-indexed maps are presented in Figure 7.12 for the 5 time points considered.

- b. Activity comparison (Input vs generated activity images)

The simulated activity-indexed pictures were compared to the activity input. Although the tumour is vividly discernible in the central slice and the 1D summed profiles for this slice is depicted in Figure 7.13 for all the time points, profiles have been created for all slices.

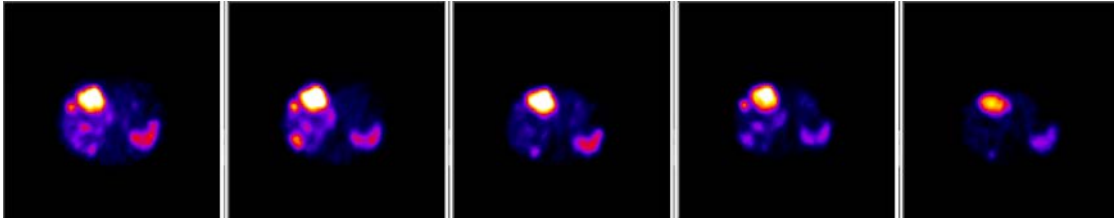


Figure 7.12: Simulated activity maps for time points 1 hour post a.a. (left) to 96 hours post a.a. (right)

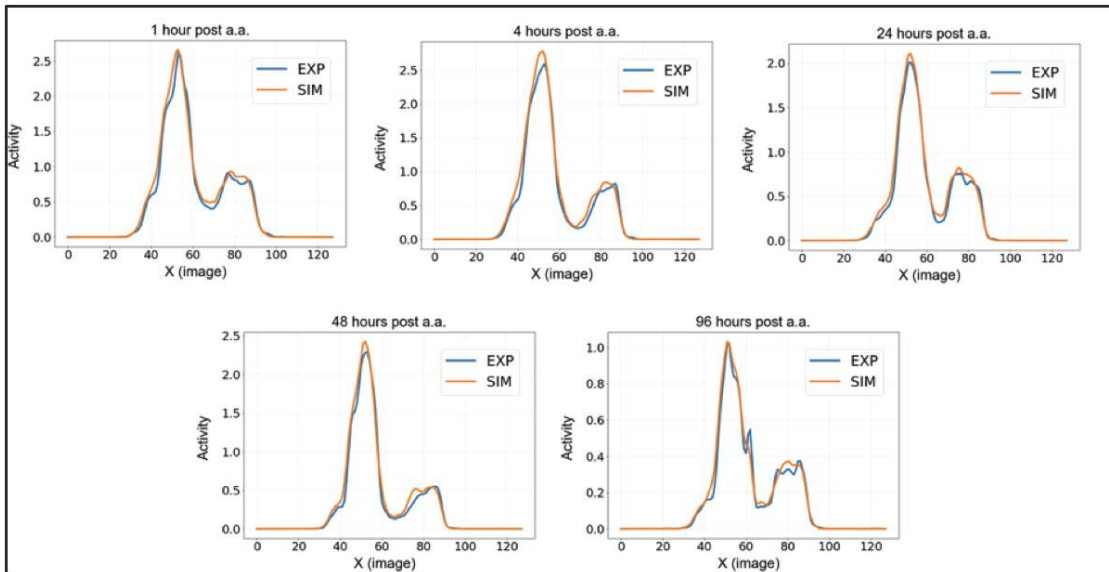


Figure 7.13: Comparison of the activity input and simulated activity-indexed maps (this comparison is referred to as ‘Activity comparison’ in [Figure 7.4](#))

The higher peak corresponds to the tumour located in the liver whereas the smaller peak refers to the activity in the spleen ([Figure 7.13](#)). The activity maps are rather noisy at 96 hours post a.a. because of the lower activity at this time point, which is also observed in the profiles for the SPECT projections at this time point in [Figure 7.11](#).

Comparison of *activity input* and activity-indexed map using average relative difference and the gamma index (GIPR and γ_{avg}) is presented in [Table 7.2](#) for each time point. The relative differences are often below 10%, except for the last time point, which reflects the noise characteristics owing to the low activity. On the other hand, as shown in [Table 7.2](#), the gamma index indicates a high degree of similarity between the two compared activity distribution maps.

Time post a.a.	Relative Diff (%)	GIPR (%)	γ_{avg}
1 hour	5.46	97.31	0.28
4 hours	6.34	97.71	0.26
24 hours	9.6	98.45	0.22
48 hours	7.95	98.91	0.19
96 hours	10.16	98.97	0.19

Table 7.2: Comparison of the activity input and activity indexed maps using relative difference and gamma index metrics

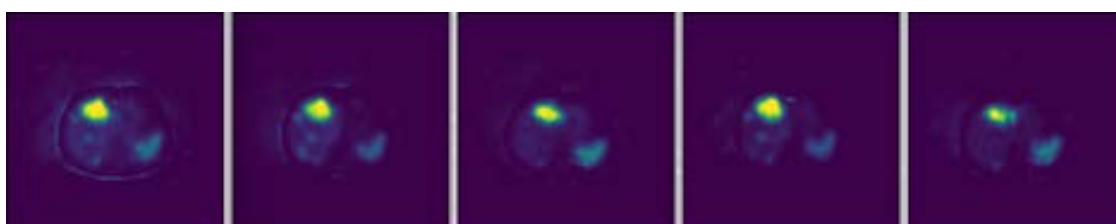


Figure 7.14: Absorbed dose rate maps for time points from 1 hour post a.a. (left) to 96 hours post a.a. (right)

7.3.3.2 Absorbed Dose Rate (ADR)

a. Generation of image-based ADR

Figure 7.14 illustrates the image-based absorbed dose rate maps generated using simulated activity-indexed maps. In the next section, these are compared to the reference (or ‘ground truth’) ADRs.

b. ADR comparison (Ground truth vs image based)

Ground truth or reference ADRs (Figure 7.7) were compared to image-based ADRs (Figure 7.14) in order to determine their degree of similarity using flattened profiles (Figure 7.15) and the gamma index.

The comparison using the gamma index and the calculation of the relative difference of the average absorbed dose rates for each time point are shown in Table 7.3. High GIPR values (and corresponding low average gamma) indicated a strong agreement between the absorbed dose rate maps. The relative difference in ADR across time points is less than 10%, signifying a negligible statistical difference.

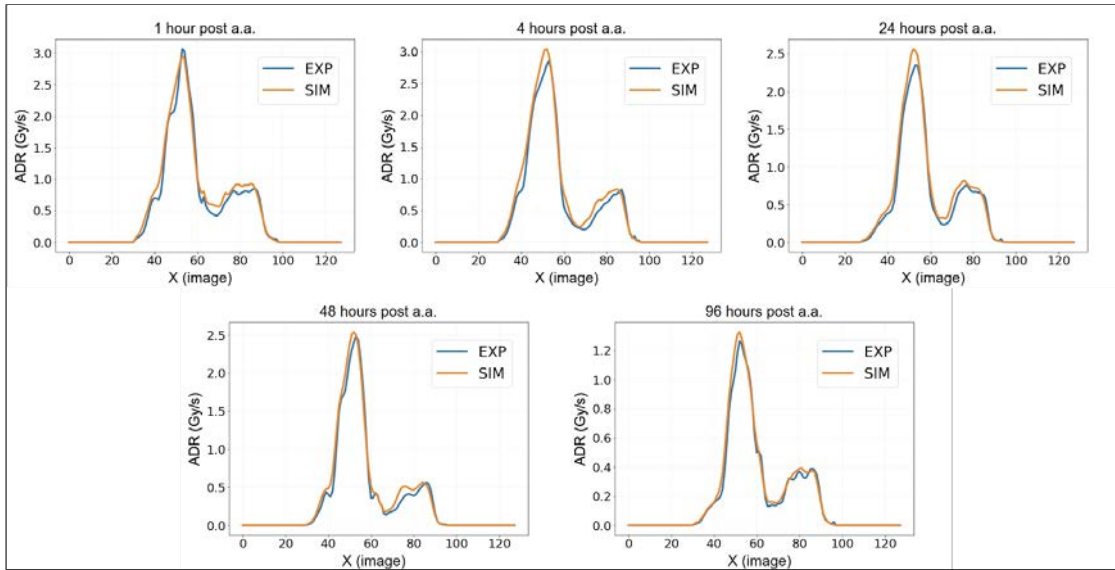


Figure 7.15: Comparison of the reference and image-based absorbed dose rate maps in Gy/s (this comparison is referred to as ‘ADR comparison’ in [Figure 7.4](#))

Time post a.a.	Relative Diff (%)	GIPR (%)	γ_{avg}
1 hour	4.27	95.63	0.3
4 hours	7.88	96.64	0.3
24 hours	8.03	97.42	0.26
48 hours	8.46	98.20	0.22
96 hours	7.59	98.04	0.23

Table 7.3: Gamma metric comparison of the reference and image-based absorbed dose rate maps for each time point

7.3.3.3 Absorbed Doses (AD)

After segmentation of volumes of interest, the reference and image-based absorbed dose rates were integrated over time and absorbed doses were determined. The difference in absorbed doses between the various volumes of interest, namely the liver, the kidneys, the spleen, and the liver tumour, is shown in [Table 7.4](#).

7.4 Discussion

This chapter describes in detail for the first time the DosiTest concept, a clinical dosimetry trial based on Monte Carlo simulation designed to evaluate the variability associated with the various phases of a clinical dosimetry workflow.

Volumes	AD_{ref} (Gy)	AD_{img} (Gy)	Rel Diff (%)
Liver	1.92	2.17	13.16
Left Kidney	4.19	4.08	2.58
Right Kidney	3.49	3.48	0.32
Spleen	7.38	6.96	5.64
Tumour	16.24	17.90	10.22

Table 7.4: Comparison of the absorbed doses (in Gy) obtained from reference (AD_{ref}) and image-based (AD_{img}) ADRs. The relative differences (Rel Diff) between the AD are computed using Equation 7.2 for the volumes of interest

A model of a patient was developed, as well as voxel-based activity at different time intervals after radiopharmaceutical administration. This facilitated the direct Monte Carlo modelling of reference 3D absorbed dose rate maps for each time point.

The second phase of DosiTest is to generate calibration and patient SPECT/CT datasets that are specific to each participating clinical centre. Calibration images generated from simple phantoms prior to patient image simulations allowed for the testing and validation of gamma camera types and acquisition protocols particular to each clinical centre. Additionally, it enabled the development of a simulated calibration factor for each centre.

The decision to use a ‘real’ patient dataset as a reference over phantom models like ICRP adult phantoms (Menzel et al. 2009) or NURBS-based XCAT phantom (Segars et al. 2010) was taken after evaluating its pros and cons for each step of the dosimetry chain. As a synopsis, the real patient images are associated with the CT images at each or various time points, therefore enabling image registration (to account for changes in patient anatomy and movement between imaging sessions), a challenging task that is likely to induce variability in the results. Additionally, it allows for the consideration of a realistic heterogeneous activity distribution within the patient model. However, a full definition of the volumes of interest (reference segmentation) is not entirely feasible.

Following this, the feasibility to generate these images (both patient and calibration) via Monte Carlo modelling with GATE was demonstrated.

One of the challenges of DosiTest is that in order to reproduce the clinical condition, each clinical centre needs to perform dosimetry using their own tools and clinical imaging workstations. This implies that the commercial image workstations must accept simulated images as “real” clinical images. Due to the fact that the patient model is derived from clinical images, it already has a DICOM header with the requisite tags. It has been demonstrated that raw simulated projections can

be “copied/pasted” or inserted into the clinical envelope and after modification of the appropriate tags can be processed in the clinical workstation.

The activity-indexed maps obtained for each time point, after reconstructing simulated images and employing a simulated calibration factor were in excellent agreement with the *activity input* (obtained using the appropriate experimental calibration factor). This emphasises the importance of determining a calibration factor for each particular dataset.

Consequently, 3D absorbed dose rate maps were derived using Monte Carlo modelling from simulated image datasets (referred to as image-based ADR) and successfully compared to reference absorbed dose rate maps obtained directly from Monte Carlo simulations without the imaging step (referred to as the ground-truth ADR).

To obtain absorbed doses for the volumes of interest using absorbed dose rates (image-based and ground truth ADR), user-dependent segmentation is required. This inevitably results in variations in absorbed dose calculations. The same segmentation was used in our feasibility study for both image-based and reference absorbed doses and resulted in comparable dosimetry data. Further investigation is needed for the AD of specific VOIs, such as the liver and tumour, for which larger differences were observed.

We believe that the feasibility of DosiTest has been demonstrated in this work. As part of the IAEA CRP project, additional efforts were made to define checkpoints, which are intermediate phases at which results may be exported and compared to a reference. These will allow for the extraction activity information at different time points and to analyse the segmentation step by providing organ or tissue masses (even though there is no reference segmentation). It is clear that only presenting the obtained average absorbed doses for each VOI towards the end of the dosimetry workflow is inadequate. Mora-Ramirez *et al.* (Mora-Ramirez et al. 2020) assessed many clinical dosimetry software packages and determined that each software package has its own dosimetric process, complicating workstation comparative studies. Depending on the dosimetry technique used in each clinical site, only end-products (i.e. absorbed doses) may be accessible, reducing the analysis’s strength. However, with the current state of the art, comparisons are typically performed on phantoms and focus on specific aspects of the clinical dosimetry process (most often the quantitative imaging step). DosiTest aims to go further and provide pertinent information that is not currently accessible.

7.5 Conclusion

A proof of concept of the DosiTest project has been established. A patient model was defined that encompasses a realistic characterization of the patient's geometry and voxel-based activity. Monte Carlo modelling was used to determine the reference dosimetry (i.e. absorbed dose rates at the various time points studied). Several realistic image datasets were generated that could be integrated into clinical image workstations, and clinical dosimetry could be conducted on these datasets according to each clinical centre's local procedure.

DosiTest has now started with the recruitment of a limited number of clinical centres to investigate the various sources of variability in the clinical dosimetry process, starting with the generation of centre-specific calibration images. This enables DosiTest to be analysed in more general scenarios, where each clinical centre may use its own clinical dosimetry software and protocols.

Acquisitions	Phantom Model	Patient Model
Reconstruction	Pros: Reconstruction with research tools (for example CaSToR (Merlin et al.; 2018))	Pros: DICOM template from clinics available to use for the simulated projections Possibility to reconstruct No issues for connecting or proprietary tags as it is already there
	Cons: Clinical CT is not available Possibility to use CT projector (XCAT) Missing DICOM template Tag values cannot be created Difficult for workstations to decode	Cons: Switching between different camera manufacturers can be challenging at times
Registration	Pros:	Pros: Possibility to register since CT at each point is available Both patient motion and change in anatomy can be accounted for
	Cons: Not possible as the patient geometry is fixed.	Cons: Golden standard not known
Segmentation	Pros: Fixed definition of each volume of interest Traceability Golden standard	Pros: Different workstations /algorithm can be tested
	Cons: Variability is probably less than in real life	Cons: Cannot be a goal standard Organs/tumours delineation are user- dependent Reproducibility hampered
Assessment of time - integrated activity or absorbed dose rates	Pros: Equation based Extrapolation to any time point possible	Pros: Realistic pharmacokinetics as it is patient based Heterogeneous distribution of activity
	Cons: Not necessarily realistic or comparable with patient PCK Homogenous activity distribution in functional volumes	Cons: Extrapolation to other time points might not be straightforward.
Absorbed Dose (AD)	Pros: Organ based dosimetry possible to obtain Voxel based dosimetry possible Golden standard (ref dosimetry possible) - average AD possible (well segmented volumes)	Pros: Generation of voxel based absorbed dose maps by Monte Carlo modelling
	Cons: Heterogeneity not considered Too good to be true	Cons: Even though voxel AD maps are available, computation of average absorbed dose would be user dependent Ground truth compromised

Table 7.5: Use of phantom vs patient models as reference along with advantages and drawbacks in each step of clinical dosimetry workflow



Conclusion and perspectives

Contents

8.1 Summary of the work	181
8.2 Contribution to the field	184
8.3 Future suggestions and perspectives	185
8.3.1 Clinical Aspect	185
8.3.2 Modelling Aspect	186
8.3.3 DosiTest project	187

8.1 Summary of the work

The thesis presents first a brief overview of treatment planning approaches in molecular radiotherapy. A “one-size-fits-all” approach is often used where every patient receives the same amount of irradiation (fixed activity) in each therapy session. However, despite the fact that this approach is simpler to adopt logistically, variable drug uptake between patients results in large variations in the treatments delivered, with possible under- or over-treatment of patients.

Patient-specific dosimetry enables a major paradigm shift in the administration of molecular radiotherapy, from this “one-size-fits-all” approach to “real personalised medicine” where administered activity is assessed specifically for each patient. This approach has demonstrated improved treatment outcomes and decreased toxicity in healthy tissues in several clinical applications. However, patient-specific treatment requires a suite of steps (broadly quantitative imaging, pharmacokinetics

assessment and absorbed dose calculation). The global accuracy of the dosimetric chain relies on the accuracy of each of these steps. ***This work focused on evaluating the variability associated with the various steps of the clinical dosimetry workflow.***

The first phase of the project (IAEA-CRP E23005) illustrated the multi-centric dosimetric analysis performed by multiple operators on the same clinical patient SPECT/CT images using the same dosimetric workflow and procedures and software. To our knowledge, this is the first time that a multi-centric dosimetry comparison of a single clinical patient dataset has been undertaken using the same technique and software by many centres worldwide. It was demonstrated that despite the use of one standard (or strict) protocol, there were significant disparities in the generated results.

A large number of transcriptional mistakes (human errors) were observed throughout this process. Variations in the dosimetric results can also be attributed to mishandling of the software, either because of inadequate training or a difficult-to-use interface. In some cases, scientifically illogical results were also obtained as discussed in Chapter 3. One of the key conclusions of this work is that, contrary to current practice in external beam radiotherapy, clinical nuclear medicine dosimetry lacks a *quality assurance* program, and quality control procedures must be developed to bridge the gap. It is important to adopt good dosimetric practices in order to ensure that the dosimetric results are reliable, traceable and reproducible. Some of the key components include establishing various checkpoints (or intermediate results) to ensure the integrity of the results; incorporation of sanity checks internally within the software in order to minimise human error and cross-validation of the results among physicists/clinicians to reduce transcriptional error.

Additionally, the results shown in this chapter required numerous iterations (varying from one to five) of the dosimetric results, brainstorming and debriefing sessions due to the large variations observed in the results provided by participants. This clearly revealed the critical need of a series of theoretical and practical training sessions (virtual and in-person) to enhance users' proficiency in clinical dosimetry. This work served as a stepping stone towards the development of good clinical dosimetry practice.

Following the high discrepancy in this independent dosimetry analysis, a '*real-time*' dosimetry analysis was performed for one cycle at IAEA headquarters in Vienna using the defined checkpoints and with training at every step. It was established that monitoring and immediate assistance from the software vendor's application specialist, in conjunction with the use of predefined checkpoints, aided significantly in the identification of the majority of sources of heterogeneity among the

participants and produced exemplary dosimetric results. This led to the in the creation of a '**benchmark dataset**' consisting of reconstructed patient SPECT/CT data at five time points with an associated calibration factor, a standard workflow to be followed in Planet[®] Dose and step-by-step dosimetry results with mean and percentage of variation for each established checkpoint, thereby providing the expected precision over the various steps of the procedure ([Appendix B](#)). It enables individuals to assess their mastery of the software on a realistic dataset, and to improve their own abilities to work with the software.

While the preceding work examined the **precision** of dosimetry analysis using the clinical dataset, a standard methodology and specific software, the next phase of the thesis contributed directly to the DosiTest project (www.dositest.org) and focused on the **accuracy** of the clinical dosimetry process. This implied developing simulated datasets that could represent the ground truth for a specific clinical dosimetry application.

Therefore, modelling of realistic SPECT images of anthropomorphic phantoms using the GATE Monte Carlo code had been performed. This required the development of auto-contour step-and-shoot SPECT acquisition mode in GATE. The impact of modelling circular (CO) vs non-circular (NCO) orbit detector motion for SPECT imaging was assessed using two radionuclides: ^{177}Lu (low septal penetration) and ^{131}I (high septal penetration), comparison of which revealed disparities of 2.6% for ^{177}Lu and around 1% for ^{131}I . This highlighted the need for employing the NCO acquisition mode in simulations, especially for radionuclides with a high septal penetration. The impact could therefore be important in the context of MRT dosimetry, as a possible underestimation of the activity in the patient due to the use of a CO vs. NCO acquisition mode may have an effect on the determination of the absorbed dose.

After the successful implementation of NCO for phantom models, realistic SPECT imaging for a clinical patient dataset with realistic activities in therapeutic context was modelled. It was then validated against clinical projections. Furthermore, the integration of these simulated SPECT projections into clinical DICOM headers was addressed, such that the resulting SPECT/CT projections could be read by commercial workstations. This was a pivotal factor and a challenging task towards the evolution of the DosiTest project. Transitioning DICOM headers from one manufacturer to another is further essential, but that possibility has only been partially explored.

The last phase of the thesis demonstrated the feasibility of the DosiTest project. First, from the same clinical dataset (SPECT/CT), the virtual patient geometry

associated with voxel-based activity at various time points after radiopharmaceutical administration was derived so as to enable the direct Monte Carlo modelling of reference three-dimensional absorbed dose rate maps for each time point. Then, calibration and realistic patient image datasets were modelled and integrated into the clinical workstations, so as to perform clinical dosimetry on these datasets. Calibration phantom images were simulated prior to patient images, allowing the validation of gamma camera modelling and that of the acquisition procedures specific to each clinical facility.

The reference dosimetry was compared with the image-based dosimetry (considering the same segmentation file) at various intermediary steps (activity-indexed maps, absorbed dose rates). The largest relative differences between activity maps and absorbed dose rate maps were 10.2% and 8.5%, respectively, and these values were primarily attributable to the last time point that suffers from poor counting statistics due to the low remaining activities. The relative differences between absorbed doses assessed among identical segmented regions were <13.2%.

The proof-of-concept of the DosiTest project was illustrated. A limited number of clinical centres were chosen to participate in the project, which begins with the generation of calibration images specific to each of the participating centres. The deployment of DosiTest in more broad circumstances, in which each clinical centre may use its own clinical dosimetry procedure (acquisition settings, software and processing methodology), should provide a general overview of the variabilities that can be expected in clinical dosimetry procedures.

8.2 Contribution to the field

During this doctoral project, new techniques were developed to account for the auto-contouring step and shoot SPECT acquisition mode in GATE. The technical details related to this are available in Chapter 5. An example of the GATE files and the necessary python codes required for the modelling of this detector motion will be made available in the Gitlab (<https://gitlab.com/gkayal/spect-auto-contouring-motion-in-gate>).

This work highlighted the lack of quality assurance in clinical nuclear medicine dosimetry and the need to develop quality control procedures.

A benchmark dataset, consisting of a reconstructed patient SPECT/CT data at five time points with an associated calibration factor, a standard workflow to be followed in Planet[®] Dose and step-by-step dosimetry results (with mean and percentage of variation for each established checkpoint) was developed which will

allow individuals to assess their mastery of the software. The standard protocol used with the step-by-step results are available in [Appendix B](#). This benchmark dataset will be made available by the International Atomic Energy Agency (IAEA) as a part of the Coordinated Research Project E23005.

Alternatively, DOSIsoft may disseminate this training benchmark dataset to individuals willing to train themselves with the software.

8.3 Future suggestions and perspectives

8.3.1 Clinical Aspect

This comparison of clinical dosimetry results was performed on a reconstructed clinical patient dataset with an associated calibration factor (Chapter [3](#)). The calibration and the reconstruction steps are known to have an impact on activity determination and ultimately on the absorbed dose calculations (D'Arienzo et al. [2016](#); Zimmerman et al. [2017](#); Wevrett, Fenwick, Scuffham, and Nisbet [2017](#); Tran-Gia et al. [2021](#)) and therefore these steps should be included in the inter-comparison exercise to assess the variations among participants.

The benchmark dataset was generated (Chapter [4](#)) to study the precision of clinical dosimetry and operator-dependent variability in a constrained context (same patient dataset, same dosimetry procedure, same software). It may be worthwhile to vary individual steps, such as registration/segmentation within Planet[®] Dose, to gain a better understanding of the spectrum of possible variations and their consequences on the absorbed doses. Additionally, it would be relevant to process the same dataset using the same (or a similar) protocol but on another dosimetry software package to see the variations in results. This, however, may not always be straightforward due to the fact that not all dosimetry software allows the exportation of intermediate results (Mora-Ramirez et al. [2020](#); Huizing, Peters, et al. [2020](#); Della Gala et al. [2021](#)).

On the other hand, as can be seen from the results in Chapter [3](#), even though it was possible to export intermediate results from the software, providing too many processing possibilities increased the likelihood of deviating from the systematic approach. In that regard, developing and implementing predefined clinical dosimetry workflows would undoubtedly aid in reducing occurrences of human error. Furthermore, built-in sanity checks should be implemented directly into the dosimetry software at different phases of the workflow to flag abnormal results.

It is also critical to establish a standard template, such as a DICOM template for reporting dosimetry results, that would include general information about the

administered activity, time/date of injection; registration/segmentation-related information, such as the type/modality of registration process used, how segmentation is performed on anatomical or functional images; pharmacokinetics-related information, such as the time points used, the type of fitting model used, interpolation and extrapolation of fit (from time zero to first time point and last time point to infinity), absorbed dose-related information such as organ/voxel based, algorithm used, accounting for mass/density correction and so on. In essence, clinical dosimetry is a complex process, and traceability may only be ensured by reporting the step-by-step procedure and intermediary results.

8.3.2 Modelling Aspect

Voxelised phantom/patient models were transformed to tessellated mesh geometry for use in modelling the auto-contouring detector motion in the virtual GATE environment. This was done to prevent collision of the phantom/patient model with the detector head in the virtual GATE environment. For this, segmentation of the phantom/patient geometry is required to create separate mesh compartments. This limits the modelling of a heterogeneous density distribution within a single volume of interest. It may not be a concern for this work as the critical organs are mainly soft tissues such as the kidneys or spleen, but it may have a significant impact on the activity quantification of bone and/or lung where the density is variable. Additional work to incorporate variable densities in tessellated mesh structures in GATE may aid in the accurate activity quantification of ^{131}I (for example) where lungs are the critical organs.

The simulation of images is based on a clinical dataset and therefore the extraction of pertinent information relies on the “standard” DICOM template. However, the DICOM standard is not always consistently implemented, which means that the same tag may relate to a different property between manufacturers. An example of this variation, a difference in the ‘Radial position’ tag between GE and Siemens DICOM template, is illustrated in Chapter 5. As a consequence, rigorous observation and analysis are required when decoding DICOM headers from a range of suppliers.

A real challenge associated with simulations is the computation time. The brute generation of one SPECT image of a patient injected with around 2 GBq (translating to 318 billion primaries in GATE) would require 9.6 years of computation time (with a single CPU core with 2.6 GHz, 16 GB). We managed to get results within a reasonable time frame thanks to our access to the regional High Performance Computing (HPC) centre CALMIP. Alternate possibilities would

have required implementing variance reduction techniques and other approaches to increase computing efficiency. This would obviously have required further development and validation.

8.3.3 DosiTest project

The practical feasibility of the DosiTest project is studied in Chapter 7. Six clinical centres were enrolled in the project.

The first task was related to calibration.

Each centre was asked to provide the host centre with information about the gamma camera available in their centre, their local acquisition protocols along with an example of calibration images (SPECT images, series of CT images and reconstructed SPECT/CT image). Then, centre-specific calibration images were simulated and sent to the respective clinical centre.

The second task was related to the reconstruction of a simulated calibration image.

At this stage, three clinical centres provided us with the reconstructed simulated calibration image along with the simulated calibration factor. This task is still ongoing.

The next task involved the generation of SPECT/CT patient dataset for each centre according to their gamma camera setting and acquisition protocols but with the defined patient model and activity distributions. One of the anticipated challenges in this work will be to extrapolate the available activity distribution (i.e. at five particular time points) to different time points that may be required by the centre due to its local procedures. This would require further research. Incorporating hybrid dosimetry (SPECT/CT and planar image combination) would also be challenging, and would probably require combining model and real patient images to generate the input files. Yet, DosiTest, under its current format, has proven feasible. Further tasks include performing dosimetry on the simulated dataset and the benchmarking of these results with the reference dosimetry.

At present, all the work done for this project focuses on Lutathera[®] treatment (¹⁷⁷Lu SPECT/CT image generation, activity distribution). The concept of DosiTest can obviously be extended to other MRT applications. Inherently, the methodologies, tools and knowledge developed during this PhD can be used for that purpose, thereby decreasing the time required to develop a different instance of DosiTest. This project is a long lasting effort, and all developments are freely accessible to allow its continuation.

Conclusions et perspectives futures

La thèse présente d’abord un bref aperçu des approches de planification du traitement en radiothérapie moléculaire. Une approche “one-size-fits-all” est souvent utilisée, où chaque patient reçoit la même quantité de irradiation (activité fixe) à chaque session de traitement. Cependant, bien que cette approche soit plus simple à adopter d’un point de vue logistique, l’absorption variable de médicaments entre les patients entraîne de grandes variations dans les traitements délivrés, avec un risque de sous ou sur traitement des patients. La dosimétrie spécifique au patient permet un changement de paradigme majeur dans l’administration de la radiothérapie moléculaire, passant de cette approche “one-size-fits-all” à une “véritable médecine personnalisée” où l’activité administrée est évaluée spécifiquement pour chaque patient. Cette approche a permis d’améliorer les résultats du traitement et de réduire la toxicité dans les tissus sains dans plusieurs applications cliniques. Cependant, le traitement spécifique au patient nécessite une série d’étapes (imagerie largement quantitative, évaluation pharmacocinétique et calcul de la dose absorbée). La exactitude globale de la chaîne dosimétrique repose sur la précision de chacune de ces étapes. *Ce travail a porté sur l’évaluation de la variabilité associée aux différentes étapes de la chaîne dosimétrique clinique.*

La première phase du travail a illustré l’analyse dosimétrique multicentrique effectuée par plusieurs opérateurs sur les images TEMP/TDM d’un même patient clinique en utilisant le même flux de travail dosimétrique et les mêmes procédures et logiciels (IAEA-CRP E23005). À notre connaissance, c’est la première fois qu’une comparaison dosimétrique multicentrique d’un seul ensemble de données sur un patient clinique a été entreprise en utilisant la même technique et le même logiciel par de nombreux centres dans le monde entier. Il a été démontré que malgré l’utilisation d’un protocole standard (ou strict), il existait des disparités significatives dans les résultats générés.

Un grand nombre d’erreurs de transcription (erreurs humaines) a été observé tout au long de ce processus. Les variations des résultats dosimétriques peuvent également être attribuées à une mauvaise utilisation du logiciel, soit en raison d’une formation inadéquate, soit en raison d’une interface difficile à utiliser. Dans

certains cas, des résultats scientifiquement illogiques ont également été obtenus, comme indiqué au Chapitre 3. L'une des principales conclusions de ce travail est que, contrairement à la pratique actuelle en radiothérapie externe, la dosimétrie en médecine nucléaire clinique manque d'un programme d'assurance qualité, et que des procédures de contrôle de la qualité doivent être développées pour combler cette lacune. Il est important d'adopter de bonnes pratiques dosimétriques afin de garantir que les résultats dosimétriques sont fiables, traçables et reproductibles. Parmi les éléments clés, citons l'établissement de divers points de contrôle (ou résultats intermédiaires) pour garantir l'intégrité des résultats, l'incorporation de contrôles de santé en interne dans le logiciel afin de minimiser l'erreur humaine et la validation croisée des résultats entre physiciens/cliniciens pour réduire les erreurs de transcription.

De plus, les résultats présentés dans ce chapitre ont nécessité de nombreuses itérations (variant de une à cinq) des résultats dosimétriques, des séances de brainstorming et de débriefing en raison des grandes variations observées dans les résultats fournis par les participants. Cela a clairement révélé le besoin critique d'une série de sessions de formation théorique et pratique (virtuelles et en personne) pour améliorer les compétences des utilisateurs en dosimétrie clinique. Ce travail a servi de tremplin vers le développement d'une bonne pratique de la dosimétrie clinique.

En outre, les résultats présentés dans ce chapitre ont nécessité de nombreuses itérations (variant de une à cinq), des séances de remue-méninges lors du compte-rendu des résultats en raison des grandes variations observées dans les résultats fournis par les participants. Cela a clairement fait ressortir le besoin essentiel d'une série de sessions de formation théorique et pratique (virtuelles et en personne) pour améliorer les compétences des utilisateurs en dosimétrie clinique.

Suite à l'écart important constaté dans cette analyse dosimétrique indépendante, une analyse dosimétrique *“temps réel”* a été réalisée pendant un cycle au siège de l'AIEA à Vienne en utilisant les points de contrôle définis et avec une formation à chaque étape. Il a été établi que le suivi et l'assistance immédiate du spécialiste des applications du fournisseur de logiciels, associés à l'utilisation de points de contrôle prédéfinis, ont considérablement aidé à identifier la majorité des sources d'hétérogénéité parmi les participants et ont produit des résultats dosimétriques exemplaires. Cela a conduit à la création d'un *“ensemble de données de référence”* composé de données TEMP/TDM reconstruites de patients à cinq points dans le temps avec un facteur d'étalonnage associé, un flux de travail standard à suivre dans Planet[®] Dose et des résultats dosimétriques étape par étape avec la moyenne et le pourcentage de variation pour chaque point de contrôle établi,

fournissant ainsi la précision attendue pour les différentes étapes de la procédure (Appendix B). Il permet aux individus d'évaluer leur maîtrise du logiciel sur un jeu de données réaliste, et d'améliorer leurs propres capacités à travailler avec le logiciel.

Alors que le travail précédent a examiné la *précision* de l'analyse dosimétrique en utilisant l'ensemble des données cliniques, une méthodologie standard et un logiciel spécifique, la phase suivante de la thèse a contribué directement au projet DosiTest (www.dositest.org) et s'est concentrée sur *l'exactitude* du processus de dosimétrie clinique. Cela impliquait le développement d'ensembles de données simulées qui pourraient représenter la vérité du terrain pour une application de dosimétrie clinique spécifique.

Par conséquent, la modélisation d'images SPECT réalistes de fantômes anthropomorphes à l'aide du code Monte Carlo de GATE a été réalisée. Cela a nécessité le développement du mode d'acquisition SPECT auto-contour step-and-shoot dans GATE. L'impact de la modélisation du mouvement du détecteur en orbite circulaire (CO) par rapport à celui en orbite non circulaire (NCO) pour l'imagerie SPECT a été évalué en utilisant deux radionucléides : ^{177}Lu (faible pénétration septale) et ^{131}I (forte pénétration septale), dont la comparaison a révélé des disparités de 2,6 % pour ^{177}Lu et d'environ 13 % pour ^{131}I . Cela a mis en évidence la nécessité d'utiliser le mode d'acquisition NCO dans les simulations, en particulier pour les radionucléides à forte pénétration septale. L'impact pourrait donc être important dans le contexte de la dosimétrie MRT, car une éventuelle sous-estimation de l'activité dans le patient due à l'utilisation d'un mode d'acquisition CO vs. NCO peut avoir un effet sur la détermination de la dose absorbée.

Après la mise en œuvre réussie du NCO pour les modèles fantômes, l'imagerie SPECT réaliste pour un ensemble de données de patients cliniques avec des activités réalistes dans un contexte thérapeutique a été modélisée. Elle a ensuite été validée par rapport aux projections cliniques. En outre, l'intégration de ces projections SPECT simulées dans les en-têtes DICOM cliniques a été abordée, de sorte que les projections SPECT/CT résultantes puissent être lues par des stations de travail commerciales.. Il s'agissait d'un facteur déterminant et d'une tâche difficile pour l'évolution du projet DosiTest. L'adaptation des en-têtes DICOM d'un constructeur à l'autre est également essentielle, mais cette possibilité n'a été que partiellement explorée.

La dernière phase de la thèse a démontré la faisabilité du projet DosiTest. Tout d'abord, à partir du même ensemble de données cliniques (TEMP/TDM), la géométrie du patient virtuel associée à l'activité basée sur les voxels à différents points temporels après l'administration du radiopharmaceutique a été dérivée afin

de permettre la modélisation directe de Monte Carlo des cartes de débit de dose absorbée tridimensionnelles de référence pour chaque point temporel. Ensuite, des ensembles de données d'étalonnage et d'images réalistes de patients ont été modélisés et intégrés dans les stations de travail cliniques, de manière à effectuer la dosimétrie clinique sur ces ensembles de données. L'image du fantôme d'étalonnage a été simulée avant les images du patient, ce qui a permis de valider la modélisation de la gamma-caméra et celle des procédures d'acquisition propres à chaque installation clinique.

La dosimétrie de référence a été comparée à la dosimétrie basée sur l'image (en considérant le même fichier de segmentation) à différentes étapes intermédiaires (cartes indexées sur l'activité, débits de dose absorbés). Les différences relatives les plus importantes entre les cartes d'activité et les cartes de débit de dose absorbée étaient de 10,2 % et 8,5 %, respectivement, et ces valeurs étaient principalement attribuables au dernier point temporel qui souffre de statistiques de comptage médiocres en raison des faibles activités restantes. Les différences relatives entre les doses absorbées évaluées parmi des régions segmentées identiques étaient $<13,2$ %.

La preuve de concept du projet DosiTest a été illustrée. Un nombre limité de centres cliniques a été choisi pour participer au projet, qui commence par la génération d'images de calibration spécifiques à chacun des centres participants. Le déroulement de DosiTest dans un contexte plus large, où chaque centre peut utiliser sa propre procédure de dosimétrie clinique (paramètres d'acquisition, logiciel et méthodologie de traitement), devrait fournir un aperçu général des variabilités auxquelles on peut s'attendre dans les procédures de dosimétrie clinique.

Contribution à la discipline

Au cours de ce projet de doctorat, de nouvelles techniques ont été développées pour tenir compte de l'étape de contourage automatique et du mode d'acquisition (step-and-shoot) TEMP dans GATE. Les détails techniques y afférents sont disponibles au chapitre 5. Un exemple des fichiers GATE et les codes python nécessaires à la modélisation du mouvement du détecteur seront disponibles sur le site Gitlab (<https://gitlab.com/gkayal/spect-auto-contouring-motion-in-gate>).

Ce travail a mis en évidence le manque d'assurance qualité en dosimétrie de médecine nucléaire clinique et la nécessité de développer des procédures de contrôle de la qualité.

Un jeu de données de référence, composé de données TEMP/TDM reconstruites d'un patient à cinq points temporels avec un facteur d'étalonnage associé, un

protocole standard à suivre dans Planet[®] Dose et des résultats dosimétriques étape par étape (avec la moyenne et le pourcentage de variation pour chaque point de contrôle établi) a été développé pour permettre aux individus d'évaluer leur maîtrise du logiciel. Le protocole standard utilisé et les résultats étape par étape sont disponibles à l'annexe II. Cet ensemble de données de référence sera mis à disposition par l'Agence internationale de l'énergie atomique (AIEA) dans le cadre du projet de recherche coordonné E23005.

DOSIsoft pourrait également diffuser cet ensemble de données de référence pour la formation aux personnes désireuses de s'entraîner elles-mêmes avec le logiciel.

Suggestions et perspectives futures

L'aspect clinique

Cette comparaison des résultats de dosimétrie clinique a été réalisée sur un ensemble de données cliniques de patients reconstruites avec un facteur de calibration associé (chapitre 3). Les étapes d'étalonnage et de reconstruction sont connues pour avoir un impact sur la détermination de l'activité et, en fin de compte, sur les calculs de la dose absorbée (D'Arienzo et al. 2016; Zimmerman et al. 2017; Wevrett, Fenwick, Scuffham, and Nisbet 2017; Tran-Gia et al. 2021); ces étapes doivent donc être incluses dans l'exercice d'inter-comparaison pour évaluer les variations entre les participants.

Le jeu de données de référence a été généré (chapitre 4) pour étudier la précision de la dosimétrie clinique et la variabilité dépendant de l'opérateur dans un contexte de contrainte (même jeu de données de patients, même procédure de dosimétrie, même logiciel). Il pourrait être intéressant de faire varier certaines étapes, comme l'enregistrement/la segmentation dans Planet[®] Dose, afin de mieux comprendre le spectre des variations possibles et leurs conséquences sur les doses absorbées. En outre, il serait pertinent de traiter le même ensemble de données en utilisant le même protocole (ou un protocole similaire) mais sur un autre logiciel de dosimétrie pour voir les variations des résultats. Cependant, cela n'est pas toujours simple, car tous les logiciels de dosimétrie ne permettent pas d'exporter les résultats intermédiaires (Mora-Ramirez et al. 2020; Huizing, Peters, et al. 2020; Della Gala et al. 2021).

D'autre part, comme le montrent les résultats du chapitre 3, même s'il était possible d'exporter des résultats intermédiaires à partir du logiciel, le fait d'offrir trop de possibilités de traitement augmentait la probabilité de s'écarter de l'approche systématique. À cet égard, le développement et la mise en œuvre de procédures

prédéfinies en dosimétrie clinique contribuent sans aucun doute à réduire les occurrences d'erreurs humaines. En outre, des contrôles de santé intégrés devraient être mis en œuvre directement dans le logiciel de dosimétrie à différentes phases du flux de travail afin de signaler les comportements anormaux.

Il est également essentiel d'établir un standard, tel que la standard DICOM, spécifiquement pour la communication des résultats de dosimétrie, qui comprendrait des informations générales sur l'activité administrée, l'heure et la date de l'injection; des informations relatives au recalage et à la segmentation (le type/modalité du processus de recalage utilisé, la manière dont la segmentation est effectuée sur les images anatomiques ou fonctionnelles); les informations relatives à la détermination de la pharmacocinétique, telles que les points temporels utilisés, le type de modèle d'ajustement utilisé, l'interpolation et l'extrapolation de la courbe (du temps zéro au premier temps d'acquisition, et du dernier temps d'acquisition à l'infini), les informations relatives au calcul de la dose absorbée, son échelle (organe/voxel), l'algorithme utilisé, la prise en compte de la correction de masse/densité, etc.

Fondamentalement, la dosimétrie clinique est un processus complexe, et la traçabilité ne peut être assurée qu'en rapportant la procédure étape par étape et les résultats intermédiaires.

L'aspect de la modélisation

Les modèles de fantômes/patients voxélisés ont été transformés en géométrie de mailles tessellées (tessellated en anglais) pour être utilisés dans la modélisation du mouvement du détecteur à contourage automatique dans l'environnement virtuel GATE. Cette opération a été réalisée pour éviter toute collision du modèle de fantôme/patient avec la tête du détecteur dans GATE. Pour cela, une segmentation de la géométrie du fantôme/patient est nécessaire pour créer des compartiments de maillage séparés. Cela limite la modélisation d'une distribution de densité hétérogène dans un seul volume d'intérêt. Ce n'est peut-être pas un problème pour ce travail puisque les organes critiques sont principalement des tissus mous tels que les reins ou la rate, mais cela peut avoir un impact significatif sur la quantification de l'activité des os et/ou des poumons où la densité est variable. Des travaux supplémentaires visant à incorporer des densités variables dans des structures à mailles tessellées dans GATE pourraient contribuer à une quantification précise de l'activité du ^{131}I (par exemple) lorsque les poumons sont les organes critiques.

La simulation d'images est basée sur un ensemble de données cliniques et l'on dépend donc du modèle DICOM "standard" pour l'extraction d'informations pertinentes. Cependant, la norme DICOM n'est pas toujours mise en œuvre de

manière cohérente, ce qui signifie que la même balise peut se rapporter à une propriété différente selon les constructeurs. Un exemple de cette variation pour l'étiquette "Radial position" dans les modèles DICOM de GE et Siemens est illustré au chapitre 5. Par conséquent, une observation et une analyse rigoureuses sont nécessaires lors du décodage d'en-têtes DICOM provenant de divers fournisseurs.

Un véritable défi associé aux simulations est le temps de calcul. La génération brute d'une image TEMP d'un patient injecté avec environ 2 GBq (ce qui correspond à 318 milliards de primaires dans GATE) nécessiterait 9,6 années de temps de calcul (avec un seul cœur de CPU à 2,6 GHz, 16 Go). Nous avons réussi à obtenir des résultats dans un délai raisonnable grâce à notre accès au centre régional de calcul haute performance (HPC) CALMIP. D'autres possibilités auraient nécessité la mise en œuvre de techniques de réduction de la variance et d'autres approches visant à accroître l'efficacité du calcul. Cela aurait évidemment nécessité un développement et une validation supplémentaires.

Le projet DosiTest

La faisabilité pratique du projet DosiTest est étudiée au chapitre 7. Six centres cliniques ont été recrutés dans le cadre du projet, qui est toujours en cours.

La première tâche était liée à l'étalonnage. Il a été demandé à chaque centre de fournir au centre hôte des informations sur la gamma-caméra disponible dans leur centre, leurs protocoles d'acquisition locaux ainsi qu'un exemple d'image de calibration (images TEMP, série d'images TDM et image TEMP/TDM reconstruite). Ensuite, des images de calibration spécifiques au centre ont été simulées et envoyées au centre clinique respectif.

La deuxième tâche est liée à la reconstruction d'une image de calibration simulée.

À ce jour, trois centres cliniques nous ont fourni l'image de calibration simulée reconstruite ainsi que le facteur de calibration simulé. Cette tâche est toujours en cours.

La tâche suivante consiste à générer un ensemble de données TEMP/TDM sur les patients pour chaque centre en fonction du réglage de leur gamma-caméra et de leurs protocoles d'acquisition, mais avec le modèle de patient et les distributions d'activité définis. L'un des défis anticipés dans ce travail serait d'extrapoler la distribution d'activité disponible (c'est-à-dire à cinq points de temps particuliers) à différents points de temps qui pourraient être requis par le centre en raison de ses procédures locales. Cela nécessiterait des recherches supplémentaires. L'incorporation d'une dosimétrie hybride (combinaison d'images TEMP/TDM et

d'images planaires) serait également un défi, et nécessiterait probablement de combiner des images de modèles et de patients réels pour générer les fichiers d'entrée. Pourtant, DosiTest, dans son format actuel, s'est avéré réalisable. Les tâches ultérieures comprennent la réalisation de la dosimétrie sur l'ensemble des données simulées et l'évaluation comparative de ces résultats avec la dosimétrie de référence.

À l'heure actuelle, tous les travaux réalisés dans le cadre de ce projet ont porté sur le traitement au Lutathera[®] (génération d'images TEMP/TDM au ¹⁷⁷Lu, distribution de l'activité). Le concept de DosiTest peut évidemment être étendu à d'autres applications de MRT. En principe, les méthodologies, les outils et les connaissances développés au cours de ce doctorat peuvent être utilisés à cette fin, réduisant ainsi le temps nécessaire pour développer une instance différente de DosiTest. Ce projet est un effort à long terme, et tous les développements sont librement accessibles pour permettre sa continuation.

Appendices



Sample Google spreadsheet used for the data collection

A google spreadsheet was circulated to each participant for them to provide intermediary results. Each spreadsheet contains seven distinct sheets, each corresponding to intermediate results (registration, volume, counts, activity, time-integrated activity, absorbed dose rates and absorbed dose).

	A	B	C
1		C1	
2	Software version:		
3	Study used: Folder:		
4	Time points (SPECT/CT) added : T1 (1h), T2 (4h), T3 (24h), T4 (48h), T5 (96h)		
5	1. Step: REGISTRATION (points:T1, T2, T3, T4), "Rigid" used?		
6	Registration validation used: Diagonal fusion		
7			
8			
9			
10			
11			
12			
13			
14			
15			
16			
17			
18			
19			
20			
21			
22			
23			
24			
25			
26			

Sheet 1 is about registration

	A	B	C
1	STRUCTURE CREATION	C1	
2			
3	'Anatom mode' selected?		
4	For the liver		
5	Confirm sequence: Add a structure → Structure edition; → Contour edition: brush		
6	'Simple 2D brush' used?		
7	Confirm sequence: Advanced options→ Threshold→ Absolute		
8	If Yes, enter Min value		
9	If Yes, enter Max value		
10	Contour smoothing unselected?		
11	Named Whole_Liver?		
12	Whole Liver Volume (cm ³) T1		
13	Whole Liver Voxels T1		
14	Whole Liver Volume (cm ³) T2		
15	Whole Liver Voxels T2		
16	Whole Liver Volume (cm ³) T3		
17	Whole Liver Voxels T3		
18	Whole Liver Volume (cm ³) T4		
19	Whole Liver Voxels T4		
20	Whole Liver Volume (cm ³) T5		
21	Whole Liver Voxels T5		
22	For the kidneys		
23	Confirm sequence: Add a structure → Structure edition; → Contour edition: brush		
24	'Simple 2D brush' used?		

Sheet 2 is about segmentation (volumes and voxels for each time point and liver)

	A	B	C
1	STRUCTURE CREATION	C1	
22	For the kidneys		
23	Confirm sequence: Add a structure → Structure edition; → Contour edition: brush		
24	'Simple 2D brush' used?		
25	Confirm sequence: Advanced options → Threshold → Absolute		
26	If Yes, enter Min value		
27	If Yes, enter Max value		
28	Confirm contour smoothing is unselected		
29	Confirm hole filling is unselected		
30	Named R_Kidney?		
31	R-kidney Volume (cm ³) T1		
32	R-kidney Voxels T1		
33	R-kidney Volume (cm ³) T2		
34	R-kidney Voxels T2		
35	R-kidney Volume (cm ³) T3		
36	R-kidney Voxels T3		
37	R-kidney Volume (cm ³) T4		
38	R-kidney Voxels T5		
39	R-kidney Volume (cm ³) T5		
40	R-kidney Voxels T4		
41	Named L_Kidney?		
42	L-kidney Volume (cm ³) T1		
43	L-kidney Voxels T1		

Sheet 2 is about segmentation (volumes and voxels for each time point and each kidney)

	A	B	C
1	STRUCTURE CREATION	C1	
41	Named L_Kidney?		
42	L-kidney Volume (cm ³) T1		
43	L-kidney Voxels T1		
44	L-kidney Volume (cm ³) T2		
45	L-kidney Voxels T2		
46	L-kidney Volume (cm ³) T3		
47	L-kidney Voxels T3		
48	L-kidney Volume (cm ³) T4		
49	L-kidney Voxels T4		
50	L-kidney Volume (cm ³) T5		
51	L-kidney Voxels T5		
52	All structures were propagated on the rigid way, through all time points?		
53	For the lesions		
54	'Func mode' selected?		
55	Uptake area of detection were created on each time point?		
56	On segmentation methods: Fixed threshold of 40%?		
57	Created four structures (1-Anterior, 2-Lateral, 3-Posterior, 4-Inferior)?		
58	Structures created with the help of medical doctor?		
59	For 1-Anterior		
60	A_Lesion Volume (cm ³) T1		
61	A_Lesion Voxels T1		
62	A_Lesion Volume (cm ³) T2		

Sheet 2 is about segmentation (volumes and voxels for each time point and each lesion)

	A	B	C
1	STRUCTURE CREATION	C1	
59	For 1-Anterior		
60	A_Lesion Volume (cm ³) T1		
61	A_Lesion Voxels T1		
62	A_Lesion Volume (cm ³) T2		
63	A_Lesion Voxels T2		
64	A_Lesion Volume (cm ³) T3		
65	A_Lesion Voxels T3		
66	A_Lesion Volume (cm ³) T4		
67	A_Lesion Voxels T4		
68	A_Lesion Volume (cm ³) T5		
69	A_Lesion Voxels T5		
70	For 2-Lateral		
71	L_Lesion Volume (cm ³) T1		
72	L_Lesion Voxels T1		
73	L_Lesion Volume (cm ³) T2		
74	L_Lesion Voxels T2		
75	L_Lesion Volume (cm ³) T3		
76	L_Lesion Voxels T3		
77	L_Lesion Volume (cm ³) T4		
78	L_Lesion Voxels T4		
79	L_Lesion Volume (cm ³) T5		
80	L_Lesion Voxels T5		

Sheet 2 is about segmentation (volumes and voxels for each time point and two lesions)

	A	B	C
1	STRUCTURE CREATION	C1	
80	L_Lesion Voxels T5		
81	For 3-Posterior		
82	P_Lesion Volume (cm ³) T1		
83	P_Lesion Voxels T1		
84	P_Lesion Volume (cm ³) T2		
85	P_Lesion Voxels T2		
86	P_Lesion Volume (cm ³) T3		
87	P_Lesion Voxels T3		
88	P_Lesion Volume (cm ³) T4		
89	P_Lesion Voxels T4		
90	P_Lesion Volume (cm ³) T5		
91	P_Lesion Voxels T5		
92	For 4-Inferior		
93	I_Lesion Volume (cm ³) T1		
94	I_Lesion Voxels T1		
95	I_Lesion Volume (cm ³) T2		
96	I_Lesion Voxels T2		
97	I_Lesion Volume (cm ³) T3		
98	I_Lesion Voxels T3		
99	I_Lesion Volume (cm ³) T4		
100	I_Lesion Voxels T4		
101	I_Lesion Volume (cm ³) T5		

Sheet 2 is about segmentation (volumes and voxels for each time point and other lesions)

	A	B	C
1	STRUCTURE CREATION	C1	
99	I_Lesion Volume (cm ³) T4		
100	I_Lesion Voxels T4		
101	I_Lesion Volume (cm ³) T5		
102	I_Lesion Voxels T5		
103	All functional structures were propagated on Anat mode, through all time points?		
104	Confirm Forcer la propagation is unchecked		
105	A boolean operation was done between liver and all the four lesions?		
106	The new structure was selected as a "Standard structure"?		
107	Named Normal_Liver?		
108	Normal Liver Volume (cm ³) T1		
109	Normal Liver Voxels T1		
110	Normal Liver Volume (cm ³) T2		
111	Normal Liver Voxels T2		
112	Normal Liver Volume (cm ³) T3		
113	Normal Liver Voxels T3		
114	Normal Liver Volume (cm ³) T4		
115	Normal Liver Voxels T4		
116	Normal Liver Volume (cm ³) T5		
117	Normal Liver Voxels T5		
118	STRUCTURE EXPORTATION		
119	Exportation → 'Inserion into database of structures at RT Struct format'		
120	Confirm choosing all structures created, EXCEPT for the lesions (anatomical mode)		

Sheet 2 is about segmentation (volumes and voxels for each time point and normal liver)

	A	B	C
1	Total Counts	C1	
2	Unit		
3	Whole_Liver		
4	T1		
5	T2		
6	T3		
7	T4		
8	T5		
9			
10	R_Kidney		
11	T1		
12	T2		
13	T3		
14	T4		
15	T5		
16			
17	L_Kidney		
18	T1		
19	T2		
20	T3		
21	T4		
22	T5		
23			
24	Normal_Liver		
25	T1		
26	T2		

Sheet 3 is about total counts for each time point and healthy organs

	A	B	C
1	Total Counts	C1	
2	Unit		
24	Normal_Liver		
25	T1		
26	T2		
27	T3		
28	T4		
29	T5		
30			
31	1-Anterior (Lesion)		
32	T1		
33	T2		
34	T3		
35	T4		
36	T5		
37			
38	2-Lateral (Lesion)		
39	T1		
40	T2		
41	T3		
42	T4		
43	T5		
44			
45	3-Posterior (Lesion)		
46	T1		
47	T2		

Registration Segmentation **Total Counts** Activity TIA&Fitting ADR AD calc

Sheet 3 is about total counts for each time point and normal liver with lesions

	A	B	C
1	Total Counts	C1	
2	Unit		
44			
45	3-Posterior (Lesion)		
46	T1		
47	T2		
48	T3		
49	T4		
50	T5		
51			
52	4-Inferior (Lesion)		
53	T1		
54	T2		
55	T3		
56	T4		
57	T5		
58			
59			
60			
61			
62			
63			
64			
65			
66			
67			

Registration Segmentation **Total Counts** Activity TIA&Fitting ADR AD calc

Sheet 3 is about total counts for each time point and other lesions

	A	B	C
1	Activity quantification in each VOI	C1	
2	Unit		
3	Whole_Liver		
4	T1		
5	T2		
6	T3		
7	T4		
8	T5		
9	R_Kidney		
10	T1		
11	T2		
12	T3		
13	T4		
14	T5		
15	L_Kidney		
16	T1		
17	T2		
18	T3		
19	T4		
20	T5		
21	Normal_Liver		
22	T1		
23	T2		
24	T3		
25	T4		
26	T5		

Sheet 4 is about total activity for each time point and healthy organs

	A	B	C
1	Activity quantification in each VOI	C1	
2	Unit		
21	Normal_Liver		
22	T1		
23	T2		
24	T3		
25	T4		
26	T5		
27	1-Anterior (Lesion)		
28	T1		
29	T2		
30	T3		
31	T4		
32	T5		
33	2-Lateral (Lesion)		
34	T1		
35	T2		
36	T3		
37	T4		
38	T5		
39	3-Posterior (Lesion)		
40	T1		
41	T2		
42	T3		
43	T4		
44	T5		

Sheet 4 is about total activity for each time point and normal liver with lesions

	A	B	C
1	Activity quantification in each VOI	C1	
2	Unit		
39	3-Posterior (Lesion)		
40	T1		
41	T2		
42	T3		
43	T4		
44	T5		
45	4-Inferior (Lesion)		
46	T1		
47	T2		
48	T3		
49	T4		
50	T5		
51			
52			
53			
54			
55			
56			
57			
58			
59			
60			
61			
62			

Sheet 4 is about total activity for each time point and other lesions

	A	B	C
1	TIA & Fitting	C1	
2	Time Integrated Activity Unit		
3	Segments		
4	Whole_Liver		
5	R_Kidney		
6	L_Kidney		
7	Normal_Liver		
8	1-Anterior (Lesion)		
9	2-Lateral (Lesion)		
10	3-Posterior (Lesion)		
11	4-Inferior (Lesion)		
12			
13	TIA (in interpolation)		
14	Segments		
15	Whole_Liver		
16	R_Kidney		
17	L_Kidney		
18	Normal_Liver		
19	1-Anterior (Lesion)		
20	2-Lateral (Lesion)		
21	3-Posterior (Lesion)		
22	4-Inferior (Lesion)		
23			
24	Fitting Equation		
25	Whole_Liver		
26	PHARMACOKINETIC FIT		

Sheet 5 is about time integrated activity (TIA) for various VOIs

	A	B	C
1	TIA & Fitting	C1	
2	Time Integrated Activity Unit		
23			
24	Fitting Equation		
25	Whole_Liver		
26	PHARMACOKINETIC FIT		
27	Model		
28	Equation		
29	MSD		
30	Rho		
31	Rho trap		
32			
33	R_Kidney		
34	PHARMACOKINETIC FIT		
35	Model		
36	Equation		
37	MSD		
38	Rho		
39	Rho trap		
40			
41	L_Kidney		
42	PHARMACOKINETIC FIT		
43	Model		
44	Equation		
45	MSD		
46	Rho		

Sheet 5 is about time integrated activity (TIA) fitting for healthy organs

	A	B	C
1	TIA & Fitting	C1	
2	Time Integrated Activity Unit		
42	PHARMACOKINETIC FIT		
43	Model		
44	Equation		
45	MSD		
46	Rho		
47	Rho trap		
48			
49	Normal_Liver		
50	PHARMACOKINETIC FIT		
51	Model		
52	Equation		
53	MSD		
54	Rho		
55	Rho trap		
56			
57	1-Anterior (Lesion)		
58	PHARMACOKINETIC FIT		
59	Model		
60	Equation		
61	MSD		
62	Rho		
63	Rho trap		
64			
65	2-Lateral (Lesion)		

Sheet 5 is about time integrated activity (TIA) fitting for normal liver and anterior lesion

	A	B	C
1	TIA & Fitting	C1	
2	Time Integrated Activity Unit		
65	2-Lateral (Lesion)		
66	PHARMACOKINETIC FIT		
67	Model		
68	Equation		
69	MSD		
70	Rho		
71	Rho trap		
72			
73	3-Posterior (Lesion)		
74	PHARMACOKINETIC FIT		
75	Model		
76	Equation		
77	MSD		
78	Rho		
79	Rho trap		
80			
81	4-Inferior (Lesion)		
82	PHARMACOKINETIC FIT		
83	Model		
84	Equation		
85	MSD		
86	Rho		
87	Rho trap		
88			

Sheet 5 is about time integrated activity (TIA) fitting for three lesions

	A	B	C
1	Average Absorbed Dose Rate	C1	
2	Unit		
3	Whole_Liver		
4	T1		
5	T2		
6	T3		
7	T4		
8	T5		
9	R_Kidney		
10	T1		
11	T2		
12	T3		
13	T4		
14	T5		
15	L_Kidney		
16	T1		
17	T2		
18	T3		
19	T4		
20	T5		
21	Normal_Liver		
22	T1		
23	T2		
24			

Sheet 6 is about absorbed dose rates (ADR) for each time point and healthy organs

	A	B	C
1	Average Absorbed Dose Rate	C1	
2	Unit		
21	Normal_Liver		
22	T1		
23	T2		
24	T3		
25	T4		
26	T5		
27	1-Anterior		
28	T1		
29	T2		
30	T3		
31	T4		
32	T5		
33	2-Lateral		
34	T1		
35	T2		
36	T3		
37	T4		
38	T5		
39	3-Posterior		
40	T1		
41	T2		

Sheet 6 is about absorbed dose rates (ADR) for each time point and normal liver and lesions

	A	B	C
1	Average Absorbed Dose Rate	C1	
2	Unit		
39	3-Posterior		
40	T1		
41	T2		
42	T3		
43	T4		
44	T5		
45	4-Inferior		
46	T1		
47	T2		
48	T3		
49	T4		
50	T5		
51			
52			
53			
54			
55			
56			
57			
58			
59			
60			

Sheet 6 is about absorbed dose rates (ADR) for each time point and lesions

	A	B	C
1	Average Absorbed Dose Rate	C1	
2	Unit		
59	Fitting Equation		
60	Whole_Liver_FIT		
61	PHARMACOKINETIC FIT		
62	Model		
63	Equation		
64	MSD		
65	Rho		
66	Rho trap		
67			
68	R_Kidney_FIT		
69	PHARMACOKINETIC FIT		
70	Model		
71	Equation		
72	MSD		
73	Rho		
74	Rho trap		
75			
76	L_Kidney_FIT		
77	PHARMACOKINETIC FIT		
78	Model		
79	Equation		
80	MSD		

Sheet 6 is about absorbed dose rates (ADR) fitting for each time point and healthy organs

	A	B	C
1	Average Absorbed Dose Rate	C1	
2	Unit		
76	L_Kidney_FIT		
77	PHARMACOKINETIC FIT		
78	Model		
79	Equation		
80	MSD		
81	Rho		
82	Rho trap		
83			
84	Normal_Liver_FIT		
85	PHARMACOKINETIC FIT		
86	Model		
87	Equation		
88	MSD		
89	Rho		
90	Rho trap		
91			
92	1-Anterior (Lesion)_FIT		
93	PHARMACOKINETIC FIT		
94	Model		
95	Equation		
96	MSD		
97	Rho		

Sheet 6 is about absorbed dose rates (ADR) for each time point and organs with lesions

	A	B	C
1	Average Absorbed Dose Rate	C1	
2	Unit		
92	1-Anterior (Lesion)_FIT		
93	PHARMACOKINETIC FIT		
94	Model		
95	Equation		
96	MSD		
97	Rho		
98	Rho trap		
99			
100	2-Lateral (Lesion)_FIT		
101	PHARMACOKINETIC FIT		
102	Model		
103	Equation		
104	MSD		
105	Rho		
106	Rho trap		
107			
108	3-Posterior (Lesion)_FIT		
109	PHARMACOKINETIC FIT		
110	Model		
111	Equation		
112	MSD		
113	Rho		

Sheet 6 is about absorbed dose rates (ADR) fitting for each time point and lesions

	A	B	C
1	Average Absorbed Dose Rate	C1	
2	Unit		
107			
108	3-Posterior (Lesion)_FIT		
109	PHARMACOKINETIC FIT		
110	Model		
111	Equation		
112	MSD		
113	Rho		
114	Rho trap		
115			
116	4-Inferior (Lesion)_FIT		
117	PHARMACOKINETIC FIT		
118	Model		
119	Equation		
120	MSD		
121	Rho		
122	Rho trap		
123			
124			
125			
126			
127			
128			

Sheet 6 is about absorbed dose rates (ADR) fitting for each time point and other lesions

	A	B	C
1	Absorbed Dose Calculation	C1	
2	Unit		
3	Radionuclide' section: Type: Lu177		
4	Radionuclide' section: Half-life: 9571 sec		
5	Activity (MBq):		
6	Time of administration: (in AM)		
7	Enter 'Calibration factor' (Bq) used: should be (Bq)		
8	Confirm integration range from 0 to 2400 days		
9	Following options used: 'Conv' and 'Dens' should be checked		
10	Av. absorbed dose (Gy) R-kidney		
11	Av. absorbed dose (Gy) L-kidney		
12	Av. absorbed dose (Gy) Whole Liver		
13	Av. absorbed dose (Gy) Normal Liver		
14	Av. absorbed dose (Gy) Lesion 1 Anterior		
15	Av. absorbed dose (Gy) Lesion 2 Lateral		
16	Av. absorbed dose (Gy) Lesion 3 Posterior		
17	Av. absorbed dose (Gy) Lesion 4 Inferior		
18			
19			
20			
21			
22			
23			
24			

+ ☰ Registration ▾ Segmentation ▾ Total Counts ▾ Activity ▾ TIA&Fitting ▾ ADR ▾ **AD calc ▾**

Sheet 7 is about absorbed dose (AD) for each VOI

B

Benchmark Dataset

Our contribution to IAEA-CRP E23005 resulted in the generation of a '*benchmark dataset*' consisting of:

- reconstructed patient SPECT/CT data at five time points
- an associated calibration factor
- a standard workflow to be followed in Planet[®] Dose
- Step-by-step dosimetry results (with mean and percentage of variation for each established checkpoint)

B.1 Reconstructed patient SPECT/CT data at five time points

The reconstructed patient SPECT/CT images at five time points (1 hour, 4 hours, 24 hours, 48 hours and 96 hours post injection) will be made available on the IAEA website.

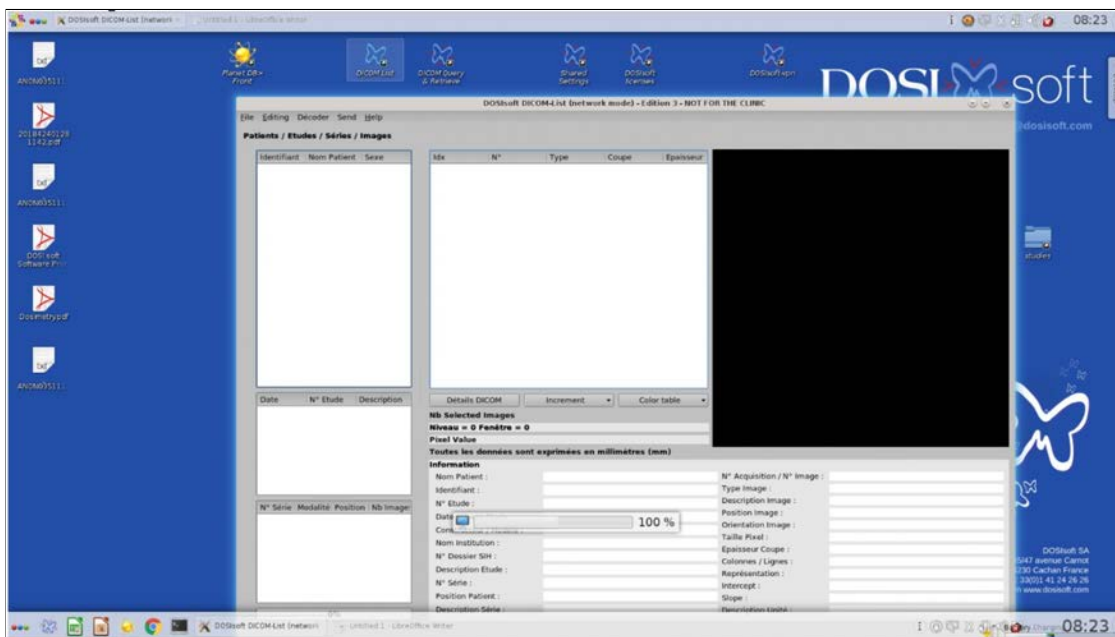
In the meantime, the project coordinator: Mr Peter Knoll (P.Knoll@iaea.org) can be contacted.

B.2 Associated calibration factor

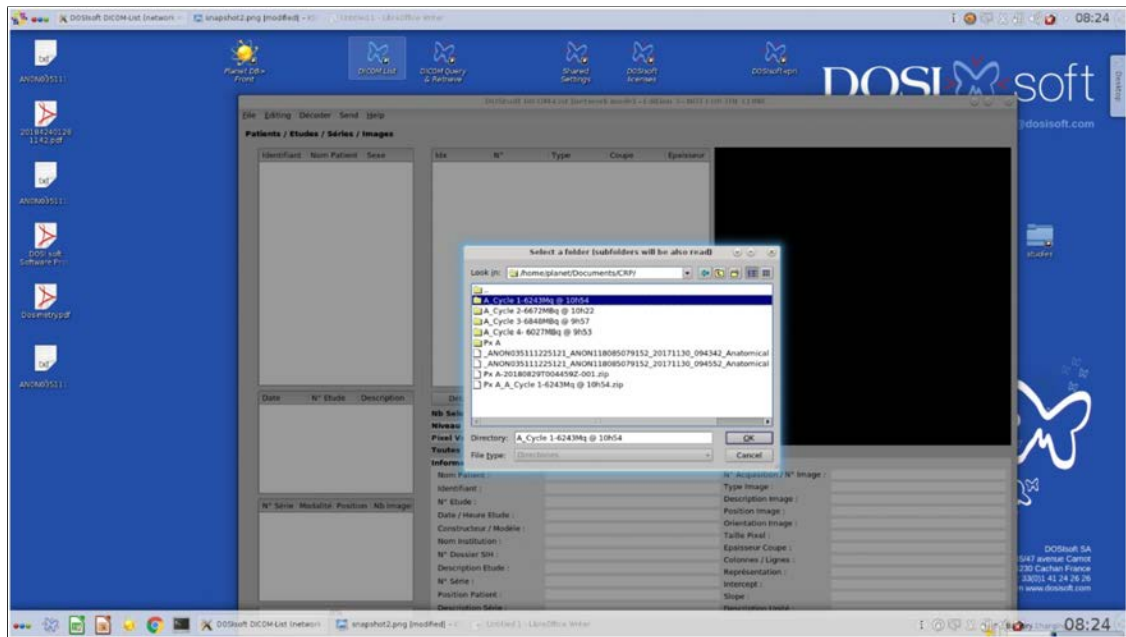
The associated calibration factor corresponding to the patient images is 122.6 Bq/counts (considering 1800 seconds calibration acquisition time).

B.3 Standard Protocol (SOP) in Planet[®] Dose

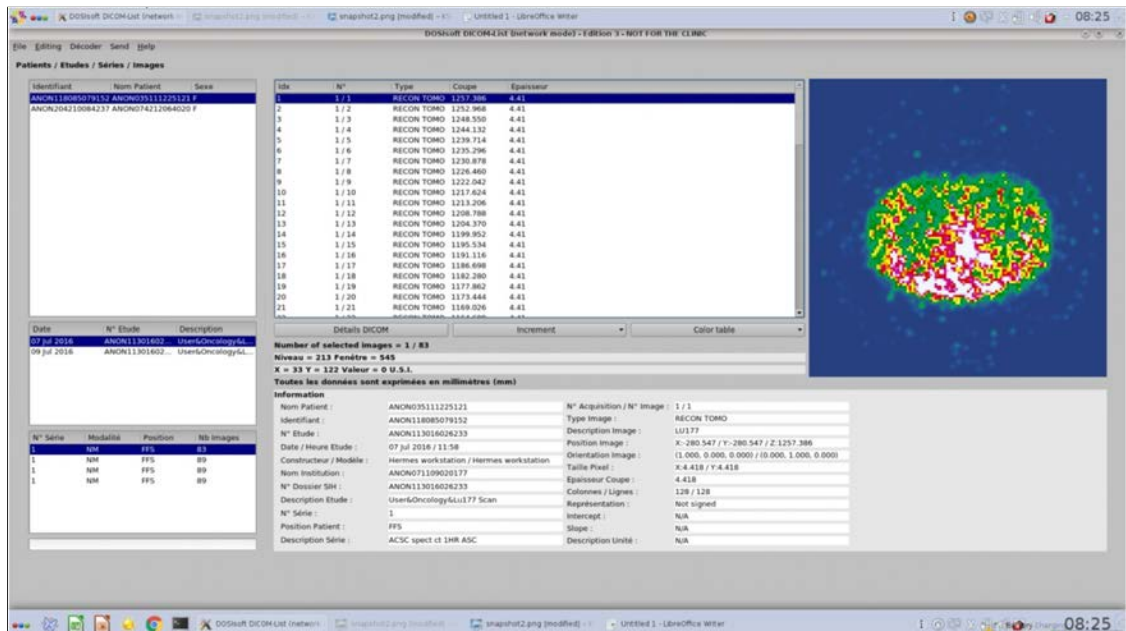
The following images describes the different steps for processing the images starting from uploading the images, creating a Planet onco study, registration, segmentation, pharmacokinetic assessment and fitting methods along with computation of absorbed doses. Finally, a brief description of where to find the data to put into the circulated Google spreadsheet ([Appendix A](#)) is provided.



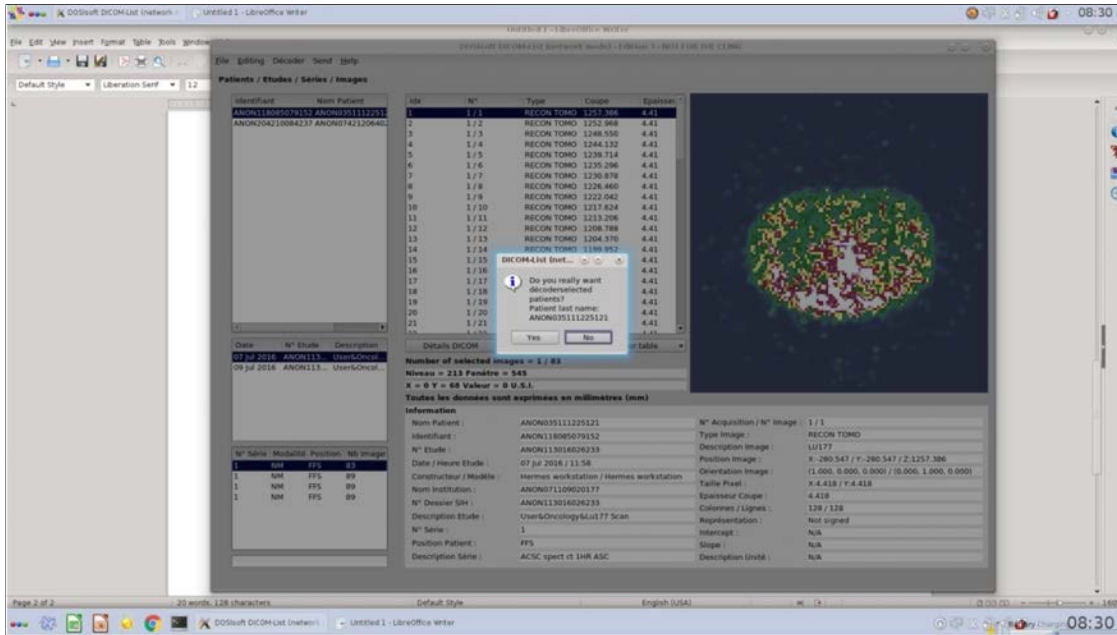
Open DICOM List



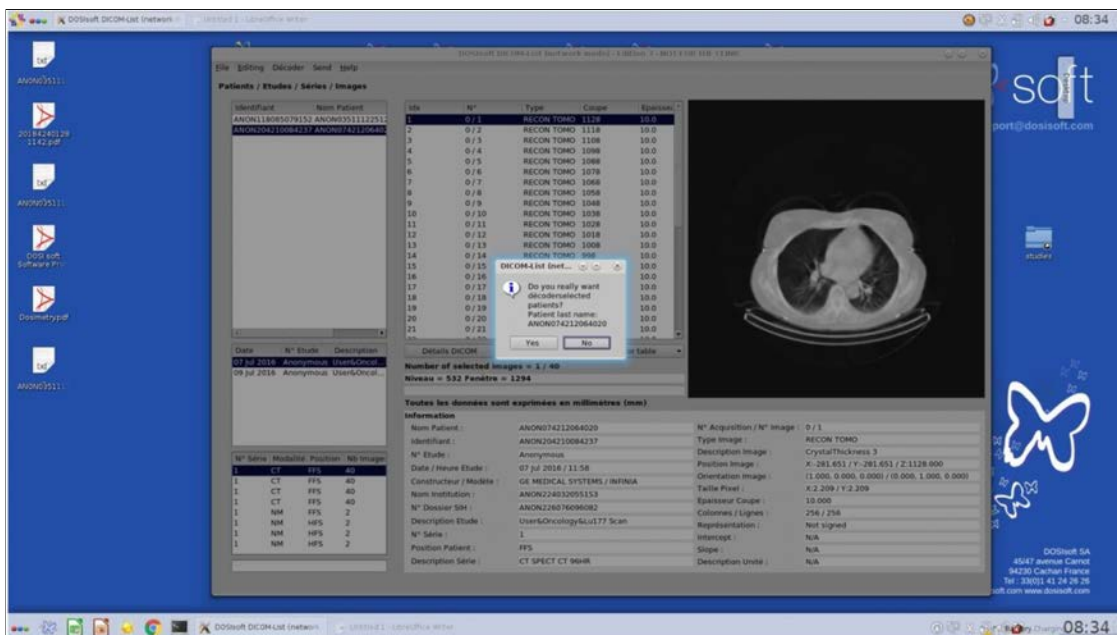
Select File > Select Folder, or directly drag and drop from the folder



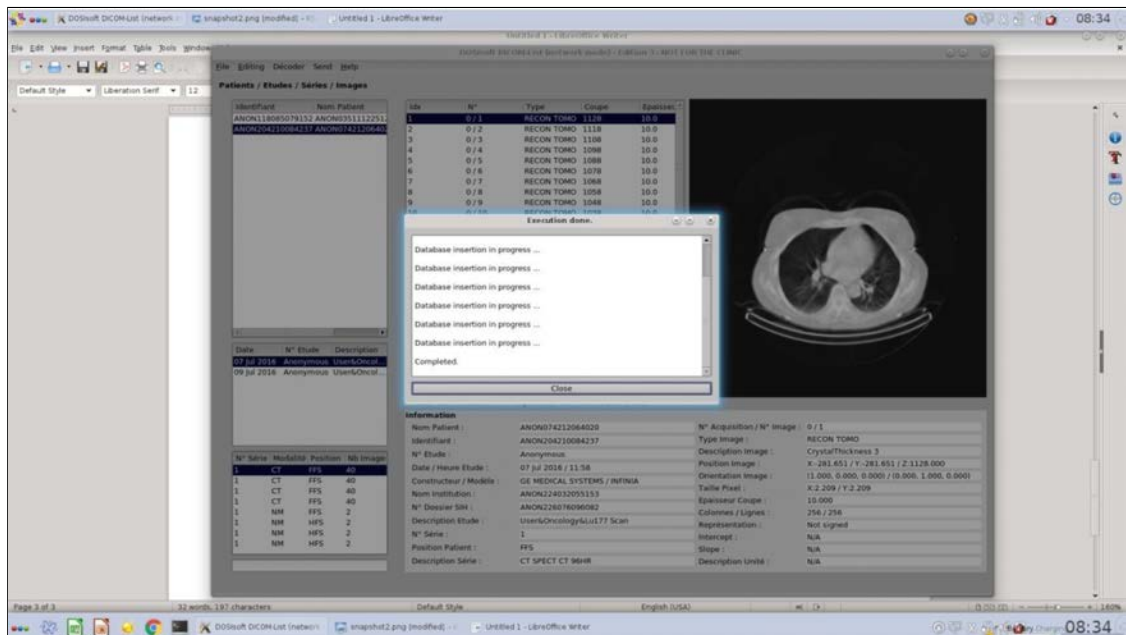
In the images, because the patient has been anonymized, 2 different patients are recognized by the DICOM List



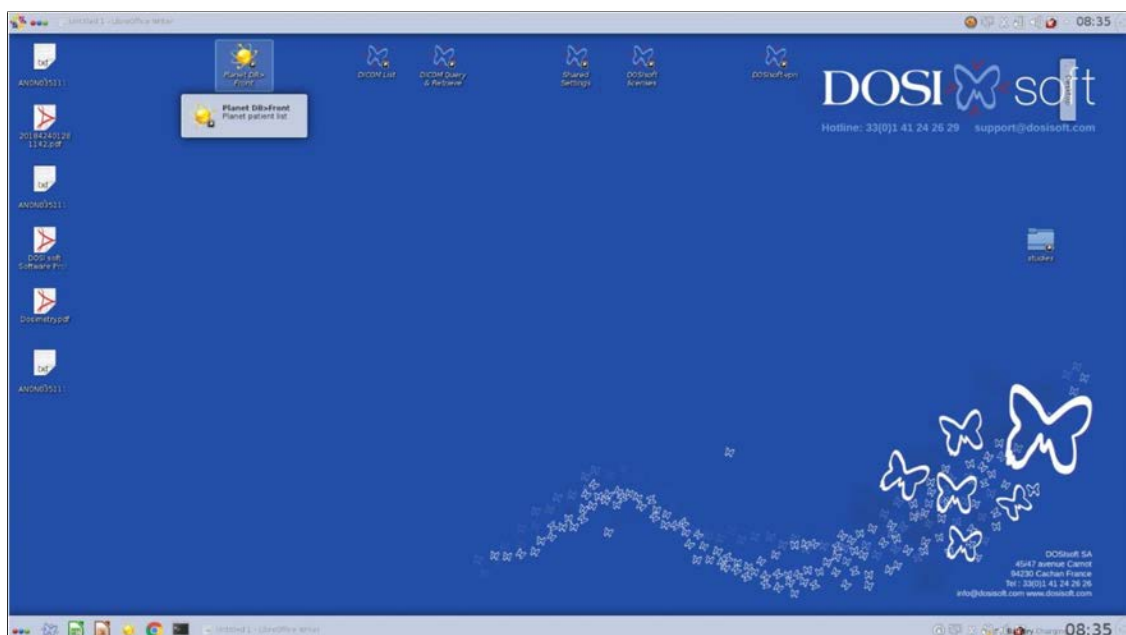
Now, you must decode the 2 patients. In Decoder selected patients



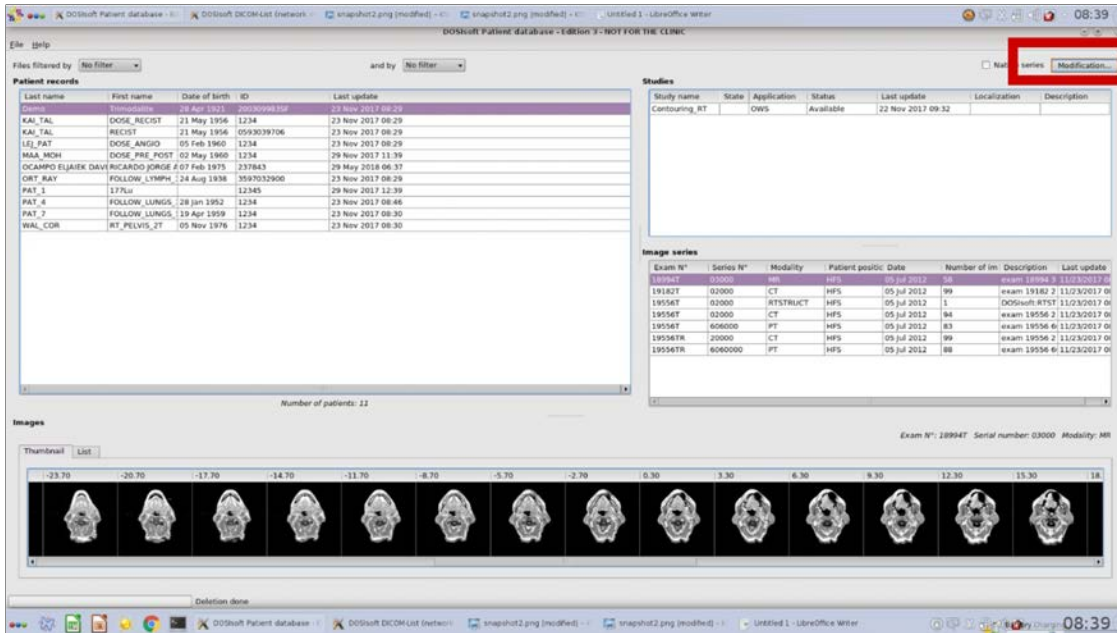
Click on Yes



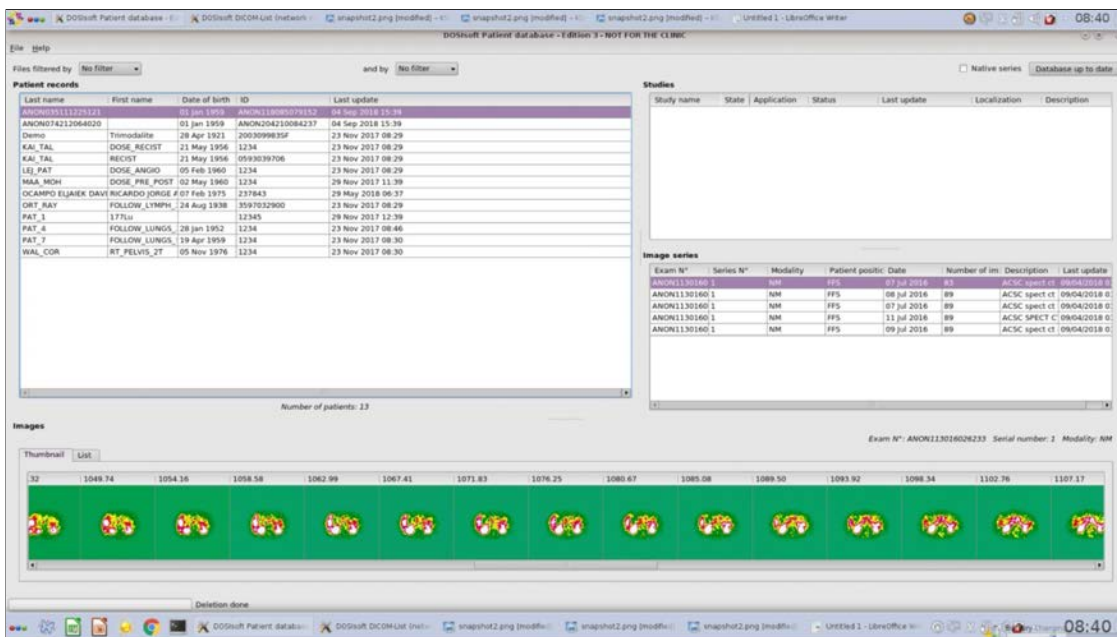
Once the process is completed, click Close



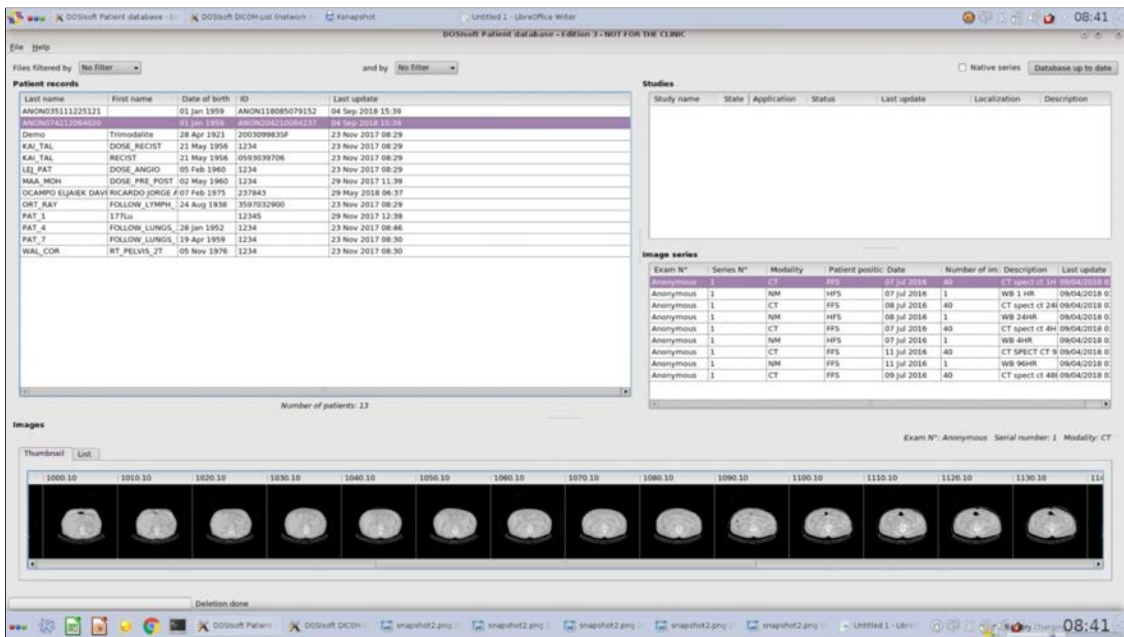
Now, you can open Planet



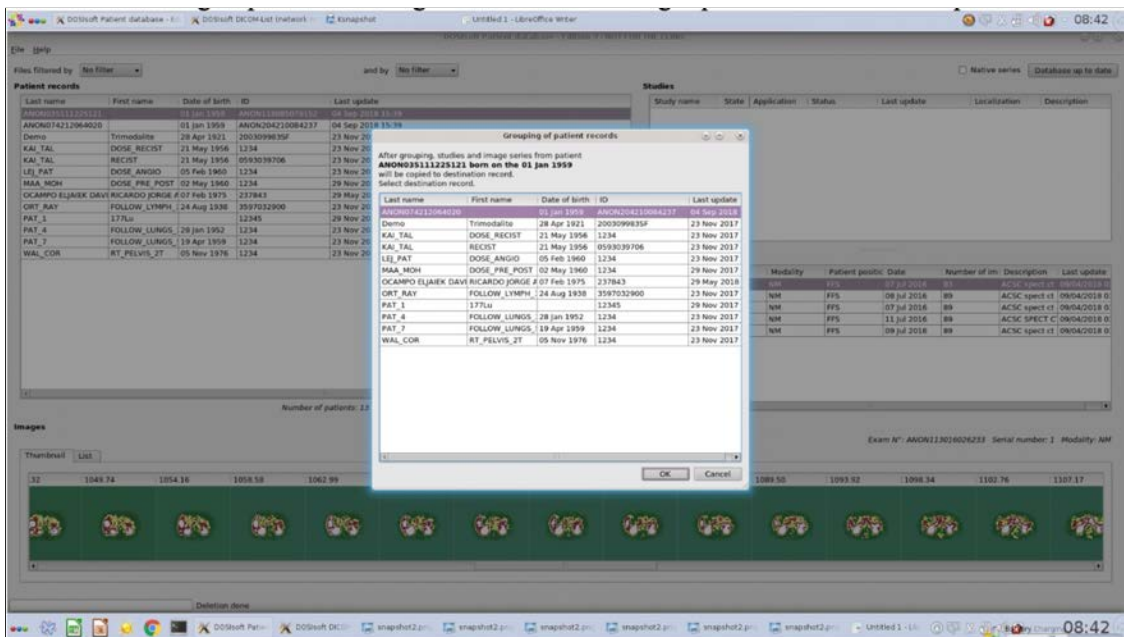
Update the images



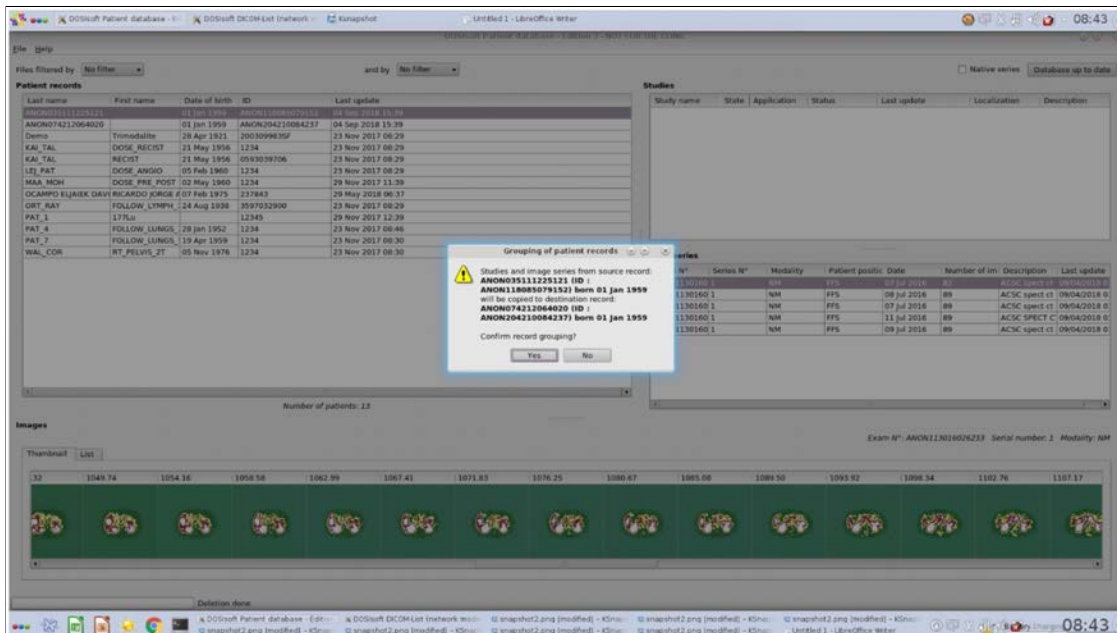
Now, the first patient has the SPECT images



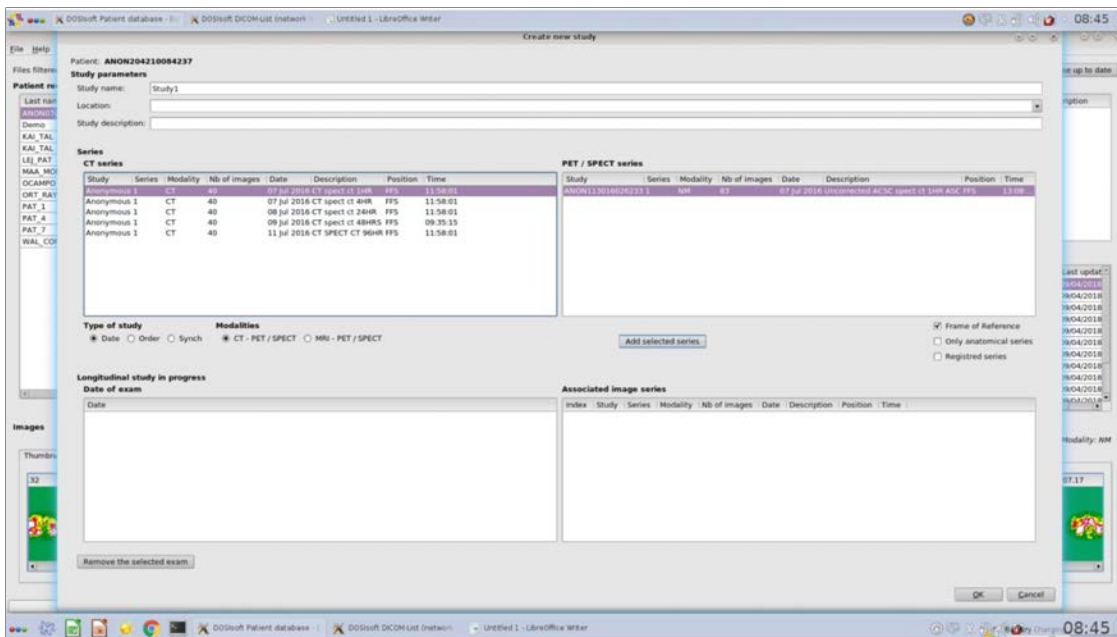
And the second the CT and the WB images



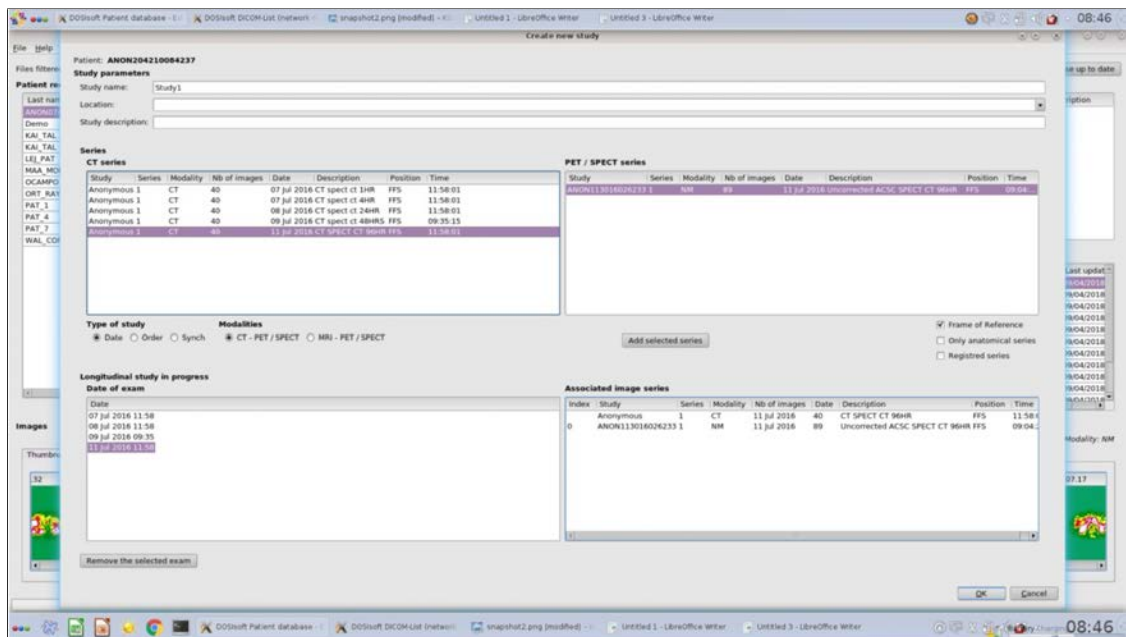
You must group both. Right click on the SPECT images patient and select Group



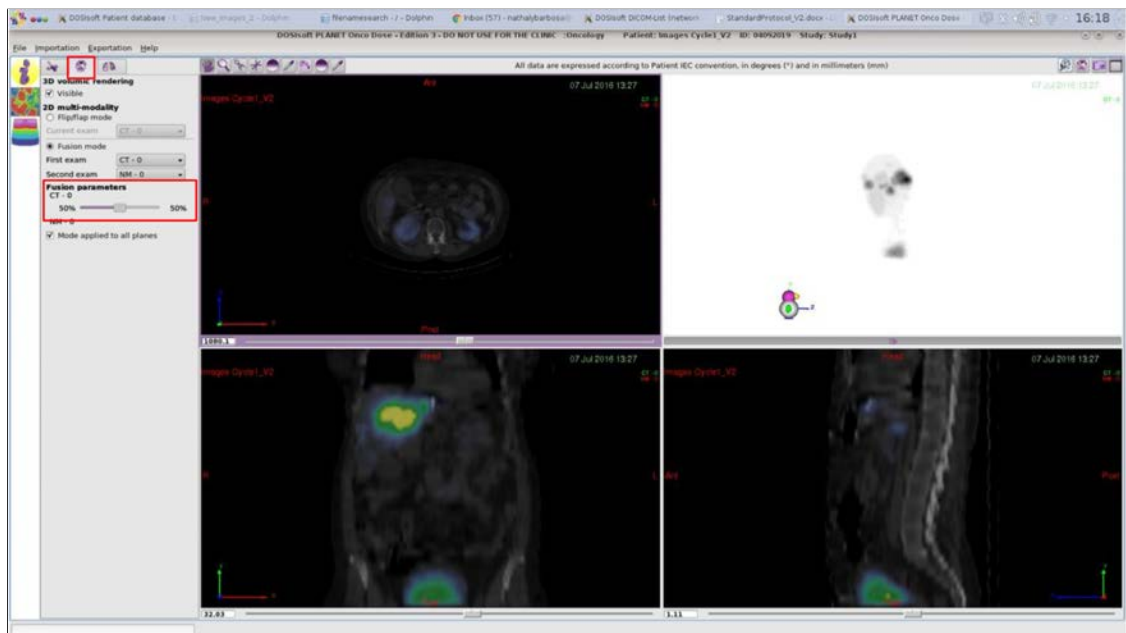
Select the CT patient, and ok



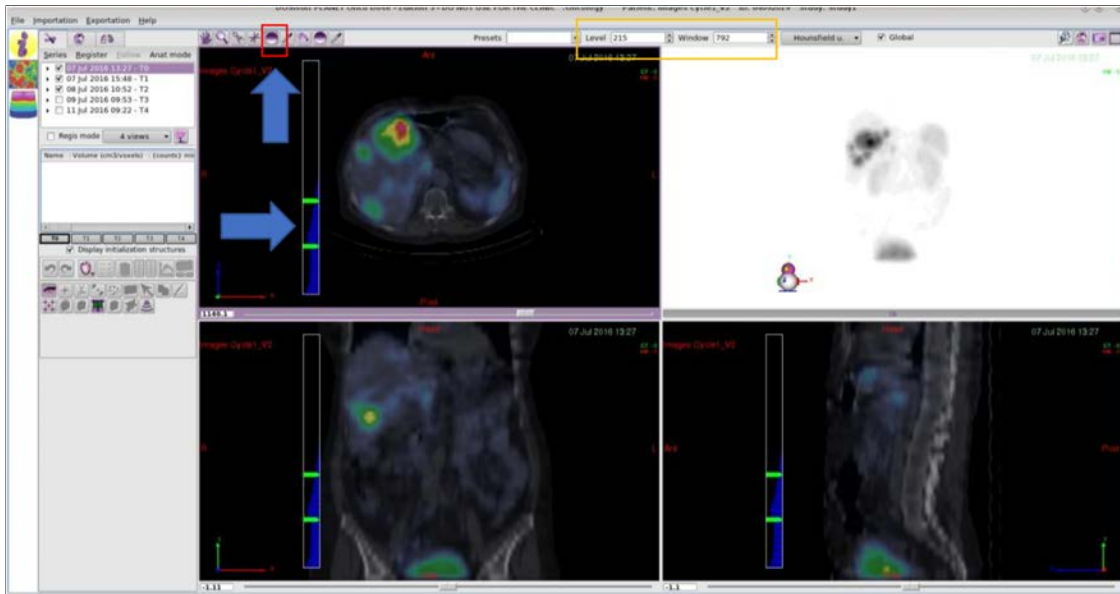
Confirm the grouping. Now, one patient contains all the images



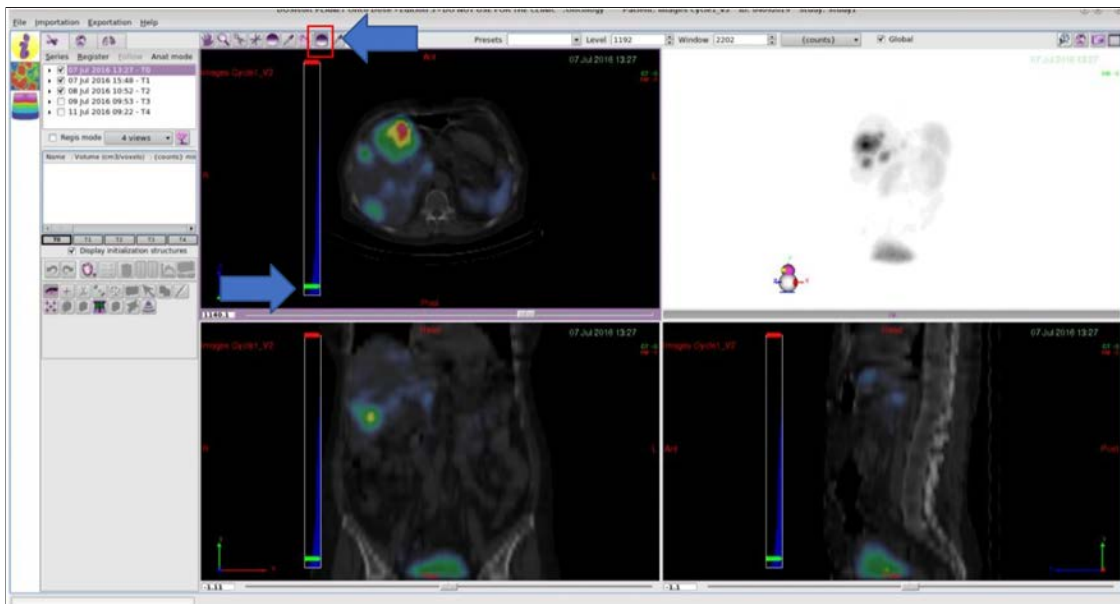
Click right on the patient, select “Create a study Planet onco” and select the images as needed



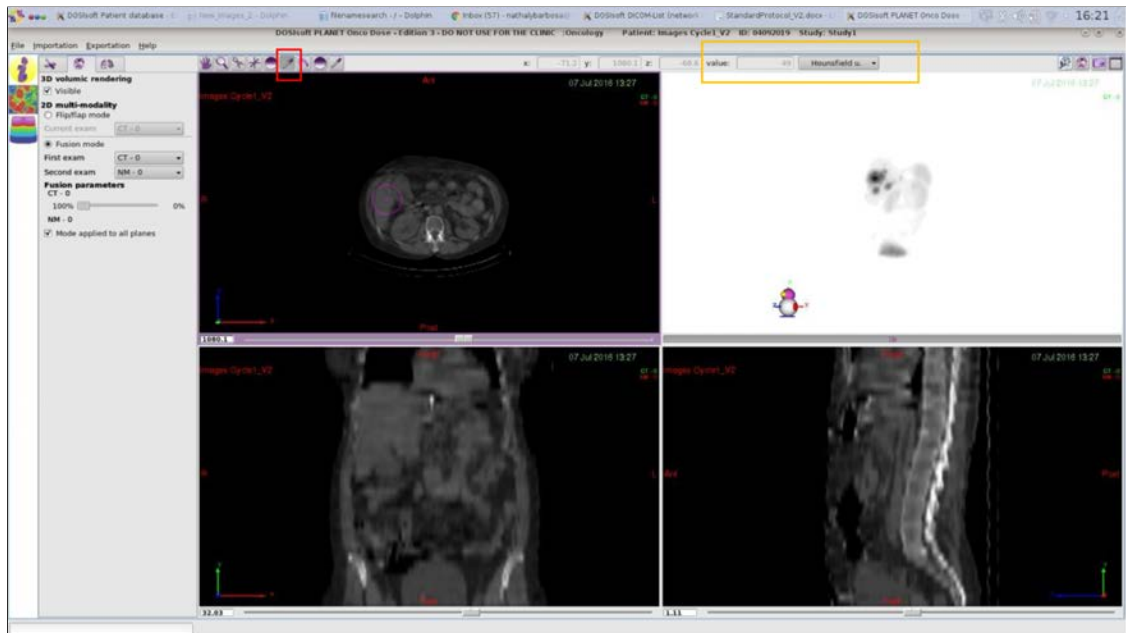
Fusion Properties allows the user to visualise CT or MN as needed. To navigate between the slices of the image, press Ctrl while using the scroll wheel of your mouse



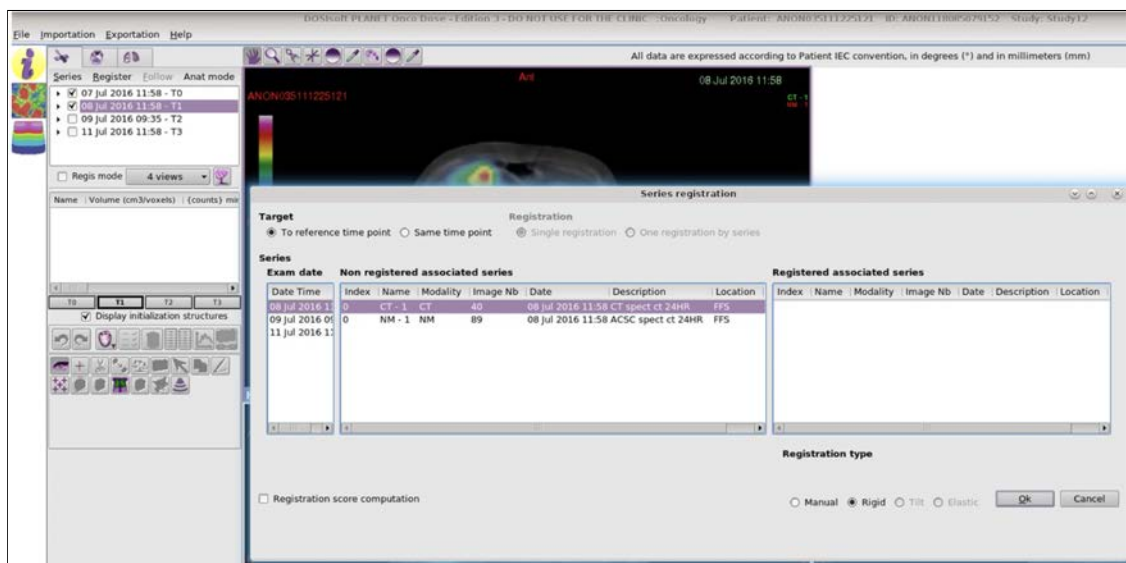
For the CT, to change the window width/level of the images, first click on the red box. Using the green marks, select the level and the window desired



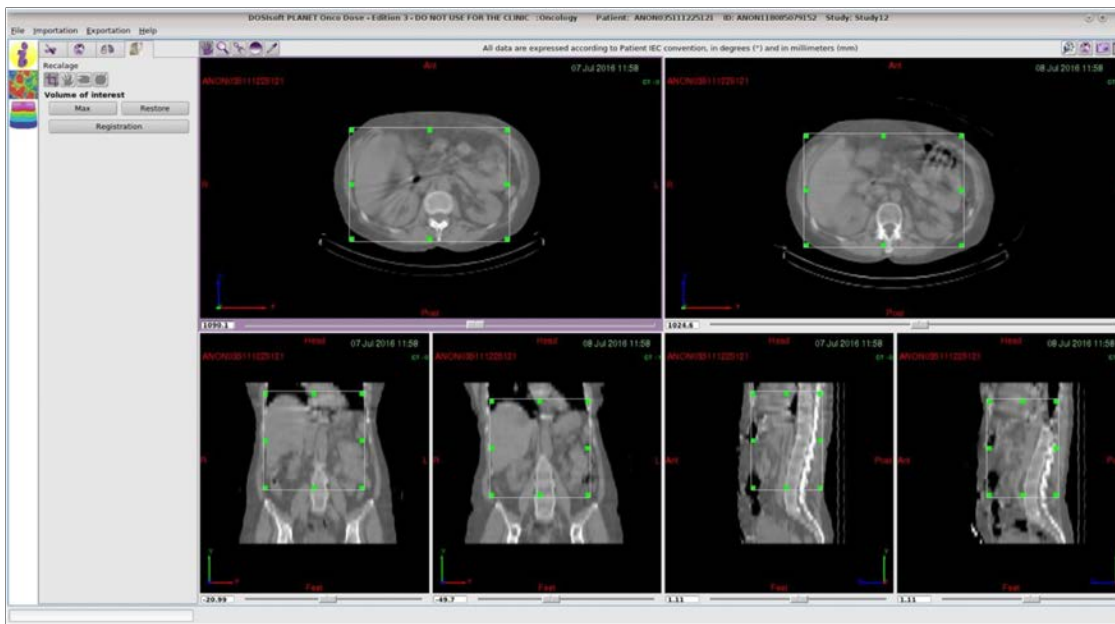
For the NM, same way as the NM can be used to change the window width/level of the images



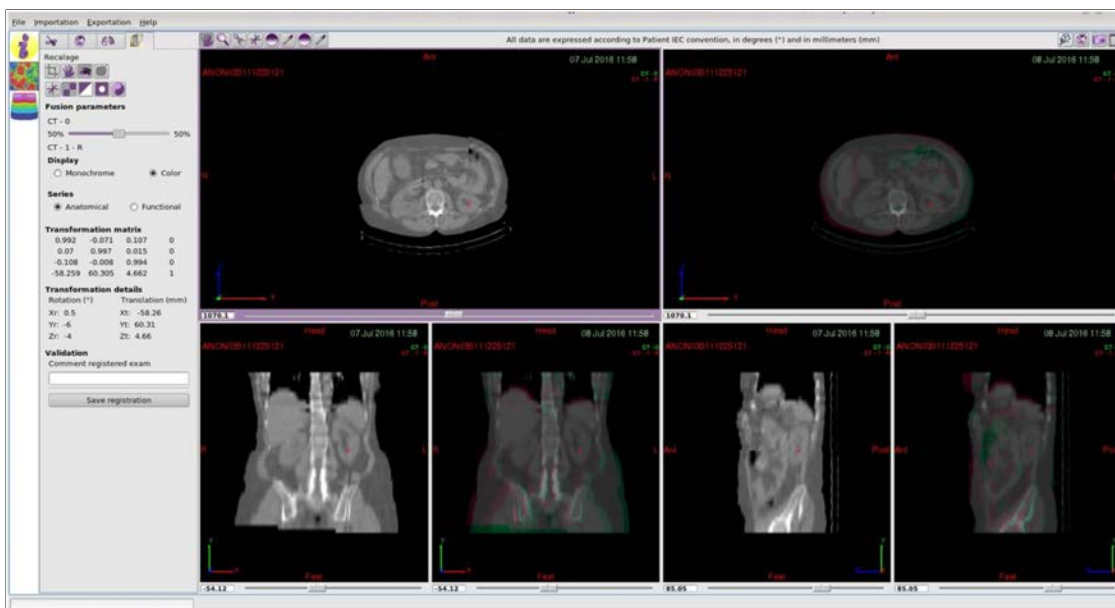
To see a pixel value, click on the first red box for CT values, or the second to NM values, put the pencil on the pixel you want to evaluate. While you are delineating the structure, you will need to press the Ctrl key at the same time to obtain the pixel value, without drawing anything.



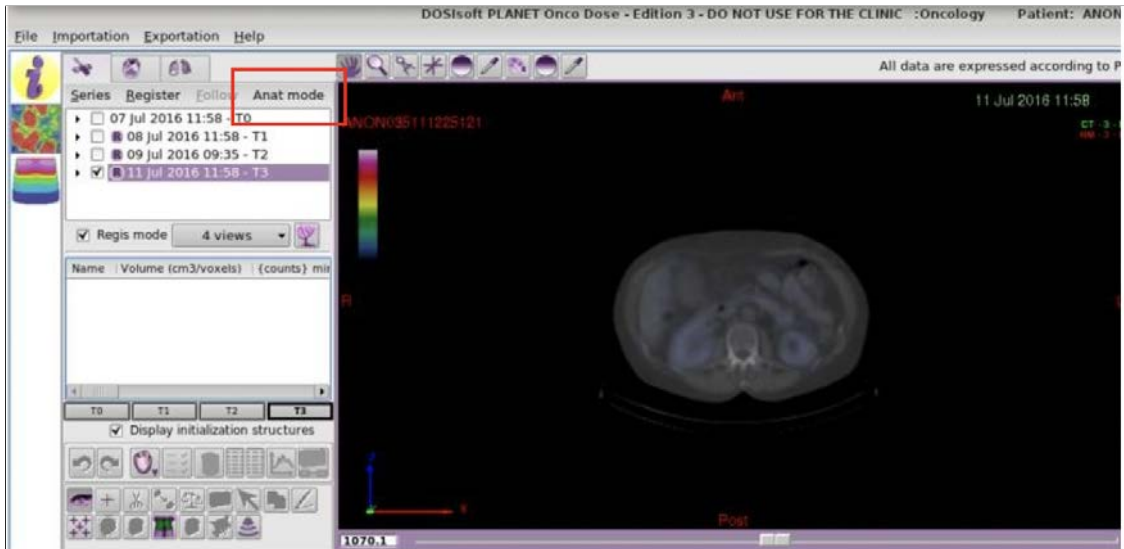
Choose rigid modality to be registered, clicking on CT-1, and then press Ok



As a “registration volume box,” a box including the whole liver, the spleen, and both kidneys should be used. Adjust the box slightly to fix these organs in both images, as shown



Even when visualisation of the registration is desirable (to know if no strange results are obtained) you should not use any other adjustment, especially in manual mode



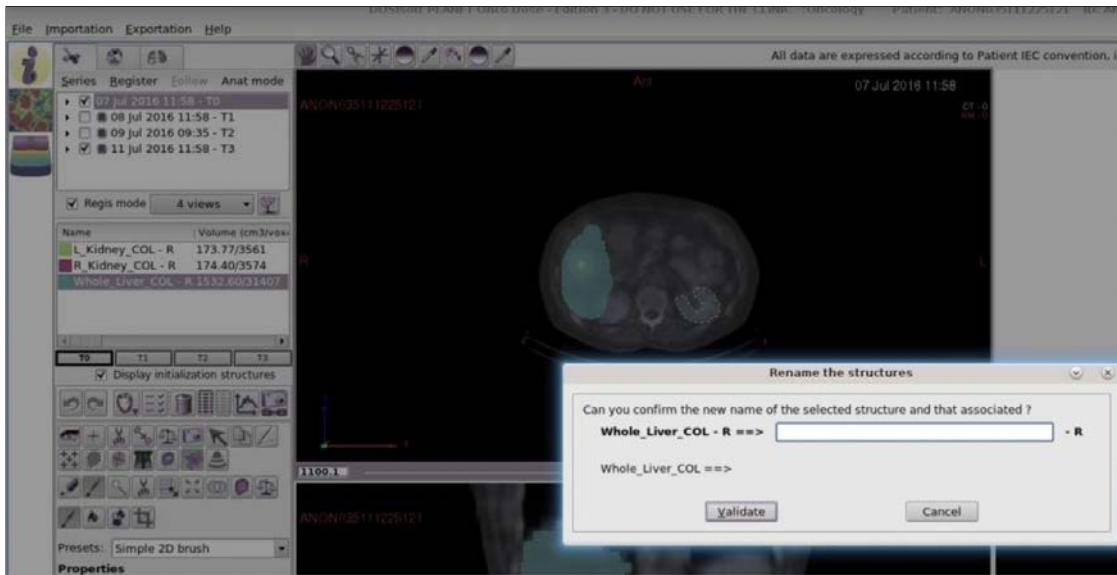
The same should be done with all-time points. Once all the images are all registered, the “Regis mode” should be checked and “Anat mode” selected

In anatomical mode

1. Create a new structure
2. Open structure edition
3. Select “brush mode”
4. On advanced options, select “absolute threshold” with appropriate Min and Max values if needed.
5. On advanced options, deselect “Contour smoothing”
6. When the structure has been defined, click on validate.
7. Once it's validated, the box becomes green.

Note: By clicking the right button of the mouse you will undo the draw you made by clicking with the left button.

Once you have the liver, and both kidneys segmented, you should rename them, double-clicking in the structure name



Remember to name the VOI in the following structure, where XXX corresponds to your country.

Liver: Whole_Liver_XXX, Right kidney: R_Kidney_XXX, Left kidney: L_Kidney_XXX

The screenshot shows the 'Structures of interest' panel on the left. It has several sections: 'Current' (with a red circle 1), 'Segmentation' (with a red circle 2), 'Registration' (with a red circle 3 and 'Temporal option' checked), 'Force propagation' (with a red circle 4), and 'Temporal option' (with a red circle 5). A 'Propagate' button is highlighted with a red box. The main window shows a 3D anatomical model of a patient's torso with colored VOIs.

Click on structure propagation:


1. Select “all” in Structures of interest
2. Select “Segmentation”
3. Select “Registration” and check “Temporal options”
4. Select on Temporal Options, “all-time”
5. And finally, click on “Propagate”

Note: “Display initialization structures” should be marked.

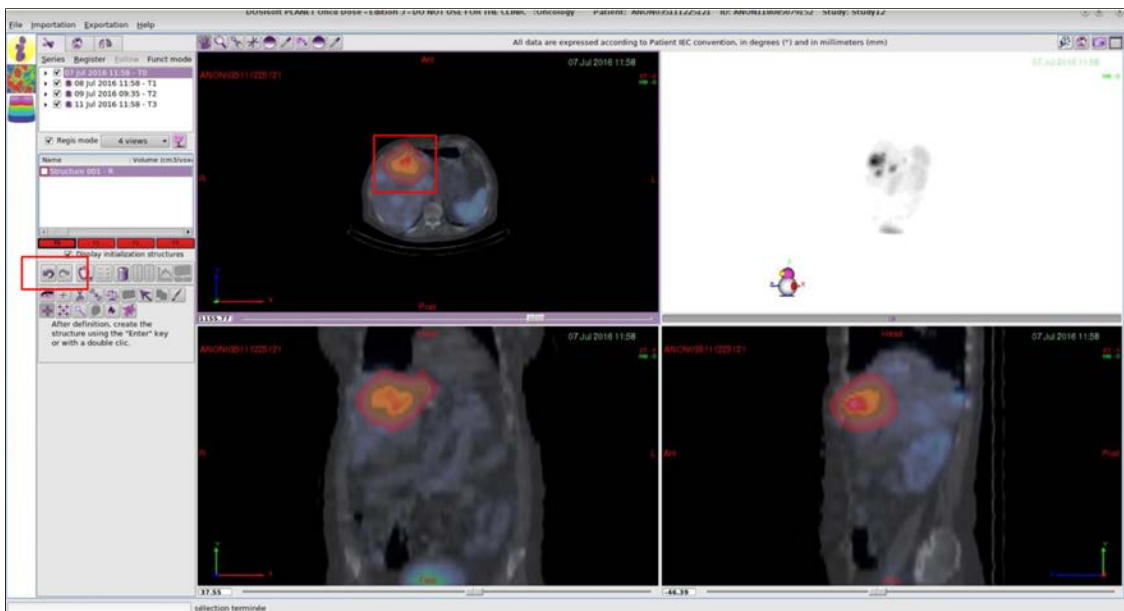
After the propagation, all the time points become green.

The inset screenshot shows a table with columns 'Name' and 'Value'. It lists 'L_Kidney_COL - R' (174), 'R_Kidney_COL - R' (174), and 'Whole_Liver_COL - R' (1532). Below the table, a red box highlights the 'Display initialization structures' button.

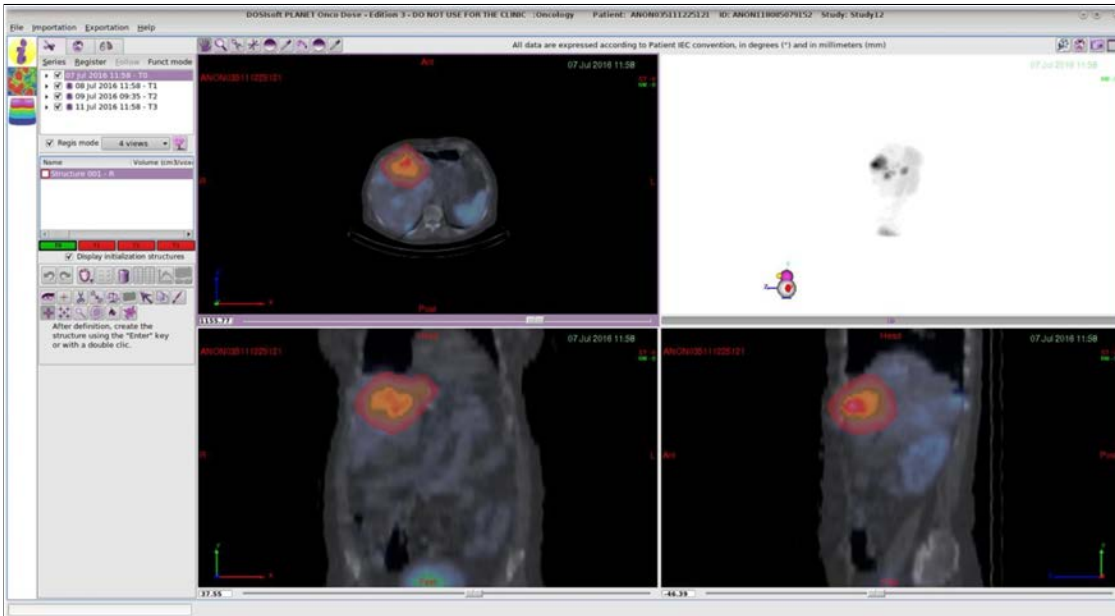
Time propagation of structures

	<p>Create a new structure,</p> <ol style="list-style-type: none"> 1. You will see that the square beside the Structure name is empty. That means that this Structure has been created as an “Initialization Structure”. 2. With the structure selected click on “Uptake areas detection”
---	--

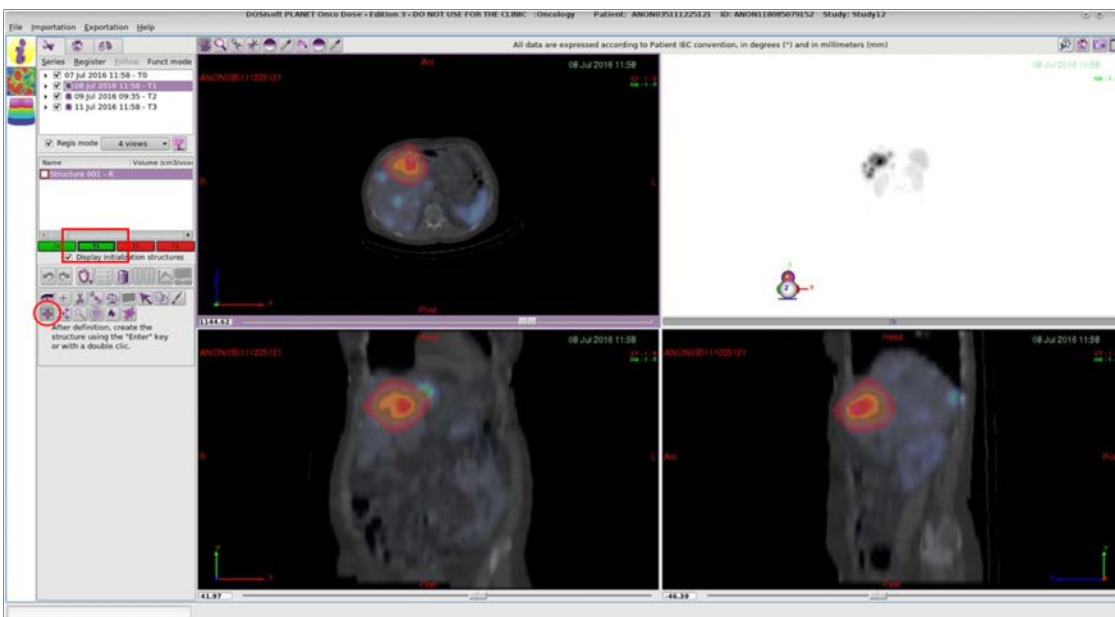
Initialisation of structures



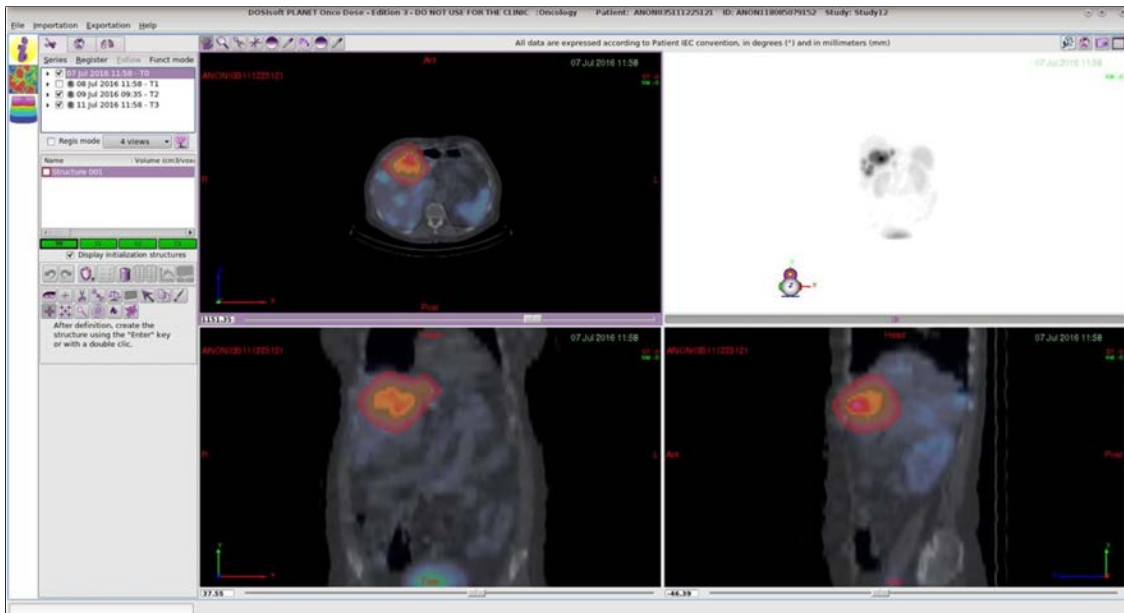
Click inside the region you want to define, and a Structure is going to appear surrounding the area you clicked. Press “enter”



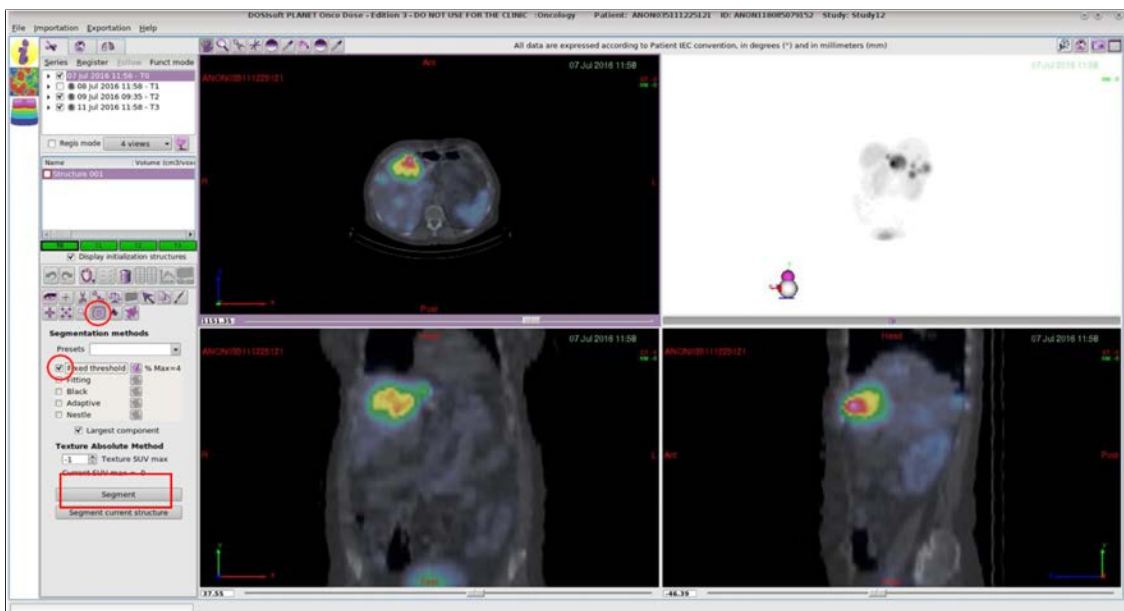
Now, the first-time point box becomes green



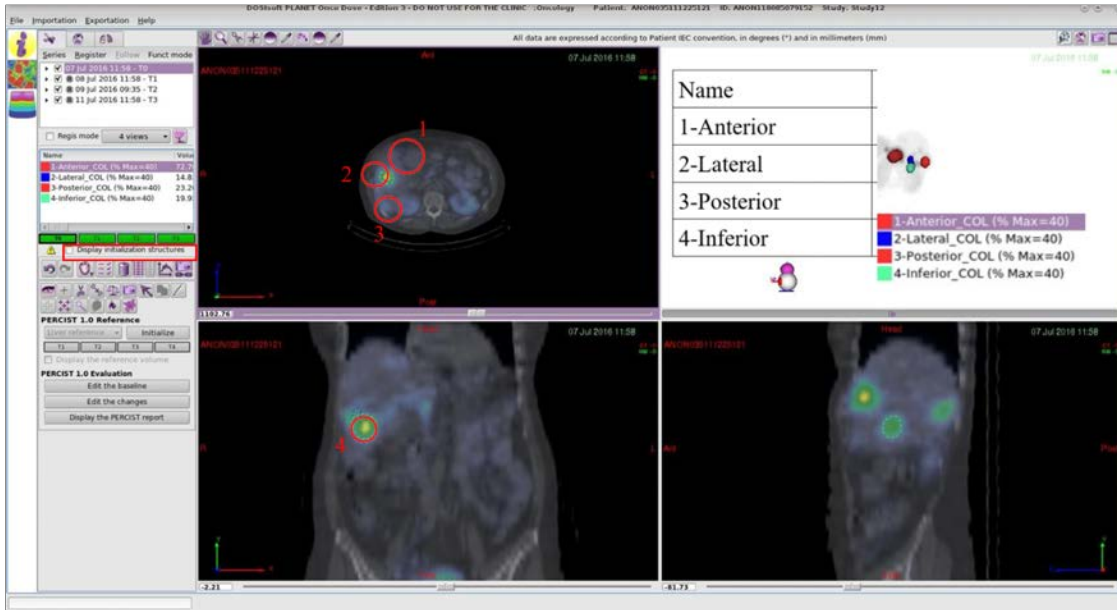
Select the second time point and repeat as shown



Repeat with all-time points. Once you have all four initialization structures created (all the boxes are green)



Click on “Segmentation Methods”; Select the “Fixed Threshold” options with a 40% and then Click on “Segment”. The structure created is already propagated through all time points

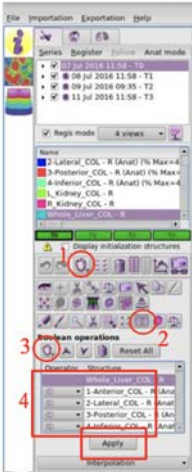


Rename this structure as 1-Anterior_XXX where XXX corresponds to your country.
Repeat the same segmentation with the other three lesions to be analysed

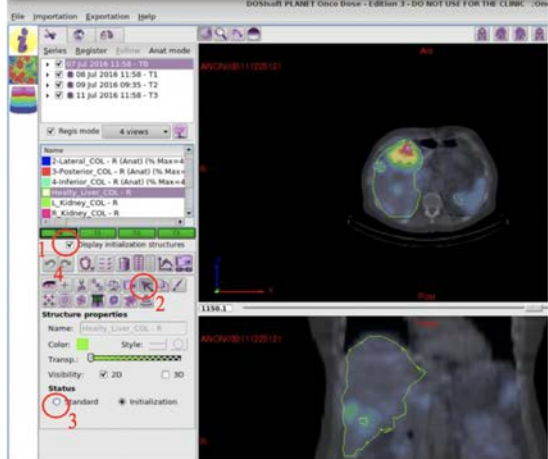
1. Click on “Structures propagation”
2. Select in “Structures of interest”:
- “All” and “Segmentation”
3. In “Propagation”: “Modality”
Note: NEVER check the “Force la propagation”
4. In “Temporal option”: “All time”
5. Click on propagated

Now, on “Anatomical mode”, you will see the Lesions drawn, with “(Anat)” on its name.

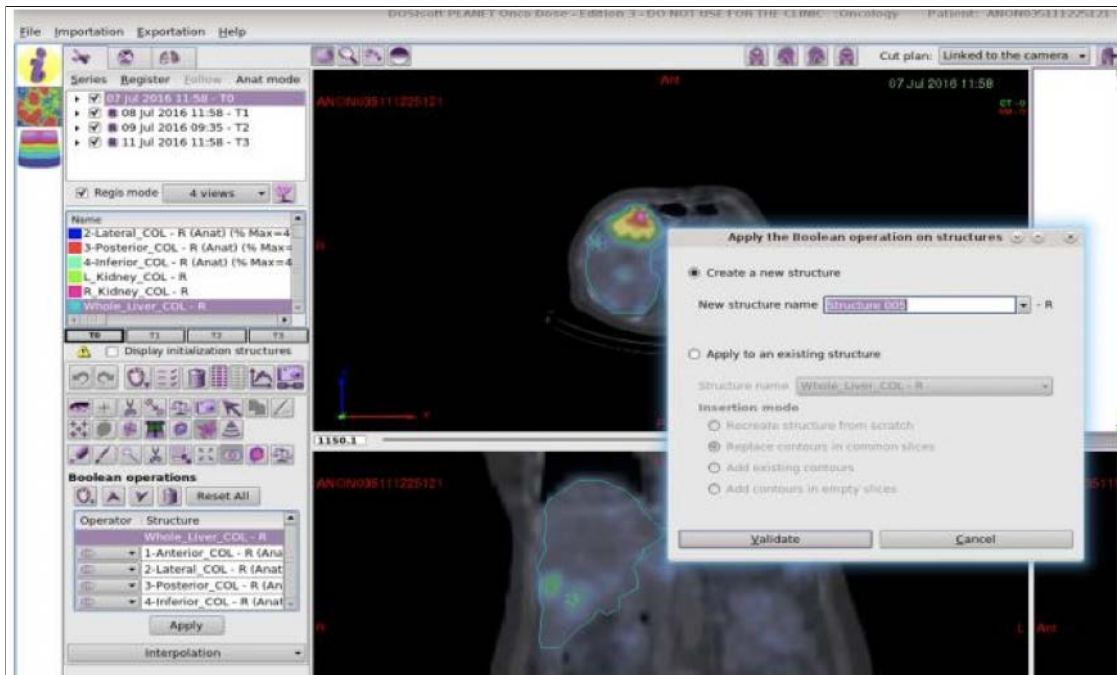
To hide the initialization studies, uncheck “Display initialization structures”. Now, the “Functional mode” structures should be propagated as an “Anatomical mode”

	<ol style="list-style-type: none"> 1. Click on structure edition 2. Click on “Boolean operation on structures” 3. Add structures to the operation list. First the liver, and then the four lesions. 4. Select the third option, to subtract the lesions to the liver. Click on apply.
---	---

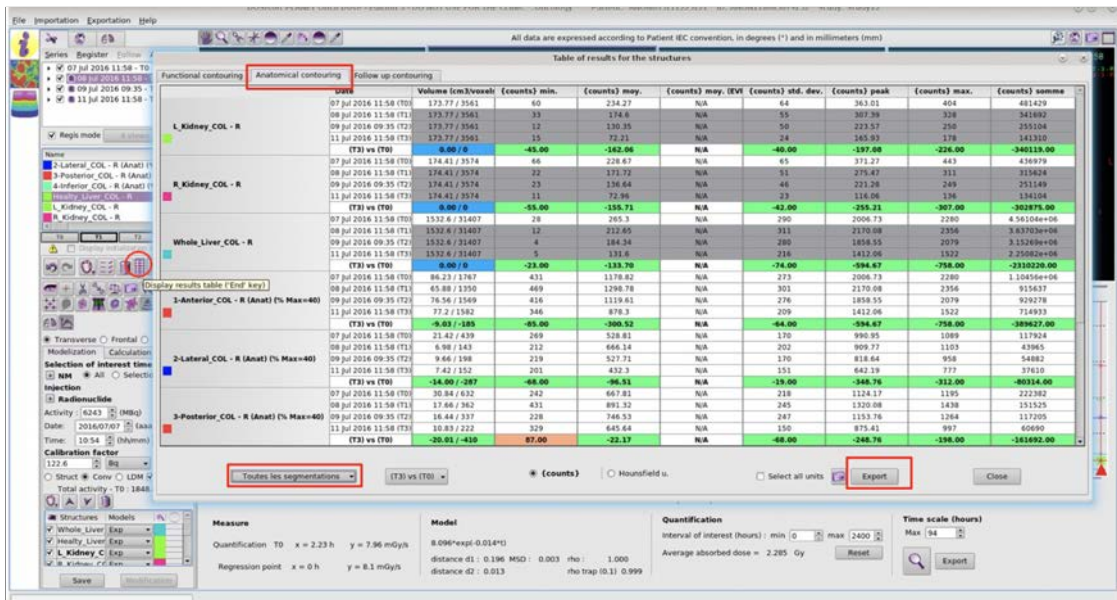
Defining the normal liver

<p>You will see a new structure created.</p> <ol style="list-style-type: none"> 1. Check “Display initialization structures” 2. Select “Structure properties” 3. Status: select “Standard” 4. Uncheck “Display initialization structures”. 	
--	--

Display initialisation structures



Rename the structure as Normal_Liver_XXX. Validate it



To obtain the information of the organs VOI (including normal liver), “Display the results table”. Select “Anatomical contouring” and “All the Segmentations (All the segmentations)” and click on “Export”

Segmentation	Date	Time point	Volume (cm3)	Volume (voxels)	(counts) min.	(counts) moy.	(counts) moy (EVP c)	(counts) std dev.	(counts) peak	(counts) max.	(counts) somme
L_Kidney_COL - R		Time point -1	0	173 77	3561	60	234 27 N/A	64	363 01	404	481429
L_Kidney_COL - R		Time point 0	1	173 77	3561	33	174 6 N/A	55	307 39	328	341692
L_Kidney_COL - R		Time point 1	2	173 77	3561	12	130 35 N/A	50	223 57	250	255104
L_Kidney_COL - R		Time point 2	3	173 77	3561	15	72 21 N/A	24	165 93	176	141310
T3 vs T0			0	0	0	45	-182 06 N/A	40	-197 08	-226	-340118
R_Kidney_COL - R		Time point -1	0	174 41	3574	66	228 67 N/A	65	371 27	443	436979
R_Kidney_COL - R		Time point 0	1	174 41	3574	22	171 72 N/A	51	275 47	311	315624
R_Kidney_COL - R		Time point 1	2	174 41	3574	29	139 84 N/A	46	221 28	249	251149
R_Kidney_COL - R		Time point 2	3	174 41	3574	11	72 96 N/A	23	116 06	136	134104
T3 vs T0			0	0	0	55	-155 71 N/A	42	-255 21	-307	-302875
Whole_Liver_COL - R		Time point -1	0	1532 6	31407	28	265 3 N/A	290	2006 73	2280	4561040
Whole_Liver_COL - R		Time point 0	1	1532 6	31407	12	212 85 N/A	311	2170 08	2356	3637030
Whole_Liver_COL - R		Time point 1	2	1532 6	31407	4	184 34 N/A	280	1856 55	2079	3152890
Whole_Liver_COL - R		Time point 2	3	1532 6	31407	5	121 6 N/A	216	1412 06	1522	2256020
T3 vs T0			0	0	0	23	-133 7 N/A	-74	-594 67	-758	-2310220
1-Anterior_COL - R (Anat) % Max+40		Time point -1	0	86 23	1767	431	1178 82 N/A	273	2006 73	2280	1104560
1-Anterior_COL - R (Anat) % Max+40		Time point 0	1	85 88	1350	469	1298 78 N/A	301	2170 08	2356	3637030
1-Anterior_COL - R (Anat) % Max+40		Time point 1	2	76 56	1569	416	1119 81 N/A	276	1856 55	2079	929278
1-Anterior_COL - R (Anat) % Max+40		Time point 2	3	77 2	1592	346	878 3 N/A	209	1412 06	1522	714933
T3 vs T0			0	-9 03	-185	-85	-300 52 N/A	-64	-594 67	-758	-389627
2-Lateral_COL - R (Anat) % Max+40		Time point -1	0	21 42	439	269	528 81 N/A	170	990 95	1089	117924
2-Lateral_COL - R (Anat) % Max+40		Time point 0	1	6 98	143	212	666 14 N/A	202	909 77	1103	43965
2-Lateral_COL - R (Anat) % Max+40		Time point 1	2	9 66	198	219	527 71 N/A	170	818 64	958	54882
2-Lateral_COL - R (Anat) % Max+40		Time point 2	3	7 42	152	201	432 3 N/A	151	642 19	777	37610
T3 vs T0			0	-14	-287	-58	-96 51 N/A	-19	-348 76	-312	-80314
3-Posterior_COL - R (Anat) % Max+40		Time point -1	0	30 84	632	242	667 81 N/A	218	1124 17	1195	222382
3-Posterior_COL - R (Anat) % Max+40		Time point 0	1	17 66	362	431	891 32 N/A	245	1320 09	1438	151525
3-Posterior_COL - R (Anat) % Max+40		Time point 1	2	16 44	337	228	746 53 N/A	247	1153 76	1264	117205
3-Posterior_COL - R (Anat) % Max+40		Time point 2	3	10 82	222	329	645 64 N/A	150	875 41	997	60960
T3 vs T0			0	-20 01	-410	87	-22 17 N/A	-68	-248 76	-198	-161692
4-Inferior_COL - R (Anat) % Max+40		Time point -1	0	24 2	496	380	759 66 N/A	236	1248 04	1372	202930
4-Inferior_COL - R (Anat) % Max+40		Time point 0	1	17 13	351	384	902 77 N/A	273	1408 06	1617	186180
4-Inferior_COL - R (Anat) % Max+40		Time point 1	2	16 4	326	279	820 71 N/A	224	1214 52	1347	126200
4-Inferior_COL - R (Anat) % Max+40		Time point 2	3	15 57	319	218	606 5 N/A	162	931 21	1045	90975
T3 vs T0			0	-8 63	-177	-162	-153 16 N/A	-54	-316 83	-327	-111855
Healthy_Liver_COL - R		Time point -1	0	1373 77	28152	32	196 58 N/A	162	1248 04	1372	3032270
Healthy_Liver_COL - R		Time point 0	1	1398 94	28668	10	161 52 N/A	208	1455 86	1617	2579810
Healthy_Liver_COL - R		Time point 1	2	1397 53	28659	4	134 82 N/A	180	1292 05	1395	2131300
Healthy_Liver_COL - R		Time point 2	3	1403 92	28770	5	95 16 N/A	138	1038 8	1105	1515840
T3 vs T0			0	30 15	618	-27	-101 42 N/A	-24	211 24	-287	-151730
All structures (n=8)		Time point -1	0	3417 24	70028	28	507 48 N/A	N/A	N/A	N/A	1016041
All structures (n=8)		Time point 0	1	3287 37	69416	10	559 94 N/A	N/A	N/A	2286	8147392
All structures (n=8)		Time point 1	2	3287 37	69416	4	475 08 N/A	N/A	N/A	2079	7018978
All structures (n=8)		Time point 2	3	3295 72	69587	5	366 85 N/A	N/A	N/A	1532	4845382

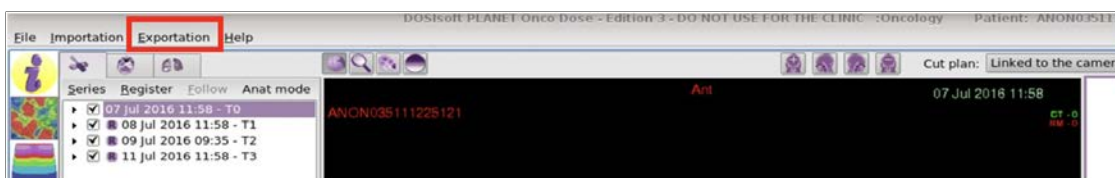
You will obtain a .txt file with the VOI information. In this file, you can find the information on the volume of the VOI in voxels and cm³

Date	Volume (cm3/voxels)	(counts) min.	(counts) moy.	(counts) moy (EVP c)	(counts) std dev.	(counts) peak	(counts) max.	(counts) somme
07 Jul 2016 11:58 (T0)	173 77 / 3561	60	234 27	N/A	64	363 01	404	481429
08 Jul 2016 11:58 (T1)	173 77 / 3561	33	174 6	N/A	55	307 39	328	341692
09 Jul 2016 09:35 (T2)	173 77 / 3561	12	130 35	N/A	50	223 57	250	255104
11 Jul 2016 11:58 (T3)	173 77 / 3561	15	72 21	N/A	24	165 93	176	141310
(T3) vs (T0)	0 00 / 0	-85 00	-182 06	N/A	-40	-197 08	-226	-340118
07 Jul 2016 11:58 (T0)	174 41 / 3574	66	228 67	N/A	65	371 27	443	436979
08 Jul 2016 11:58 (T1)	174 41 / 3574	22	171 72	N/A	51	275 47	311	315624
09 Jul 2016 09:35 (T2)	174 41 / 3574	29	139 84	N/A	46	221 28	249	251149
11 Jul 2016 11:58 (T3)	174 41 / 3574	11	72 96	N/A	23	116 06	136	134104
(T3) vs (T0)	0 00 / 0	-55 00	-155 71	N/A	42	-255 21	-307	-302875
07 Jul 2016 11:58 (T0)	1532 6 / 31407	28	265 3	N/A	290	2006 73	2280	4 561 04e+06
08 Jul 2016 11:58 (T1)	1532 6 / 31407	12	212 85	N/A	311	2170 08	2356	3 637 03e+06
09 Jul 2016 09:35 (T2)	1532 6 / 31407	4	184 34	N/A	280	1856 55	2079	3 152 89e+06
11 Jul 2016 11:58 (T3)	1532 6 / 31407	5	121 6	N/A	216	1412 06	1522	2 256 02e+06
(T3) vs (T0)	0 00 / 0	-23 00	-133 70	N/A	-74	-594 67	-758	-2 310 22e+06
07 Jul 2016 11:58 (T0)	86 23 / 1767	431	1178 82	N/A	273	2006 73	2280	11 045 6e+06
08 Jul 2016 11:58 (T1)	85 88 / 1350	469	1298 78	N/A	301	2170 08	2356	9 292 78e+06
09 Jul 2016 09:35 (T2)	76 56 / 1569	416	1119 81	N/A	276	1856 55	2079	6 096 6e+06
11 Jul 2016 11:58 (T3)	77 2 / 1592	346	878 3	N/A	209	1412 06	1522	4 845 38e+06
(T3) vs (T0)	-9 03 / -185	-85 00	-300 52	N/A	-64	-594 67	-758	-3 896 27e+06
07 Jul 2016 11:58 (T0)	21 42 / 439	269	528 81	N/A	170	990 95	1089	1 179 24e+06
08 Jul 2016 11:58 (T1)	6 98 / 143	212	666 14	N/A	202	909 77	1103	439 65e+05
09 Jul 2016 09:35 (T2)	9 66 / 198	219	527 71	N/A	170	818 64	958	548 82e+05
11 Jul 2016 11:58 (T3)	7 42 / 152	201	432 3	N/A	151	642 19	777	376 10e+05
(T3) vs (T0)	-14 00 / -287	-58 00	-96 51	N/A	-19	-348 76	-312	-803 14e+05
07 Jul 2016 11:58 (T0)	30 84 / 632	242	667 81	N/A	218	1124 17	1195	222 382e+05
08 Jul 2016 11:58 (T1)	17 66 / 362	433	891 32	N/A	245	1320 09	1438	151 525e+05
09 Jul 2016 09:35 (T2)	16 44 / 337	228	746 53	N/A	247	1153 76	1264	117 205e+05
11 Jul 2016 11:58 (T3)	10 82 / 222	329	645 64	N/A	150	875 41	997	60 960e+05
(T3) vs (T0)	-20 01 / -410	87 00	-22 17	N/A	-68	-248 76	-198	-161 692e+05

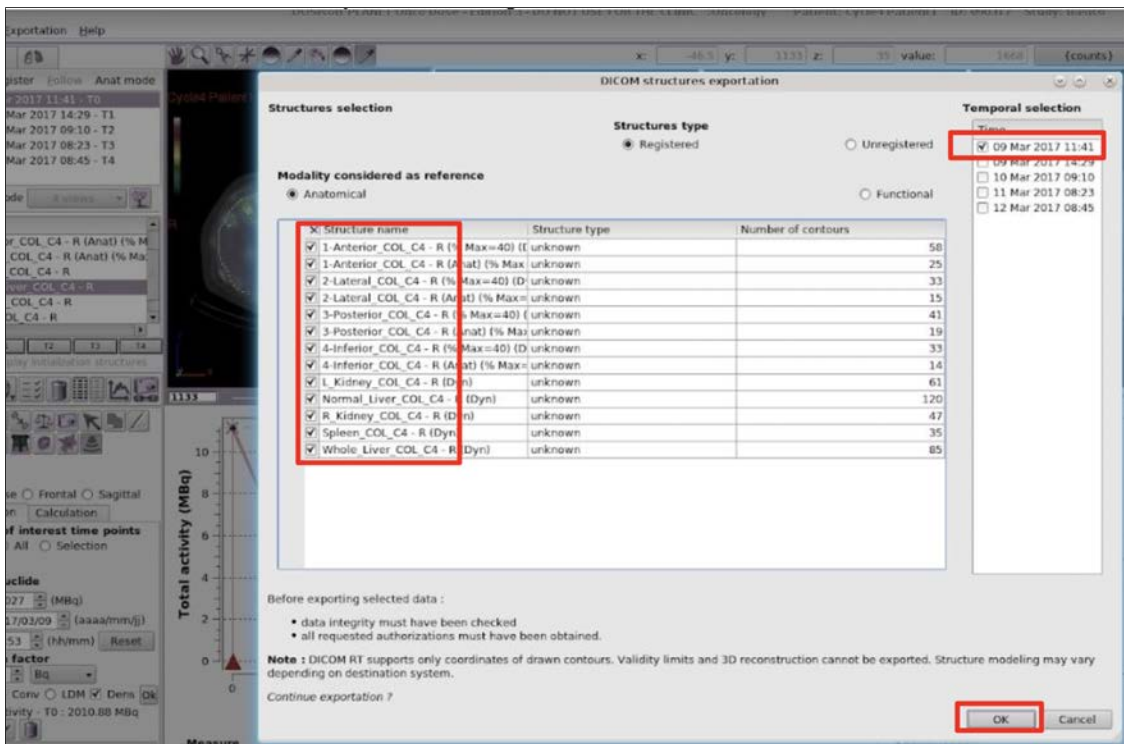
To obtain the information of the lesions VOI, “Display the results table”. Select “Functional contouring” and “Toutes les Segmentations (All the segmentations)” and click on “Export”

Structure	Segmentation	Date	Time point	Volume (cm3)	Volume (voxels)	(counts) min	(counts) moy	(counts) moy, (EXP C)	(counts) std. dev.	(counts) peak	(counts) max	(counts) summe
1 CT_Anatomy_(counts)												
2 Structure												
3 L_Kidney_COL - R			Time point -1	0	173.77	3561	60	234.27 N/A	64	363.01	404	481429
4 L_Kidney_COL - R			Time point 0	1	173.77	3561	33	174.6 N/A	55	307.28	228	341892
5 L_Kidney_COL - R			Time point 1	2	173.77	3561	12	120.35 N/A	50	223.57	256	255194
6 R_Kidney_COL - R			Time point 2	3	173.77	3561	15	72.21 N/A	24	165.83	178	141310
7 L_Kidney_COL - R			3 vs 0	0	0	0	-45	-162.06 N/A	-40	-197.88	-226	-340119
8 R_Kidney_COL - R			Time point -1	0	174.41	3574	66	228.87 N/A	65	371.27	443	436979
9 R_Kidney_COL - R			Time point 0	1	174.41	3574	22	171.72 N/A	51	275.47	311	315624
10 R_Kidney_COL - R			Time point 1	2	174.41	3574	23	126.64 N/A	46	221.28	248	251149
11 R_Kidney_COL - R			Time point 2	3	174.41	3574	11	72.96 N/A	23	116.06	136	134104
12 R_Kidney_COL - R			3 vs 0	0	0	0	-55	-155.71 N/A	-42	-255.21	-307	-302875
13 Whole_Liver_COL - R			Time point -1	0	1532.6	31407	28	265.3 N/A	290	2006.73	2280	4561040
14 Whole_Liver_COL - R			Time point 0	1	1532.6	31407	12	212.65 N/A	311	2170.58	2356	3637030
15 Whole_Liver_COL - R			Time point 1	2	1532.6	31407	4	184.34 N/A	280	1858.55	2079	2152690
16 Whole_Liver_COL - R			Time point 2	3	1532.6	31407	5	131.6 N/A	216	1412.06	1522	2250820
17 Whole_Liver_COL - R			3 vs 0	0	0	0	-23	-133.7 N/A	-74	-594.67	-758	-2310220
18 1.Anterior_COL - R (Anat)	% Max=40		Time point -1	0	86.23	1767	431	1178.82 N/A	273	2006.73	2280	1104560
19 1.Anterior_COL - R (Anat)	% Max=40		Time point 0	1	85.88	1750	469	1298.78 N/A	301	2170.58	2356	915637
20 1.Anterior_COL - R (Anat)	% Max=40		Time point 1	2	76.56	1559	416	1119.61 N/A	276	1858.55	2079	929278
21 1.Anterior_COL - R (Anat)	% Max=40		Time point 2	3	77.2	1582	346	878.3 N/A	209	1412.06	1522	714933
22 1.Anterior_COL - R (Anat)	% Max=40		3 vs 0	0	-9.03	-185	-85	-300.52 N/A	-64	-594.67	-758	-389627
23 2.Lateral_COL - R (Anat)	% Max=40		Time point -1	0	21.42	439	269	528.81 N/A	170	990.95	1089	117924
24 2.Lateral_COL - R (Anat)	% Max=40		Time point 0	1	6.98	143	212	686.14 N/A	202	909.77	1103	43965
25 2.Lateral_COL - R (Anat)	% Max=40		Time point 1	2	9.66	198	218	527.71 N/A	170	818.64	958	54882
26 2.Lateral_COL - R (Anat)	% Max=40		Time point 2	3	7.42	152	201	432.3 N/A	151	642.19	777	37810
27 2.Lateral_COL - R (Anat)	% Max=40		3 vs 0	0	-14	-287	-68	-98.51 N/A	-19	-348.76	-312	-80314
28 3.Posterior_COL - R (Anat)	% Max=40		Time point -1	0	30.84	632	242	667.81 N/A	218	1124.17	1195	222382
29 3.Posterior_COL - R (Anat)	% Max=40		Time point 0	1	17.66	362	431	891.32 N/A	245	1230.88	1438	151525
30 3.Posterior_COL - R (Anat)	% Max=40		Time point 1	2	16.44	337	278	746.53 N/A	247	1153.78	1264	117205
31 3.Posterior_COL - R (Anat)	% Max=40		Time point 2	3	10.83	222	329	645.64 N/A	150	875.41	897	60690
32 3.Posterior_COL - R (Anat)	% Max=40		3 vs 0	0	-20.01	-410	87	-22.17 N/A	-68	-248.78	-198	-161692
33 4.interior_COL - R (Anat)	% Max=40		Time point -1	0	24.2	496	380	759.88 N/A	236	1248.04	1372	202830
34 4.interior_COL - R (Anat)	% Max=40		Time point 0	1	17.13	351	384	902.77 N/A	273	1408.06	1553	188109
35 4.interior_COL - R (Anat)	% Max=40		Time point 1	2	16.4	338	278	820.71 N/A	224	1214.52	1347	128030
36 4.interior_COL - R (Anat)	% Max=40		Time point 2	3	15.57	319	219	608.5 N/A	182	931.21	1045	90975
37 4.interior_COL - R (Anat)	% Max=40		3 vs 0	0	-8.63	-177	-162	-153.16 N/A	-54	-316.83	-327	-111855
38 Healthy_Liver_COL - R			Time point -1	0	1373.77	28152	32	196.58 N/A	162	1248.04	1372	2023270
39 Healthy_Liver_COL - R			Time point 0	1	1398.94	28668	10	161.52 N/A	208	1455.86	1617	257810
40 Healthy_Liver_COL - R			Time point 1	2	1397.53	28639	4	134.82 N/A	180	1292.05	1395	2131300
41 Healthy_Liver_COL - R			Time point 2	3	1403.92	28770	5	95.18 N/A	138	1036.8	1105	1515940
42 Healthy_Liver_COL - R			3 vs 0	0	30.15	618	-27	-101.42 N/A	-24	-211.24	-267	-1517330
43 All structures (n=8)			Time point -1	0	3411.24	70028	28	507.48 N/A	N/A	N/A	2280	10160414
44 All structures (n=8)			Time point 0	1	3397.37	69416	10	559.94 N/A	N/A	N/A	2356	8147392
45 All structures (n=8)			Time point 1	2	3397.37	69621	4	475.08 N/A	N/A	N/A	2079	7019638
46 All structures (n=8)			Time point 2	3	3395.72	69587	5	366.85 N/A	N/A	N/A	1522	4846382

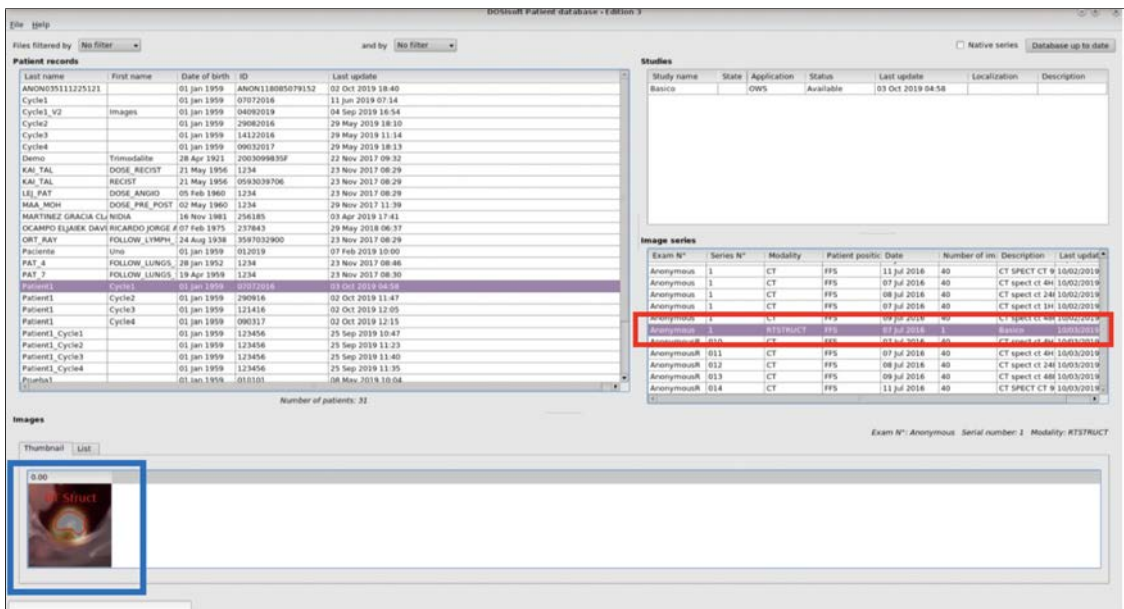
You will obtain a .txt file with the VOI information. In this file, you can find the information on the volume of the VOI in voxels and cm^3



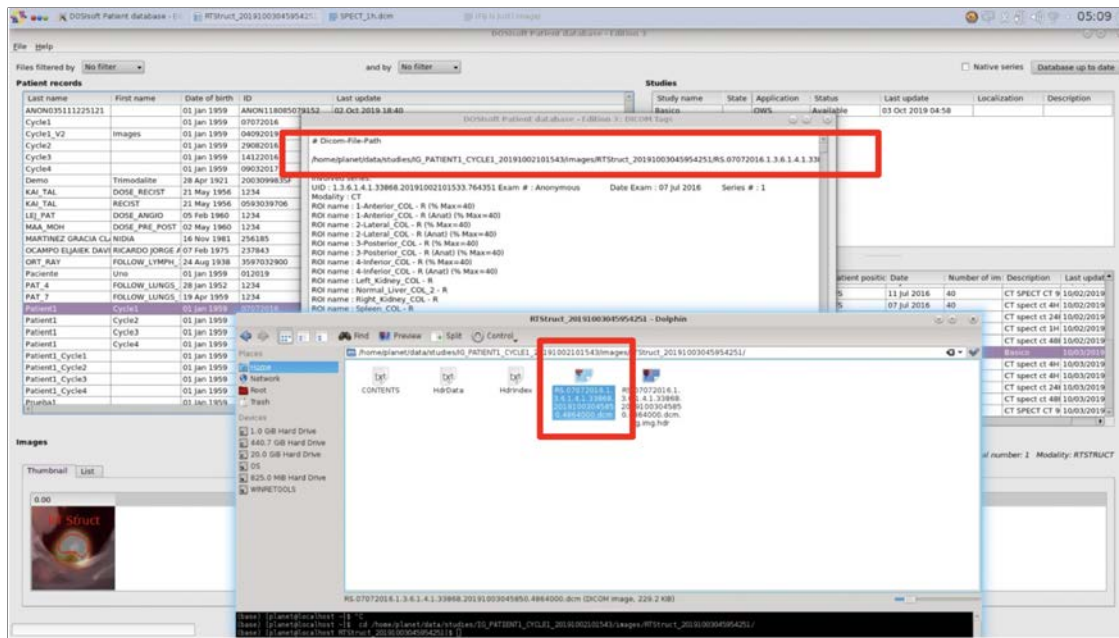
Once all the structures were defined, you need to export the Dicom file of the structures segmented on the first time point. On exportation, select Insertion into the database of the structure of RT struct format



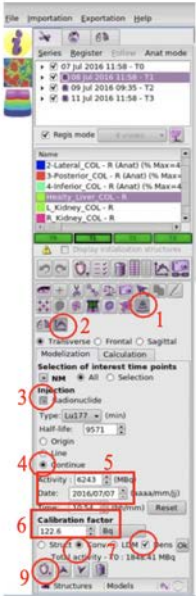
Select all the structures and only the first time point. And click “ok”



A window will pop out saying: “The DICOM RT Struct file is already inserted into the database”, click ok. On the DOSISoft database, you can find now an “RTSTRUCT” modality image



With the mouse wheel, click on the image of the RT Struct (Blue square on the image above). The DICOM tags will pop out, the second line of the file contains the image path. Search for the file, and save it somewhere else. You can share it via mail or drive

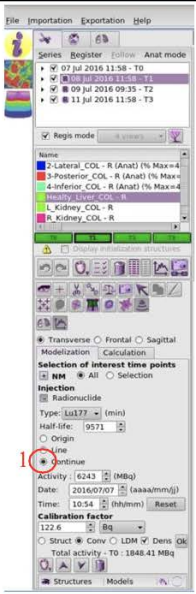


1. Click on “Tools for dosimetry”
2. And Pharmacokinetics fits computation
3. Click on “Radionuclide”
4. Select “Continue”
5. Change the activity and the time

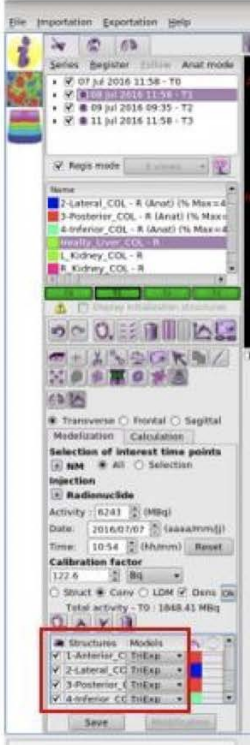
Cycle	Activity administered (MBq)	Initial infusion time
Cycle 1	6243	10:54
Cycle 2	6672	10:22
Cycle 3	6848	09:57
Cycle 4	6027	09:53

6. The calibration factor for this acquisition protocol is 122.6 Bq. The total activity should be 1848.41 MBq at the first time point.
7. Select “Convolution” and check on density correction
8. Clicking on “OK” the calculation of the absorbed dose rates is performed.
9. Add the structures to be analyzed:
 - ✓ Whole Liver XXX
 - ✓ R Kidney XXX
 - ✓ L Kidney XXX
 - ✓ Normal Liver XXX
 - ✓ In functional mode:
 - 1-Anterior_XXX
 - 2-Lateral_XXX
 - 3-Posterior_XXX
 - 4-Inferior_XXX

Now all the structures are defined to start the dosimetry calculations

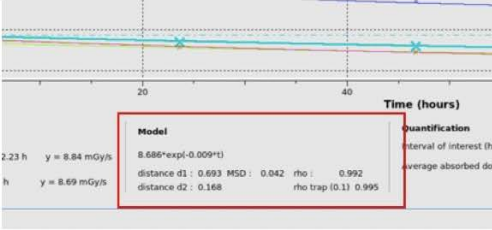


1. Select “Origin” if you want to include the (0,0)¹ point otherwise select “Continue”.

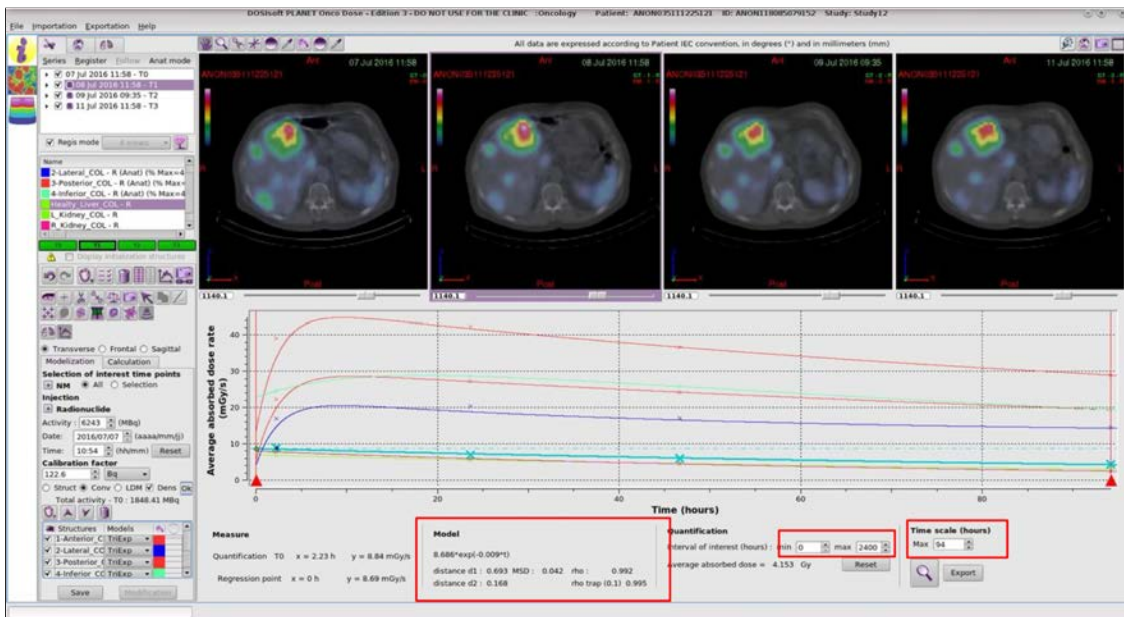


As a model for the fitting, select the “Trap”, “Exp” exponential to the organs or “BiExp”.

Register the MSD, rho, and rho trap of your fitting.



This figure describes the fitting step. The interval of interest should be from 0 to 2400 hours



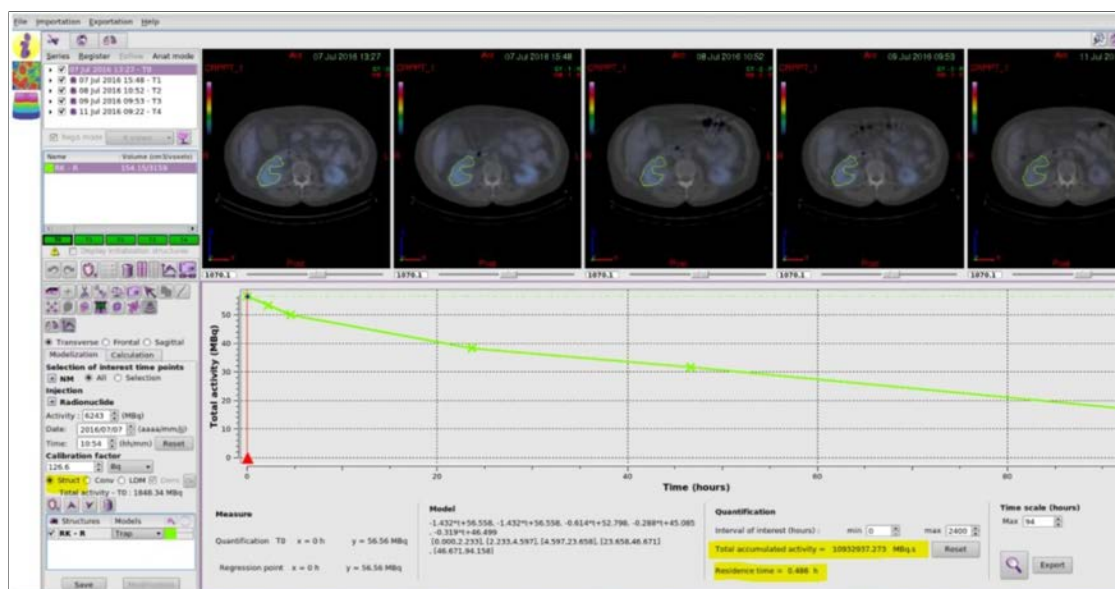
Clicking on “Export” you will obtain a .csv file with the information related to the calculation. In this file you can find the information related to the absorbed dose rate in each time point, for all the VOI and absorbed dose in the VOI

Structure	Time	Volume (cm3)	Volume (ccels)	Delay (d)	Average absorbed dose rate (mGy/s)	Calibration factor	Unit
Whole_Liver_COL - R - Flow	T0	1482.58	17192	23.6581	7.00286	122.6	Bq
Whole_Liver_COL - R - Flow	T1	1474.91	17103	46.6714	6.04479	122.6	Bq
Whole_Liver_COL - R - Flow	T2	1474.91	17103	94.1583	4.33568	122.6	Bq
Whole_Liver_COL - R - Flow	T3	1474.91	17103	2.23333	8.94011	122.6	Bq
Healthy_Liver_COL - R - Flow	T0	1348.22	15634	23.6581	5.66615	122.6	Bq
Healthy_Liver_COL - R - Flow	T1	1415.66	16416	46.6714	4.56691	122.6	Bq
Healthy_Liver_COL - R - Flow	T2	1399.62	16230	94.1583	2.98613	122.6	Bq
Healthy_Liver_COL - R - Flow	T3	1386.86	16082	2.23333	6.77555	122.6	Bq
L_Kidney_COL - R - Flow	T0	177.22	2055	23.6581	5.92703	122.6	Bq
L_Kidney_COL - R - Flow	T1	168.77	1957	46.6714	4.43167	122.6	Bq
L_Kidney_COL - R - Flow	T2	168.77	1957	94.1583	2.44992	122.6	Bq
L_Kidney_COL - R - Flow	T3	168.77	1957	2.23333	7.95972	122.6	Bq
R_Kidney_COL - R - Flow	T0	164.9	1911	23.6581	5.80956	122.6	Bq
R_Kidney_COL - R - Flow	T1	159.5	1838	46.6714	4.62495	122.6	Bq
R_Kidney_COL - R - Flow	T2	159.5	1838	94.1583	2.46545	122.6	Bq
R_Kidney_COL - R - Flow	T3	159.5	1838	2.23333	7.25147	122.6	Bq
1-Anterior_COL - R (% Max=40) - Flow	T0	80.98	939	23.6581	42.3623	122.6	Bq
1-Anterior_COL - R (% Max=40) - Flow	T1	64.85	752	46.6714	36.6165	122.6	Bq
1-Anterior_COL - R (% Max=40) - Flow	T2	74.34	862	94.1583	28.8714	122.6	Bq
1-Anterior_COL - R (% Max=40) - Flow	T3	72.61	842	2.23333	39.1477	122.6	Bq
2-Lateral_COL - R (% Max=40) - Flow	T0	18.54	215	23.6581	20.3481	122.6	Bq
2-Lateral_COL - R (% Max=40) - Flow	T1	7.33	85	46.6714	17.1785	122.6	Bq
2-Lateral_COL - R (% Max=40) - Flow	T2	8.71	101	94.1583	14.4662	122.6	Bq
2-Lateral_COL - R (% Max=40) - Flow	T3	6.99	81	2.23333	16.9099	122.6	Bq
3-Posterior_COL - R (% Max=40) - Flow	T0	27.42	318	23.6581	27.366	122.6	Bq
3-Posterior_COL - R (% Max=40) - Flow	T1	17.76	206	46.6714	24.2125	122.6	Bq
3-Posterior_COL - R (% Max=40) - Flow	T2	15.7	182	94.1583	19.4571	122.6	Bq
3-Posterior_COL - R (% Max=40) - Flow	T3	11.56	134	2.23333	22.3081	122.6	Bq
4-Inferior_COL - R (% Max=40) - Flow	T0	23.97	278	23.6581	28.6943	122.6	Bq
4-Inferior_COL - R (% Max=40) - Flow	T1	16.82	195	46.6714	25.832	122.6	Bq
4-Inferior_COL - R (% Max=40) - Flow	T2	14.32	166	94.1583	19.4328	122.6	Bq
4-Inferior_COL - R (% Max=40) - Flow	T3	13.88	161	2.23333	24.6031	122.6	Bq

In the results, you must see the functional mode results “(% Max = 40)” without (Anat) included in the name of the Structure

	A	B	C	D	E	F	G	H
1	Structure	Time	Volume (cm ³)	Volume (voxels)	Delay (d)	Average absorbed dose rate (mGy/s)	Calibration factor	Unit
2	Whole_Liver_COL - R - Flow	T0	1482.58	1719	23.6581	7.00286	122.6	Bq
3	Whole_Liver_COL - R - Flow	T1	1474.91	1710	46.6714	6.04479	122.6	Bq
4	Whole_Liver_COL - R - Flow	T2	1474.91	1710	94.1583	4.33568	122.6	Bq
5	Whole_Liver_COL - R - Flow	T3	1474.91	1710	2.23333	8.84011	122.6	Bq
6	Whole_Liver_COL - R - Flow	T4	1540.77	1662	77.6501	4.65514	122.6	Bq

If "Continue" mode for the behaviour at origin is used with one of the following fitting function "Linear", "Exp", "Xexp", "BiExp", "TriExp" and "TriExp-Desc", then the order of time points is "inverted" in the result file. T0 values are in the row of T4 and T1/T2/T3 respectively in T0/T1/T2. You can check this issue with the "Delay (d)" column for which the time points are not in chronological order.



If activity, TIA, and residence times information are needed, select "Struct" and then click on "Export". You will obtain a .csv file with the information related to the total activity in each time point for all the VOI, total cumulated activity (MBq.s) in the VOI and residence time. If the total cumulated activity is needed in different intervals of interest, the information can be obtained directly on Planet (in yellow).

STRUCTURE CREATION	
'Anatom mode' selected?	
For the liver	
Confirm sequence: Add a structure → Structure edition; → Contour edition: brush mode	
'Simple 2D brush' used?	
Confirm sequence: Advanced options→ Threshold→ Absolute	
If Yes, enter Min value	
If Yes, enter Max value	
Contour smoothing unselected?	
Named Whole_Liver?	
Whole Liver Volume (cm ³)	Anatomical contouring results table
Whole Liver Voxels	
For the kidneys	
Confirm sequence: Add a structure → Structure edition; → Contour edition: brush mode	
'Simple 2D brush' used?	
Confirm sequence: Advanced options→ Threshold→ Absolute	
If Yes, enter Min value	
If Yes, enter Max value	
Confirm contour smoothing is unselected	
Confirm hole filling is unselected	
Named R_Kidney?	
R-kidney Volume (cm ³) T1	
R-kidney Voxels T1	
R-kidney Volume (cm ³) T2	
R-kidney Voxels T2	
R-kidney Volume (cm ³) T3	
R-kidney Voxels T3	
R-kidney Volume (cm ³) T4	
R-kidney Voxels T4	
R-kidney Volume (cm ³) T5	
R-kidney Voxels T5	
Named L_Kidney?	
L-kidney Volume (cm ³) T1	
L-kidney Voxels T1	
L-kidney Volume (cm ³) T2	
L-kidney Voxels T2	

Exportation of segmentation (1)

L-kidney Volume (cm ³) T3	
L-kidney Voxels T3	
L-kidney Volume (cm ³) T4	
L-kidney Voxels T4	
L-kidney Volume (cm ³) T5	
L-kidney Voxels T5	
All structures were propagated rigidly, through all time points?	
For the lesions	
'Fund mode' selected?	
Uptake areas of detection were created at each time point?	
On segmentation methods: Fixed threshold of 40%?	
Created four structures (1-Anterior, 2-Lateral, 3-Posterior, 4-Inferior)?	
Structures created with the help of a medical doctor?	
For 1-Anterior	
Lesion Volume (cm ³) T1	Functional contouring results table
Lesion Voxels T1	
Lesion Volume (cm ³) T2	
Lesion Voxels T2	
Lesion Volume (cm ³) T3	
Lesion Voxels T3	
Lesion Volume (cm ³) T4	
Lesion Voxels T4	
Lesion Volume (cm ³) T5	
Lesion Voxels T5	
For 2-Lateral	
Lesion Volume (cm ³) T1	Functional contouring results table
Lesion Voxels T1	
Lesion Volume (cm ³) T2	
Lesion Voxels T2	
Lesion Volume (cm ³) T3	
Lesion Voxels T3	
Lesion Volume (cm ³) T4	
Lesion Voxels T4	
Lesion Volume (cm ³) T5	
Lesion Voxels T5	
For 3-Posterior	
Lesion Volume (cm ³) T1	Functional contouring results table
Lesion Voxels T1	
Lesion Volume (cm ³) T2	
Lesion Voxels T2	
Lesion Volume (cm ³) T3	
Lesion Voxels T3	
Lesion Volume (cm ³) T4	
Lesion Voxels T4	
Lesion Volume (cm ³) T5	
Lesion Voxels T5	

Exportation of segmentation (2)

<p>For 4-inferior</p> <p>Lesion Volume (cm³) T1</p> <p>Lesion Voxels T1</p> <p>Lesion Volume (cm³) T2</p> <p>Lesion Voxels T2</p> <p>Lesion Volume (cm³) T3</p> <p>Lesion Voxels T3</p> <p>Lesion Volume (cm³) T4</p> <p>Lesion Voxels T4</p> <p>Lesion Volume (cm³) T5</p> <p>Lesion Voxels T5</p> <p>All functional structures were propagated on Anat mode, through all time points?</p> <p>Confirm Forcer la propagation is unchecked</p> <p>A boolean operation was done between the liver and all four lesions?</p> <p>The new structure was selected as a "Standard structure"?</p> <p>Named Normal_Liver?</p> <p>Normal Liver Volume (cm³) T1</p> <p>Normal Liver Voxels T1</p> <p>Normal Liver Volume (cm³) T2</p> <p>Normal Liver Voxels T2</p> <p>Normal Liver Volume (cm³) T3</p> <p>Normal Liver Voxels T3</p> <p>Normal Liver Volume (cm³) T4</p> <p>Normal Liver Voxels T4</p> <p>Normal Liver Volume (cm³) T5</p> <p>Normal Liver Voxels T5</p> <p>STRUCTURE EXPORTATION</p> <p>Exportation→ 'Insertion into the database of structures at RT Struct format'</p> <p>Confirm choosing all structures created, EXCEPT for the lesions (anatomical mode)</p>	<p>Functional contouring results table</p>
	<p>Anatomical contouring results table</p>

Exportation of segmentation (3)

Total Counts	
Time	Whole Liver
T1	
T2	
T3	Anatomical contouring results table
T4	
T5	
Time	R_Kidney
T1	
T2	
T3	Anatomical contouring results table
T4	
T5	
Time	L_Kidney
T1	
T2	
T3	Anatomical contouring results table
T4	
T5	
Time	Normal_Liver
T1	
T2	
T3	Anatomical contouring results table
T4	
T5	
Time	1-Anterior (Lesion)
T1	
T2	
T3	Functional contouring results table
T4	
T5	
Time	2-Lateral (Lesion)
T1	
T2	
T3	Functional contouring results table
T4	
T5	

Exportation of total counts (1)

Time	3-Posterior (Lesion)
T1	Functional contouring results table
T2	
T3	
T4	
T5	
Time	4-Inferior (Lesion)
T1	Functional contouring results table
T2	
T3	
T4	
T5	
Time	Patient FOV
T1	Anatomical contouring results table
T2	
T3	
T4	
T5	

Exportation of total counts (2)

Activity quantification in each VOI	
Unit	MBq
	Whole_Liver
T1	Time integrated activity results table
T2	
T3	
T4	
T5	
	R_Kidney
T1	Time integrated activity results table
T2	
T3	
T4	
T5	
	L_Kidney
T1	Time integrated activity results table
T2	
T3	
T4	
T5	
	Normal_Liver
T1	Time integrated activity results table
T2	
T3	
T4	
T5	
	1- Anterior (Lesion)
T1	Time integrated activity results table The structure without "(anat)" suffix in the name must be used
T2	
T3	
T4	
T5	
	2- Lateral (Lesion)
T1	Time integrated activity results table The structure without "(anat)" suffix in the name must be used
T2	
T3	
T4	
T5	
	3- Posterior (Lesion)
T1	

Exportation of total activity (1)

T2	Time integrated activity results table The structure without "(anat)" suffix in the name must be used
T3	
T4	
T5	
	4-Inferior (Lesion)
T1	Time integrated activity results table The structure without "(anat)" suffix in the name must be used
T2	
T3	
T4	
T5	

Exportation of total activity (2)

Cumulated Activity & Fitting	
Cumulated Activity Unit	MBq.s
Segments	
Whole_Liver	Time integrated activity results table
R_Kidney	Time integrated activity results table
L_Kidney	Time integrated activity results table
Normal_Liver	Time integrated activity results table
1-Anterior (Lesion)	Time integrated activity results table. The structure without "(anat)" suffix in the name must be used.
2-Lateral (Lesion)	Time integrated activity results table. The structure without "(anat)" suffix in the name must be used.
3-Posterior (Lesion)	Time integrated activity results table. The structure without "(anat)" suffix in the name must be used.
4-Inferior (Lesion)	Time integrated activity results table. The structure without "(anat)" suffix in the name must be used.
Patient FOV	Time integrated activity results table
Cumulated activity (in interpolation)	
Segments	
Whole_Liver	Time integrated activity results table
R_Kidney	Time integrated activity results table
L_Kidney	Time integrated activity results table
Normal_Liver	Time integrated activity results table

Exportation of time integrated activity (TIA) and its fitting (1)

1-Anterior (Lesion)	Time integrated activity results table. The structure without "(anat)" suffix in the name must be used.
2-Lateral (Lesion)	Time integrated activity results table. The structure without "(anat)" suffix in the name must be used.
3-Posterior (Lesion)	Time integrated activity results table. The structure without "(anat)" suffix in the name must be used.
4-Inferior (Lesion)	Time integrated activity results table. The structure without "(anat)" suffix in the name must be used.
Patient FOV	Time integrated activity results table
Fitting Equation	
	Whole_Liver
PHARMACOKINETIC FIT	Time integrated activity results table
Model	
Equation	
MSD	
Rho trap	
	R_Kidney
PHARMACOKINETIC FIT	Time integrated activity results table
Model	
Equation	
MSD	
Rho trap	
	L_Kidney
PHARMACOKINETIC FIT	Time integrated activity results table
Model	
Equation	
MSD	
Rho trap	
	Normal_Liver
PHARMACOKINETIC FIT	Time integrated activity results table
Model	
Equation	
MSD	
Rho trap	
	1-Anterior (Lesion)

Exportation of time integrated activity (TIA) and its fitting (2)

PHARMACOKINETIC FIT Model Equation MSD Rho Rho trap	<p style="text-align: center;">Time integrated activity results table The structure without "(anat)" suffix in the name must be used</p>
	2-Lateral (Lesion)
PHARMACOKINETIC FIT Model Equation MSD Rho Rho trap	<p style="text-align: center;">Time integrated activity results table The structure without "(anat)" suffix in the name must be used</p>
	3-Posterior (Lesion)
PHARMACOKINETIC FIT Model Equation MSD Rho Rho trap	<p style="text-align: center;">Time integrated activity results table The structure without "(anat)" suffix in the name must be used</p>
	4-Inferior (Lesion)
PHARMACOKINETIC FIT Model Equation MSD Rho Rho trap	<p style="text-align: center;">Time integrated activity results table The structure without "(anat)" suffix in the name must be used</p>
	Patient FOV
PHARMACOKINETIC FIT Model Equation MSD Rho Rho trap	<p style="text-align: center;">Time integrated activity results table</p>

Exportation of time integrated activity (TIA) and its fitting (3)

Average Absorbed Dose Rate	$\mu\text{Gy/S}$
Time	Whole_Liver
T1	Dose rate results table
T2	
T3	Check/correct for the issue described in the email if "Continue" mode was used for the behavior at the injection time point.
T4	
T5	
Time	R_Kidney
T1	Dose rate results table
T2	
T3	Check/correct for the issue described in the email if "Continue" mode was used for the behavior at the injection time point.
T4	
T5	
Time	L_Kidney
T1	Dose rate results table
T2	
T3	Check/correct for the issue described in the email if "Continue" mode was used for the behavior at the injection time point.
T4	
T5	
Time	Normal_Liver
T1	Dose rate results table
T2	
T3	Check/correct for the issue described in the email if "Continue" mode was used for the behavior at the injection time point.
T4	
T5	
Time	1-Anterior (Lesion)
T1	Dose rate results table
T2	The structure without "(anat)" suffix in the name must be used
T3	
T4	Check/correct for the issue described in the email if "Continue" mode was used for the behavior at the injection time point.
T5	
Time	2-Lateral (Lesion)
T1	Dose rate results table
T2	The structure without "(anat)" suffix in the name must be used
T3	
T4	Check/correct for the issue described in the email if "Continue" mode was used for the behavior at the injection time point.
T5	
Time	3-Posterior (Lesion)
T1	Dose rate results table
T2	The structure without "(anat)" suffix in the name must be used
T3	
T4	
T5	

Exportation of absorbed Dose Rate (ADR) (1)

Time	Check/correct for the issue described in the email if "Continue" mode was used for the behavior at the injection time point.
T1	4-Inferior (Lesion)
T2	Dose rate results table
T3	The structure without "(anat)" suffix in the name must be used
T4	
T5	Check/correct for the issue described in the email if "Continue" mode was used for the behavior at the injection time point.
Fitting Equation	
PHARMACOKINETIC FIT	Whole_Liver
Model	
Equation	Dose rate results table
MSD	
Rho	
Rho trap	
PHARMACOKINETIC FIT	R_Kidney
Model	
Equation	Dose rate results table
MSD	
Rho	
Rho trap	
PHARMACOKINETIC FIT	L_Kidney
Model	
Equation	Dose rate results table
MSD	
Rho	
Rho trap	
PHARMACOKINETIC FIT	Normal_Liver
Model	
Equation	Dose rate results table
MSD	
Rho	
Rho trap	

Exportation of absorbed Dose Rate (ADR) (2)

PHARMACOKINETIC FIT Model Equation MSD Rho Rho trap	1-Anterior (Lesion) Dose rate results table The structure without "(anat)" suffix in the name must be used
PHARMACOKINETIC FIT Model Equation MSD Rho Rho trap	2-Lateral (Lesion) Dose rate results table The structure without "(anat)" suffix in the name must be used
PHARMACOKINETIC FIT Model Equation MSD Rho Rho trap	3-Posterior (Lesion) Dose rate results table The structure without "(anat)" suffix in the name must be used
PHARMACOKINETIC FIT Model Equation MSD Rho Rho trap	4-Inferior (Lesion) Dose rate results table The structure without "(anat)" suffix in the name must be used
PHARMACOKINETIC FIT Model Equation MSD Rho Rho trap	Patient FOV Dose rate results table

Exportation of absorbed Dose Rate (ADR) (3)

Absorbed Dose Calculation Unit Radionuclide' section: Type: Lu177 Radionuclide' section: Half-life: 9571 sec Activity (MBq): Time of administration: (in AM) Enter 'Calibration factor' (Bq) used: should be (Bq) Confirm integration range from 0 to 2400 days Following options used: 'Conv' and 'Dens' should be checked Av. absorbed dose (Gy) R-kidney Av. absorbed dose (Gy) L-kidney Av. absorbed dose (Gy) Whole Liver Av. absorbed dose (Gy) Normal Liver Av. absorbed dose (Gy) Lesion 1 Anterior Av. absorbed dose (Gy) Lesion 2 Lateral Av. absorbed dose (Gy) Lesion 3 Posterior Av. absorbed dose (Gy) Lesion 4 Inferior	Dose rate results table Dose rate results table Dose rate results table Dose rate results table Dose rate results table. The structure without "(anat)" suffix in the name must be used. Dose rate results table. The structure without "(anat)" suffix in the name must be used. Dose rate results table. The structure without "(anat)" suffix in the name must be used. Dose rate results table. The structure without "(anat)" suffix in the name must be used.
---	--

Exportation of absorbed Dose (AD)

B.4 Step-by-step Dosimetry Results

For each parameter compared, mean for each volume of interest is given in the corresponding table along with the coefficient of variation (CoV)¹ in percentage. R-kidney, L-kidney, A_Lesion, L_Lesion, P_Lesion and I_Lesion correspond to right kidney, left kidney, anterior lesion, lateral lesion, posterior lesion and inferior lesion respectively.

In the case of absorbed doses, the mean and standard deviation (S.D.) for each type of time-absorbed dose rate fitting (mono-exponential or bi-exponential) are provided, as well as the number of centres that employed the fitting (number of centres).

¹Coefficient of variation (CoV) is the ratio of standard deviation computed among participants and the mean value.

VOI	Time points	Volumes	
		Mean (in cm ³)	CoV (in %)
Whole Liver	T1	1681.91	9.26
	T2	1681.91	9.26
	T3	1681.91	9.26
	T4	1681.91	9.26
	T5	1681.91	9.26
Normal Liver	T1	1567.93	7.32
	T2	1566.65	8.53
	T3	1571.98	8.56
	T4	1572.00	8.34
	T5	1583.9	9.12
R-kidney	T1	159.09	14.11
	T2	159.09	14.11
	T3	159.09	14.11
	T4	159.09	14.11
	T5	159.09	14.11
L-kidney	T1	175.41	9.38
	T2	175.41	9.38
	T3	175.41	9.38
	T4	175.41	9.38
	T5	175.41	9.38
A_Lesion	T1	82.53	0.00
	T2	85.55	0.00
	T3	73.31	0.04
	T4	74.08	0.00
	T5	65.97	0.00
L_Lesion	T1	15.61	0.02
	T2	13.79	2.91
	T3	9.26	4.71
	T4	10.88	0.99
	T5	5.61	0.00
P_Lesion	T1	23.97	0.00
	T2	27.68	0.00
	T3	20.96	0.00
	T4	19.06	0.00
	T5	15.95	0.00
I_Lesion	T1	21.13	0.00
	T2	20.54	5.00
	T3	15.51	0.00
	T4	16.44	1.00
	T5	14.92	0.00

Mean volumes for each VOI at each time point

VOI	Time points	Total counts		Activity		Activity/ counts	
		Mean (kcounts)	CoV (%)	Mean (MBq)	CoV (%)	Mean (Bq/counts)	CoV (%)
Whole Liver	T1	5314.70	6.70	667.71	6.79	125.64	1.02
	T2	5300.80	6.35	675.27	6.35	127.41	1.49
	T3	4216.22	6.85	537.09	6.85	127.40	1.49
	T4	3493.91	7.43	445.11	7.43	127.40	1.49
	T5	2435.92	7.30	310.35	7.52	127.40	1.49
Normal Liver	T1	4042.30	9.80	502.12	10.21	124.25	3.47
	T2	4287.44	11.64	533.42	11.64	124.48	1.56
	T3	3334.94	10.80	409.78	10.24	122.98	2.57
	T4	2833.45	11.10	349.01	9.95	123.31	2.08
	T5	1987.73	7.90	245.31	8.54	123.39	2.53
R-kidney	T1	668.35	13.70	87.05	11.43	130.75	3.81
	T2	551.23	13.20	73.12	12.06	132.92	3.47
	T3	469.51	11.10	62.31	10.29	132.92	3.47
	T4	358.21	12.00	47.54	11.17	132.92	3.47
	T5	188.89	11.70	25.08	11.54	132.92	3.47
L-kidney	T1	735.26	7.50	92.91	6.51	126.50	3.26
	T2	675.33	7.40	85.48	8.18	126.64	4.88
	T3	535.08	7.70	67.54	9.34	126.21	5.32
	T4	387.23	7.20	48.78	8.82	126.00	5.55
	T5	211.15	7.50	26.72	7.83	126.65	4.87
A_Lesion	T1	1203.08	0.00	149.70	4.17	124.43	4.17
	T2	1282.25	0.00	157.63	0.76	122.93	0.76
	T3	1138.71	0.00	139.71	0.20	122.69	0.21
	T4	1014.25	0.00	124.95	1.37	123.20	1.37
	T5	682.90	0.00	84.31	1.95	123.45	1.95
L_Lesion	T1	106.16	0.00	13.04	0.43	122.79	0.43
	T2	112.22	2.60	13.76	2.60	122.60	0.00
	T3	72.66	4.22	8.91	4.22	122.60	0.00
	T4	72.76	0.92	8.92	0.92	122.60	0.00
	T5	33.09	0.00	4.06	0.00	122.60	0.00
P_Lesion	T1	215.179	1.20	26.38	1.20	122.60	0.00
	T2	245.99	0.16	30.16	0.16	122.60	0.00
	T3	186.02	2.56	22.81	2.56	122.60	0.00
	T4	154.72	1.99	18.97	1.99	122.60	0.00
	T5	113.44	0.88	13.90	0.88	122.57	0.06
I_Lesion	T1	209.70	1.23	25.71	1.23	122.60	0.00
	T2	246.23	3.90	30.19	3.90	122.60	0.00
	T3	175.94	2.76	21.57	2.76	122.60	0.00
	T4	160.13	1.76	19.63	1.76	122.60	0.00
	T5	111.31	0.89	13.65	0.89	122.60	0.00

Mean counts, activity and activity/counts ratio for each VOI at each time point

VOI	Time points	Activity Conc. (AC)		Absorbed Dose Rate (ADR)		ADR/AC ratio	
		Mean (MBq/ml)	CoV (%)	Mean (μ Gy/s)	CoV (%)	Mean (μ Gy/s)/ (MBq/ml)	CoV (%)
Whole Liver	T1	0.40	3.18	9.16	2.84	23.03	1.74
	T2	0.40	4.11	9.30	3.63	23.11	1.06
	T3	0.32	3.65	7.29	3.31	22.77	1.07
	T4	0.27	3.94	6.06	3.62	22.87	1.04
	T5	0.18	4.40	4.24	4.17	22.96	0.97
Normal Liver	T1	0.32	13.39	7.81	11.01	24.36	5.26
	T2	0.34	12.05	7.79	11.79	22.84	3.51
	T3	0.26	13.38	6.00	12.47	22.91	3.22
	T4	0.22	13.75	5.05	14.12	22.61	6.07
	T5	0.16	11.48	3.58	12.55	23	3.94
R-kidney	T1	0.55	3.59	12.90	3.70	23.48	1.25
	T2	0.46	4.82	10.93	5.09	23.68	1.68
	T3	0.39	5.27	9.26	5.38	23.51	1.76
	T4	0.30	4.11	7.09	4.27	23.61	1.68
	T5	0.16	4.87	3.74	5.18	23.6	1.73
L-kidney	T1	0.53	3.79	12.62	2.82	23.78	2.21
	T2	0.49	4.37	11.81	3.45	24.23	5.75
	T3	0.39	4.91	9.36	4.32	24.35	7.51
	T4	0.28	5.30	6.79	4.24	24.45	7.62
	T5	0.15	4.83	3.69	3.37	24.22	5.53
A_Lesion	T1	1.81	4.17	39.59	1.77	21.85	3.67
	T2	1.84	0.76	40.77	1.59	22.13	1.46
	T3	1.91	0.21	42.19	1.33	22.14	1.23
	T4	1.69	1.37	36.90	1.40	21.88	1.43
	T5	1.28	1.95	28.14	1.19	22.03	1.86
L_Lesion	T1	0.84	0.46	17.50	3.87	21	3.87
	T2	1.00	0.37	21.75	1.82	21.8	1.99
	T3	0.96	0.58	19.26	4.39	20	4.22
	T4	0.82	0.09	17.80	3.38	21.7	3.39
	T5	0.72	0.00	15.10	3.18	20.9	3.18
P_Lesion	T1	1.10	1.20	23.82	2.91	21.64	3.30
	T2	1.09	0.16	23.09	3.39	21.2	3.47
	T3	1.09	2.56	23.53	2.18	21.64	3.67
	T4	1.00	1.99	20.73	3.06	20.84	3.52
	T5	0.87	0.88	18.73	2.64	21.48	3.22
I_Lesion	T1	1.22	1.23	26.01	2.77	21.37	2.82
	T2	1.47	1.09	31.72	3.45	21.56	2.76
	T3	1.39	2.73	28.30	3.48	20.35	3.22
	T4	1.19	1.92	25.47	3.37	21.34	4.22
	T5	0.91	0.89	19.57	3.17	21.39	2.96

Activity concentration (AC), absorbed dose rate (ADR) and ADR/AC ratio for each VOI at each time point

<i>VOI</i>	<i>Absorbed Doses (Gy)</i>					
	<i>Mono-exponential Fit</i>			<i>Bi-exponential Fit</i>		
	Mean (Gy)	CoV (%)	#centres	Mean (Gy)	CoV (%)	#centres
Whole Liver	4.01	2.99	7	3.49	n.a.	1
Normal Liver	3.42	14.62	7	2.64	n.a.	1
R-kidney	3.62	4.42	7	3.45	n.a.	1
L-kidney	3.51	3.99	7	3.39	n.a.	1
A_Lesion	39.48	1.49	3	30.61	5.10	5
L_Lesion	27.43	6.09	4	17.32	6.47	4
P_Lesion	33.52	7.88	6	39.93	1.45	2
I_Lesion	24.72	2.47	3	20.14	8.19	5

Absorbed Doses for each defined volume of interest (VOIs)

Bibliography

- Agostinelli, S. et al. (July 2003). “Geant4—a simulation toolkit”. In: *Nucl. Instrum. Methods Phys. Res. A* 506.3, pp. 250–303.
- Ahmadzadehfar, H. (2016). “Targeted Therapy for Metastatic Prostate Cancer with Radionuclides”. In: *Prostate Cancer*. Ed. by R. Mohan. Rijeka: IntechOpen. Chap. 6.
- Ahnesjö, A. (July 1989). “Collapsed cone convolution of radiant energy for photon dose calculation in heterogeneous media”. en. In: *Med. Phys.* 16.4, pp. 577–592.
- Amato, E. et al. (Nov. 2012). “An analytical method for computing voxel S values for electrons and photons”. en. In: *Med. Phys.* 39.11, pp. 6808–6817.
- Andersson, M. et al. (Nov. 2017). “IDAC-Dose 2.1, an internal dosimetry program for diagnostic nuclear medicine based on the ICRP adult reference voxel phantoms”. en. In: *EJNMMI Res.* 7.1, p. 88.
- Anthropomorphic SPECT phantom* (2021). en. <https://www.biodex.com/nuclear-medicine/products/phantoms/anthropomorphic-spect-phantom>. Accessed: 2021-12-05.
- Anwar, S. M. et al. (Oct. 2018). “Medical Image Analysis using Convolutional Neural Networks: A Review”. en. In: *J. Med. Syst.* 42.11, p. 226.
- Asl, M. N. et al. (2013). “Analytical image reconstruction methods in emission tomography”. In: *J. Biomed. Sci. Eng.* 06.01, pp. 100–107.
- Assié, K., A. Dieudonné, et al. (Feb. 2008). “Comparison between 2D and 3D dosimetry protocols in 90Y-ibritumomab tiuxetan radioimmunotherapy of patients with non-Hodgkin’s lymphoma”. en. In: *Cancer Biother. Radiopharm.* 23.1, pp. 53–64.
- Assié, K., V. Breton, et al. (July 2004). “Monte Carlo simulation in PET and SPECT instrumentation using GATE”. In: *Nucl. Instrum. Methods Phys. Res. A* 527.1, pp. 180–189.
- Autret, D. et al. (Feb. 2005). “Monte Carlo modeling of gamma cameras for I-131 imaging in targeted radiotherapy”. en. In: *Cancer Biother. Radiopharm.* 20.1, pp. 77–84.
- Bailey, D. L., J. L. Humm, et al. (2014). “Nuclear Medicine Physics: A Handbook for Teachers and Students. Endorsed by: American Association of Physicists in Medicine (AAPM), Asia–Oceania Federation of ...” In.
- Bailey, D. L. and J. L. Humm (2014). *Nuclear medicine physics: a handbook for teachers and students*. Iaea.
- Balakrishnan, G. et al. (Feb. 2019). “VoxelMorph: A Learning Framework for Deformable Medical Image Registration”. en. In: *IEEE Trans. Med. Imaging*.
- Bardiès, M. (2019). “Relevance and implementation of patient-specific dosimetry in targeted radionuclide therapy”. en. In: *BIO Web of Conferences* 14, p. 07001.
- Bardiès, M. and J. I. Gear (Feb. 2021). “Scientific Developments in Imaging and Dosimetry for Molecular Radiotherapy”. en. In: *Clin. Oncol.* 33.2, pp. 117–124.
- Bardiès, M. and M. J. Myers (Oct. 1996). “Computational methods in radionuclide dosimetry”. en. In: *Phys. Med. Biol.* 41.10, pp. 1941–1955.

- Bartel, T. B. et al. (Dec. 2018). “SNMMI Procedure Standard for Bone Scintigraphy 4.0”. en. In: *J. Nucl. Med. Technol.* 46.4, pp. 398–404.
- Beekman, F. J. et al. (Aug. 2002). “Efficient fully 3-D iterative SPECT reconstruction with Monte Carlo-based scatter compensation”. en. In: *IEEE Trans. Med. Imaging* 21.8, pp. 867–877.
- Bellini, S. et al. (June 1979). “Compensation of tissue absorption in emission tomography”. In: *IEEE Trans. Acoust.* 27.3, pp. 213–218.
- Benedetto, A. R. (1987). *Physics in Nuclear Medicine, 2nd ed.* James A. Sorenson and Michael E. Phelps.
- Berker, Y. et al. (Feb. 2016). “Attenuation correction in emission tomography using the emission data—A review”. en. In: *Med. Phys.* 43.2, pp. 807–832.
- Bexelius, T. et al. (June 2018). “Implementation of GPU accelerated SPECT reconstruction with Monte Carlo-based scatter correction”. en. In: *Ann. Nucl. Med.* 32.5, pp. 337–347.
- Bidgood Jr, W. D. et al. (May 1997). “Understanding and using DICOM, the data interchange standard for biomedical imaging”. en. In: *J. Am. Med. Inform. Assoc.* 4.3, pp. 199–212.
- Bippus, R. et al. (2010). “Monte-Carlo-Based Scatter Correction for Quantitative SPECT Reconstruction”. In: *Bildverarbeitung für die Medizin* 574.
- Bolch, W. E., L. G. Bouchet, et al. (1999). “MIRD pamphlet no. 17: the dosimetry of nonuniform activity distributions—radionuclide S values at the voxel level”. In: *Journal of Nuclear*.
- Bolch, W. E., D. Jokisch, et al. (Nov. 2016). “ICRP Publication 133: The ICRP computational framework for internal dose assessment for reference adults: specific absorbed fractions”. en. In: *Ann. ICRP* 45.2, pp. 5–73.
- Bolch, W. E., K. F. Eckerman, et al. (Mar. 2009). “MIRD Pamphlet No. 21: A Generalized Schema for Radiopharmaceutical Dosimetry—Standardization of Nomenclature”. en. In: *J. Nucl. Med.* 50.3, pp. 477–484.
- Bombardieri, E. et al. (2001). “Nuclear medicine imaging of neuroendocrine tumours”. en. In: *Ann. Oncol.* 12 Suppl 2, S51–61.
- Botta, F., A. Mairani, G. Battistoni, et al. (July 2011). “Calculation of electron and isotopes dose point kernels with FLUKA Monte Carlo code for dosimetry in nuclear medicine therapy”. en. In: *Med. Phys.* 38.7, pp. 3944–3954.
- Botta, F., A. Mairani, R. F. Hobbs, et al. (Nov. 2013). “Use of the FLUKA Monte Carlo code for 3D patient-specific dosimetry on PET-CT and SPECT-CT images”. en. In: *Phys. Med. Biol.* 58.22, pp. 8099–8120.
- Boudraa, A. O. et al. (2006). “Image Segmentation Techniques in Nuclear Medicine Imaging”. In: *Quantitative Analysis in Nuclear Medicine Imaging*. Ed. by H. Zaidi. Boston, MA: Springer US, pp. 308–357.
- Brinkmann, B. H. et al. (July 1999). “Quantitative and clinical analysis of SPECT image registration for epilepsy studies”. en. In: *J. Nucl. Med.* 40.7, pp. 1098–1105.
- Brock, K. K. et al. (July 2017). “Use of image registration and fusion algorithms and techniques in radiotherapy: Report of the AAPM Radiation Therapy Committee Task Group No. 132”. en. In: *Med. Phys.* 44.7, e43–e76.
- Brolin, G. et al. (Aug. 2015). “Pharmacokinetic digital phantoms for accuracy assessment of image-based dosimetry in (177)Lu-DOTATATE peptide receptor radionuclide therapy”. en. In: *Phys. Med. Biol.* 60.15, pp. 6131–6149.

- Brun, R. et al. (Apr. 1997). “ROOT — An object oriented data analysis framework”. en. In: *Nucl. Instrum. Methods Phys. Res. A* 389.1-2, pp. 81–86.
- Bruyant, P. P. (Oct. 2002). “Analytic and iterative reconstruction algorithms in SPECT”. en. In: *J. Nucl. Med.* 43.10, pp. 1343–1358.
- Bücking, T. M. et al. (May 2017). “From medical imaging data to 3D printed anatomical models”. en. In: *PLoS One* 12.5, e0178540.
- Budinger, L. R. et al. (1991). “MIRD Primer for Absorbed Dose Calculations, Revised”. In: *New York: The Society of Nuclear Medicine*.
- Buvat, I. and I. Castiglioni (Mar. 2002). “Monte Carlo simulations in SPET and PET”. en. In: *Q. J. Nucl. Med.* 46.1, pp. 48–61.
- Buvat, I. and D. Lazaro (Dec. 2006). “Monte Carlo simulations in emission tomography and GATE: An overview”. In: *Nucl. Instrum. Methods Phys. Res. A* 569.2, pp. 323–329.
- Cao, Z. et al. (Dec. 1996). “Comparison of continuous step-and-shoot versus step-and-shoot acquisition SPECT”. en. In: *J. Nucl. Med.* 37.12, pp. 2037–2040.
- Capala, J. et al. (Dec. 2021). “Dosimetry for Radiopharmaceutical Therapy: Current Practices and Commercial Resources”. en. In: *J. Nucl. Med.* 62.Suppl 3, 3S–11S.
- Caplin, M. E. et al. (Sept. 1998). “Carcinoid tumour”. en. In: *Lancet* 352.9130, pp. 799–805.
- Chang, L.-T. (Feb. 1978). “A Method for Attenuation Correction in Radionuclide Computed Tomography”. In: *IEEE Trans. Nucl. Sci.* 25.1, pp. 638–643.
- Chauvin, M. et al. (Oct. 2020). “OpenDose: Open-Access Resource for Nuclear Medicine Dosimetry”. en. In: *J. Nucl. Med.* 61.10, pp. 1514–1519.
- Cheimariotis, G.-A. et al. (Feb. 2018). “Automatic lung segmentation in functional SPECT images using active shape models trained on reference lung shapes from CT”. en. In: *Ann. Nucl. Med.* 32.2, pp. 94–104.
- Chen, J. and E. C. Frey (Jan. 2020). “Medical Image Segmentation via Unsupervised Convolutional Neural Network”. In: arXiv: [2001.10155 \[cs.CV\]](https://arxiv.org/abs/2001.10155).
- Chen, J., A. K. Jha, et al. (Mar. 2019). “Incorporating CT prior information in the robust fuzzy C-means algorithm for QSPECT image segmentation”. en. In: *Medical Imaging 2019: Image Processing*. Vol. 10949. SPIE, pp. 492–498.
- Cheplygina, V. et al. (2019). *Not-so-supervised: A survey of semi-supervised, multi-instance, and transfer learning in medical image analysis*.
- Cherry, S. R. et al. (Jan. 2012a). “chapter 9 - Nuclear Counting Statistics”. In: *Physics in Nuclear Medicine (Fourth Edition)*. Ed. by S. R. Cherry et al. Philadelphia: W.B. Saunders, pp. 125–140.
- (2012b). *Nuclear Counting Statistics*.
- (Feb. 2012c). *Physics in Nuclear Medicine E-Book*. en. Elsevier Health Sciences.
- (Feb. 2012d). *Physics in Nuclear Medicine E-Book*. en. Elsevier Health Sciences.
- Chiesa, C. et al. (Oct. 2017). “The conflict between treatment optimization and registration of radiopharmaceuticals with fixed activity posology in oncological nuclear medicine therapy”. en. In: *Eur. J. Nucl. Med. Mol. Imaging* 44.11, pp. 1783–1786.
- Chun, S. Y. et al. (2013). *Correction for Collimator-Detector Response in SPECT Using Point Spread Function Template*.
- Cicone, F. et al. (Aug. 2020). “Preclinical Evaluation and Dosimetry of [111In]CHX-DTPA-scFv78-Fc Targeting Endosialin/Tumor Endothelial Marker 1 (TEM1)”. en. In: *Mol. Imaging Biol.* 22.4, pp. 979–991.

- Cooksey, R. W. (2020). “Descriptive Statistics for Summarising Data”. In: *Illustrating Statistical Procedures: Finding Meaning in Quantitative Data*. Ed. by R. W. Cooksey. Singapore: Springer Singapore, pp. 61–139.
- Costa, G. C. A., D. A. B. Bonifácio, et al. (Oct. 2017). “Optimization of GATE simulations for whole-body planar scintigraphic acquisitions using the XCAT male phantom with ^{177}Lu -DOTATATE biokinetics in a Siemens Symbia T2”. In: *Phys. Med.* 42, pp. 292–297.
- Costa, R. P., D. Cardile, et al. (Apr. 2018). “Ra223 in Bone Metastases with Osteolytic Activity”. en. In: *World J. Nucl. Med.* 17.2, pp. 116–119.
- Cristy, M. et al. (1987a). “Specific Absorbed fractions of energy at various ages from internal photon sources: 1, Methods”. In.
- (1987b). “Specific absorbed fractions of energy at various ages from internal photon sources: 2, One-year-old”. In.
- (1987c). “Specific absorbed fractions of energy at various ages from internal photon sources: 3, Five-year-old”. In.
- (1987d). *Specific absorbed fractions of energy at various ages from internal photon sources: 4, Ten-year-old*. Tech. rep. Oak Ridge National Lab., TN (USA).
- (1987e). “Specific absorbed fractions of energy at various ages from internal photon sources: 5, Fifteen-year-old male and adult female”. In.
- (1987f). “Specific absorbed fractions of energy at various ages from internal photon sources: 6, Newborn”. In.
- (1987g). *Specific absorbed fractions of energy at various ages from internal photon sources: 7, Adult male*.
- Cross, W. G. et al. (1992). *Tables of beta-ray dose distributions in water*. Tech. rep. AECL-10521. Atomic Energy of Canada Ltd.
- Crum, W. R. et al. (2004). “Non-rigid image registration: theory and practice”. en. In: *Br. J. Radiol.* 77 Spec No 2, S140–53.
- Cwikla, J. B. et al. (Apr. 2010). “Efficacy of radionuclide treatment DOTATATE Y-90 in patients with progressive metastatic gastroenteropancreatic neuroendocrine carcinomas (GEP-NETs): a phase II study”. en. In: *Ann. Oncol.* 21.4, pp. 787–794.
- d’Abadie, P. et al. (June 2021). “Microspheres Used in Liver Radioembolization: From Conception to Clinical Effects”. en. In: *Molecules* 26.13.
- D’Arienzo, M. et al. (June 2016). “Gamma camera calibration and validation for quantitative SPECT imaging with (^{177}Lu) ”. en. In: *Appl. Radiat. Isot.* 112, pp. 156–164.
- Daisne, J.-F. et al. (Dec. 2003). “Tri-dimensional automatic segmentation of PET volumes based on measured source-to-background ratios: influence of reconstruction algorithms”. en. In: *Radiother. Oncol.* 69.3, pp. 247–250.
- Dash, A. et al. (Mar. 2015). “Peptide receptor radionuclide therapy: an overview”. en. In: *Cancer Biother. Radiopharm.* 30.2, pp. 47–71.
- Davies, A. J. (May 2007). “Radioimmunotherapy for B-cell lymphoma: Y90 ibritumomab tiuxetan and I(131) tositumomab”. en. In: *Oncogene* 26.25, pp. 3614–3628.
- Della Gala, G. et al. (Dec. 2021). “Overview of commercial treatment planning systems for targeted radionuclide therapy”. en. In: *Phys. Med.* 92, pp. 52–61.
- Dewaraja, Y. K., M. Ljungberg, and K. F. Koral (Jan. 2000). “Characterization of scatter and penetration using Monte Carlo simulation in ^{131}I imaging”. en. In: *J. Nucl. Med.* 41.1, pp. 123–130.

- Dewaraja, Y., J. Li, et al. (Nov. 1997). “Quantitative ^{131}I SPECT with triple energy window Compton scatter correction”. In: *1997 IEEE Nuclear Science Symposium Conference Record*. Vol. 2, 1644–1648 vol.2.
- Dewaraja, Y. K., E. C. Frey, et al. (Aug. 2012). “MIRD pamphlet No. 23: quantitative SPECT for patient-specific 3-dimensional dosimetry in internal radionuclide therapy”. en. In: *J. Nucl. Med.* 53.8, pp. 1310–1325.
- Dewaraja, Y. K., M. Ljungberg, and J. A. Fessler (2006). “3-D Monte Carlo-Based Scatter Compensation in Quantitative I-131 SPECT Reconstruction”. en. In: *IEEE Trans. Nucl. Sci.* 53.1, p. 181.
- Dewaraja, Y. K., S. J. Wilderman, et al. (May 2005). “Accurate dosimetry in ^{131}I radionuclide therapy using patient-specific, 3-dimensional methods for SPECT reconstruction and absorbed dose calculation”. en. In: *J. Nucl. Med.* 46.5, pp. 840–849.
- Dieudonné, A. et al. (Oct. 2010). “Fine-resolution voxel S values for constructing absorbed dose distributions at variable voxel size”. en. In: *J. Nucl. Med.* 51.10, pp. 1600–1607.
- Eckerman, K. et al. (2008). “MIRD: radionuclide data and decay schemes 2nd edn (Reston, VA: Society for Nuclear Medicine)”. In: *Published online*.
- EM Opt3* (n.d.). <https://geant4-userdoc.web.cern.ch/geant4-userdoc/UsersGuides/PhysicsListGuide/html/electromagnetic/Opt3.html>. Accessed: 2021-12-10.
- Erdi, Y. E., O. Mawlawi, et al. (Dec. 1997). “Segmentation of lung lesion volume by adaptive positron emission tomography image thresholding”. en. In: *Cancer* 80.12 Suppl, pp. 2505–2509.
- Erdi, Y. E., B. W. Wessels, et al. (Dec. 1995). “Threshold estimation in single photon emission computed tomography and planar imaging for clinical radioimmunotherapy”. en. In: *Cancer Res.* 55.23 Suppl, 5823s–5826s.
- Erlandsson, K., I. Buvat, et al. (Nov. 2012). “A review of partial volume correction techniques for emission tomography and their applications in neurology, cardiology and oncology”. en. In: *Phys. Med. Biol.* 57.21, R119–59.
- Erlandsson, K., B. Thomas, et al. (Aug. 2011). “Partial volume correction in SPECT reconstruction with OSEM”. In: *Nucl. Instrum. Methods Phys. Res. A* 648, S85–S88.
- Fedorov, A. et al. (Nov. 2012). “3D Slicer as an image computing platform for the Quantitative Imaging Network”. en. In: *Magn. Reson. Imaging* 30.9, pp. 1323–1341.
- Fernández, M. et al. (Aug. 2013). “A fast method for rescaling voxel S values for arbitrary voxel sizes in targeted radionuclide therapy from a single Monte Carlo calculation”. en. In: *Med. Phys.* 40.8, p. 082502.
- Ferrer, L., N. Chouin, et al. (2007). *Implementing Dosimetry in GATE: Dose-Point Kernel Validation with GEANT4 4.8.1*.
- Ferrer, L., E. McKay, et al. (May 2009). “DosiTest: Accuracy of a radio-immunotherapy dosimetry protocol”. en. In: *J. Nucl. Med.* 50.supplement 2, pp. 1865–1865.
- Finocchiaro, D., S. Berenato, et al. (Aug. 2020). “Comparison of different calculation techniques for absorbed dose assessment in patient specific peptide receptor radionuclide therapy”. en. In: *PLoS One* 15.8, e0236466.
- Finocchiaro, D., J. I. Gear, et al. (Oct. 2020). “Uncertainty analysis of tumour absorbed dose calculations in molecular radiotherapy”. en. In: *EJNMMI Phys* 7.1, p. 63.

- Firusian, N. et al. (Dec. 1976). “Results of 89 strontium therapy in patients with carcinoma of the prostate and incurable pain from bone metastases: A preliminary report”. en. In: *J. Urol.* 116.6, pp. 764–768.
- Fischer, M. et al. (Apr. 2012). “Radionuclide Therapy of Bone Metastases”. en. In: *Breast Care* 7.2, pp. 100–107.
- Fleming, J. S. et al. (Aug. 1998). “A rule based method for context sensitive threshold segmentation in SPECT using simulation”. en. In: *Phys. Med. Biol.* 43.8, pp. 2309–2323.
- Flower, M. A. (June 2012). *Webb’s Physics of Medical Imaging, Second Edition*. en. CRC Press.
- Flux, G. et al. (2006). “The impact of PET and SPECT on dosimetry for targeted radionuclide therapy”. en. In: *Z. Med. Phys.* 16.1, pp. 47–59.
- Foxx, J. et al. (Dec. 2021). “The SEQC2 epigenomics quality control (EpiQC) study”. en. In: *Genome Biol.* 22.1, p. 332.
- Forrer, F. et al. (Jan. 2006). “Targeted radionuclide therapy with ^{90}Y -DOTATOC in patients with neuroendocrine tumors”. en. In: *Anticancer Res.* 26.1B, pp. 703–707.
- Francis, H. et al. (Apr. 2015). “Quantification of radionuclide uptake levels for primary bone tumors”. In: *Journal of Radiation Research and Applied Sciences* 8.2, pp. 182–189.
- Frey, E. C. and B. M. W. Tsui (2002). “A new method for modeling the spatially-variant, object-dependent scatter response function in SPECT”. In: *1996 IEEE Nuclear Science Symposium. Conference Record*. Anaheim, CA, USA: IEEE.
- Frey, E. C., J. L. Humm, et al. (May 2012). “Accuracy and precision of radioactivity quantification in nuclear medicine images”. en. In: *Semin. Nucl. Med.* 42.3, pp. 208–218.
- Furhang, E. E. et al. (July 1997). “Implementation of a Monte Carlo dosimetry method for patient-specific internal emitter therapy”. en. In: *Med. Phys.* 24.7, pp. 1163–1172.
- Garcia, M.-P. et al. (Dec. 2015). “TestDose: A nuclear medicine software based on Monte Carlo modeling for generating gamma camera acquisitions and dosimetry”. en. In: *Med. Phys.* 42.12, pp. 6885–6894.
- GATE documentation (2018). (*2. Defining a geometry*). https://opengate.readthedocs.io/en/latest/defining_a_geometry.html. Accessed: 2021-12-6.
- GATE documentation (2018). (*Voxelized source and phantom*). https://opengate.readthedocs.io/en/latest/voxelized_source_and_phantom.html. Accessed: 2021-9-28.
- Gates, V. L. et al. (Feb. 2007). “Radioembolization with Yttrium-90 microspheres: review of an emerging treatment for liver tumors”. en. In: *Future Oncol.* 3.1, pp. 73–81.
- Gear, J. I. et al. (Dec. 2018). “EANM practical guidance on uncertainty analysis for molecular radiotherapy absorbed dose calculations”. en. In: *Eur. J. Nucl. Med. Mol. Imaging* 45.13, pp. 2456–2474.
- Ghaly, M. et al. (2016). “Collimator optimization and collimator-detector response compensation in myocardial perfusion SPECT using the ideal observer with and without model mismatch and an anthropomorphic model observer”. In: *Physics in Medicine and Biology* 61.5, pp. 2109–2123.

- Gil, A. V. et al. (2020). “OpenDose3D: A free, collaborative 3D Slicer module for patient-specific dosimetry”. In: *Eur. J. Nucl. Med. Mol. Imaging* 47.SUPPL 1, S314–S315.
- Glatting, G. (2022). “Time-activity Curves”. In: *Handbook of Nuclear Medicine and Molecular Imaging for Physicists*. New York: CRC Press, pp. 69–81.
- Glatting, G., M. Bardiès, et al. (Dec. 2013). “Treatment planning in molecular radiotherapy”. en. In: *Z. Med. Phys.* 23.4, pp. 262–269.
- Glatting, G., P. Kletting, et al. (Nov. 2007). “Choosing the optimal fit function: comparison of the Akaike information criterion and the F-test”. en. In: *Med. Phys.* 34.11, pp. 4285–4292.
- Goetze, S. et al. (July 2007). “Attenuation correction in myocardial perfusion SPECT/CT: effects of misregistration and value of reregistration”. en. In: *J. Nucl. Med.* 48.7, pp. 1090–1095.
- Goldsmith, S. J. (Jan. 2020). “Targeted Radionuclide Therapy: A Historical and Personal Review”. en. In: *Semin. Nucl. Med.* 50.1, pp. 87–97.
- Gottschalk, S. C. et al. (Sept. 1983). “SPECT resolution and uniformity improvements by noncircular orbit”. en. In: *J. Nucl. Med.* 24.9, pp. 822–828.
- Gregory, R. A., I. Murray, J. Gear, M. D. Aldridge, et al. (Jan. 2017). “Objective comparison of lesion detectability in low and medium-energy collimator iodine-123 mIBG images using a channelized Hotelling observer”. en. In: *Phys. Med. Biol.* 62.1, pp. 17–30.
- Gregory, R. A., I. Murray, J. Gear, F. Leek, et al. (Dec. 2019). “Standardised quantitative radioiodine SPECT/CT Imaging for multicentre dosimetry trials in molecular radiotherapy”. en. In: *Phys. Med. Biol.* 64.24, p. 245013.
- Grimes, J. et al. (Dec. 2012). “The accuracy and reproducibility of SPECT target volumes and activities estimated using an iterative adaptive thresholding technique”. en. In: *Nucl. Med. Commun.* 33.12, pp. 1254–1266.
- Gustafsson, J. et al. (Dec. 2017). “SPECT image segmentation for estimation of tumour volume and activity concentration in 177Lu-DOTATATE radionuclide therapy”. en. In: *EJNMMI Res.* 7.1, p. 18.
- H, B. et al. (Sept. 2021). “Nuclear Renal Scan”. In: *StatPearls*. Treasure Island (FL): StatPearls Publishing.
- Hapdey, S. et al. (Oct. 2004). “Quantification in SPECT: myth or reality? A multi-centric study”. In: *IEEE Symposium Conference Record Nuclear Science 2004*. Vol. 5, 3170–3173 Vol. 5.
- Harris, C. R. et al. (Sept. 2020). “Array programming with NumPy”. en. In: *Nature* 585.7825, pp. 357–362.
- Haug, A. R. (Apr. 2020). “PRRT of neuroendocrine tumors: individualized dosimetry or fixed dose scheme?” en. In: *EJNMMI Res.* 10.1, p. 35.
- Heller, S. L. et al. (July 1987). “SPECT instrumentation: performance, lesion detection, and recent innovations”. en. In: *Semin. Nucl. Med.* 17.3, pp. 184–199.
- Henrich, U. et al. (July 2019). “Lutathera®: The First FDA- and EMA-Approved Radiopharmaceutical for Peptide Receptor Radionuclide Therapy”. en. In: *Pharmaceuticals* 12.3, p. 114.
- Hertz, S. et al. (May 1946). “Radioactive iodine in the study of thyroid physiology; the use of radioactive iodine therapy in hyperthyroidism”. en. In: *J. Am. Med. Assoc.* 131, pp. 81–86.

- Hesz, G. et al. (2013). *Optimization of an iterative SPECT reconstruction algorithm utilizing a partial volume effect correction method*.
- Hindorf, C. (Dec. 2014). *Internal dosimetry. Chapter 18*. en.
- Hindorf, C. et al. (June 2010). “EANM Dosimetry Committee guidelines for bone marrow and whole-body dosimetry”. en. In: *Eur. J. Nucl. Med. Mol. Imaging* 37.6, pp. 1238–1250.
- Hippeläinen, E. et al. (Dec. 2016). “Quantitative accuracy of (177)Lu SPECT reconstruction using different compensation methods: phantom and patient studies”. en. In: *EJNMMI Res.* 6.1, p. 16.
- Hirayama, H. et al. (2005). *The EGS5 code system*. Tech. rep. United States. Department of Energy.
- Home - Dositest (Aug. 2021). fr. <http://www.dositest.org>. Accessed: 2022-1-2.
- Huizing, D. M. V., S. M. B. Peters, et al. (June 2020). “A head-to-head comparison between two commercial software packages for hybrid dosimetry after peptide receptor radionuclide therapy”. en. In: *EJNMMI Phys* 7.1, p. 36.
- Huizing, D. M. V., M. Sinaasappel, et al. (Sept. 2020). “177 Lutetium SPECT/CT: Evaluation of collimator, photopeak and scatter correction”. en. In: *J. Appl. Clin. Med. Phys.* 21.9, pp. 272–277.
- Hussein, M. et al. (Dec. 2013). “A comparison of the gamma index analysis in various commercial IMRT/VMAT QA systems”. en. In: *Radiother. Oncol.* 109.3, pp. 370–376.
- Hutton, B. F. (Aug. 2011). “Recent advances in iterative reconstruction for clinical SPECT/PET and CT”. en. In: *Acta Oncol.* 50.6, pp. 851–858.
- Hutton, B. F. et al. (July 2011). “Review and current status of SPECT scatter correction”. en. In: *Phys. Med. Biol.* 56.14, R85–112.
- Ichikawa, H. et al. (2020). “Current state of bone scintigraphy protocols and practice in Japan”. en. In: *Asia Ocean J Nucl Med Biol* 8.2, pp. 116–122.
- ICRP. (2009). “Adult reference computational phantoms”. In: *Ann. ICRP* 39, pp. 1–166.
- International Atomic Energy Agency (2014). *Quantitative Nuclear Medicine Imaging: Concepts, Requirements and Methods, Human Health Reports No. 9*. en. International Atomic Energy Agency.
- Issy-les-Moulineaux, F. (2001). “PENELOPE—a code system for Monte Carlo simulation of electron and photon transport”. In.
- Jacene, H. A. et al. (Sept. 2008). “Advantages of hybrid SPECT/CT vs SPECT alone”. In: *Open Med. Imaging J.* 2.1, pp. 67–79.
- Jackson Collie Miller, L. F. (Mar. 1995). “A Review of Activity Quantification by Planar Imaging Methods”. In: *J. Nucl. Med. Technol.* 23.1, pp. 3–9.
- Jan, S. et al. (Oct. 2004). “GATE: a simulation toolkit for PET and SPECT”. en. In: *Phys. Med. Biol.* 49.19, pp. 4543–4561.
- Janicki, C. et al. (Apr. 2004). “Accurate determination of dose-point-kernel functions close to the origin using Monte Carlo simulations”. en. In: *Med. Phys.* 31.4, pp. 814–818.
- Jaszczak, R. J. et al. (Aug. 1984). “Improved SPECT Quantification Using Compensation for Scattered Photons”. en. In: *J. Nucl. Med.* 25.8, pp. 893–900.
- Jentzen, W. et al. (Jan. 2007). “Segmentation of PET volumes by iterative image thresholding”. en. In: *J. Nucl. Med.* 48.1, pp. 108–114.

- Kadrmas, D. J. et al. (1998). “Application of reconstruction-based scatter compensation to thallium-201 SPECT: implementations for reduced reconstructed image noise”. In: *IEEE Transactions on Medical Imaging* 17.3, pp. 325–333.
- Kawrakow, I. (2001). “The EGSnrc Code System, Monte Carlo Simulation of Electron and photon Transport”. In: *NRCC Report PIRS-701*.
- Kayal, G., M. Chauvin, E. Mora-Ramirez, et al. (2020). *Modeling SPECT auto-contouring acquisition for ^{177}Lu & ^{131}I Molecular Radiotherapy using new developments in Geant4/GATE*. Under review.
- Kayal, G., M. Chauvin, A. Vergara-Gil, et al. (May 2021). “Generation of clinical ^{177}Lu SPECT/CT images based on Monte Carlo simulation with GATE”. en. In: *Phys. Med.* 85, pp. 24–31.
- Keidar, Z. et al. (July 2003). “SPECT/CT in tumor imaging: technical aspects and clinical applications”. en. In: *Semin. Nucl. Med.* 33.3, pp. 205–218.
- Kennedy, A. et al. (Dec. 2017). “Safety of selective internal radiation therapy (SIRT) with yttrium-90 microspheres combined with systemic anticancer agents: expert consensus”. en. In: *J. Gastrointest. Oncol.* 8.6, pp. 1079–1099.
- Ker, J. et al. (2018). “Deep Learning Applications in Medical Image Analysis”. In: *IEEE Access* 6, pp. 9375–9389.
- Kim, C. H. et al. (Oct. 2018). “New mesh-type phantoms and their dosimetric applications, including emergencies”. en. In: *Ann. ICRP* 47.3-4, pp. 45–62.
- Kind, F. et al. (Dec. 2021). “Early PSA Change after [^{177}Lu]PSMA-617 Radioligand Therapy as a Predictor of Biochemical Response and Overall Survival”. en. In: *Cancers* 14.1.
- King, M. A., D. J. deVries, et al. (June 1997). “An investigation of the filtering of TEW scatter estimates used to compensate for scatter with ordered subset reconstructions”. In: *IEEE Trans. Nucl. Sci.* 44.3, pp. 1140–1145.
- King, M. A., D. T. Long, et al. (Sept. 1991). “SPECT volume quantitation: influence of spatial resolution, source size and shape, and voxel size”. en. In: *Med. Phys.* 18.5, pp. 1016–1024.
- King, M. and T. Farncombe (Apr. 2003). “An overview of attenuation and scatter correction of planar and SPECT data for dosimetry studies”. en. In: *Cancer Biother. Radiopharm.* 18.2, pp. 181–190.
- Kletting, P. et al. (Nov. 2009). “Comparing time activity curves using the Akaike information criterion”. en. In: *Phys. Med. Biol.* 54.21, N501–7.
- Knoll, P. et al. (Feb. 2012). “Comparison of advanced iterative reconstruction methods for SPECT/CT”. en. In: *Z. Med. Phys.* 22.1, pp. 58–69.
- Lagerburg, V. et al. (July 2012). “A comparison of different energy window subtraction methods to correct for scatter and downscatter in I-123 SPECT imaging”. en. In: *Nucl. Med. Commun.* 33.7, pp. 708–718.
- Lanconelli, N. et al. (2012). “A free database of radionuclide voxel S values for the dosimetry of nonuniform activity distributions”. In: *Physics in Medicine and Biology* 57.2, pp. 517–533.
- Lassmann, M., U. Eberlein, and J. Tran-Gia (Feb. 2021). “Multicentre Trials on Standardised Quantitative Imaging and Dosimetry for Radionuclide Therapies”. en. In: *Clin. Oncol.* 33.2, pp. 125–130.
- Lassmann, M. and U. Eberlein (Oct. 2018). “The Relevance of Dosimetry in Precision Medicine”. en. In: *J. Nucl. Med.* 59.10, pp. 1494–1499.

- Lawrence, J. H. et al. (June 1949). "Chronic lymphatic leukemia; a study of 100 patients treated with radioactive phosphorus". en. In: *J. Am. Med. Assoc.* 140.7, pp. 585–588.
- Lee, C., D. Lodwick, et al. (June 2007). "Hybrid computational phantoms of the male and female newborn patient: NURBS-based whole-body models". en. In: *Phys. Med. Biol.* 52.12, pp. 3309–3333.
- Lee, I. J., J. Y. Park, et al. (Jan. 2017). "Image-Based Analysis of Tumor Localization After Intra-Arterial Delivery of Technetium-99m-Labeled SPIO Using SPECT/CT and MRI". en. In: *Mol. Imaging* 16, p. 1536012116689001.
- Lee, J.-D., C.-H. Huang, et al. (2007). "An automatic MRI/SPECT registration algorithm using image intensity and anatomical feature as matching characters: application on the evaluation of Parkinson's disease". In: *Nuclear Medicine and Biology* 34.4, pp. 447–457.
- Lee, T. C., A. M. Alessio, et al. (Mar. 2016). "Morphology supporting function: attenuation correction for SPECT/CT, PET/CT, and PET/MR imaging". en. In: *Q. J. Nucl. Med. Mol. Imaging* 60.1, pp. 25–39.
- Levi, J. et al. (May 2007). "Use of SPECT/CT in tumor localization: SPECT/CT versus planar and SPECT imaging in tumor localization". en. In: *J. Nucl. Med.* 48.supplement 2, 477P–477P.
- Lewis, D. P. et al. (Nov. 1998). "Characterization of medium and high energy collimators using ray-tracing and Monte Carlo methods". In: *1998 IEEE Nuclear Science Symposium Conference Record. 1998 IEEE Nuclear Science Symposium and Medical Imaging Conference (Cat. No.98CH36255)*. Vol. 3, 2026–2030 vol.3.
- Li, J., Z. Liang, et al. (Nov. 1998). "An investigation on analytical methods for correction of distance-dependent resolution variation in 3D SPECT imaging". In: *1998 IEEE Nuclear Science Symposium Conference Record. 1998 IEEE Nuclear Science Symposium and Medical Imaging Conference (Cat. No.98CH36255)*. Vol. 3, 1620–1624 vol.3.
- Li, T., L. Zhu, et al. (2020). *BIGDOSE: software for 3D personalized targeted radionuclide therapy dosimetry*.
- Litjens, G. et al. (Dec. 2017). "A survey on deep learning in medical image analysis". en. In: *Med. Image Anal.* 42, pp. 60–88.
- Livieratos, L. et al. (May 2009). "Partial volume effect (PVE) correction in SPECT during or post reconstruction: A comparison study". en. In: *J. Nucl. Med.* 50.supplement 2, pp. 1498–1498.
- Ljungberg, M. (2022). "Handbook of Nuclear Medicine and Molecular Imaging for Physicists: Modelling, Dosimetry and Radiation Protection, Volume II". In.
- Ljungberg, M., A. Celler, et al. (Jan. 2016). "MIRD Pamphlet No. 26: Joint EANM/MIRD Guidelines for Quantitative ¹⁷⁷Lu SPECT Applied for Dosimetry of Radiopharmaceutical Therapy". en. In: *J. Nucl. Med.* 57.1, pp. 151–162.
- Ljungberg, M. and K. S. Gleisner (July 2015). "Hybrid Imaging for Patient-Specific Dosimetry in Radionuclide Therapy". en. In: *Diagnostics (Basel)* 5.3, pp. 296–317.
- Ljungberg, M. and P. H. Pretorius (Jan. 2018). "SPECT/CT: an update on technological developments and clinical applications". en. In: *Br. J. Radiol.* 91.1081, p. 20160402.
- Ljungberg, M., K. Sjögreen, et al. (Aug. 2002). "A 3-Dimensional Absorbed Dose Calculation Method Based on Quantitative SPECT for Radionuclide Therapy:

- Evaluation for ^{131}I Using Monte Carlo Simulation”. en. In: *J. Nucl. Med.* 43.8, pp. 1101–1109.
- Ljungberg, M. and K. Sjögreen Gleisner (Nov. 2016). “Personalized Dosimetry for Radionuclide Therapy Using Molecular Imaging Tools”. en. In: *Biomedicines* 4.4.
- Ljungberg, M., S.-E. Strand, et al. (Nov. 2012). *Monte Carlo Calculations in Nuclear Medicine, Second Edition: Applications in Diagnostic Imaging*. en. CRC Press.
- Love, C. et al. (Mar. 2003). “Radionuclide bone imaging: an illustrative review”. en. In: *Radiographics* 23.2, pp. 341–358.
- Low, D. A. et al. (May 1998). “A technique for the quantitative evaluation of dose distributions”. en. In: *Med. Phys.* 25.5, pp. 656–661.
- Low Ph.D, D. A. (Nov. 2010). “Gamma Dose Distribution Evaluation Tool”. In: *J. Phys. Conf. Ser.* 250, p. 012071.
- Lu, A. (n.d.). *Comparative assessment of several SPECT scatter correction methods using SimSPECT*.
<https://dspace.mit.edu/bitstream/handle/1721.1/39773/37520851-MIT.pdf;sequence=2>. Accessed: 2021-9-7.
- Lycklama à Nijeholt, G. A. B. et al. (Dec. 1986). “The reliability of Tc-99m-DMSA scintigraphy in obstructive uropathy: is late scanning at 24 hours necessary?” In: *World J. Urol.* 3.4, pp. 253–255.
- Maintz, J. B. et al. (Mar. 1998). “A survey of medical image registration”. en. In: *Med. Image Anal.* 2.1, pp. 1–36.
- Marinelli, M. et al. (Apr. 2012). “Automatic PET-CT image registration method based on mutual information and genetic algorithms”. en. In: *ScientificWorldJournal* 2012, p. 567067.
- Mason, D. (June 2011). “SU-E-T-33: Pydicom: An Open Source DICOM Library”. In: *Med. Phys.* 38.6Part10, pp. 3493–3493.
- McGowan, D. R. et al. (Mar. 2015). “Time to demand dosimetry for molecular radiotherapy?” en. In: *Br. J. Radiol.* 88.1047, p. 20140720.
- McKay, E. et al. (May 2009). “TestDose: Software for creating dosimetry problems”. en. In: *J. Nucl. Med.* 50.supplement 2, pp. 1864–1864.
- McParland, B. J. (July 2010). *Nuclear Medicine Radiation Dosimetry: Advanced Theoretical Principles*. en. Springer Science & Business Media.
- Meijering, E. H. W. et al. (1999). “Quantitative Comparison of Sinc-Approximating Kernels for Medical Image Interpolation”. In: *Medical Image Computing and Computer-Assisted Intervention – MICCAI’99*. Springer Berlin Heidelberg, pp. 210–217.
- Menzel, H.-G. et al. (2009). “ICRP Publication 110. Realistic reference phantoms: an ICRP/ICRU joint effort. A report of adult reference computational phantoms”. en. In: *Ann. ICRP* 39.2, pp. 1–164.
- Mettler, F. A. et al. (Jan. 2012). *Essentials of Nuclear Medicine Imaging*. un. Elsevier Health Sciences.
- Meyers, N. et al. (May 2020). “Inter-observer variability of ^{90}Y PET/CT dosimetry in hepatocellular carcinoma after glass microspheres transarterial radioembolization”. en. In: *EJNMMI Phys* 7.1, p. 29.
- Mezzenga, E. et al. (Aug. 2017). “Quantitative accuracy of ^{177}Lu SPECT imaging for molecular radiotherapy”. en. In: *PLoS One* 12.8, e0182888.
- MIRD (2021). <https://www.nndc.bnl.gov/nudat2/mird/>. Accessed: 2020-09-10.

- Mora-Ramirez, E. et al. (Sept. 2020). “Comparison of commercial dosimetric software platforms in patients treated with 177 Lu-DOTATATE for peptide receptor radionuclide therapy”. en. In: *Med. Phys.* 47.9, pp. 4602–4615.
- Mortelmans, L. et al. (1986). “A new thresholding method for volume determination by SPECT”. en. In: *Eur. J. Nucl. Med.* 12.5-6, pp. 284–290.
- Motulsky, H. et al. (May 2004). *Fitting Models to Biological Data Using Linear and Nonlinear Regression: A Practical Guide to Curve Fitting*. en. Oxford University Press.
- MRTDosimetry* (2016). en. <http://mrtdosimetry-empir.eu/>. Accessed: 2021-12-5.
- Müller, J. W. (July 2000). “Possible Advantages of a Robust Evaluation of Comparisons”. en. In: *J. Res. Natl. Inst. Stand. Technol.* 105.4, pp. 551–555.
- Munley, M. T. et al. (Feb. 1999). “Multimodality nuclear medicine imaging in three-dimensional radiation treatment planning for lung cancer: challenges and prospects”. en. In: *Lung Cancer* 23.2, pp. 105–114.
- Nijssen, J. F. W. et al. (Jan. 2002). “Advances in nuclear oncology: microspheres for internal radionuclide therapy of liver tumours”. en. In: *Curr. Med. Chem.* 9.1, pp. 73–82.
- Ogawa, K. et al. (1991). “A practical method for position-dependent Compton-scatter correction in single photon emission CT”. en. In: *IEEE Trans. Med. Imaging* 10.3, pp. 408–412.
- OpenDose* (2018). en. <http://opendose.org>. Accessed: 2021-12-31.
- Pacilio, M., C. Basile, et al. (June 2011). “An innovative iterative thresholding algorithm for tumour segmentation and volumetric quantification on SPECT images: Monte Carlo-based methodology and validation”. en. In: *Med. Phys.* 38.6, pp. 3050–3061.
- Pacilio, M., N. Lanconelli, et al. (May 2009). “Differences among Monte Carlo codes in the calculations of voxel S values for radionuclide targeted therapy and analysis of their impact on absorbed dose evaluations”. en. In: *Med. Phys.* 36.5, pp. 1543–1552.
- Papadimitroulas, P. et al. (Aug. 2012). “A dose point kernel database using GATE Monte Carlo simulation toolkit for nuclear medicine applications: comparison with other Monte Carlo codes”. en. In: *Med. Phys.* 39.8, pp. 5238–5247.
- Pereira, J. M. et al. (Nov. 2010). “Image quantification for radiation dose calculations—limitations and uncertainties”. en. In: *Health Phys.* 99.5, pp. 688–701.
- Peters, S. M. B. et al. (Dec. 2019). “Towards standardization of absolute SPECT/CT quantification: a multi-center and multi-vendor phantom study”. en. In: *EJNMMI Phys* 6.1, p. 29.
- Petoussi-Henss, N. et al. (Sept. 2014). “ICRP Publication 116—the first ICRP/ICRU application of the male and female adult reference computational phantoms”. en. In: *Phys. Med. Biol.* 59.18, pp. 5209–5224.
- Pham, D. L. et al. (2000). “Current methods in medical image segmentation”. en. In: *Annu. Rev. Biomed. Eng.* 2, pp. 315–337.
- Pinter, C. et al. (Oct. 2012). “SlicerRT: radiation therapy research toolkit for 3D Slicer”. en. In: *Med. Phys.* 39.10, pp. 6332–6338.
- Rahmim, A. et al. (Mar. 2008). “PET versus SPECT: strengths, limitations and challenges”. en. In: *Nucl. Med. Commun.* 29.3, pp. 193–207.
- Renard, F. et al. (Aug. 2020). “Variability and reproducibility in deep learning for medical image segmentation”. en. In: *Sci. Rep.* 10.1, p. 13724.

- Renze, K. J. (1995). "Unstructured surface and volume decimation of tessellated domains". PhD thesis. Iowa State University.
- Ritt, P. et al. (Dec. 2014). "SPECT/CT technology". In: *Clinical and Translational Imaging* 2.6, pp. 445–457.
- Robinson, A. (Feb. 2021). *MRTDosimetry data repository. 2021.*
<https://doi.org/10.17605/OSF.IO/69NGE>.
- Rousset, O. G. et al. (2006). "Correction for Partial Volume Effects in Emission Tomography". In: *Quantitative Analysis in Nuclear Medicine Imaging*. Ed. by H. Zaidi. Boston, MA: Springer US, pp. 236–271.
- Roy, K. K. et al. (2014). "Automated medical image segmentation: a survey". In: *Computing, Communication & Manufacturing* 1, pp. 1–5.
- Saini, A. et al. (Jan. 2019). "History and Evolution of Yttrium-90 Radioembolization for Hepatocellular Carcinoma". en. In: *J. Clin. Med. Res.* 8.1.
- Salem, R. et al. (Aug. 2006). "Radioembolization with 90Yttrium Microspheres: A State-of-the-Art Brachytherapy Treatment for Primary and Secondary Liver Malignancies: Part 1: Technical and Methodologic Considerations". In: *J. Vasc. Interv. Radiol.* 17.8, pp. 1251–1278.
- Sanders, J. C. et al. (Aug. 2015). "Quantitative SPECT/CT Imaging of (177)Lu with In Vivo Validation in Patients Undergoing Peptide Receptor Radionuclide Therapy". en. In: *Mol. Imaging Biol.* 17.4, pp. 585–593.
- Santin, G. et al. (Oct. 2003). "GATE: a Geant4-based simulation platform for PET and SPECT integrating movement and time management". In: *IEEE Trans. Nucl. Sci.* 50.5, pp. 1516–1521.
- Santoro, L. et al. (2021). "Clinical implementation of PLANET® Dose for dosimetric assessment after [177Lu]Lu-DOTA-TATE: comparison with Dosimetry Toolkit® and OLINDA/EXM® V1.0". In: *EJNMMI Research* 11.1.
- Sarrut, D., A. Halty, et al. (Dec. 2017). "Voxel-based multimodel fitting method for modeling time activity curves in SPECT images". en. In: *Med. Phys.* 44.12, pp. 6280–6288.
- Sarrut, D., M. Bała, et al. (May 2021). "Advanced Monte Carlo simulations of emission tomography imaging systems with GATE". en. In: *Phys. Med. Biol.* 66.10.
- Sarrut, D., M. Bardiès, et al. (June 2014). "A review of the use and potential of the GATE Monte Carlo simulation code for radiation therapy and dosimetry applications". en. In: *Med. Phys.* 41.6, p. 064301.
- Sayed, I. S. (2020). "Influence of source-to-collimator distance on image quality in single photon emission computed tomography (SPECT): A phantom study". In: *INTERNATIONAL JOURNAL OF ALLIED HEALTH SCIENCES* 4.4, pp. 1683–1692.
- Schmidt, M. et al. (Apr. 2016). "I-131-mIBG therapy in neuroblastoma: established role and prospective applications". In: *Clinical and Translational Imaging* 4.2, pp. 87–101.
- Schneider, W. et al. (Feb. 2000). "Correlation between CT numbers and tissue parameters needed for Monte Carlo simulations of clinical dose distributions". en. In: *Phys. Med. Biol.* 45.2, pp. 459–478.
- Seco, J. et al. (Nov. 2021). *Monte Carlo Techniques in Radiation Therapy: Applications to Dosimetry, Imaging, and Preclinical Radiotherapy*. en. CRC Press.
- Seco, J. et al. (Apr. 2016). *Monte Carlo Techniques in Radiation Therapy*. en. Taylor & Francis.

- Segars, W. P. et al. (Sept. 2010). “4D XCAT phantom for multimodality imaging research”. en. In: *Med. Phys.* 37.9, pp. 4902–4915.
- Seret, A. et al. (Aug. 2012). “Quantitative capabilities of four state-of-the-art SPECT-CT cameras”. en. In: *EJNMMI Res.* 2.1, p. 45.
- Sgouros, G., L. Bodei, et al. (Sept. 2020). “Radiopharmaceutical therapy in cancer: clinical advances and challenges”. en. In: *Nat. Rev. Drug Discov.* 19.9, pp. 589–608.
- Sgouros, G. and R. F. Hobbs (2012). “Patient-specific dosimetry, radiobiology, and the previously-treated patient”. In: *Therapeutic Nuclear Medicine*. Berlin, Heidelberg: Springer Berlin Heidelberg, pp. 737–745.
- Shanei, A. et al. (Oct. 2015). “Estimation of Organ Activity using Four Different Methods of Background Correction in Conjugate View Method”. en. In: *J. Med. Signals Sens.* 5.4, pp. 253–258.
- Sharma, N. et al. (Jan. 2010). “Automated medical image segmentation techniques”. en. In: *J. Med. Phys.* 35.1, pp. 3–14.
- Shcherbinin, S. et al. (Sept. 2008). “Accuracy of quantitative reconstructions in SPECT/CT imaging”. en. In: *Phys. Med. Biol.* 53.17, pp. 4595–4604.
- Shepp, L. A. et al. (1982). “Maximum likelihood reconstruction for emission tomography”. en. In: *IEEE Trans. Med. Imaging* 1.2, pp. 113–122.
- Shin, W.-G. et al. (Sept. 2021). “A Geant4-DNA Evaluation of Radiation-Induced DNA Damage on a Human Fibroblast”. en. In: *Cancers* 13.19.
- Siegel, J. A. et al. (Feb. 1999). “MIRD pamphlet no. 16: Techniques for quantitative radiopharmaceutical biodistribution data acquisition and analysis for use in human radiation dose estimates”. en. In: *J. Nucl. Med.* 40.2, 37S–61S.
- Singh, I., B. Singh, et al. (July 2020). “Comparative study for intermediate crystal size of NaI(Tl) scintillation detector”. en. In: *Rev. Sci. Instrum.* 91.7, p. 073105.
- Singh, S. P., L. Wang, et al. (Sept. 2020). “3D Deep Learning on Medical Images: A Review”. en. In: *Sensors* 20.18.
- Sjögreen Gleisner, K. et al. (Dec. 2017). “Variations in the practice of molecular radiotherapy and implementation of dosimetry: results from a European survey”. en. In: *EJNMMI Phys* 4.1, p. 28.
- Smith, N. B. et al. (Nov. 2010). *Introduction to Medical Imaging: Physics, Engineering and Clinical Applications*. en. Cambridge University Press.
- “SNMMI 177Lu Dosimetry Challenge 2021” (Apr. 2021). en. In: *J. Nucl. Med.* 62.4, 10N.
- Snyder, W. S. (1975). ““ S” absorbed dose per unit cumulated activity for selected radionuclides and organs”. In: *MIRD Pamphlet no. 11*.
- Spiess, A.-N. et al. (June 2010). “An evaluation of R2 as an inadequate measure for nonlinear models in pharmacological and biochemical research: a Monte Carlo approach”. en. In: 10, p. 6.
- St James, S. et al. (Mar. 2021). “Current Status of Radiopharmaceutical Therapy”. en. In: *Int. J. Radiat. Oncol. Biol. Phys.* 109.4, pp. 891–901.
- Stabin, M. G., M. T. Madsen, et al. (Nov. 2019). “Personalized dosimetry is a must for appropriate molecular radiotherapy”. en. In: *Med. Phys.* 46.11, pp. 4713–4716.
- Stabin, M. G. and J. A. Siegel (Jan. 2018). “RADAR Dose Estimate Report: A Compendium of Radiopharmaceutical Dose Estimates Based on OLINDA/EXM Version 2.0”. en. In: *J. Nucl. Med.* 59.1, pp. 154–160.

- Stabin, M. G., R. B. Sparks, et al. (June 2005). "OLINDA/EXM: the second-generation personal computer software for internal dose assessment in nuclear medicine". en. In: *J. Nucl. Med.* 46.6, pp. 1023–1027.
- Stabin, M. G., X. G. Xu, et al. (Nov. 2012). "RADAR reference adult, pediatric, and pregnant female phantom series for internal and external dosimetry". en. In: *J. Nucl. Med.* 53.11, pp. 1807–1813.
- Staelens, S. et al. (Sept. 2003). "Monte Carlo simulations of a scintillation camera using GATE: validation and application modelling". en. In: *Phys. Med. Biol.* 48.18, pp. 3021–3042.
- Stokke, C. et al. (Nov. 2017). "Dosimetry-based treatment planning for molecular radiotherapy: a summary of the 2017 report from the Internal Dosimetry Task Force". en. In: *EJNMMI Phys* 4.1, p. 27.
- Strigari, L. et al. (Sept. 2006). "Monte Carlo dose voxel kernel calculations of beta-emitting and Auger-emitting radionuclides for internal dosimetry: A comparison between EGSnrcMP and EGS4". en. In: *Med. Phys.* 33.9, pp. 3383–3389.
- Strulab, D. et al. (Sept. 2003). "GATE (geant4 application for tomographic emission): a PET/SPECT general-purpose simulation platform". In: *Nuclear Physics B - Proceedings Supplements* 125, pp. 75–79.
- Stute, S. et al. (Oct. 2011). "Monte Carlo simulations of clinical PET and SPECT scans: impact of the input data on the simulated images". en. In: *Phys. Med. Biol.* 56.19, pp. 6441–6457.
- Tang, L. et al. (Aug. 2006). "Co-registration of Bone CT and SPECT Images Using Mutual Information". In: *2006 IEEE International Symposium on Signal Processing and Information Technology*, pp. 116–121.
- Taprogge, J. et al. (Oct. 2020). "Setting up a quantitative SPECT imaging network for a European multi-centre dosimetry study of radioiodine treatment for thyroid cancer as part of the MEDIRAD project". en. In: *EJNMMI Phys* 7.1, p. 61.
- Taylor, A. T. (May 2014). "Radionuclides in nephrourology, Part 2: pitfalls and diagnostic applications". en. In: *J. Nucl. Med.* 55.5, pp. 786–798.
- Taylor, A. T. et al. (July 2018). "SNMMI procedure standard/EANM practice guideline for diuretic renal scintigraphy in adults with suspected upper urinary tract obstruction 1.0". en. In: *Semin. Nucl. Med.* 48.4, pp. 377–390.
- Teunissen, J. J. M. et al. (Oct. 2011). "Nuclear medicine techniques for the imaging and treatment of neuroendocrine tumours". en. In: *Endocr. Relat. Cancer* 18 Suppl 1, S27–51.
- Themes, U. F. O. (Mar. 2016). *Nuclear medicine imaging*.
<https://radiologykey.com/nuclear-medicine-imaging-2/>. Accessed: 2021-9-2.
- Tran-Gia, J. et al. (July 2021). "A multicentre and multi-national evaluation of the accuracy of quantitative Lu-177 SPECT/CT imaging performed within the MRTDosimetry project". en. In: *EJNMMI Phys* 8.1, p. 55.
- Urago, Y. et al. (Sept. 2021). "Evaluation of auto-segmentation accuracy of cloud-based artificial intelligence and atlas-based models". en. In: *Radiat. Oncol.* 16.1, p. 175.
- Uribe, C. F. et al. (Dec. 2017). "Accuracy of ¹⁷⁷Lu activity quantification in SPECT imaging: a phantom study". en. In: *EJNMMI Phys.* 4.1, p. 2.
- Van Audenhaege, K. et al. (Aug. 2015). "Review of SPECT collimator selection, optimization, and fabrication for clinical and preclinical imaging". en. In: *Med. Phys.* 42.8, pp. 4796–4813.

- Van den Wyngaert, T. et al. (Aug. 2016). “The EANM practice guidelines for bone scintigraphy”. en. In: *Eur. J. Nucl. Med. Mol. Imaging* 43.9, pp. 1723–1738.
- Van Gils, C. A. J. et al. (2016). “Impact of reconstruction parameters on quantitative I-131 SPECT”. In: *Physics in Medicine & Biology*.
- Van Rossum, G. et al. (2009). “Python 3 Reference Manual CreateSpace”. In: *Scotts Valley, CA*.
- Vandenberghe, S. et al. (Mar. 2001). “Iterative reconstruction algorithms in nuclear medicine”. en. In: *Comput. Med. Imaging Graph.* 25.2, pp. 105–111.
- Van Elmbt, L. et al. (Sept. 1993). “Simultaneous correction of attenuation and distance-dependent resolution in SPECT: an analytical approach”. en. In: *Phys. Med. Biol.* 38.9, p. 1207.
- Varma, D. R. (July 2021). “Managing DICOM images: Tips and tricks for the radiologist”. en. In: *Indian J. Radiol. Imaging* 22.01, pp. 4–13.
- Vértes, A. et al. (Dec. 2010). *Handbook of Nuclear Chemistry: Vol. 1: Basics of Nuclear Science; Vol. 2: Elements and Isotopes: Formation, Transformation, Distribution; Vol. 3: Chemical Applications of Nuclear Reactions and Radiation; Vol. 4: Radiochemistry and Radiopharmaceutical Chemistry in Life Sciences; Vol. 5: Instrumentation, Separation Techniques, Environmental Issues; Vol. 6: Nuclear Energy Production and Safety Issues*. en. Springer Science & Business Media.
- Villeneuve, J.-C. et al. (2019). *CALMIP*. <https://www.calmip.univ-toulouse.fr/>. Accessed: 2021-12-12.
- Villoing, D. et al. (Mar. 2017). “Internal dosimetry with the Monte Carlo code GATE: validation using the ICRP/ICRU female reference computational model”. en. In: *Phys. Med. Biol.* 62.5, pp. 1885–1904.
- Virgolini, I. et al. (June 2005). “Nuclear medicine in the detection and management of pancreatic islet-cell tumours”. en. In: *Best Pract. Res. Clin. Endocrinol. Metab.* 19.2, pp. 213–227.
- Waters, L. S. et al. (2007). “The MCNPX Monte Carlo Radiation Transport Code”. In: *AIP Conference Proceedings*. Batavia, Illinois (USA): AIP.
- Welch, A. et al. (Oct. 1997). “Toward accurate attenuation correction in SPECT without transmission measurements”. en. In: *IEEE Trans. Med. Imaging* 16.5, pp. 532–541.
- Wendling, M. et al. (May 2007). “A fast algorithm for gamma evaluation in 3D”. en. In: *Med. Phys.* 34.5, pp. 1647–1654.
- Westcott, M. A. et al. (Oct. 2016). “The development, commercialization, and clinical context of yttrium-90 radiolabeled resin and glass microspheres”. en. In: *Adv Radiat Oncol* 1.4, pp. 351–364.
- Wevrett, J., A. Fenwick, J. Scuffham, and A. Nisbet (Nov. 2017). “Development of a calibration protocol for quantitative imaging for molecular radiotherapy dosimetry”. In: *Radiat. Phys. Chem.* 140, pp. 355–360.
- Wevrett, J., A. Fenwick, J. Scuffham, L. Johansson, et al. (Aug. 2018). “Inter-comparison of quantitative imaging of lutetium-177 (¹⁷⁷Lu) in European hospitals”. en. In: *EJNMMI Phys* 5.1, p. 17.
- Williamson, D. F. et al. (June 1989). “The box plot: a simple visual method to interpret data”. en. In: *Ann. Intern. Med.* 110.11, pp. 916–921.
- Wu, J. et al. (Nov. 2012). “Dose point kernel simulation for monoenergetic electrons and radionuclides using Monte Carlo techniques”. en. In: *Radiat. Prot. Dosimetry* 152.1-3, pp. 119–124.

- Xiao, J. et al. (Apr. 2007). “Evaluation of 3D Monte Carlo–Based Scatter Correction for 201Tl Cardiac Perfusion SPECT”. en. In: *J. Nucl. Med.* 48.4, pp. 637–644.
- Xu, X. G. (Sept. 2014). “An exponential growth of computational phantom research in radiation protection, imaging, and radiotherapy: a review of the fifty-year history”. en. In: *Phys. Med. Biol.* 59.18, R233–302.
- Xu, X. G. et al. (2007). “A boundary-representation method for designing whole-body radiation dosimetry models: pregnant females at the ends of three gestational periods—RPI-P3,-P6 and-P9”. In: *Physics in Medicine & Biology* 52.23, p. 7023.
- Yaniv, Z. et al. (June 2018). “SimpleITK Image-Analysis Notebooks: a Collaborative Environment for Education and Reproducible Research”. en. In: *J. Digit. Imaging* 31.3, pp. 290–303.
- Yeong, C.-H. et al. (Oct. 2014). “Therapeutic radionuclides in nuclear medicine: current and future prospects”. en. In: *J. Zhejiang Univ. Sci. B* 15.10, pp. 845–863.
- Yordanova, A. et al. (Oct. 2017). “Theranostics in nuclear medicine practice”. en. In: *Onco. Targets. Ther.* 10, pp. 4821–4828.
- Zaidi, H. and G. Sgouros (Sept. 2002). *Therapeutic Applications of Monte Carlo Calculations in Nuclear Medicine*. en. CRC Press.
- Zaidi, H., ed. (2006). *Quantitative Analysis in Nuclear Medicine Imaging*. Springer, Boston, MA.
- Zaidi, H. and P. Andreo (2002). “Monte Carlo techniques in nuclear medicine dosimetry”. In: *Therapeutic Applications of Monte Carlo Calculations in Nuclear Medicine*. CRC Press, pp. 28–54.
- Zaidi, H. and K. F. Koral (May 2004). “Scatter modelling and compensation in emission tomography”. en. In: *Eur. J. Nucl. Med. Mol. Imaging* 31.5, pp. 761–782.
- Zaidi, H. and X. G. Xu (2007). “Computational anthropomorphic models of the human anatomy: the path to realistic Monte Carlo modeling in radiological sciences”. en. In: *Annu. Rev. Biomed. Eng.* 9, pp. 471–500.
- Zanzonico, P. (Apr. 2012). “Principles of nuclear medicine imaging: planar, SPECT, PET, multi-modality, and autoradiography systems”. en. In: *Radiat. Res.* 177.4, pp. 349–364.
- Zanzonico, P. B. (Dec. 2002). “Model-based versus patient-specific dosimetry: blurring the lines”. en. In: *J. Nucl. Med.* 43.12, pp. 1665–1666.
- Zechmann, C. M. et al. (2014). *Radiation dosimetry and first therapy results with a 124I/131I-labeled small molecule (MIP-1095) targeting PSMA for prostate cancer therapy*.
- Zeintl, J. et al. (June 2010). “Quantitative accuracy of clinical 99mTc SPECT/CT using ordered-subset expectation maximization with 3-dimensional resolution recovery, attenuation, and scatter correction”. en. In: *J. Nucl. Med.* 51.6, pp. 921–928.
- Zeng, G. L. (Mar. 2001). “Image reconstruction—a tutorial”. en. In: *Comput. Med. Imaging Graph.* 25.2, pp. 97–103.
- Zeng, G. L. et al. (Jan. 2004). “CHAPTER 7 - Single-Photon Emission Computed Tomography”. In: *Emission Tomography*. Ed. by M. N. Wernick et al. San Diego: Academic Press, pp. 127–152.
- Zhang, X. et al. (Jan. 2020). “A Comparative Study for Non-rigid Image Registration and Rigid Image Registration”. In: arXiv: [2001.03831 \[cs.CV\]](https://arxiv.org/abs/2001.03831).
- Zhao, W. et al. (May 2018). “Determination of gamma camera calibration factors for quantitation of therapeutic radioisotopes”. en. In: *EJNMMI Phys* 5.1, p. 8.

- Zhou, T. et al. (2019). *A review: Deep learning for medical image segmentation using multi-modality fusion*.
- Zimmerman, B. E. et al. (June 2017). “Multi-centre evaluation of accuracy and reproducibility of planar and SPECT image quantification: An IAEA phantom study”. en. In: *Z. Med. Phys.* 27.2, pp. 98–112.
- Zimmermann, R. (Mar. 2019). *Nuclear Medicine: Radioactivity for diagnosis and therapy*. en. EDP sciences.
- Zubal, I. G. et al. (July 1992). “Voxel based Monte Carlo calculations of nuclear medicine images and applied variance reduction techniques”. In: *Image Vis. Comput.* 10.6, pp. 342–348.

Scientific production

Publications

G Kayal, N Clayton, A Vergara-Gil, L Struelens, M Bardiès. Proof-of-concept of DosiTest: A virtual multicentric clinical trial for assessing uncertainties in Molecular Radiotherapy dosimetry (2022). Phys. Med. 97; 25-35. (<https://doi.org/10.1016/j.ejmp.2022.03.011>)

G Kayal, M Chauvin, E Mora-Ramirez, N Clayton, A Vergara-Gil, J Tran-Gia, M Lassmann, N Calvert, J Tipping, L Struelens, The MRTDosimetry Collaboration, M Bardiès. Modelling SPECT auto-contouring acquisition for ^{177}Lu & ^{131}I Molecular Radiotherapy using new developments in Geant4/GATE (2022). Phys. Med. 96; 101-113. (<https://doi.org/10.1016/j.ejmp.2022.03.003>)

D Sarrut, M Bała, M Bardiès, J Bert, M Chauvin, K Chatzipapas, M Dupont, A Etxebeste, L M Fanchon, S Jan, **G Kayal**, ..., E Roncali. Advanced Monte Carlo simulations of emission tomography imaging systems with GATE (2021). Phys. Med. Biol. 66 10TR03. (<https://doi.org/10.1088/1361-6560/abf276>)

G Kayal, M Chauvin, A Vergara-Gil, N Clayton, L Ferrer, T Moalosi, P Knoll, L Struelens, M Bardiès. Generation of clinical ^{177}Lu SPECT/CT images based on Monte Carlo simulation with GATE (2021). Phys. Med. 85; 24-31. (<https://doi.org/10.1016/j.ejmp.2021.04.002>)

Mora-Ramirez E, Santoro L, Cassol E, Ocampo-Ramos JC, Clayton N, **Kayal G**, Chouaf S, Trauchessec D, Pouget J-P, Kotzki P-O, Deshayes E and Bardiès M. Comparison of commercial dosimetric software platforms in patients treated with ^{177}Lu -DOTATATE for peptide receptor radionuclide therapy (2020). Med. Phys. (<https://doi.org/10.1002/mp.14375>)

Tran-Gia J, ..., The MRTDosimetry Collaboration & Lassmann M. A multi-centre and multi-national evaluation of the accuracy of quantitative Lu-177 SPECT/CT imaging performed within the MRTDosimetry project (2021). EJNMMI Phys 8, 55 (as a part of the MRTDosimetry Collaboration). <https://doi.org/10.1186/s40658-021-00397-0>

Book Chapter

M Bardiès, N Clayton, **G Kayal** and A Vergara-Gil. “Patient-Specific Dosimetry Calculations”. In: Handbook of Nuclear Medicine and Molecular Imaging for Physicists (Dec. 2021). New York: CRC Press, pp. 155-168. <https://doi.org/10.1201/9780429489549-10>.

International Conferences

Oral Presentations

G Kayal et al., Generation of realistic patient-specific SPECT images with GATE Monte Carlo simulation for ^{177}Lu dosimetry in Molecular Radiotherapy (MRT), ECMP, Italy 2021.

G Kayal, A Vergara-Gil, M Bardiès. Gate Activities in CRCT, INSERM, France - Nuclear Medicine. OpenGATE scientific meeting France, 2021 <https://indico.in2p3.fr/event/24079/contributions/>

G Kayal, M Chauvin, A Vergara-Gil, N Clayton, L Ferrer, T Moalosi, P Knoll, L Struelens, M Bardiès, Generating clinical SPECT images for dosimetry in Molecular Radiotherapy with GATE Monte Carlo simulation, BHPA Belgium 2021

G Kayal, M Chauvin, E Mora-Ramirez, L Struelens, M Bardiès, Implementation of SPECT auto-contouring detector motion in GATE Monte Carlo simulation for ^{177}Lu and ^{131}I Molecular Radiotherapy (MRT) dosimetry, EANM 2020

G Kayal, M Chauvin, E Mora-Ramirez, L Struelens, M Bardiès, Generation of realistic SPECT/CT images for Lu dosimetry in Molecular Radiotherapy (MRT) based on Monte Carlo simulation with GATE, EANM 2020

A Vergara Gil, E Amato, L Auditore, M Brenet, M Chauvin, N Clayton, L Ferrer, B Gibaud, S Gnesin, A Italiano, **G Kayal**, T Lima, J Camilo Ocampo, D Pistone, G Quan, E. Mora-Ramirez, Jannick Ruegger, Manuel Bardiès, OpenDose3D: A free, collaborative 3D Slicer module for patient-specific dosimetry, EANM 2020

G Kayal, M Chauvin, M Bardiès, L Struelens. Modeling SPECT auto-contouring acquisition for ^{177}Lu Molecular Radiotherapy (MRT) using new developments in GATE. MCMA International Conference held in Montreal, Canada 2019

G Kayal, M Chauvin, M Bardiès, L Struelens. Monte Carlo Simulation of SPECT Imaging. European Workshop on The Clinical Implementation of Dosimetry for Molecular Radiotherapy held in NPL, UK 2019

G Kayal, M Chauvin, A Vergara Gil, E Mora-Ramirez, L Struelens, M Bardiès. Monte Carlo Simulation of SPECT Imaging. European Consortium Meeting and Workshop for the MRT Dosimetry Project held in Thessaloniki, Greece 2019

G Kayal, M Chauvin, M Bardiès, L Struelens. SPECT Modeling for MRT Dosimetry in Open GATE Meeting held in Paris, France 2018

G Kayal, M Chauvin, A Vergara Gil, M Bardiès, L Struelens. MRT Dosimetry Collaboration Meeting (M27). European Consortium Meeting and Workshop for the MRT Dosimetry Project held in Prague, Czech Republic 2018

G Kayal, M Chauvin, M Bardiès, L Struelens. Clinical Dosimetry in Molecular Radiotherapy. SCK CEN PhD Day Mol, Belgium 2020

G Kayal, M Chauvin, M Bardiès, L Struelens. Clinical Dosimetry in Molecular Radiotherapy. SCK CEN PhD Day held in Mol, Belgium 2019

Poster Presentations

A Vergara Gil, E Amato, L Auditore, M Brenet, M Chauvin, N Clayton, L Ferrer, B Gibaud, S Gnesin, A Italiano, **G Kayal et al.**, Opendose3D a free, collaborative 3d slicer module for patient-specific dosimetry, 67th International Meeting of Radiation Research Society, San Juan Puerto Rico 3-6 October 2021

G Kayal et al., DosiTest: a virtual multicentric clinical trial for assessing uncertainties in clinical dosimetry in Molecular RadioTherapy based on Monte Carlo simulation, 67th International Meeting of Radiation Research Society, San Juan Puerto Rico 3-6 October 2021

G Kayal et al., Implementation of SPECT auto-contouring detector motion in GATE Monte Carlo simulation for ¹⁷⁷Lu and ¹³¹I Molecular Radiotherapy (MRT) dosimetry, ECMP Italy, 16-19 June 2021

G Kayal et al., Generation of clinical ¹⁷⁷Lu SPECT/CT images for dosimetry in Molecular Radiotherapy based on Monte Carlo simulation with GATE SNMMI, USA, 11-15 June 2021

A. Vergara Gil, M. Chauvin, **G. Kayal**, J. Ocampo, M. Bardiès. Geant4/GATE ion source implementation for internal dosimetry applications, Annual Congress of the European Association of Nuclear Medicine (EANM), European Journal of Nuclear Medicine and Molecular Imaging (2019) 46 (Suppl 1): S1–S952. (<https://doi.org/10.1007/s00259-019-04486-2>)

National Conferences

Oral Presentations

G Kayal et al., DosiTest: Generation of simulated datasets for patient-specific dosimetry in molecular radiotherapy, SFPM, Rennes 2021.